Painted Roads:

A super-resolution study of the neuronal cytoskeleton

ISBN: 978-94-632-3765-9

The studies described in this thesis were performed at the division of Cell Biology at the Faculty of Science of Utrecht University, The Netherlands.

This work is supported by the European Research Council (ERC)

Printed by: Gildeprint, Enschede

Copyright by R.P. Tas, 2019
All rights reserved

Painted Roads:

A super-resolution study of the neuronal cytoskeleton

Geschilderde wegen:
Een superresolutiestudie van het neuronale celskelet

(met een samenvatting in het Nederlands)

Proefschrift

ter verkrijging van de graad van doctor aan de
Universiteit Utrecht
op gezag van de
rector magnificus, prof.dr. H.R.B.M. Kummeling,
ingevolge het besluit van het college voor promoties
in het openbaar te verdedigen op

woensdag 4 september 2019 des middags te 2.30 uur

door

Roderick Prudent Tas

geboren op 15 juni 1991
te Den Helder

Promotoren:

Prof. dr. L.C. Kapitein
Prof. dr. C.C. Hoogenraad

TABLE OF CONTENTS

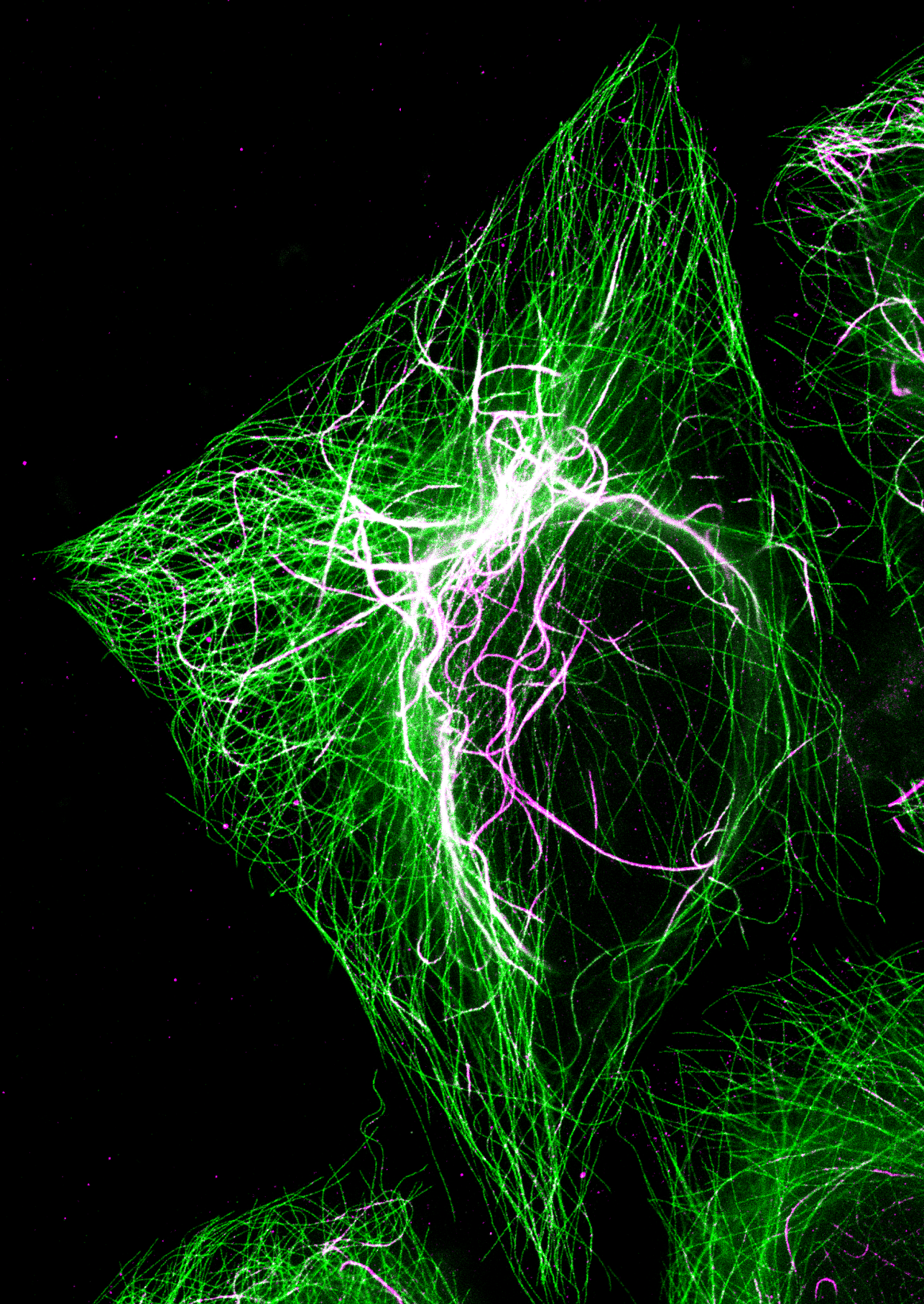

1

General Introduction

Roderick P. Tas[1]

[1] Division of Cell Biology, Faculty of Science, Utrecht University, The Netherlands

GENERAL INTRODUCTION

The adult mammalian brain consists of hundreds of billions of neurons that are interconnected into functional circuits. These circuits are able to process information in the form of electrochemical stimuli and regulate the basal functions of our body, such as movement, breathing and heart rate, but also more complex actions such as our thoughts, memories and emotions.

To propagate the signals within these constantly changing circuits, neurons need to develop highly specialized compartments. In the hippocampus, neurons consist of multiple branched dendrites and a long single axon**.** The dendrites are able to receive multiple signals, sent from axons of neurons upstream in the circuit. If enough signals are received, a threshold is reached and a propagating signal from the initial segment of the axon is sent further along the axon into the circuit. The fast propagating signal along the shaft of the axon and dendrites is electrical, whereas the transmission of the signal from the axon to the dendrites of the next neuron is chemical. The electrochemical conversion occurs at the contact points between axons and dendrites that are called synapses. When the electrical signal of a firing axon reaches a synapse, an influx of calcium is triggered, which in turn results in the release of synaptic vesicles into the synaptic cleft. These vesicles contain neurotransmitters that bind to the receptor at the dendritic spines, thereby activating these receptors and causing an influx of ions. This triggers the propagation of a small electrical signal in the next neuron.

Cellular and molecular compartmentalization underlies biological functionality

The complex cascade of events during neuronal activation relies on the right proteins being at the right compartment at the right time. For example, neurotransmitters need to be localized exclusively to the presynapse in the axon, while their receptors need to be in dendrites. This level of molecular compartmentalization is not unique to neurons. For instance, the DNA of interphase cells is confined within the nucleus. Additionally, cellular metabolism, protein sorting and synthesis are regulated within specific membrane-bound compartments such as mitochondria, endosomes and the endoplasmatic reticulum. Another example of molecular compartmentalization includes asymmetric distribution of proteins. This is necessary to set up cellular polarity in for example epithelial gut cells and migrating cells, to determine the apical site and leading edge, respectively[1, 2].

The examples mentioned above all show that cellular compartmentalization underlies biological function. These compartments exist across multiple length scales. Whereas an individual axonal compartment of a single neuron can extend up to a meter, most cellular structures, such as the mitotic spindle, membrane-bound compartments, cilia or the leading edge of a migrating cell, are compartmentalized on the length scale of only a few micrometers. All of these compartments are built up by the distribution of single, nanometer sized, molecules and their interactions. Therefore, one central challenge in molecular biology

is to elucidate how the small molecules organize into the large cellular compartments.

One way in which cells control cellular organization is by intracellular transport of cellular constituents. This is driven by motor proteins that can move over the cytoskeleton, a network of protein-based biopolymers that gives cells their shape and mechanical properties. For example, in neurons motor proteins can transport cargoes selectively into either axons or dendrites. In this chapter, I will introduce the microtubule and actin cytoskeleton and their associated motor proteins. I will highlight the unique features of the neuronal cytoskeleton and the proposed principles involved in selective sorting. Next, advanced microscopy techniques that can be used to study cytoskeletal organization beyond the diffraction limit are briefly discussed. Finally, I will discuss the scope of this thesis and define the research questions that I have addressed in this thesis.

THE CYTOSKELETON AND ITS MOTORS

Within the cells of all species, filaments of different proteins form an intricate network that provide a skeletal framework to control cell shape and motility. These interconnected filaments form the cytoskeleton and can rapidly reorganize to respond to cellular and environmental cues. The cytoskeleton of eukaryotic cells is made up of filaments of actin, microtubules, intermediate filaments and septins. In addition to their role in cell shaping and motility, actin and microtubules play an important role in the distribution of cellular components. Unlike intermediate filaments and septins, actin and microtubule filaments are polarized. During the course of evolution, molecular motor-proteins have evolved to recognize this internal polarity and use the actin and microtubule network as cellular highways for directed transport. This active transport by molecular motors is important to regulate selective transport of specific molecules between membranous organelles within the cytoplasm as well as for sorting between cellular compartments such as the axon and dendrites. Furthermore, active transport along the cellular highways can provide and remove essential molecules for cellular plasticity much faster than diffusion. For example it would take a few weeks for diffusion to span an axon of only one centimeter whereas it would take motor based transport only a few hours. Additionally, a variety of motors with different properties can be used to selectively sort molecules throughout the cells, as will be discussed below.

Microtubules

Microtubules are long hollow polymers that consist of αβ-tubulin heterodimers. The αβ-tubulin heterodimers assemble head to tail into filaments and typically 13 of these filaments associate laterally to form a hollow polymer. As a consequence of the asymmetric building blocks the microtubule itself is also an asymmetric structure. The α-tubulin subunit of the dimer faces the so-called minus-end while the β-tubulin faces the plus-end [3]. In cells, microtubule nucleation is believed to start with a template, such as the gamma tubulin ring

complex. This complex mimics a pre-formed plus-end and allows for rapid polymerization of a new microtubule. Subsequently, the minus-end of the newly formed lattice remains capped or is stabilized by minus-end binding proteins to prevent depolymerization [4]. Because of the stable minus-end, the dynamics of the microtubule is almost exclusively regulated at its plus-end. After incorporation, the exchangeable GTP in the β-subunit is slowly hydrolyzed to GDP, reducing the overall stability of the lateral interface. This delayed hydrolysis upon incorporation of a tubulin dimer results in a GTP-cap at the polymerizing plus-end that prevents the microtubule from depolymerization[3, 5]. Loss of the GTP-cap results in a catastrophe event and reversible depolymerization of the microtubule. In order to properly maintain the microtubule cytoskeleton, minus-end stability and the dynamic instability of the plus-end need to be tightly controlled by specific proteins.

While each microtubule is generated by αβ-tubulin heterodimers, diversity can be generated by incorporation of different tubulin isoforms, recruitment of microtubule associated proteins (MAPs) and post-translational modifications (PTMs) [6, 7]. The eukaryotic genome encodes for eight isoforms of both α- and β-tubulin that are expressed differentially among tissues [8, 9]. Recently, it has been shown that the composition of tubulin isoforms influences microtubule dynamics [8]. Furthermore, MAPs decorate the microtubule tips and lattice to regulate microtubule dynamics and stability [3, 5, 10, 11]. MAPs can also act to stabilize, bundle and localize microtubules or to indirectly recruit additional factors [12-15]. Whereas MAPs rely on dynamic protein-protein interactions, PTMs covalently decorate the microtubules. The C-terminus of the microtubule subunits is the major site of modification, but modifications can also occur in the interface between the tubulin dimers or the lumen of the microtubule. Several PTMs consist of the addition and removal of a single chemical group, such as acetylation, phosphorylation and (de)tyrosination. Additionally, more complex chains of glutamate, glycine or various amines can be added to the microtubules. In general, stable microtubules are associated with a high level of PTMs, with detyrosination and acetylation often serving as a marker for stable microtubules[6, 7]. Interestingly, recent *in vitro* studies have shown that PTMs can directly alter the binding of modifying enzymes and the mechanical stability of the microtubule[16, 17]. However, the direct relation between microtubule stability and PTMs remains to be elucidated. Over the years, almost all the enzymes responsible for PTMs have been identified, opening up possibilities to study the role of microtubule modifications in cells and *in vitro*[7, 18].

The signature of isoforms, MAPs and PTMs on a microtubule is referred to as the tubulin code [7, 19] and regulates its mechanical properties and functioning. As a consequence, differential regulation of the tubulin code within the cell can create subsets of microtubules that could act as functionally different highways for transport.

Actin

Each actin filament (F-actin) consists of actin monomers that polymerize into two

protofilaments that are helically wrapped around each other. Actin filaments are often much shorter than microtubules. Similar to microtubules, the ATP in actin is slowly hydrolyzed after incorporation, resulting in a polymerizing, ATP-rich, plus-end and an ADP-rich minus-end [20]. Since the spontaneous nucleation of F-actin within the cell is energetically unfavorable, nucleators and regulators are necessary to initiate and elongate actin filaments[21]. Depending on which proteins initiate actin polymerization, different networks can be formed. While formins and spire proteins drive the polymerization of a single actin filament, Arp2/3 initiates branched nucleation of actin from previously formed filaments. The mode of nucleation can therefore determine the structure of a newly formed actin network. For example, single filaments can be bundled either antiparallel or parallel to form contractile fibers or dynamic protrusions, respectively. Alternatively, the branched actin network created by Arp2/3 is necessary in lamellipodia to drive the leading edge during cell migration. These nucleating factors are under the control of small GTPases such as Rac, Rho and Cdc42. The spatiotemporal activation of each of these regulators by internal and external cues, results in a highly dynamic and adaptable actin network[22]. Similar to microtubules, the multiple isoforms that encode for actin (muscle and non-muscle specific) undergo a wide range of PTMs that modify the dynamics, structural properties and functionality. The major actin PTMs are: methylation, acetylation, ribosylation, oxidation, phosphorylation, ubiquitinylation, GlcNAcylation and arginylation, but many more have been described. Disruption of actin PTMs has been associated with altered dynamics and several disorders[23, 24].

In addition to the diversity described above, many actin-binding proteins exist that can further regulate actin dynamics, cross-linking, accessibility and localization [25]. Tropomyosin isoforms are important regulators of the actin cytoskeleton. For example, muscle cell troponin and tropomyosin, under the control of calcium ions, directly regulate the accessibility of the myosin-binding site on actin. In other cell types, such as neurons and epithelial cells of the gut, different tropomyosin isoforms localize to specific compartments in different stages of development. The spatiotemporal distribution of tropomyosin isoforms has been associated with embryogenesis, morphogenesis, cell-cell contacts and many more essential cellular functions [26, 27]. Further work is necessary to determine the cellular distribution, function and interplay of actin isoforms, modifications and binding proteins like tropomyosin.

Motor proteins

Because of their structural asymmetry, microtubules and actin can serve as directional roads for transport. Motor proteins serve as the molecular motors that carry cellular cargoes to either the plus- or minus-end of microtubules and actin filaments. Kinesin and dynein motors are responsible for long-range transport along microtubules. More than 40 genes divided into 14 families encode for the kinesin superfamily, most of which are responsible for plus-end directed transport. In contrast, only two genes encode for the minus-end directed cytoplasmic

dyneins [28, 29]. Dynein is structurally very different from kinesins and its activity depends on the interaction with a multi-subunit complex containing microtubule recruitment factors, activators and adapters [30]. Because the remainder of this thesis is mostly about kinesins, I will not further discuss dynein.

Kinesins involved in transport of cargo mostly exist as dimers with two motor domains. These domains are connected to a set of coiled-coil structures which induce dimerization and interact with cargoes and other binding proteins directly or via a light chain. Each motor domain uses the energy derived from ATP hydrolysis to cycle between different conformations that have different affinities for the microtubule. In processive motors, intramolecular tension between the two motor domains keeps these mechanochemical cycles out of phase to ensure continuous attachment while stepping along the microtubules [31]. Each kinesin has unique properties such as run length, speed and microtubule affinity. Without cargoes, most kinesins remain auto-inhibited by folding upon themselves with their tail domain attached to the motor domain. Activation occurs when this auto-inhibition is relieved, for example by binding of cargo to the tail domain. Adapters that bind to the tail domain, determine which kinesin binds to which cargo. Additional factors, such as MAPs and other interactors, can further tune kinesin activity and localization. In turn, kinesin activity can modify the mechanical properties of the microtubule[32, 33]. One interesting property is that different kinesins have been described to prefer a specific subset of microtubules. For example, it has been well established that Kinesin-1/Kif5 exclusively prefers stable modified microtubules, whereas Kinesin-3/Kif1 prefers more dynamic microtubules[34-38]. Microtubule lattice conformation, PTMs, MAPs and co-operative binding have been proposed to recruit and activate kinesins on specific subsets of microtubules [32, 33, 39, 40]. The diversity in kinesins, generated by differential activation and microtubule recognition, results in a highly tunable toolbox for cellular transport in different compartments along specific microtubule tracks. Future work will hopefully provide further insights how the complex microtubule environment affects different motor proteins. Furthermore, the molecular mechanisms underlying microtubule specificity need to be elucidated.

Myosins move along the actin cytoskeleton and are generally associated with dynamics at short length scales. For example, Myosin-V is involved in short range cargo transport and anchoring in actin dense regions such as cortical actin and the apical site of endothelial gut cells [2, 41]. The myosin superfamily in mammals contains more than 40 genes that encode for many isoforms among 15 subclasses [42]. Famously, muscle Myosin-II oligomerizes in thick filaments to work in ensemble in muscle contraction. Like kinesins, dimeric myosins that are responsible for transport walk hand-over-hand and are dimerized by a coiled-coil structure with a variable C-terminal domain, which can be involved in protein interaction and cargo binding [43]. Furthermore, light-chains bind to the C-terminal portion of the motor head and affect protein binding and myosin activity [28]. Interestingly, Myosin-VI is the only subclass that walks towards the minus–end of actin filaments. Like kinesins,

the activity of different myosins can also be tuned by a variety of factors. Actin accessibility, binding of cargoes, interactors, light chains, actin binding proteins and small molecules such as calcium all strongly affect myosin binding and motility [43].

Motor proteins that move along actin and microtubules regulate cellular process at different length and time scales. In addition to active transport of molecular cargoes, motors can organize the cytoskeleton to regulate cell division, differentiation, migration, compartmentalization and many more vital processes of the cell. The fine tuning of these processes relies on the recruitment and activation of the right motors at the right time. *In vitro* it has been shown that recruitment of multiple motors with opposite directions will result in a tug-of-war. Tuning the stoichiometry of opposing motors will alter the outcome and dynamics of transport [44, 45]. However, the extent to which activity of different motor proteins bound to the same cargo is coordinated in cells remains unclear. Defects in kinesins, dyneins and myosins have been associated with a wide range of severe disorders such as Alzheimer, ALS, multiple sclerosis and lissencephaly [46-48]. Understanding the individual motor proteins and multi-motor assemblies will provide valuable insights in fundamental biological processes and the disease phenotypes associated with the defects in these processes.

NEURONAL CYTOSKELETON ORGANIZATION

The polarized organization of neurons highly depends on selective transport by kinesins to either the axon or dendrites. As described above, cytoskeletal organization directly underlies directional transport by motor proteins[6, 49, 50]. Throughout neuronal development, neurons adopt a highly specialized cytoskeleton. In non-neuronal cells and neurons of lower organisms, the microtubule cytoskeleton is mostly organized uniformly. For example, in proliferating and migrating cells most microtubules are organized radially around the microtubule organizing center (MTOC) and in the epithelial gut cells, the majority of microtubules is organized with the minus-end at the apical site[51]. Additionally, the neuronal microtubules in *C. elegans* and *Drosophila* are uniformly organized in both axons and dendrites. In these organisms, axonal microtubules are organized with their plus-end outwards, whereas they are oppositely oriented in the dendrites. Because of the uniform microtubule array in the aforementioned examples, kinesin- and dynein-driven transport will lead to a predictable direction of transport; kinesin drives axon- selective transport whereas dynein will only enter the dendrite [52-54]. In contrast, dendrites of mammalian neurons contain microtubules of both orientations [55, 56] (**Fig 1**). This mixed microtubule array poses immediate challenges for selective transport by kinesins into either the axon or dendrite. It has been reported that kinesins from different superfamilies preferentially target the axon while others target both the axon and dendrites[57-60]. Since microtubules in the axon are still organized with their plus-end out, dynein driven transport will not enter the axons but can drive dendritic transport via the minus-end out microtubules of the dendrites[61] (**Fig 1**).

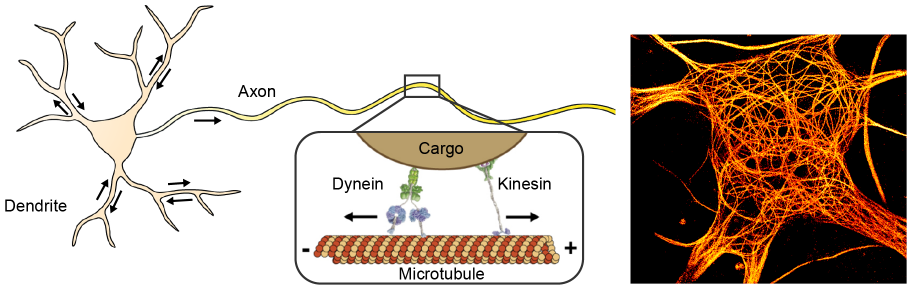

Figure 1: Neuronal microtubule cytoskeleton
A schematic representation of the neuronal microtubule cytoskeleton organization in the axon and dendrites. Arrows along the neurites indicate the microtubule orientations observed in the axon and dendrites. Axons contain plus-end out microtubules whereas dendritic microtubules are mixed. The box depicts cargo transport along the plus-end out microtubules of the axon by kinesin and dynein. Molecular models of motor proteins are adapted from [28]. The right panel shows a super-resolved image of the intricate network of microtubules in the neuronal cell body to illustrate the acentrosomal microtubule network in the neuron. Image adapted from [10].

However, both the axon and dendrites contain plus-end out microtubules. Therefore, axon or dendrite selectivity by different kinesins needs additional traffic rules.

These rules are likely to be dictated by the tubulin code. The specific distribution of tubulin isoforms, MAPs and PTMs generates microtubule diversity throughout the neuron that could locally recruit and activate specific motor proteins. For example, MAP2 localizes exclusively to the dendrites whereas Tau localizes to the axon[46]. Furthermore, the microtubules in the pre-axonal exclusion zone and the initial segment are specifically decorated and bundled by TRIM46, which in turn regulates axon differentiation and identity[62, 63]. The MAPs in specific compartments of the neurons can alter microtubule properties such as dynamics, lattice structure and accessibility, which can affect motor proteins. In addition, motors can be directly regulated through interaction with specific MAPs[64-66]. Recent reports have proposed a model in which the recruitment of MAPs to the proximal neurites can differentially affect the activity of specific motor proteins to prevent or assist entry or exclusion from neuronal compartments such as the dendrites[39, 40, 67]. Furthermore, neuronal microtubules are subjected to high levels of post-translational modifications that are differentially distributed in the neurons. In general, the population of axonal microtubules is more modified than the dendritic population[68]. Finally, it should be considered that microtubules within the axon or dendrites can have different properties. Microtubule stability, modification levels and MAP decoration can differ from microtubule to microtubule. As a consequence different subsets of microtubules recognized by selective motors can exist within the same compartment. However, so far the exact organization of the different microtubule subsets in the dendrites and their effects on polarized sorting by

kinesins have remained elusive.

Different actin structures have been observed throughout the compartments of hippocampal neurons. For example, growth cones of developing neurons and dendritic spines after maturation are highly enriched in actin. Axon outgrowth is driven by continuous remodeling of the actin cytoskeleton to push the growth cone forward. Furthermore, actin in dendritic spines serves as a scaffolding network for the post-synaptic density and regulates spine size and dynamics. Interestingly, recruitment of Myosin-V leads to spine entries of cargo, whereas Myosin-VI results in exits [69]. This suggests that the majority of actin is organized with its plus-end pointed toward the spine, thereby serving as a directional track for spine targeting by myosins. Other actin structures have also been identified using advanced live- and super-resolution microscopy; actin-dense patches have been shown along the length of the axon. In the proximal axon, myosins can prevent cargoes from entering the axon by tethering them to these actin patches[70]. More distally, actin filaments (actin trails) emerge from the actin-patches, suggesting different mechanisms of formation and function. Recently, alternating ~190 nm spaced rings of actin and its cross linker spectrin have been shown along the length of the axons and dendrites[71]. These rings have been observed among many different types of neurons in a variety of species[72]. So far, it has been shown that they provide mechanical support, preserve microtubule integrity, maintain axon caliber and serve as a diffusion barrier for membrane proteins[73-76].

The function of actin in each of these compartments is highly dependent on its exact dynamics and architecture. Additional binding proteins can affect actin organization or use actin as a scaffold. For example, Ankyrin G binds neurofascin and sodium channels and uses the actin rings in the initial segment as a tether[77]. Furthermore, actin remodeling is associated with pre-synaptic release. However, the exact structure and function of presynaptic actin need to be elucidated[78]. Similar to microtubules, the overall polarity of the actin network directly affects transport by myosins. Even though the structures of the actin network are now visualized using super-resolution techniques, more information about actin orientation is necessary to determine its role in active directional transport.

SUPER-RESOLUTION TECHNIQUES TO STUDY CELLULAR ARCHITECTURE

Visualizing the exact architecture of the neuronal cytoskeleton to understand its function has always been a major challenge. Especially in neurons, microtubules and actin are organized into dense arrays and cannot be visualized by diffraction-limited light microscopy techniques, which have a maximum resolution of ~250 nm. Therefore, electron microscopy (EM) has been used to study the smaller details of cytoskeleton organization. For example, EM preparations revealed microtubule spacing of ~25 nm and ~65 nm in axons and dendrites respectively [12]. Despite its unmatched resolution, EM requires labor-intensive sectioning and reconstruction

procedures and labelling of specific proteins or modifications has remained challenging. In the last two decades, several diffraction-unlimited light microscopy techniques have become available to study cellular processes at high resolution. Even though resolutions of ~150 and ~50 nm can be achieved by structured illumination microscopy (SIM) and stimulated emission depletion (STED), respectively, the highest resolution is achieved using single-molecule localization microscopy (SMLM)[79, 80].

Single Molecule Localization Microscopy

Instead of simultaneously imaging the ensemble of fluorophores that decorate a structure, SMLM techniques image the individual probes sequentially. Subsequently, by fitting the point spread function, the midpoint of each individual fluorophore can be determined with an accuracy of a few nanometers. The individual localizations can then be accurately combined, resulting in a super-resolved reconstruction with approximately a 10-fold resolution increase [80] (**Fig 2a**).

Different strategies for SMLM exist. Single-particle tracking photo-activated localization microscopy (sptPALM) is typically used to study the dynamics of single molecules in living samples. Here, genetically encoded photo-switchable tags attached to the protein of interest can be tracked with several nanometer accuracy to study the localization and dynamics of individual molecules in the cell [81, 82] (**Fig 2b**). To map the exact organization of cellular structures and to overcome photo-toxicity, bleaching and structural fluctuations, SMLM strategies are often used on fixed cells. Fixed strategies are compatible with high labelling densities, high laser powers and long imaging times to sample the structure repeatedly. These advantages allow for a reconstruction using only the highest accuracy localizations, increasing the resolution of the final image. Direct stochastic optical reconstruction microscopy (dSTORM) and dynamically exchangeable probes targeted to the structure of interest (often called: point accumulation for imaging in nanoscale topography, PAINT) are used to achieve such high resolution reconstructions (**Fig 2b**). dSTORM relies on an ensemble labelling of the structure of interest, followed by active transitioning the majority of fluorophores into a 'dark state' so that only single molecule events remain [79]. In contrast, selective exchangeable probes stochastically bind and unbind the structure of interest from solution. Therefore, fine-tuning the concentration of the probe in solution will result in a regime where single molecules can be observed to transiently interact with the structure of interest (**Fig. 2b**). One increasingly used example of this method is DNA-PAINT. Here, a DNA docking strand is targeted to a structure using antibodies or functionalized groups. Subsequently, a complementary imager sequence coupled to a fluorophore is added to solution, which binds transiently to the docking strand[83]. More recently, labelled protein fragments that transiently bind to their target after fixation have also been used[84].

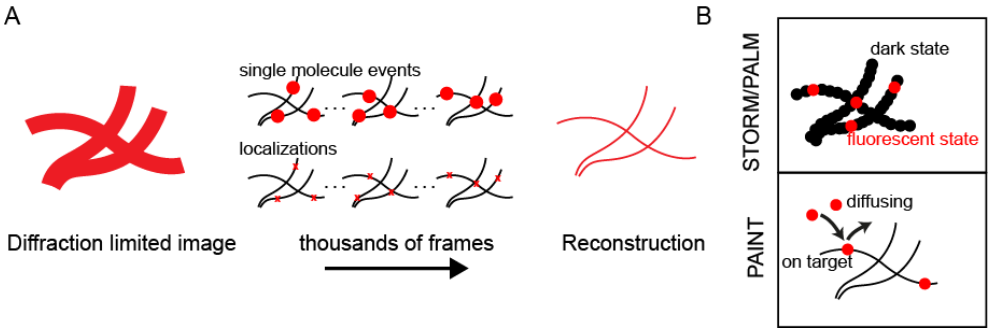

Figure 2: Single Molecule Localization microscopy
A) *Principle of single molecule localization microscopy. Simultaneous imaging of excited fluorophores along the target structure results in a diffraction limited image (left panel). During the single molecule localization acquisition, single fluorophores are imaged along the target structured and the entire structure is sampled in thousands of frames. These coordinates of the fluorophores can be determined by Gaussian fitting and the localizations can be accurately determined (middle panel). Finally the localizations can be combined into a single super resolved reconstruction (right panel).*
B) *Principle of STORM/ PALM and PAINT for single molecule localization microscopy.*

SCOPE OF THIS THESIS

As described above, neuronal polarization and function rely on the proper sorting of cellular cargoes. Molecular motors drive transport along the actin and microtubule cytoskeleton to ensure selective transport to either axons or dendrites. In this thesis we explore the relation between cytoskeletal organization and polarized sorting in neurons. Using advanced live- and super-resolution microscopy, we elucidate the exact neuronal roadmap for active transport at the nanoscale.

Small selective probes are one of the major requirements to image cytoskeletal structures beyond the diffraction limit using SMLM. **Chapter 2** focuses on an improved purification and labelling method of a lifeAct probe to accurately image actin using SMLM. Subsequently, application of this probe allowed us to study how different actin structures in several compartments contribute to selective sorting in different neuronal compartments. **Chapter 3** explores the role of actin and myosins in the retention of cargoes in the initial segment. We report that chemically-induced coupling of myosins to cargoes in the initial segment resulted in immobilization or retrograde transport. Additionally, we use dual-color nanoscopy to determine the actin structures that were associated with the myosin-coupled cargoes. Furthermore, in **Chapter 4**, we examine the role of actin as a barrier to retain kinesin-associated cargoes in the initial segment. We assessed the differential behavior of peroxisomes after chemically-induced coupling to different truncations of the kinesin Kif17 in the presence or absence of actin. Based on the results, we propose a three-step model in

which Kif17-based transport to dendrites depends on actin-dependent retention in the initial segment and on dynein for subsequent dendritic targeting.

Compartmentalization and dynamics of dendritic spines are also strongly dependent on actin organization. Previously, it has been shown that microtubule entries into spines correlate with synaptic activity to potentially provide supply routes for synaptic cargo [85]. However, how spine activity enables microtubule entries has remained poorly understood. In **Chapter 5** we investigated whether activity-dependent actin dynamics and actin structures at the spine base can facilitate microtubule entries. Furthermore, using nanoscopy, we visualized the distinct actin structures at the spine base that could be responsible for microtubule recruitment. Combining this with DNA-PAINT, we then further investigated the correlation between these actin structures and a regulator involved in microtubule entries.

One of the central questions in neuronal sorting is why several kinesins only target the axon, while others also enter the dendrites. For example Kinesin-1/Kif5 only targets axons, while Kinesin-3/Kif1 targets both axon and dendrites and accumulates in dendritic tips. We hypothesized that to achieve such selectivity, the identity of the microtubules in either direction in the dendrites has to differ to provide distinct highways that can be selectively recognized by different kinesins. In **Chapter 6** we explore the relation between microtubule orientation and identity using a novel assay, termed motor-PAINT, to directly probe microtubule orientation along the entire lattice with nanometer resolution. This revealed that minus-end out microtubules were more stable and subjected to acetylation. In contrast, plus-end out microtubules were more dynamic and tyrosinated. These data support a new model for selective sorting in which the preferred orientation of specific microtubule subsets guides the direction of motor proteins that selectively recognize that subset. **Chapter 7** reviews recent key contributions to the understanding of cytoskeleton diversity in neurons and suggests avenues to further elucidate the range of cytoskeletal structures and functions.

Now that we start to understand how cytoskeletal organization contributes to its functions, one next major challenge is to control it. **Chapter 8** focuses on the optical control of *in vitro* microtubules in gliding assays. Using light-sensitive protein-protein interaction, spatiotemporal control of protein patterning and microtubule gliding activity was achieved. **Chapter 9** concludes with a summary of the key findings in this thesis and discusses remaining research questions.

REFERENCES

1. Huttenlocher, A., *Cell polarization mechanisms during directed cell migration.* Nat Cell Biol, 2005. **7**(4): p. 336-7.
2. Klunder, L.J., et al., *Mechanisms of Cell Polarity-Controlled Epithelial Homeostasis and Immunity in the Intestine.* Cold Spring Harb Perspect Biol, 2017. **9**(7).
3. Aher, A. and A. Akhmanova, *Tipping microtubule dynamics, one protofilament at a time.* Curr Opin Cell Biol, 2018. **50**: p. 86-93.
4. Akhmanova, A. and C.C. Hoogenraad, *Microtubule minus-end-targeting proteins.* Curr Biol, 2015.

25(4): p. R162-71.
5. Aher, A., et al., *CLASP Suppresses Microtubule Catastrophes through a Single TOG Domain.* Dev Cell, 2018. **46**(1): p. 40-58 e8.
6. Park, J.H. and A. Roll-Mecak, *The tubulin code in neuronal polarity.* Curr Opin Neurobiol, 2018. **51**: p. 95-102.
7. Gadadhar, S., et al., *The tubulin code at a glance.* J Cell Sci, 2017. **130**(8): p. 1347-1353.
8. Vemu, A., et al., *Tubulin isoform composition tunes microtubule dynamics.* Mol Biol Cell, 2017. **28**(25): p. 3564-3572.
9. Redeker, V., *Mass spectrometry analysis of C-terminal posttranslational modifications of tubulins.* Methods Cell Biol, 2010. **95**: p. 77-103.
10. Yau, K.W., et al., *Microtubule minus-end binding protein CAMSAP2 controls axon specification and dendrite development.* Neuron, 2014. **82**(5): p. 1058-73.
11. Jiang, K., et al., *Microtubule minus-end stabilization by polymerization-driven CAMSAP deposition.* Dev Cell, 2014. **28**(3): p. 295-309.
12. Chen, J., et al., *Projection domains of MAP2 and tau determine spacings between microtubules in dendrites and axons.* Nature, 1992. **360**(6405): p. 674-7.
13. Takemura, R., et al., *Increased microtubule stability and alpha tubulin acetylation in cells transfected with microtubule-associated proteins MAP1B, MAP2 or tau.* J Cell Sci, 1992. **103 (Pt 4)**: p. 953-64.
14. Jiang, K., et al., *Microtubule minus-end regulation at spindle poles by an ASPM-katanin complex.* Nat Cell Biol, 2017. **19**(5): p. 480-492.
15. Luo, J., et al., *The microtubule-associated protein EML3 regulates mitotic spindle assembly by recruiting the Augmin complex to spindle microtubules.* J Biol Chem, 2019.
16. Xu, Z., et al., *Microtubules acquire resistance from mechanical breakage through intralumenal acetylation.* Science, 2017. **356**(6335): p. 328-332.
17. Valenstein, M.L. and A. Roll-Mecak, *Graded Control of Microtubule Severing by Tubulin Glutamylation.* Cell, 2016. **164**(5): p. 911-21.
18. Nieuwenhuis, J., et al., *Vasohibins encode tubulin detyrosinating activity.* Science, 2017. **358**(6369): p. 1453-1456.
19. Verhey, K.J. and J. Gaertig, *The tubulin code.* Cell Cycle, 2007. **6**(17): p. 2152-60.
20. Pollard, T.D., L. Blanchoin, and R.D. Mullins, *Molecular mechanisms controlling actin filament dynamics in nonmuscle cells.* Annu Rev Biophys Biomol Struct, 2000. **29**: p. 545-76.
21. Chesarone, M.A. and B.L. Goode, *Actin nucleation and elongation factors: mechanisms and interplay.* Curr Opin Cell Biol, 2009. **21**(1): p. 28-37.
22. Lee, S.H. and R. Dominguez, *Regulation of actin cytoskeleton dynamics in cells.* Mol Cells, 2010. **29**(4): p. 311-25.
23. Terman, J.R. and A. Kashina, *Post-translational modification and regulation of actin.* Curr Opin Cell Biol, 2013. **25**(1): p. 30-8.
24. Vedula, P. and A. Kashina, *The makings of the 'actin code': regulation of actin's biological function at the amino acid and nucleotide level.* Journal of Cell Science, 2018. **131**(9).
25. Winder, S.J. and K.R. Ayscough, *Actin-binding proteins.* J Cell Sci, 2005. **118**(Pt 4): p. 651-4.
26. Gunning, P.W., et al., *Tropomyosin - master regulator of actin filament function in the cytoskeleton.* J Cell Sci, 2015. **128**(16): p. 2965-74.
27. Gunning, P.W., et al., *Tropomyosin isoforms: divining rods for actin cytoskeleton function.* Trends Cell Biol, 2005. **15**(6): p. 333-41.
28. Vale, R.D., *The molecular motor toolbox for intracellular transport.* Cell, 2003. **112**(4): p. 467-80.
29. Miki, H., et al., *All kinesin superfamily protein, KIF, genes in mouse and human.* Proc Natl Acad Sci U S A, 2001. **98**(13): p. 7004-11.
30. Reck-Peterson, S.L., et al., *The cytoplasmic dynein transport machinery and its many cargoes.* Nat Rev Mol Cell Biol, 2018. **19**(6): p. 382-398.
31. Yildiz, A., et al., *Kinesin walks hand-over-hand.* Science, 2004. **303**(5658): p. 676-8.
32. Peet, D.R., N.J. Burroughs, and R.A. Cross, *Kinesin expands and stabilizes the GDP-microtubule*

lattice. Nat Nanotechnol, 2018. **13**(5): p. 386-391.
33. Shima, T., et al., *Kinesin-binding-triggered conformation switching of microtubules contributes to polarized transport.* J Cell Biol, 2018. **217**(12): p. 4164-4183.
34. Guardia, C.M., et al., *BORC Functions Upstream of Kinesins 1 and 3 to Coordinate Regional Movement of Lysosomes along Different Microtubule Tracks.* Cell Rep, 2016. **17**(8): p. 1950-1961.
35. Sirajuddin, M., L.M. Rice, and R.D. Vale, *Regulation of microtubule motors by tubulin isotypes and post-translational modifications.* Nat Cell Biol, 2014. **16**(4): p. 335-44.
36. Atherton, J., A. Houdusse, and C. Moores, *MAPping out distribution routes for kinesin couriers.* Biol Cell, 2013. **105**(10): p. 465-87.
37. Cai, D., et al., *Single molecule imaging reveals differences in microtubule track selection between Kinesin motors.* PLoS Biol, 2009. **7**(10): p. e1000216.
38. Konishi, Y. and M. Setou, *Tubulin tyrosination navigates the kinesin-1 motor domain to axons.* Nat Neurosci, 2009. **12**(5): p. 559-67.
39. Karasmanis, E.P., et al., *Polarity of Neuronal Membrane Traffic Requires Sorting of Kinesin Motor Cargo during Entry into Dendrites by a Microtubule-Associated Septin.* Dev Cell, 2018. **46**(4): p. 518-524.
40. Gumy, L.F., et al., *MAP2 Defines a Pre-axonal Filtering Zone to Regulate KIF1- versus KIF5-Dependent Cargo Transport in Sensory Neurons.* Neuron, 2017. **94**(2): p. 347-362 e7.
41. Kapitein, L.C., et al., *Myosin-V opposes microtubule-based cargo transport and drives directional motility on cortical actin.* Curr Biol, 2013. **23**(9): p. 828-34.
42. Berg, J.S., B.C. Powell, and R.E. Cheney, *A millennial myosin census.* Mol Biol Cell, 2001. **12**(4): p. 780-94.
43. Heissler, S.M. and J.R. Sellers, *Various Themes of Myosin Regulation.* J Mol Biol, 2016. **428**(9 Pt B): p. 1927-46.
44. Derr, N.D., et al., *Tug-of-war in motor protein ensembles revealed with a programmable DNA origami scaffold.* Science, 2012. **338**(6107): p. 662-5.
45. Soppina, V., et al., *Tug-of-war between dissimilar teams of microtubule motors regulates transport and fission of endosomes.* Proc Natl Acad Sci U S A, 2009. **106**(46): p. 19381-6.
46. Kapitein, L.C. and C.C. Hoogenraad, *Building the Neuronal Microtubule Cytoskeleton.* Neuron, 2015. **87**(3): p. 492-506.
47. Hanemann, C.O. and A.C. Ludolph, *Motor protein diseases of the nervous system.* Amyotroph Lateral Scler Other Motor Neuron Disord, 2005. **6**(4): p. 197-201.
48. Millecamps, S. and J.P. Julien, *Axonal transport deficits and neurodegenerative diseases.* Nat Rev Neurosci, 2013. **14**(3): p. 161-76.
49. Bentley, M. and G. Banker, *The cellular mechanisms that maintain neuronal polarity.* Nat Rev Neurosci, 2016. **17**(10): p. 611-22.
50. Kapitein, L.C. and C.C. Hoogenraad, *Which way to go? Cytoskeletal organization and polarized transport in neurons.* Mol Cell Neurosci, 2011. **46**(1): p. 9-20.
51. Bartolini, F. and G.G. Gundersen, *Generation of noncentrosomal microtubule arrays.* J Cell Sci, 2006. **119**(Pt 20): p. 4155-63.
52. Harterink, M., et al., *Local microtubule organization promotes cargo transport in C. elegans dendrites.* J Cell Sci, 2018. **131**(20).
53. Harterink, M., et al., *Light-controlled intracellular transport in Caenorhabditis elegans.* Curr Biol, 2016. **26**(4): p. R153-4.
54. Mattie, F.J., et al., *Directed microtubule growth, +TIPs, and kinesin-2 are required for uniform microtubule polarity in dendrites.* Curr Biol, 2010. **20**(24): p. 2169-77.
55. Baas, P.W., M.M. Black, and G.A. Banker, *Changes in microtubule polarity orientation during the development of hippocampal neurons in culture.* J Cell Biol, 1989. **109**(6 Pt 1): p. 3085-94.
56. Yau, K.W., et al., *Dendrites In Vitro and In Vivo Contain Microtubules of Opposite Polarity and Axon Formation Correlates with Uniform Plus-End-Out Microtubule Orientation.* J Neurosci, 2016. **36**(4): p. 1071-85.

57. Nakata, T. and N. Hirokawa, *Microtubules provide directional cues for polarized axonal transport through interaction with kinesin motor head.* J Cell Biol, 2003. **162**(6): p. 1045-55.
58. Jacobson, C., B. Schnapp, and G.A. Banker, *A change in the selective translocation of the Kinesin-1 motor domain marks the initial specification of the axon.* Neuron, 2006. **49**(6): p. 797-804.
59. Lipka, J., et al., *Microtubule-binding protein doublecortin-like kinase 1 (DCLK1) guides kinesin-3-mediated cargo transport to dendrites.* EMBO J, 2016. **35**(3): p. 302-18.
60. Huang, C.F. and G. Banker, *The translocation selectivity of the kinesins that mediate neuronal organelle transport.* Traffic, 2012. **13**(4): p. 549-64.
61. Kapitein, L.C., et al., *Mixed microtubules steer dynein-driven cargo transport into dendrites.* Curr Biol, 2010. **20**(4): p. 290-9.
62. van Beuningen, S.F.B., et al., *TRIM46 Controls Neuronal Polarity and Axon Specification by Driving the Formation of Parallel Microtubule Arrays.* Neuron, 2015. **88**(6): p. 1208-1226.
63. Farias, G.G., et al., *Sorting of Dendritic and Axonal Vesicles at the Pre-axonal Exclusion Zone.* Cell Rep, 2015. **13**(6): p. 1221-1232.
64. Hooikaas, P.J., et al., *MAP7 family proteins regulate kinesin-1 recruitment and activation.* J Cell Biol, 2019.
65. Dixit, R., et al., *Differential regulation of dynein and kinesin motor proteins by tau.* Science, 2008. **319**(5866): p. 1086-9.
66. Monroy, B.Y., et al., *Competition between microtubule-associated proteins directs motor transport.* Nat Commun, 2018. **9**(1): p. 1487.
67. Pan, X., et al., *MAP7D2 Localizes to the Proximal Axon and Locally Promotes Kinesin-1-Mediated Cargo Transport into the Axon.* Cell Rep, 2019. **26**(8): p. 1988-1999 e6.
68. Hammond, J.W., et al., *Posttranslational modifications of tubulin and the polarized transport of kinesin-1 in neurons.* Mol Biol Cell, 2010. **21**(4): p. 572-83.
69. Esteves da Silva, M., et al., *Positioning of AMPA Receptor-Containing Endosomes Regulates Synapse Architecture.* Cell Rep, 2015. **13**(5): p. 933-43.
70. Watanabe, K., et al., *Networks of Polarized Actin Filaments in the Axon Initial Segment Provide a Mechanism for Sorting Axonal and Dendritic Proteins.* Cell Reports, 2012. **2**(6): p. 1546-1553.
71. Xu, K., G. Zhong, and X. Zhuang, *Actin, spectrin, and associated proteins form a periodic cytoskeletal structure in axons.* Science, 2013. **339**(6118): p. 452-6.
72. He, J., et al., *Prevalent presence of periodic actin-spectrin-based membrane skeleton in a broad range of neuronal cell types and animal species.* Proc Natl Acad Sci U S A, 2016. **113**(21): p. 6029-34.
73. Qu, Y., et al., *Periodic actin structures in neuronal axons are required to maintain microtubules.* Mol Biol Cell, 2017. **28**(2): p. 296-308.
74. Costa, A.R., et al., *The Regulation of Axon Diameter: From Axonal Circumferential Contractility to Activity-Dependent Axon Swelling.* Front Mol Neurosci, 2018. **11**: p. 319.
75. de Wit, G., et al., *Revealing Compartmentalized Diffusion in Living Cells with Interferometric Scattering Microscopy.* Biophys J, 2018. **114**(12): p. 2945-2950.
76. Albrecht, D., et al., *Nanoscopic compartmentalization of membrane protein motion at the axon initial segment.* J Cell Biol, 2016. **215**(1): p. 37-46.
77. Leterrier, C., P. Dubey, and S. Roy, *The nano-architecture of the axonal cytoskeleton.* Nat Rev Neurosci, 2017. **18**(12): p. 713-726.
78. Rust, M.B. and T. Maritzen, *Relevance of presynaptic actin dynamics for synapse function and mouse behavior.* Exp Cell Res, 2015. **335**(2): p. 165-71.
79. Huang, B., M. Bates, and X. Zhuang, *Super-resolution fluorescence microscopy.* Annu Rev Biochem, 2009. **78**: p. 993-1016.
80. Schermelleh, L., R. Heintzmann, and H. Leonhardt, *A guide to super-resolution fluorescence microscopy.* J Cell Biol, 2010. **190**(2): p. 165-75.
81. Patterson, G., et al., *Superresolution imaging using single-molecule localization.* Annu Rev Phys Chem, 2010. **61**: p. 345-67.
82. MacGillavry, H.D. and T.A. Blanpied, *Single-Molecule Tracking Photoactivated Localization*

Microscopy to Map Nano-Scale Structure and Dynamics in Living Spines. Curr Protoc Neurosci, 2013. **65**: p. 2 20 1-19.
83. Jungmann, R., et al., *Multiplexed 3D cellular super-resolution imaging with DNA-PAINT and Exchange-PAINT.* Nat Methods, 2014. **11**(3): p. 313-8.
84. Kiuchi, T., et al., *Multitarget super-resolution microscopy with high-density labeling by exchangeable probes.* Nat Methods, 2015. **12**(8): p. 743-6.
85. Merriam, E.B., et al., *Synaptic regulation of microtubule dynamics in dendritic spines by calcium, F-actin, and drebrin.* J Neurosci, 2013. **33**(42): p. 16471-82.

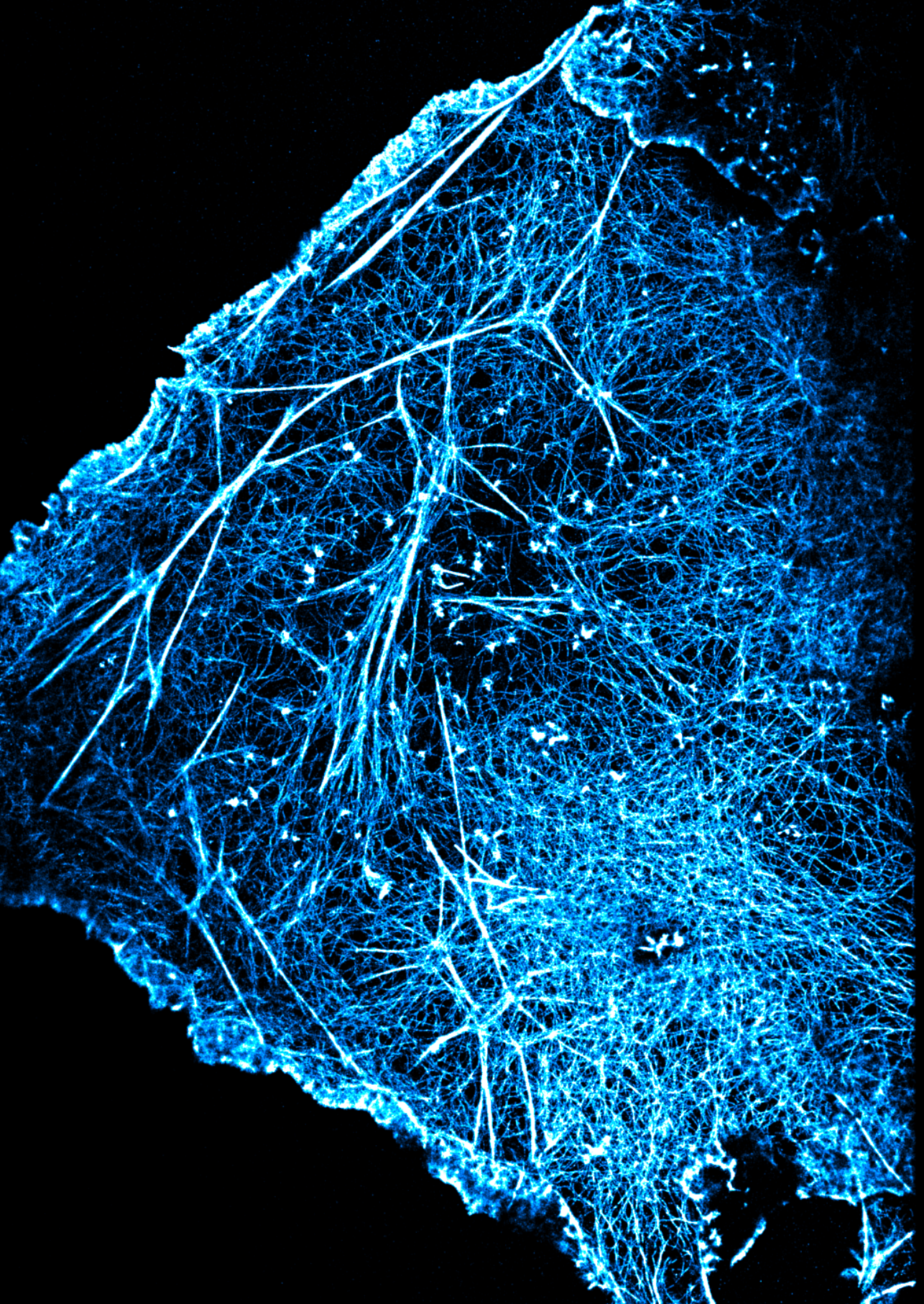

2

Purification and Application of a Small Actin Probe for Single-Molecule Localization Microscopy

Roderick P. Tas[1], Trusanne G.A.A. Bos[1] and Lukas C. Kapitein[1]

Methods in Molecular Biology (2018); 1665, pp. 155-171

[1] Division of Cell Biology, Faculty of Science, Utrecht University, The Netherlands

ABSTRACT

The cytoskeleton is involved in many cellular processes. Over the last decade, super-resolution microscopy has become widely available to image cytoskeletal structures, such as microtubules and actin, with great detail. For example, Single Molecule Localizat ion Microscopy (SMLM) achieves resolutions of 5-50 nm through repetitive sparse labeling of samples, followed by Point-Spread-Function analysis of individual fluorophores. Whereas initially this approach depended on the controlled photoswitching of fluorophores targeted to the structure of interest, alternative techniques depend on the transient binding of fluorescently labeled probes, such as the small polypeptide lifeAct that can transiently interact with polymerized actin. These techniques allow for simple multi-color imaging and are no longer limited by a fluorophore's blinking properties. Here we describe a detailed step-by-step protocol to purify, label and utilize the lifeAct fragment for SMLM. This purification and labeling strategy can potentially be extended to a variety of protein fragments compatible with SMLM.

INTRODUCTION

Cellular morphology, migration, division, polarization and differentiation are all processes that require very specific cytoskeleton organization and dynamics. The exact organization of microtubules and actin directly influences the available roads for active transport by kinesins/dyneins and myosins respectively [1-3]. A specific actin organization is important during cell migration, neuronal growth cone extension, brush border formation and many other processes [4,5]. Different actin structures underlie different functions. For example, while dense structures of actin in the axon initial segment of neurons can mediate myosin-mediated anchoring of cargoes, cortical actin structures can drive directional motility in epithelial cells [6,7]. Therefore, understanding the nanoscale organization of the actin and microtubule cytoskeleton is important to understand the mechanisms and functions of these specialized structures.

Conventional fluorescence microscopy is widely available and continues to be a powerful tool to provide new insights in cytoskeleton organization and dynamics. Better objectives, faster cameras as well as genetic tools and immunocytochemistry can be used to label and image individual proteins with high specificity and temporal resolution. However, conventional fluorescent microscopy is limited by the diffraction of light, which causes fluorophores to be imaged as a spatially extended structure of 200-300 nm. This detected pattern of a single fluorophore on the camera is called the Point Spread Function (PSF) which is shaped like an airy disk. When two fluorophores emit light at the same time while they are very close, the airy disks overlap and cannot be separated. This phenomenon limits the distance at which you can separate two fluorophores or structures to approximately half the wavelength of the detected light.

During the last decade several fluorescence based microscopy techniques have been developed that are not limited by diffraction [8,9]. Single molecule localization microscopy (SMLM) is a super-resolution technique based on the sequential detection of individual fluorophores and subsequent midpoint determination with nanometer precision. All detected fluorophores that label the structure of interest can result in a single reconstructed image where all fluorophore locations are plotted with high precision [10]. Techniques that are based on SMLM are PALM (Photoactivated Localization Microscopy - [11]), STORM (Stochastic Optical Reconstruction Microscopy - [10]), dSTORM (direct STORM - [12]), GSDIM (Ground-State-Depletion and Single Molecule return -[13]) and PAINT (Point Accumulation for Imaging in Nanoscale Topography - [14]). In fixed samples (d)STORM provides the highest resolution and is therefore commonly used to study the exact architecture of the cytoskeleton beyond the diffraction limit. One important breakthrough was the discovery of the periodic actin and spectrin rings in the axon [15]. A major limitation of dSTORM is the limited number of fluorophores compatible with robust multi-color imaging. Another limitation of dSTORM is the use of high laser intensities to bring the majority of the fluorophores in a

dark-state so that individual molecules can be detected. This results in overall bleaching of fluorophores and reduces the amount of detections over time. Additionally, achieving such high laser intensities often requires illumination of only a small area of the sample.

PAINT-like methods overcome these limitations. They rely on the transient binding of fluorophores targeted to the structure of interest. Weakly interacting probes coupled to a fluorophore will bind stochastically, serve as point emitter for a limited time and diffuse back into solution **(Fig 1a)** [16]. The imaging solution can then be washed and a second structure can be imaged using a similar or different fluorophore targeted to a different structure**.** The overall advantage of this technique lies within the transient binding. Unlike dSTORM, there is no need for high laser intensities to bring the majority of fluorophores to a dark state. In addition, the probes on the target are continuously replaced by fresh probes from solution resulting in a continuing imaging cycle not limited by bleaching. Furthermore, PAINT-like SMLM can be performed using a wide variety of fluorophores for multi-color imaging.

A limiting factor for PAINT-type approaches is the need for proper transiently interacting probes. Recently, a generic approach for PAINT, DNA-PAINT, was introduced in which structures labeled with an antibody conjugated to single-stranded DNA can be imaged very specifically with complementary DNA coupled to a fluorophore [14]. Alternatively, protein-protein interactions can be used to target fluorophores to the desired structure. It has been shown that using small protein fragments/peptides coupled to a fluorophore, SMLM by transient binding could be performed on actin and other cytoskeleton structures. The major advantage of these interactions is that they are highly specific and can rely on very small probes. Recent work showed that using these transient protein-protein interactions, the actin cytoskeleton can be visualized in high detail by lifeAct coupled to an Atto-dye [17]. LifeAct is a small 17 amino-acid fragment of the yeast Abp140 protein that was found to label actin [18]. Whereas this work used a commercially obtained synthesized lifeAct probe, we recently developed an approach to purify the lifeAct peptide, either fused to fluorescent proteins or conjugated with organic dyes after purification.

Here we describe a step-by-step protocol to purify the lifeAct domain for super resolution microscopy. This method allows for SMLM using either a fused fluorescent protein or using any organic fluorophore coupled by thiol-maleimide chemistry. For this a construct that consists of "lifeAct-Cysteine-PreScission Cleavage Site-GFP-6x His" was created, as shown in Figure 1. To perform SMLM using the fluorescent protein module (GFP) a rapid his-tag purification can be performed. To functionalize the small peptide with any organic dye, thiol-maleimide chemistry on the introduced cysteine and subsequent proteolytic cleavage by PreScission protease can be performed **(Fig 1b)**. The generation of this versatile probe can be extended to other protein fragments to label other structures of interest.

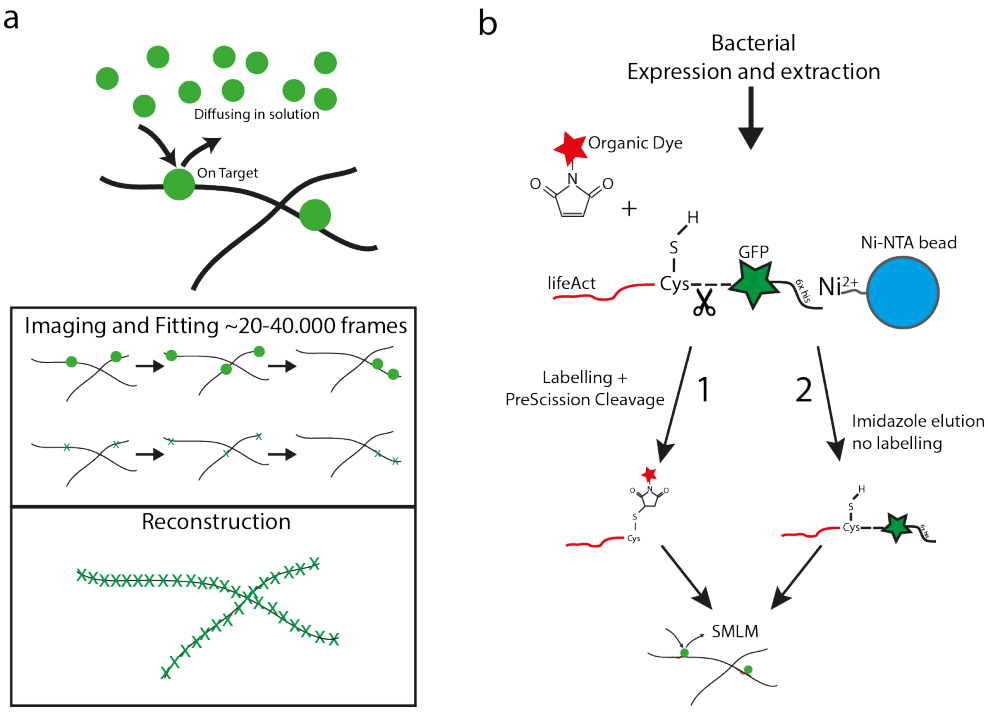

Figure 1: Single-molecule localization microscopy (SMLM) by transient binding.
a) *Principle of SMLM by transient binding. From solution, fluorophores targeted by a specific molecule transiently bind to the structure of interest so that single molecules can be observed. These single molecule events are recorded through time. Subsequently midpoint determination and reconstruction lead to a super-resolved image.*
b) *Schematic representation of the purification and labeling lifeAct probe with GFP or organic dyes to label actin. Arrow 1 represents purification through proteolytic cleavage. Arrow 2 represents the purification with a GFP as fluorescent protein. Dashed line with scissors indicates PreScission cleavage site.*

MATERIALS

All imaging experiments are performed at room temperature unless indicated otherwise. Solutions are dissolved in ultrapure water (~18 MΩ-cm at 25 °C). During purification, buffers and samples are kept on ice to avoid protein degradation.

Purification and labeling

1. *E.coli* BL21DE3 transformed with an IPTG inducible expression vector for lifeAct-cys-PreScission Site-GFP-6xHis (**note 1**).
2. Resuspension/lysis Buffer: 20 mM HNa_2PO_4, 300 mM NaCl, 0.5% glycerol, 7% glucose, EDTA-free protease inhibitor (Roche Diagnostics GmbH), 1mM dithiothreitol (DTT), pH 7.4. To a beaker containing a magnetic stir bar, add 100

ml water, 0.71 grams of HNa_2PO_4, 3.5 grams of NaCl, 14 grams of Glucose and 1 ml 100% Glycerol. Adjust pH to 7.4 and add water to a final volume of 200 ml and readjust pH if necessary. Before purification add 1 tablet of EDTA-free protease inhibitor (Roche Diagnostics GmbH) and 50 µl 1M DTT per 50 ml of buffer and incubate on ice.

3. Wash Buffer: 10 mM HNa_2PO_4, 300 mM NaCl, 30 mM imidazole, 1mM DTT, pH7.4. Prepare as previous step.
4. Labeling Buffer: 10 mM TCEP in PBS
5. Cleavage buffer: 50 mM Tris-HCl, 150 mM NaCl, 1 mM EDTA, 1 mM DTT, pH 7.0
6. Elution Buffer: 10 mM HNa_2PO_4, 300 mM NaCl, 300 mM imidazole, 1mM DTT, pH 7.4. Prepare as in the previous step.
7. Ni-NTA Agarose beads
8. 10 mM (tris(2-carboxyethyl)phosphine (TCEP) in PBS
9. AlexaFluor®-Maleimide in anhydrous dimethyl sulfoxide (DMSO). Dissolve AlexaFluor®-Maleimide in fresh DMSO to ~100 µM or as indicated by the company.
10. Glutathione-sepharose 4B beads in 20% ethanol (GE Healthcare Life Sciences)
11. PreScission protease in cleavage buffer + 20% glycerol (GE Healthcare Life Sciences)
12. LB Broth
13. 1M Isopropyl β-D-1-thiogalactopyranoside (IPTG) in water
14. Shaking incubator
15. Probe-type Sonicator for cell disruption equipped with a tip suited for 50 ml tubes.
16. Cooled Centrifuge (18000 x g)

Fixation

Cultured cells grown on any surface that is compatible with TIRF imaging: e.g. epithelial cells or neurons plated on glass coverslips (**Note 2**).

1. Cytoskeleton Buffer: 10 mM MES, 150 mM NaCl, 5mM $MgCl_2$, 5mM EGTA, 5mM Glucose, pH6.1 [15]
2. 16% Paraformaldehyde (PFA) dissolved in water
3. 1x d-PBS
4. Fixation Buffer: Cytoskeleton buffer supplemented with 0.5% Triton-X and 3% w/v PFA
5. Blocking solution: 3% w/v BSA in d-PBS
6. Optional: antibodies for detection of additional structures

Sample preparation

1. Tweezers
2. mounting chamber
3. d-PBS
4. purified lifeAct coupled to a fluorophore

Microscope setup

1. Standard inverted fluorescence microscopy equipped with a high NA objective and a total internal reflection fluorescence (TIRF) module.
2. Fluorescent filters for imaging GFP or the conjugated fluorophore.
3. Excitation lasers with the appropriate wavelength.
4. EMCCD camera or CMOS camera, sensitive enough to image single molecules
5. SMLM software for super resolution reconstruction: e.g. DoM Utrecht (Detection of Molecules, https://github.com/ekatrukha/DoM_Utrecht [19]), QuickPalm, (http://imagej.net/QuickPALM [20]), Thunderstorm (http://zitmen.github.io/thunderstorm/, [21]), RapidSTORM (http://www.super-resolution.biozentrum.uni-wuerzburg.de/research_topics/rapidstorm/, [22]), NIS Elements (Nikon instruments).
6. Microscope control via PC and dedicated software, for example Micromanager (https://micro-manager.org/, [23]).

METHODS

Expression and passivation on Ni-NTA beads

The correct expression and purification protocols vary between the two different options, i.e. with or without GFP. Because lifeAct coupled to GFP is highly soluble, standard purification protocols and buffers are used. For the lifeAct without GFP, the full recombinant protein is bound to the Ni-NTA beads and the cysteine containing lifeAct fragment is cleaved off by PreScission protease after on-bead labeling. Subsequently free PreScission is captured by glutathione beads. Full recombinant protein coupled to GFP or the short lifeAct fragment coupled to an Alexa dye by the maleimide-cysteine reaction can be obtained at high yields. However, it should be noted that the free cysteine, which was introduced in the construct, is prone to form disulfide bonds with other free cysteines in the samples, resulting in precipitation. To overcome this problem, reducing reagents like DTT or TCEP are required at all steps. A detailed step-by-step description of purification follows below.

1. Grow 0.8 L *E.coli* BL21DE3 containing the lifeAct expression plasmid to OD0.6 at 37 °C from an overnight 4ml culture in LB. Induce protein expression by addition of 800 µL 1M IPTG to achieve a final concentration of 1mM. Incubate for 3.5 hours at 37°C or 16 hours overnight at 17°C.
2. After induction, transfer the bacteria into a centrifuge compatible bucket and spin at 4000 x g for 30 minutes at 4°C. Decant supernatant carefully and incubate pellet on ice. Resuspend bacterial pellet in resuspension buffer supplemented with protease inhibitors (5ml/gram bacterial pellet) and transfer to a 50 ml tube.
3. To lyse the bacteria, sonicate the bacterial suspension 5 x 1 minute with 5 minute intervals on ice. Intermediate to high sonication powers can be used.
4. Following sonication, the soluble fraction of the bacterial suspension can be separated

from the insoluble sample fraction through centrifugation at 18,000 x g at 4°C for 40 minutes **(Note 3)**.

5. During centrifugation wash 1.0 ml of Ni-NTA resin (0.5ml Beads) in resuspension buffer. Beads can be centrifuged at 1000 x g for 3 minutes with slow deceleration. Supernatant can then be removed by a vacuum pump or pipet and replaced by resuspension buffer. Repeat the bead wash 3x in resuspension buffer with 10 times the bead resin volume (10 ml).
6. To separate the soluble fraction from the insoluble fraction after centrifugation, transfer the supernatant into a 50 ml tube to separate it from pellet. Typically, the supernatant of bacteria is a yellowish solution. However, because lifeAct is tagged with a GFP, the supernatant can appear more greenish. The pellet should be brown/yellowish, but can also be greenish because it can contain some aggregated protein or non-lysed expressing cells.
7. Add the washed Ni-NTA beads to the soluble supernatant and incubate at 4°C while gently rolling for 2 hours. The His-Tag of the recombinant lifeAct will bind to the beads.
8. After incubation spin the beads at 1,000 x g for 3 minutes with slow deceleration as described before. The lifeAct-Cys-PreScissionSite-GFP-6xHis is now bound to the beads. Supernatant containing all other soluble proteins that do not contain a His-Tag can be discarded.
9. Wash the beads 3x as described above in wash buffer to reduce non-specific interactions of proteins with the beads. The lifeAct recombinant fragment has 6xHis-Tag which binds tightly to Ni-NTA. This specific interaction will not be disrupted by the 30mM imidazole in the wash buffer.

Purification with GFP

1. To obtain the full lifeAct-Cys-PreScissionSite-GFP-6xHis for SMLM (**Note 4**), the recombinant protein can be eluted by aspiration of the last wash step as described in *section 3.1*. Addition of 3.5 ml Elution Buffer results in the elution of the recombinant His-tagged protein from the beads after 10 minutes incubation. Beads can be spun down and the supernatant containing lifeAct-GFP can be collected.
2. The eluted fraction can be used directly for SMLM as described in *section 3.5***.** For long-term storage, exchange the buffer to PBS+1mM DTT using a buffer exchange column, and add 10% glycerol. Snap-freezing followed by -80°C storage is recommended. The purity of the final sample can be determined by SDS-page. Typically, this approach yields highly pure samples.

Labelling and purification with organic dyes

The second mode in which this recombinant lifeAct fragment can be used is by labeling of the introduced cysteine through a maleimide-thiol interaction. The lifeAct-Cys, coupled to

the thiol, can subsequently be cleaved off the GFP-6xHis and further purified. The overall advantage is that almost all organic dyes and other chemical modifications are available conjugated to a maleimide. Therefore it can be used to label the lifeAct-Cys fragment with a variety of stable fluorophores, resulting in a high photon yield. Below we describe how the cysteine can be labeled with an Alexa647 through maleimide coupling on the beads, followed by cleavage at the PreScission site.

1. After the third wash in wash buffer (*section 3.1)* wash the beads 3 additional times with labeling buffer. Because DTT contains two thiol groups, it is not compatible with maleimide coupling. Replacement with of DTT with TCEP is therefore essential for protein solubility and coupling efficiency.
2. For labeling, aspirate the final wash and transfer the beads into a 2 ml Eppendorf. Add 1000µl labeling buffer supplemented with 80µl of ~100µM Alexa647-maleimide (~8 millimole Alexa647) in DMSO and incubate for 4 hours at room temperature. After incubation add an additional 60µL ~100µM Alexa647-maleimide and incubate overnight at 4°C. The maleimide-dye is added in excess and should, if incubation times are long enough, label almost all free cysteines in the sample.
3. Remove excess dye after labeling through three 1ml washes in Cleavage Buffer. This buffer allows optimal cleavage at the PreScission cleavage site, releasing lifeAct-Cysteine labeled with Alexa647 while leaving GFP-6xHis bound to the beads.
4. Cleave lifeAct-Cys-Alexa647 from the Ni-NTA beads by replacing the final wash step with 70 µL PreScission protease in 500 µL Cleavage Buffer for 5 hours at 4°C (or overnight) while gently rolling.
5. While cleaving, wash 250 µl glutathione beads with cleavage buffer as described above.
6. Capture PreScission protease on the glutathione beads by addition of the prewashed beads to the sample. Now, both PreScission and the GFP-6xHis are bound to the glutathione and Ni-NTA beads respectively while lifeAct-Cys-Alexa647 diffuses in the supernatant.
7. The supernatant containing soluble lifeAct-Cys-A647 can be collected. The final concentration of the lifeAct peptide can be determined using the Bicinchoninic Acid (BCA) protein assay [24]. The labeling efficiency can then be determined by measuring the dye concentration by spectroscopy and application of Beer-Lambert's law. Typical concentrations of labeled lifeAct range from 0.1-1 µM **(Note 5)**.
8. Finally, supplement the sample with a final concentration of 10% glycerol, snap-freeze in liquid nitrogen and store at -80°C.

Sample Preparation

Because in super resolution all details and therefore also sample errors are visualized, optimized sample preparation and dense label coverage are essential for a successful final reconstruction. Fixations and staining protocols that would result in a smooth diffraction limited image might result in sparsely labeled structures in super resolution. Sample preparation should

therefore be optimized for each individual structure or co-labeling of multiple structures. The buffer conditions during fixation also play an important role to preserve cytoskeletal structures. Whereas microtubule fixations are preferentially performed in PEM80 buffer [25], cytoskeleton buffer is the fixation buffer of choice for actin [17,15]. Finally, fixatives should be chosen carefully and such that labeling is not perturbed and structures are maintained. Actin structures are preferentially fixed by PFA or Glutaraldehyde [26]. Below a simple and fast sample preparation is described with PFA in cytoskeletal buffer to preserve the actin network.

1. Pre-warm fixation buffer to 37°C. Remove the medium from the cells coated on coverslips and gently add pre-warmed fixation buffer for 10 minutes. Triton-X ensures sufficient permeabilization of the cells, resulting in release of cytoplasm which allows the lifeAct probe to diffuse freely. Simultaneously, PFA fixes cellular structures like actin.
2. After fixation aspirate the fixation buffer and wash the sample with d-PBS for 5 minutes. Even though the samples are fixed, pipet with care not to perturb the samples. Repeat the wash 3x.
3. After washing, block the sample with blocking solution for at least 30 minutes at room temperature. Blocking reduces the number of unspecific protein-protein interactions reducing the background signal in the final image.
4. To stain for structures additional to actin, the samples can be further incubated with antibodies after blocking. Antibodies compatible with PFA fixation can be diluted in blocking solution and incubated on the sample for at least 1 hour at room temperature. Subsequently, the primary antibody incubation can be stopped by 3 additional 5-minute washes with d-PBS. Cells can then be incubated with a suitable secondary labeled antibody in blocking solution to finish the staining for the desired structure (**Note 6**).
5. After blocking and optional staining, the samples are ready to be mounted in d-PBS + DTT (**Note 7**). A suitable chamber that is compatible with the microscope stage can be used. Open chambers like Ludin chambers for 18mm round coverslips provide easy access to the imaging medium and allows for the addition or dilution of the lifeAct probe during image acquisition

Imaging

1. Secure a sample on the microscope and select a position of interest. Before image acquisition can be started, it is important to select the correct parameters for an optimal super resolution image. Focusing before acquisition is important to image the correct plane of interest. Because the low concentration of lifeAct used for imaging does not provide a full overview of the cellular outline a co-transfection or staining of an additional marker is favorable. Alternatively, an excess of lifeAct conjugated to a fluorophore can be added to the sample which results in a faint outline of the cellular actin structures. If the latter is applied, the concentration should be strongly reduced through dilution and bleaching before SMLM acquisition to be able to visualize single molecules (**Note 8**).

2. For an optimal super resolution acquisition carefully take the following parameters into account. Optimizing each condition carefully every time can increase the signal to noise ratio per imaging session:
   a. *Exposure time.* For super resolution based on probe exchange, the on- and off- rates should guide the exposure time. Low off rates allow for high exposure times and collection of more photons. However, a single molecule binding event should not be obscured by another molecule binding in the vicinity rendering the software unable to detect them both as separate localizations. The latter has a higher chance at higher on rates. Therefore, a balanced exposure time is necessary. For lifeAct the reported half-life on the actin filaments is 23 ms [17] and it is preferentially imaged with 50-100 ms exposure time.
   b. *Laser Power.* Laser power and exposure time are co-dependent on each other and on fluorophore stability. Fluorescent proteins like GFP are easily bleached compared to organic dyes. It is important that a maximum amount of photons is collected from one single molecule during the selected exposure time. Therefore, laser power can be varied between probes with higher laser powers for more stable probes (**Note 7**). Because the sample is crowded with diffusing lifeAct-fluorophore molecules the laser power should also be kept at moderate levels to minimize background. Starting at low laser powers and gradually increasing them usually results in the rapid recognition of the optimum laser power.
   c. *Number of collected frames.* The more frames can be collected, the better. Reconstruction of a single molecule image preferentially relies only on the most accurate localizations, which can be filtered based on localization precision. Collecting more frames at optimal settings allows more stringent filters on localization precision, but care should be taken to minimize and correct sample drift. Selecting only the most accurate detection already results in a full overview of the image with high resolution. Typically we record 30,000-40,000 frames.
   d. *Fluorophore density.* SMLM relies on the detection of individual fluorophores conjugated to lifeAct that are binding sequentially. Therefore, lifeAct should be diluted to a concentration such that every frame single molecules can be observed. In 2D and 3D imaging the plane in focus will be the plane where the point spread function of the single molecules are symmetrical. For SMLM imaging, labeled lifeAct is typically diluted to 1-5 nM in d-PBS (**Note 9)**.
   e. *Laser angle*. Total Internal Reflection of the laser at the coverslip-sample interface results in an evanescent wave of typically a few hundred nanometers, which prevents excitation of out-of-focus fluorophores. Reducing the incident laser angle results in a more oblique illumination field which yields deeper sample penetration and fluorophore excitation. The latter can be favorable because of imaging depth, but also increases background fluorescence. The incident laser angle should thus be

adjusted dependent on required imaging depth and the background intensity that is acceptable.

Analysis

The final super resolution image is created by accumulation of all single molecule positions that were acquired during imaging. Single molecule positions can be accurately determined by fitting the PSF to a Gaussian and determine the midpoint. The midpoint can be localized with nanometer precision based on the width of the Gaussian. Detection/fitting and subsequent reconstruction of the super resolved image is performed by dedicated software packages. There are several freely available packages (e.g. DoM Utrecht [19], RapidSTORM [22], ThunderSTORM [21], QuickPALM [20]) or commercially available packages to reconstruct a super resolved image.

1. Detection and fitting of the imaged fluorophores is dependent on the image parameters as well as on the recorded PSF. The software usually requires input of the pixel size and several threshold values like estimated PSF size to exclude abnormal detections that cannot result from single molecules. The midpoint of included localizations is then determined with nanometer precision by fitting or maximum likelihood estimation.
2. The detection and fitting process results in a table that contains information about all the individual detected fluorophores. Fluorophore parameters include: the *x*- and *y*-coordinate, the image number in which it was acquired, PSF symmetry (in *x* and *y)*, PSF shape, PSF brightness *etc*.
3. Next, reconstruction of the super resolution image can be done based on this particle table. All the stored *x*- and *y*-coordinate are used to plot the midpoint of these molecules. The midpoint can be plotted as a small Gaussian of a constant size or each midpoint can be plotted as a spot based on its individual localization error. This localization error can be calculated from the fitting parameters and used as a threshold. Fluorophores with more precise localizations can then be plotted as tight spots while less well localized fluorophores are represented as more spread localizations. Several parameters should be taken into account while reconstructing the final image. The pixel size of the reconstructed image should be selected in such a way that they are at least half the size of the smallest details according to the Nyquist criterion. Furthermore, the localizations used in the final reconstruction can be filtered on the localization precision. It should be noted that filtering too much or selecting a very low pixel size will eventually result in very sparse localizations. Both these parameters can be varied and optimized per image to obtain a successful and informative super resolution reconstruction.
4. Drift correction is a final important step in the analysis. Because of the nanometer localization accuracy, any drift of the sample with respect to the objective will be clearly visible in the final reconstruction. Long imaging times combined with small thermal fluctuations will result in noticeable drift in the final reconstruction. The available

software packages usually support drift correction based on frame-to-frame cross-correlation of fiducial markers or cross-correlation of intermediate super resolution reconstructions [27,28]. The fiducial markers can be small particles like beads that are fixed to the coverslip and do not move within the sample. When drift correction based on intermediate super resolution reconstructions is applied, a frame interval should be chosen in such a way that the images can be correctly correlated and drift can be detected (**Note 9**).

5. An example of a successful super resolution reconstruction of actin, imaged with either GFP or Alexa647 coupled to lifeAct is shown in figure 2.

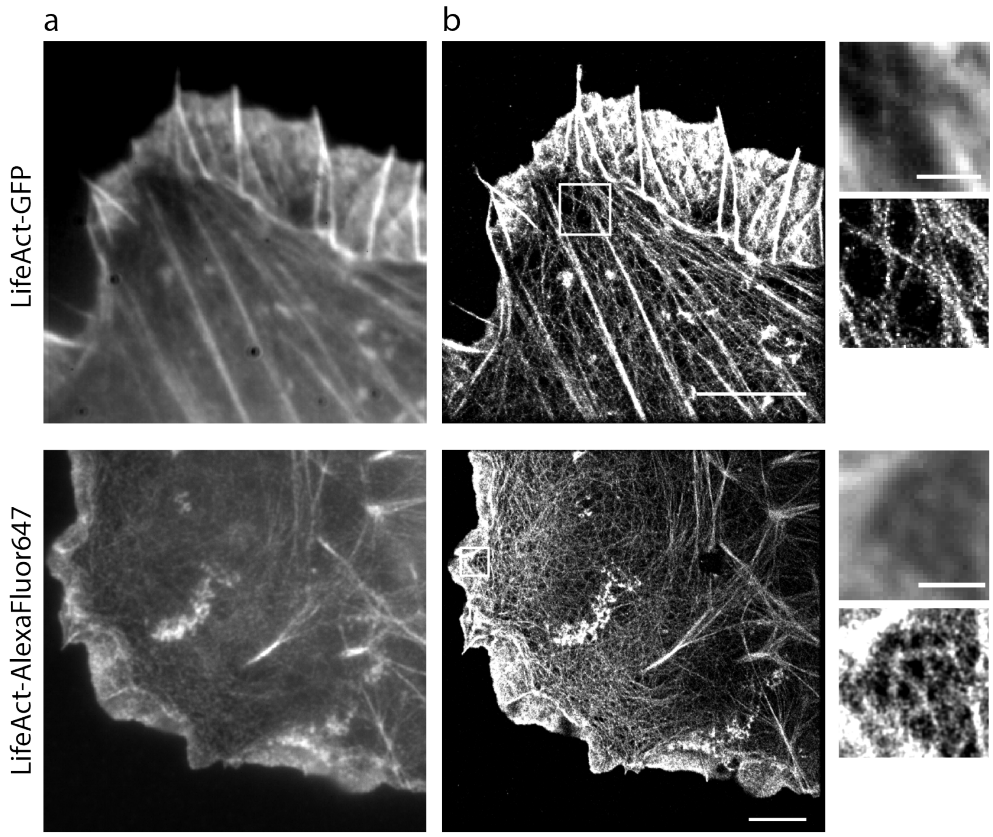

Figure 2: Representative super resolution images obtained using the lifeAct probes.
Diffraction-limited overview (a), super-resolved image (b) and zooms of lifeAct-GFP used on a HeLa cell (top) or lifeAct-AlexaFluor647 used on a COS7 cell (bottom). Scale bars in super resolved images are 5 µm and 1 µm in the zooms.

NOTES

1. The Amino Acid sequence of the **lifeAct**-cysteine-***PreScissionSite***-GFP-6xHis construct is
MGVADLIKKFESISKEEGSGS**C**EF***LEVLFQGP***VSKGEELFTGVVPILVE
LDGDVNGHKFSVSGEGEGDATYGKLTLKFICTTGKLPVPWPTLVTT
LTYGVQCFSRYPDHMKQHDFFKSAMPEGYVQERTIFFKDDGNYKTR
AEVKFEGDTLVNRIELKGIDFKEDGNILGHKLEYNYNSHNVYIMAD
KQKNGIKVNFKIRHNIEDGSVQLADHYQQNTPIGDGPVLLPDNHYL
STQSKLSKDPNEKRDHMVLLEFVTAAGITLGMDELYKLEHHHHHH

2. Identifying cells of interest. Because low concentrations of lifeAct do not provide a full overview of the cellular structures, a fill or other cellular marker can be expressed to identify cells of interest.

3. Optimizing protein yields.
   a. A greenish bacterial pellet usually indicates sufficient expression.
   b. During each step samples for SDS page can be taken to determine the presence of recombinant protein.
   c. Release of soluble protein after lysis can be increased by the addition of small amounts of lysozyme to weaken the bacterial cell wall.
   d. Overall low soluble protein levels can occur because the recombinant lifeAct can enter into inclusions bodies at too high concentrations. This can be prevented by reducing induction time to only a few hours at 20°C. In addition, DTT concentration can be increased to prevent disulfide-bond formation after lysis.

4. Alternative construct for fluorescent protein imaging only. When lifeAct is only used conjugated to GFP or other fluorescent proteins, removal of the cysteine and PreScission site could result in higher solubility and protein yields.

5. In case of low labeling efficiency of lifeAct-Cysteine:
   a. Measure the amount of labeled lifeAct by BCA assay and the concentration of labeled lifeAct as described in *section 3.4.* When the protein concentration is much higher than the concentration of the fluorophore, the sample is most likely unsaturated due to an inefficient maleimide-thiol reaction or because too little dye was added during the reaction. In the latter case, repeat the purification with an increased dye concentration. The fluorophore to lifeAct-cysteine ratio should be 10-20.
   b. In case of poor reaction efficiency, also check the pH of the buffers. Furthermore, make sure that DTT is washed from the solution and that TCEP exceeds the protein concertation approximately 10-fold to

reduce unwanted disulfide bond formation of the available cysteines.

6. Alternative protocol for multicolor super resolution:
   a. Alternative to the protocol described in *section 3.4* an extraction and fixation protocol more optimal for co-staining with microtubules can be used. In Short: pre-extract in 0.25% glutaraldehyde + 0.3% Triton-X in PEM80 for 1 minute (37°C). Replace pre-extraction with 4% PFA in PEM80 (37°C) for 7 minutes. Proceed with washing as described in *section 3.4* and add an extra permeabilization step of 0.25% Triton-X in d-PBS for 8 minutes followed by 3 more washes and blocking. Use primary labeled antibodies or nanobodies against tubulin to speed up the staining process [19].
   b. Secondary antibodies can be labeled with a variety of functionalized probes. When super resolution imaging of actin by lifeAct needs to be combined with dSTORM super resolution imaging of the second structure, Alexa647 is the best label to be used on the secondary antibody. Alexa647 has rapid blinking properties in PBS supplemented with glucose oxygen scavenger [25]. LifeAct based protein-PAINT is compatible with this buffer.

7. The rapid blinking properties make Alexa647 extremely suitable for dSTORM. However, when lifeAct-Cysteine is used for PAINT-like super resolution through transient binding a more stable fluorophore is required. Labeling lifeAct-Cysteine with other organic dyes might result in a higher photon yield. Alternatively, addition of methylviologen (MV) and ascorbic acid (AA) in the imaging buffer will stabilize Alexa647 significantly [29,30]. Concentrations of MV and AA can be varied between 50 μM and 1 mM to optimize photon yield and binding properties.

8. Cell morphology and structures appear to be affected after fixation. Handle samples carefully. Samples are very fragile during extraction and fixation. Always pipet at the sides of the dish and not directly on the sample because sheer stress can perturb the cell integrity even when fixed. Take extra care while handling samples that are sensitive to fixation techniques like neurons and thick samples.

9. Super resolution reconstruction is unclear:
   a. SMLM relies on the localizations of truly individual fluorophores. Too little localizations will result in a dotty image that can be enhanced by an increase of the pixel size. This will increase the amount of localizations per pixels. However, labeling density can also be too high. When two fluorophores emit light too close together the PSFs will obscure each other and result in mislocalization and poor localization errors. False and poorly localized detections will result in a loss of details.
   b. Adjust drift interval and other parameters of drift correction. Incorrect drift

correction can be clearly visible as a jumped image but sometimes also more subtle as a blurry reconstruction.

REFERENCES

1. Arnold DB, Gallo G (2014) Structure meets function: actin filaments and myosin motors in the axon. J Neurochem 129 (2):213-220. doi:10.1111/jnc.12503
2. Kapitein LC, Schlager MA, Kuijpers M, Wulf PS, van Spronsen M, MacKintosh FC, Hoogenraad CC (2010) Mixed microtubules steer dynein-driven cargo transport into dendrites. Current biology : CB 20 (4):290-299. doi:10.1016/j.cub.2009.12.052
3. Vale RD (2003) The molecular motor toolbox for intracellular transport. Cell 112 (4):467-480
4. Crawley SW, Mooseker MS, Tyska MJ (2014) Shaping the intestinal brush border. J Cell Biol 207 (4):441-451. doi:10.1083/jcb.201407015
5. Kapitein LC, Hoogenraad CC (2015) Building the Neuronal Microtubule Cytoskeleton. Neuron 87 (3):492-506. doi:10.1016/j.neuron.2015.05.046
6. Kapitein LC, van Bergeijk P, Lipka J, Keijzer N, Wulf PS, Katrukha EA, Akhmanova A, Hoogenraad CC (2013) Myosin-V opposes microtubule-based cargo transport and drives directional motility on cortical actin. Current biology : CB 23 (9):828-834. doi:10.1016/j.cub.2013.03.068
7. Watanabe K, Al-Bassam S, Miyazaki Y, Wandless TJ, Webster P, Arnold DB (2012) Networks of polarized actin filaments in the axon initial segment provide a mechanism for sorting axonal and dendritic proteins. Cell reports 2 (6):1546-1553. doi:10.1016/j.celrep.2012.11.015
8. Hell SW (2007) Far-field optical nanoscopy. Science 316 (5828):1153-1158. doi:10.1126/science.1137395
9. Huang B, Babcock H, Zhuang X (2010) Breaking the diffraction barrier: super-resolution imaging of cells. Cell 143 (7):1047-1058. doi:10.1016/j.cell.2010.12.002
10. Rust MJ, Bates M, Zhuang X (2006) Sub-diffraction-limit imaging by stochastic optical reconstruction microscopy (STORM). Nature methods 3 (10):793-795. doi:10.1038/nmeth929
11. Betzig E, Patterson GH, Sougrat R, Lindwasser OW, Olenych S, Bonifacino JS, Davidson MW, Lippincott-Schwartz J, Hess HF (2006) Imaging intracellular fluorescent proteins at nanometer resolution. Science 313 (5793):1642-1645. doi:10.1126/science.1127344
12. Heilemann M, van de Linde S, Schuttpelz M, Kasper R, Seefeldt B, Mukherjee A, Tinnefeld P, Sauer M (2008) Subdiffraction-resolution fluorescence imaging with conventional fluorescent obes. Angewandte Chemie 47 (33):6172-6176. doi:10.1002/anie.200802376
13. Folling J, Bossi M, Bock H, Medda R, Wurm CA, Hein B, Jakobs S, Eggeling C, Hell SW (2008) Fluorescence nanoscopy by ground-state depletion and single-molecule return. Nature methods 5 (11):943-945. doi:10.1038/nmeth.1257
14. Jungmann R, Avendano MS, Woehrstein JB, Dai M, Shih WM, Yin P (2014) Multiplexed 3D cellular super-resolution imaging with DNA-PAINT and Exchange-PAINT. Nature methods 11 (3):313-318. doi:10.1038/nmeth.2835
15. Xu K, Zhong G, Zhuang X (2013) Actin, spectrin, and associated proteins form a periodic cytoskeletal structure in axons. Science 339 (6118):452-456. doi:10.1126/science.1232251
16. Molle J, Raab M, Holzmeister S, Schmitt-Monreal D, Grohmann D, He Z, Tinnefeld P (2016) Superresolution microscopy with transient binding. Current opinion in biotechnology 39:8-16. doi:10.1016/j.copbio.2015.12.009
17. Kiuchi T, Higuchi M, Takamura A, Maruoka M, Watanabe N (2015) Multitarget super-resolution microscopy with high-density labeling by exchangeable probes. Nature methods 12 (8):743-746. doi:10.1038/nmeth.3466
18. Riedl J, Crevenna AH, Kessenbrock K, Yu JH, Neukirchen D, Bista M, Bradke F, Jenne D, Holak TA, Werb Z, Sixt M, Wedlich-Soldner R (2008) Lifeact: a versatile marker to visualize F-actin. Nature methods 5 (7):605-607. doi:10.1038/nmeth.1220

19. Mikhaylova M, Cloin BM, Finan K, van den Berg R, Teeuw J, Kijanka MM, Sokolowski M, Katrukha EA, Maidorn M, Opazo F, Moutel S, Vantard M, Perez F, van Bergen en Henegouwen PM, Hoogenraad CC, Ewers H, Kapitein LC (2015) Resolving bundled microtubules using anti-tubulin nanobodies. Nature communications 6:7933. doi:10.1038/ncomms8933
20. Henriques R, Lelek M, Fornasiero EF, Valtorta F, Zimmer C, Mhlanga MM (2010) QuickPALM: 3D real-time photoactivation nanoscopy image processing in ImageJ. Nature methods 7 (5):339-340. doi:10.1038/nmeth0510-339
21. Ovesny M, Krizek P, Borkovec J, Svindrych Z, Hagen GM (2014) ThunderSTORM: a comprehensive ImageJ plug-in for PALM and STORM data analysis and super-resolution imaging. Bioinformatics 30 (16):2389-2390. doi:10.1093/bioinformatics/btu202
22. Wolter S, Loschberger A, Holm T, Aufmkolk S, Dabauvalle MC, van de Linde S, Sauer M (2012) rapidSTORM: accurate, fast open-source software for localization microscopy. Nature methods 9 (11):1040-1041. doi:10.1038/nmeth.2224
23. Edelstein A, Amodaj N, Hoover K, Vale R, Stuurman N (2010) Computer control of microscopes using microManager. Current protocols in molecular biology Chapter 14:Unit14 20. doi:10.1002/0471142727.mb1420s92
24. Olson BJ, Markwell J (2007) Assays for determination of protein concentration. Current protocols in protein science Chapter 3:Unit 3 4. doi:10.1002/0471140864.ps0304s48
25. Yau KW, van Beuningen SF, Cunha-Ferreira I, Cloin BM, van Battum EY, Will L, Schatzle P, Tas RP, van Krugten J, Katrukha EA, Jiang K, Wulf PS, Mikhaylova M, Harterink M, Pasterkamp RJ, Akhmanova A, Kapitein LC, Hoogenraad CC (2014) Microtubule minus-end binding protein CAMSAP2 controls axon specification and dendrite development. Neuron 82 (5):1058-1073. doi:10.1016/j.neuron.2014.04.019
26. Leyton-Puig D, Kedziora KM, Isogai T, van den Broek B, Jalink K, Innocenti M (2016) PFA fixation enables artifact-free super-resolution imaging of the actin cytoskeleton and associated proteins. Biology open 5 (7):1001-1009. doi:10.1242/bio.019570
27. Lee SH, Baday M, Tjioe M, Simonson PD, Zhang R, Cai E, Selvin PR (2012) Using fixed fiduciary markers for stage drift correction. Optics express 20 (11):12177-12183. doi:10.1364/OE.20.012177
28. Mlodzianoski MJ, Schreiner JM, Callahan SP, Smolkova K, Dlaskova A, Santorova J, Jezek P, Bewersdorf J (2011) Sample drift correction in 3D fluorescence photoactivation localization microscopy. Optics express 19 (16):15009-15019. doi:10.1364/OE.19.015009
29. Vaughan JC, Jia S, Zhuang X (2012) Ultrabright photoactivatable fluorophores created by reductive caging. Nature methods 9 (12):1181-1184. doi:10.1038/nmeth.2214
30. Vogelsang J, Kasper R, Steinhauer C, Person B, Heilemann M, Sauer M, Tinnefeld P (2008) A reducing and oxidizing system minimizes photobleaching and blinking of fluorescent dyes. Angewandte Chemie 47 (29):5465-5469. doi:10.1002/anie.200801518

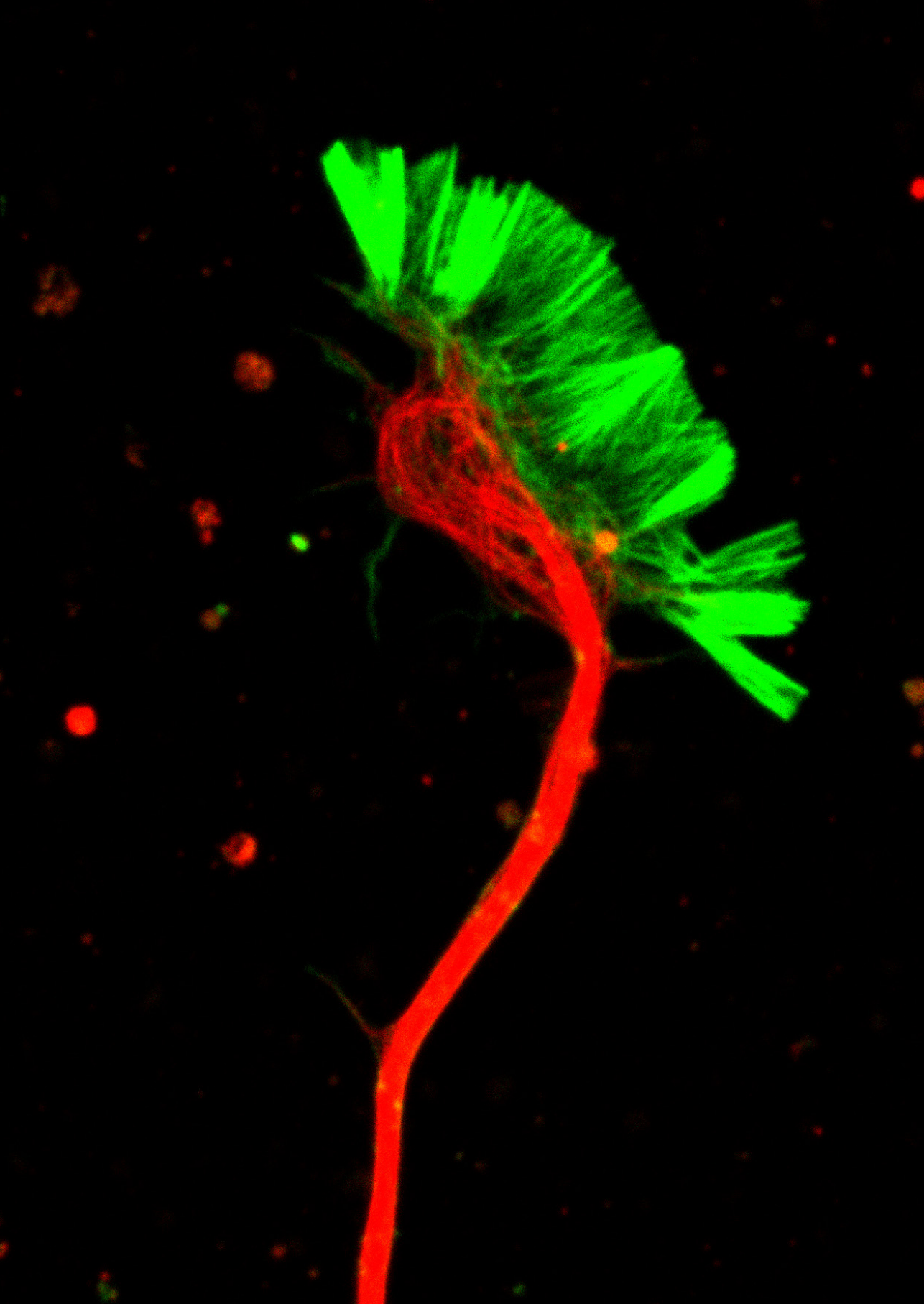

3

Myosin-V Induces Cargo Immobilization and Clustering at the Axon Initial Segment

Anne F. J. Janssen[1]†, **Roderick P. Tas[1]†**, Petra van Bergeijk[1], Rosalie Oost[1], Casper C. Hoogenraad[1] and Lukas C. Kapitein[1]

Frontiers in Cellular Neuroscience (2017); 11, article 260

[1] Division of Cell Biology, Faculty of Science, Utrecht University, The Netherlands
† Equal Contribution

ABSTRACT

The selective transport of different cargoes into axons and dendrites underlies the polarized organization of the neuron. Although it has become clear that the combined activity of different motors determines the destination and selectivity of transport, little is known about the mechanistic details of motor cooperation. For example, the exact role of myosin-V in opposing microtubule-based axon entries has remained unclear. Here we use two orthogonal chemically-induced heterodimerization systems to independently recruit different motors to cargoes. We find that recruiting myosin-V to kinesin-propelled cargoes at approximately equal numbers is sufficient to stall motility. Kinesin-driven cargoes entering the axon were arrested in the axon initial segment (AIS) upon myosin-V recruitment and accumulated in distinct actin-rich hotspots. Importantly, unlike proposed previously, myosin-V did not return these cargoes to the cell body, suggesting that additional mechanism are required to establish cargo retrieval from the AIS.

INTRODUCTION

The selective transport of different cargoes into axons and dendrites underlies the polarized organization of the neuron. Recent work has revealed that different motor proteins have a different selectivity for axons and dendrites. For example, some kinesins selectively target axons, while others target both axons and dendrites (Lipka, Kapitein et al. 2016, Huang, Banker 2012). In addition, myosin-V has been implicated in selective targeting to dendrites (Lewis, Mao et al. 2009). Expression of a dominant negative form of myosin-Va caused the non-specific localization of cargo otherwise enriched in the somatodendritic compartment. Furthermore, coupling a protein to a myosin-Va binding domain was sufficient to cause its somatodendritic localization. More recent work has reported that vesicles with dendritic cargoes often enter the axon, but stop and reverse in the axon initial segment (AIS) in a process that depends on myosin-Va and an intact actin cytoskeleton (Al-Bassam, Xu et al. 2012). Nevertheless, the exact contribution of actin and myosin-V to axonal exclusion has remained controversial, given that actin disruption also distorted the sorting of cargoes into the proper carriers (Petersen, Kaech et al. 2014). In addition, whether recruitment or activation of myosin-V is sufficient to cause the reversal of dendritic cargo has remained unclear.

Although it has become clear that the combined activity of different motors determines transport destination and selectivity, little is known about the mechanistic details of motor cooperation. For example, it is not known whether acute activation or recruitment of myosin-V is sufficient to oppose kinesin-based axon entries. More generally, how the outcome of multiple motors depends on the relative amounts of motor proteins recruited to cellular cargoes has remained unexplored. Elegant in vitro assays have used DNA origami to assemble well-defined combinations of different motor proteins (Derr, Goodman et al. 2012), but similar control has not yet been achieved inside cells. Previously, acute recruitment of different motor proteins using chemically-induced heterodimerization has been used to probe combinatorial motor activity in non-neuronal cells (Kapitein, Schlager et al. 2010b, Kapitein, van Bergeijk et al. 2013). These experiments revealed that, in non-neuronal COS7 cells, recruitment of myosin-V is sufficient to attenuate kinesin-propelled cargo (Kapitein, van Bergeijk et al. 2013). However, in these assays, the motors could not be recruited independently, which would enable sequential recruitment of different motors.

Here we introduce a new assay that allows the independent recruitment of different motor proteins. We find that recruiting myosin-V to kinesin-propelled cargoes at approximately equal numbers is sufficient to stall motility. Kinesin-driven cargoes entering the axon were arrested in the AIS upon myosin-V recruitment and accumulated in distinct actin-rich hotspots. Importantly, unlike proposed previously, myosin-V did not return these cargoes to the cell body, suggesting that additional mechanism are required to establish cargo retrieval from the AIS.

RESULTS

To establish an assay for the independent recruitment of different motors, the FKBP-rapalog-FRB heterodimerization system was combined with a recently introduced chemically-induced heterodimerization system in which the cell-permeable, AM-modified plant hormone gibberellin triggers the interaction between a GID1 and a GAI domain (Miyamoto, DeRose et al. 2012). We chose this dimerization system over light-induced systems, because, similar to the FKBP-rapalog-FRB system, the induced complex formation has been reported to be essentially irreversible. As a result, the available sites on the cargoes will be quickly saturated as long as the number of GAI-labeled motors in the cell is higher than the total number of GID1-sites on the cargoes, irrespective of the exact concentrations. Therefore, if both heterodimerization systems are combined in one peroxisome-targeting construct, PEX3-mRFP-FKBP-linker-GID1, the FRB and GAI domains will be recruited with roughly equal probabilities.

To test the independent recruitment of different motors, COS7 cells were transfected with PEX3-mRFP-FKBP-linker-GID1, Kif17-GFP-GAI and MyoVb-iRFP-FRB (Fig. 1A, B). Upon addition of gibberellin, Kif17-GFP-GAI was recruited to PEX3-mRFP-FKBP-linker-GID1 and peroxisomes were rapidly redistributed to the cell periphery (Fig 1C, middle column). Similar to previous observations, peroxisomes in the cell periphery remained mobile even after reaching the periphery of the cell (Kapitein, van Bergeijk et al. 2013). In addition, contrary to FKBP-based heterodimerization, we noted that a subset of peroxisomes was already mobile at the periphery before addition of gibberellin, indication some degree of background heterodimerization. To still ensure independent recruitment of different motors, gibberelin-based motor recruitment was always performed prior to rapalog-based recruitment.

Twenty five minutes after addition of gibberellin to recruit kinesin, rapalog was added to recruit myosin-V (Fig1A), resulting in an arrest of the kinesin-driven motility and the accumulation of peroxisomes near the cell cortex (Fig1C, right column, Fig1D; Supplemental Video 1). These effects were quantified using two previously introduced metrics (van Bergeijk, Adrian et al. 2015). First, we calculated for all frames the radius required to include 90% of the fluorescence intensity of the peroxisomes ($R_{90\%}$), which revealed that peroxisomes moved rapidly to the periphery upon recruitment of kinesin, but did not move much further upon recruitment of myosin-V (Fig. 1E, F). Second, we used image correlation analysis to measure the overall frame-to-frame similarity during the experiment. In the absence of transport, two subsequent images are largely identical and the correlation index will be close to 1, whereas a value of 0 indicates that all organelles have moved to previously unoccupied positions. The correlation index decreased upon kinesin recruitment, reflecting the increased peroxisome mobility, whereas it increased after recruitment of myosin, indicating that peroxisome became less motile (Fig. 1E, F). This decrease in motility was not observed without recruitment of myosin although cargo reached the cell periphery. This is reflected in the correlation index

which remains low without myosin recruitment. Thus, different heterodimerization systems can be combined to independently recruit different motor proteins, and the recruitment of myosin-V to kinesin motors at roughly equal numbers is sufficient to arrest kinesin-driven motility.

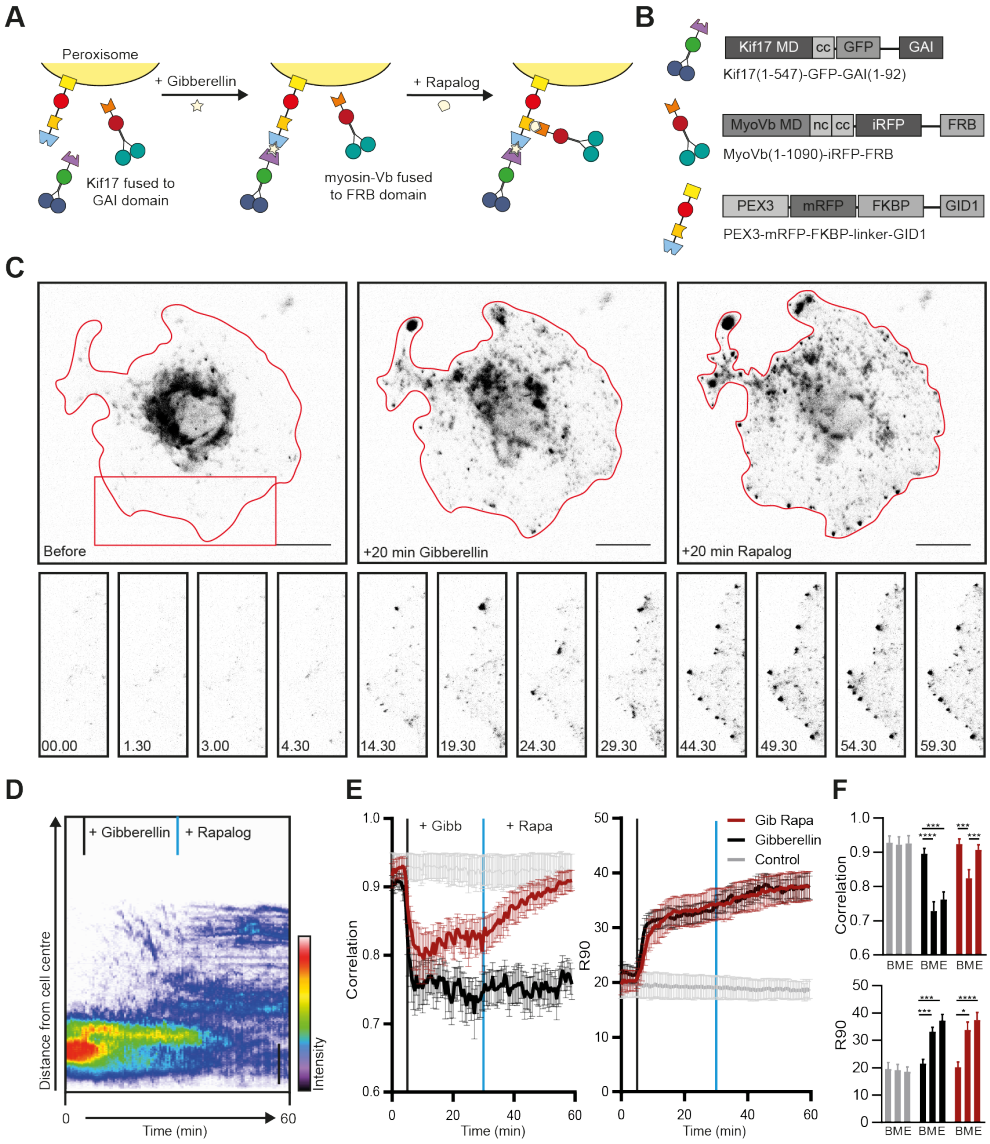

Figure 1: Sequential recruitment of kinesin and myosin-V in COS7 cells

A) *Assay: Sequential recruitment of kinesin and myosin-V by addition of gibberellin and rapalog, respectively.*

B) *Overview of constructs. MD, motor domain; CC, coiled coil; NC, neck coil; GAI, gibberellin insensitive; GID1, Gibberellin insensitive dwarf1.*

C) *Peroxisome distribution before recruitment of motors and after sequential recruitment of kinesin and myosin-V. Red curves indicate cell outline. Panels show individual frames of a cut out. Scale bar, 20 µm.*
D) *Radial kymograph indicating the redistribution of fluorescent peroxisomes relative to the cell axis. Vertical lines indicate addition of gibberellin (blue) and rapalog (black). Scale bar, 10 µm.*
E) *Displacement (expressed in R90%) and correlation (frame-to-frame similarity from 0 to 1) versus time for cells without added ligands (control, gray), cells with addition of gibberelin only (Gibberelin, black) and cells with addition of gibberellin and rapalog (Gib + rapa, red). N=12, 16 and 14 cells for control, gibbellin and gib+rapa groups respectively. Data was obtained from 2 experiments, mean ± s.e.m. Vertical lines indicate time of addition of gibberellin (blue) and rapalog (black), if added.*
F) *Averages of ten frames of each cell at t=0-4.5 min (before, B), t=25-29.5 min (middle, M) and t=55-59.5min (end, E). *P<0.05, **P<0.005, ***P<0.001, ****P<0.0001, Friedman test, Dunn's post hoc test.*

We next switched to neurons to examine how activation of myosin-V alters the kinesin-driven transport of peroxisomes into the axon. We used the kinesin-1 KIF5B, because this motor has been reported to efficiently target cargoes selectively into the axon (Petersen, Kaech et al. 2014, Kapitein, Schlager et al. 2010a, Song, Wang et al. 2009) (Supplemental Figure 1A-C). Indeed, the addition of gibberellin to dissociated hippocampal neurons expressing PEX3-mRFP-FKBP-linker-GID1, Kif5-GFP-GAI and MyoVb-iRFP-FRB induced a burst of peroxisome motility into the axon (n = 16, Fig. 2A-D). Remarkably, the subsequent addition of rapalog to recruit myosin-V resulted in the appearance of several spots in the proximal axon where axon-entering peroxisomes would cluster together, whereas further down the axon (>35 µm) such clusters did not emerge (n= 15 cells, with ≥2 induced axonal clusters and > 75 µm axon length imaged were included, Fig. 2A-D, Supplemental Video 2). Quantification revealed that the percentage of cells that had more than two proximal axonal accumulations increased from 6.25 to 75% during the first 40 minutes after addition of gibberellin (Fig. 2D). Thus, the acute, close-to-equimolar recruitment of myosin-V to kinesin-1 driven, axon-entering cargoes clusters these cargoes in the proximal axon.

Previous work has suggested that myosin-V can drive retrograde axonal transport, thereby returning to the cell body cargoes that have erroneously entered the axon (Watanabe, Al-Bassam et al. 2012). In contrast, we observed that myosin-V induced the appearance of cargo clusters that were largely immobile. To analyze the motility of the myosin-V induced peroxisome clusters in more detail and test for retrograde motility, we traced individual peroxisome clusters (Fig. 2E) and averaged their mean-squared displacements (MSD) for different time intervals (Fig. 2F). The power dependence α of the MSD with increasing time intervals τ, MSD $\propto \tau^{\alpha}$, is the anomalous diffusion exponent (Saxton, Jacobson 1997) and indicates whether motility is completely random (a≈1, diffusive), directed (1<a≤2, superdiffusive), or confined (0<α<1, subdiffusive). Our analysis revealed that the clusters were confined and that the average displacement over > 13 minutes was less than 500 nm (i.e. $(0.25\ mm^2)^{1/2}$, Fig. 2F). Thus, myosin-V does not drive retrograde transport, but anchors cargo at specific locations in the proximal axon.

To explore how myosin-V affects the motility of cargoes that autonomously travel

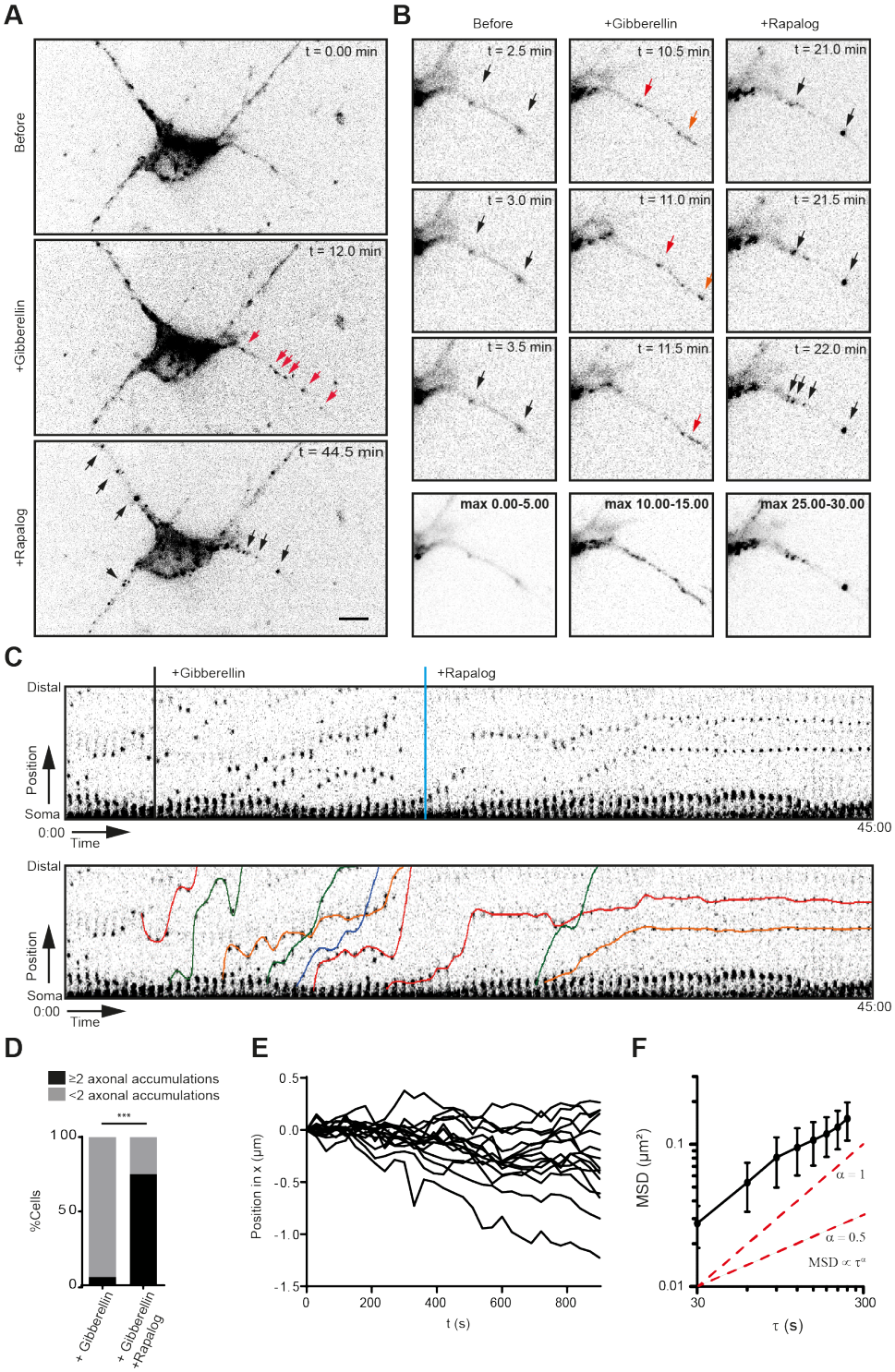
A
Before
+Gibberellin
+Rapalog
t = 0.00 min
t = 12.0 min
t = 44.5 min
B
Before
+Gibberellin
+Rapalog
t = 2.5 min
t = 10.5 min
t = 21.0 min
t = 3.0 min
t = 11.0 min
t = 21.5 min
t = 3.5 min
t = 11.5 min
t = 22.0 min
max 0.00-5.00
max 10.00-15.00
max 25.00-30.00
C
+Gibberellin
+Rapalog
Distal
Position
Soma
0:00
Time
45:00
D
≥2 axonal accumulations
<2 axonal accumulations
***
%Cells
100
50
0
+ Gibberellin
+ Gibberellin +Rapalog
E
Position in x (µm)
0.5
0.0
-0.5
-1.0
-1.5
0
200
400
600
800
t (s)
F
MSD (µm²)
0.1
0.01
α = 1
α = 0.5
MSD ∝ τ^α
30
300
τ (s)

Figure 2: Myosin-V anchors kinesin-1 propelled peroxisomes in the proximal axon and somatodendritic compartment
A) *Dissociated hippocampal neuron showing the distribution of PEX3-mRFP-FKBP-linker-GID1 before (top), after the recruitment of Kif5-GFP-GAI through addition of gibberellin (middle) and after the addition of rapalog to recruit MyoVb-iRFP-FRB (bottom). Red arrows indicate motile peroxisomes, black arrows indicate non-motile peroxisome accumulations. Scale bar, 10 μm.*
B) *Zoom of the proximal axon of neuron in A before (left), plus gibberellin (middle), and plus rapalog (right). Bottom row shows a maximum projection of a 5 minute interval before (left) or after the addition of dimerizers (middle, right).*
C) *Sequential frames of the proximal axon of a dissociated hippocampal neuron treated and imaged as in A. Manually annotated tracks are displayed superimposed on the bottom panel.*
D) *Number of stalled peroxisome accumulations in the axon before and after anchoring with MyoVb. n = 16 and n = 24 for control and +Rapalog, respectively ***, p<0.001 Fisher Exact test.*
E) *Relative displacements of myosin-V anchored clusters 10 minutes after the addition of rapalog. Negative and positive displacement indicates retrograde and anterograde movement, respectively*
F) *Mean square displacement analysis of myosin-V anchored peroxisome clusters tracked for at least 25 intervals of 30 seconds mean ± sd (n=26). Red lines show example curves with slopes $\alpha = 1$ and $\alpha = 0.5$ (i.e. $\log(MSD) \propto \alpha \log \tau$), representative of purely diffusive or confined motility, respectively.*

into the axon, we next turned to Rab3-positive vesicles. When myosin-Vb was recruited to Rab3 vesicles using the FKBP-rapalog-FRB system (Fig. 3A), we observed the emergence of immobile clusters of Rab3-positive vesicles in the first part of the axon, whereas the motility of vesicles in the distal axon did not appear affected, based on inspection of the kymographs (Fig. 3B,C; Supplemental Video 3). In addition, motility arrest and clustering was observed in the somatodendritic compartment (data not shown). Rab3 vesicle clustering was not observed upon treatment with rapalog or gibberellin in the absence of MyoVb-iRFP-FRB expression or without addition of rapalog in the presence of the motor (Supplemental Fig 2A,B). To test whether clustering was selective for the axon initial segment (AIS), we repeated the experiment, followed by staining for the AIS marker Ankyrin-G (Fig 3D-E). Quantitative analysis of the Rab3 cluster relative to the staining of Ankyrin-G revealed that 92 ± 17 % of clusters were found in AIS (average ± sd, n=9 cells) (3F). MSD analysis revealed an anomalous diffusion exponent of ~1 for time scales < 360 seconds (3G). At longer times, the MSD leveled off, suggesting that Rab3 cluster motility was confined to 700-800 nm (i.e. $(0.6\ mm^2)^{1/2}$). It is important to note that the selective clustering in the AIS could be a trivial consequence of the very low levels of myosin-V in the remainder of the axon (Fig. 3H). Nevertheless, these results demonstrate that myosin-V induces cargo clustering, rather than retrograde transport.

Recent work has suggested a role for specialized actin structures in the AIS in myosin-V based cargo retrieval (Watanabe, Al-Bassam et al. 2012). To examine the relation between myosin-V induced cargo clustering and the actin cytoskeleton, we next performed superresolution microscopy to image actin and Rab3 in MyoVb-GFP-FRB and FKBP-tdTomato-Rab3c expressing neurons (Fig. 4A-B). To visualize actin, we purified GFP-tagged Lifeact, a small probe that transiently interacts with polymerized actin and can be used to achieve the repetitive low density labeling required for single molecule localization microscopy

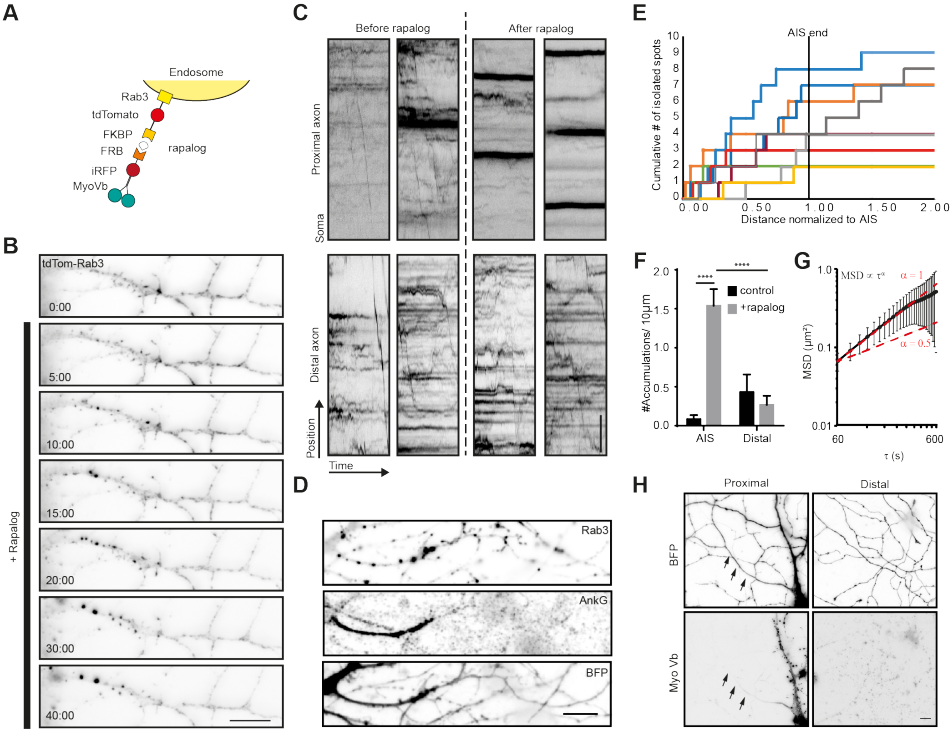

Figure 3: Myosin-V anchors Rab3 vesicles in the proximal axon of hippocampal neurons

A) *Assay: Recruitment of myosin-V to Rab3 vesicles by addition of rapalog.*

B) *Rab3 positive vesicle distribution in the proximal axon. Upon coupling of myosin-Vb to vesicles by addition of rapalog, Rab3 vesicles start accumulating in big puncta. Scale bar, 10 µm.*

C) *Kymographs of Rab3 vesicles in the proximal and distal axon. Short timelapses were acquired with 500 ms intervals before and after addition of rapalog. For imaging of distal axons after rapalog treatment, cells were chosen 1 hr after rapalog addition that showed clear Rab3 anchoring in their proximal axon. Scale bar, 5 µm.*

D) *Rab3 distribution after myosin-Vb recruitment, together with a staining for Ankyrin-G to indicate the AIS. BFP was used as a fill to show the overall morphology. Scale bar, 10 µm.*

E) *Plot of the cumulative number of Rab3 accumulations found in the axon normalized to the AIS determined for cells after rapalog addition to recruit myosin-Vb.*

F) *Number of accumulations found in the AIS and the distal axon as determined using Ankyrin-G staining. The number of accumulation were determined in fixed cells with and without addition of rapalog Mean ±sd (n=9 for both conditions), 2-way ANOVA reveals Finteraction = 26.27, p = 0.0001. Post-hoc multiple comparison testing: ****, p<0.0001.*

G) *Mean square displacement analysis of myosin-V anchored peroxisome clusters tracked for at least 25 intervals of 20 seconds. Mean ±sd (n=18).*

H) *Distribution of the MyoVb(1-1090)-EGFP-FRB construct. The axon is indicated by arrows.. Scale bar, 10 µm.*

(Kiuchi, Higuchi et al. 2015) . To visualize Rab3, we used DNA-PAINT, in which a secondary antibody is labeled with an oligonucleotide that can transiently hybridize with a fluorescently labeled complementary strand, which also ensures repetitive low density labeling (Jungmann, Avendano et al. 2014). After optimization of the extraction and fixation protocols, this enables us to perform two-color nanoscopy of the actin network and rab3 vesicles.

In control cells that were not treated with rapalog, we observed both regularly spaced actin stripes, as described previously (Xu, Zhong et al. 2013), long actin fibers and distinct actin patches with concentrated staining (Fig. 4A). No apparent colocalization between actin and Rab3 was observed in these cells. In cells treated with rapalog, a clear colocalization between Rab3 accumulations and actin-rich regions was observed (Fig. 4B). The diameter of Rab3 structures that were colocalized with actin patches was about two times greater compared to Rab3 structures outside these patches or in cells without rapalog treatment (Fig. 4C). This suggests that multiple vesicles have coalesced on these patches, consistent with our live imaging data of cluster formation (Fig. 3B, C). Furthermore, Rab3 clusters were only observed in the proximal and not the distal axon (Fig 4D-E). These data demonstrate that actin patches are the site of myosin-mediated anchoring.

DISCUSSION

We have developed an assay for the sequential recruitment of motor proteins to specific cargoes. Using this assay, we were able to show that recruiting myosin-V to kinesin-1-driven cargo is sufficient for myosin to attenuate kinesin-driven motility of peroxisomes in COS7 cells. Future work will be directed towards exploring the myosin-kinesin ratio at which stalling still occurs. In addition, the outcome of other motor combinations could also be explored, for example kinesins and dyneins or combinations of different kinesin motors.

We were able to show a similar anchoring behavior in neurons where peroxisomes coupled to kinesin entered the axon, but were subsequently anchored at the Axon Initial Segment by myosin-V recruitment. Similar results were obtained upon recruitment of myosin-V to Rab3-positive vesicles. No reversals of myosin-V anchored peroxisomes back into the cell soma were observed. These results support a model in which myosin-V stalls the motility of dendritic vesicles that erroneously entered the axon, but also demonstrate that recruitment of myosin-V is not sufficient to bring these cargoes back into the soma to facilitate delivery to their proper destination. These finding are consistent with earlier work demonstrating that the coupling of a myosin-Va binding domain of Melanophilin to vesicles with no specific localization increases their halting frequency in the AIS but not the frequency of reversals (Al-Bassam, Xu et al. 2012).

Myosin-V-induced anchoring was also observed in the dendrites and soma, suggesting that this anchoring does not depend on specific feature of the AIS, but will occur whenever cargoes with active myosin-V enter actin-rich regions. Indeed, actin hotspots in the

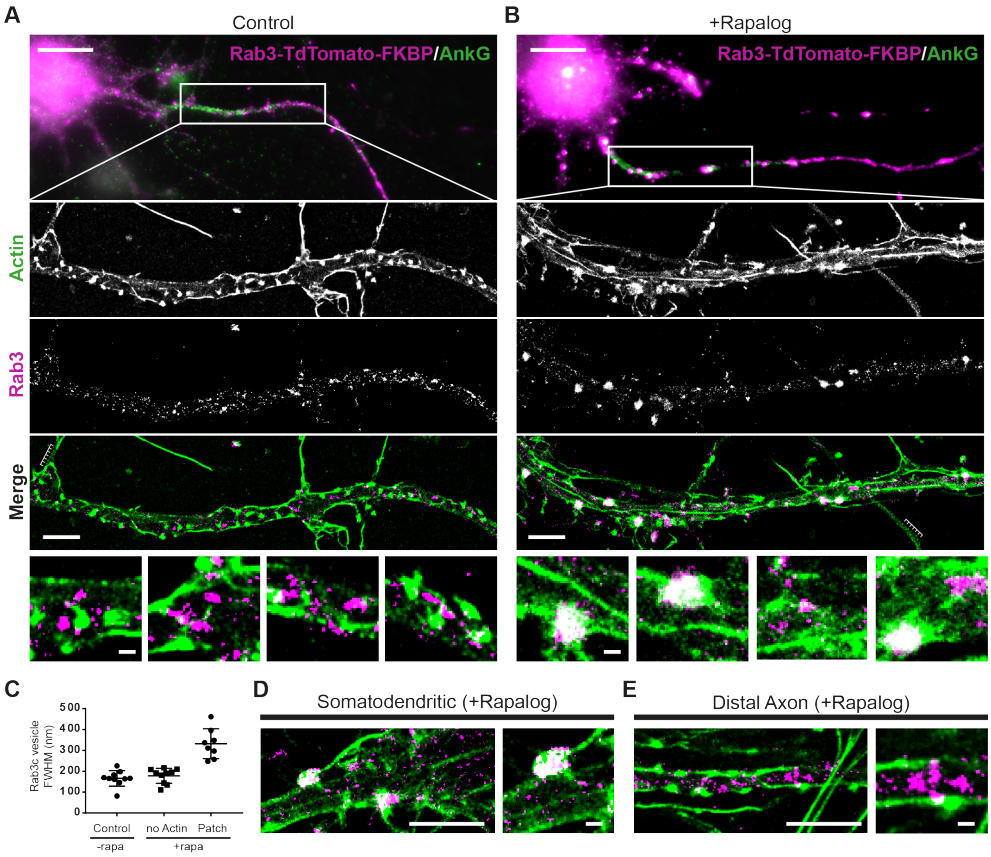

Figure 4: Myosin-V-anchored Rab-3 vesicles accumulate on actin patches in the proximal axon.
A,B) *Single molecule localization microscopy of sequentially imaged lifeAct-GFP protein-PAINT and DNA-PAINT to visualize actin and Rab3, respectively. DIV10 neurons overexpressing MyosinVb-HA-FRB and Rab3-tdTomato-FKBP, post-stained for TdTomato and AnkyrinG. Axons were identified by AnkyrinG staining. Super-resolution images are shown for the regions indicated in the widefield images (top panel). Control (A) and MyosinVb coupled Rab3 vesicles (B) are imaged together with actin (middle 3 panels). Scale bar: top panel 10 µm, middle panels 2 µm, zooms 0.2 µm*
C) *Quantification of the FWHM of Rab3 structures in control and rapalog-treated cells. Myosin-coupled Rab3 vesicles were separated based on their colocalization with actin patches. Mean±sd are depicted (n = 8-10 for 2 cells per condition).*
D) *Super-resolution image and zoom of Rab3 cluster colocalization with actin in the somatodendritic compartment. Scale bar: left panel 2µm, right panel 0.2µm*
E) *Super resolution image and zoom of Rab3 vesicles and actin in the distal axon. Scale bar: left panel 2µm, right panel 0.2µm*

distal axon were also described by others (Ganguly, Tang et al. 2015). We do not exclude that recruitment of other proteins could also affect the transport of cargoes, for example due to steric effects. However, myosin-5 is recruited to kinesin that is already attached to an organelle and therefore the increase in size is not as dramatic compared to recruiting myosin-5 to a

free kinesin. More importantly, myosin-5 recruitment stalls transport on actin patches, which suggests that this effect is at least specific to a actin-binding protein. Although myosin-V based anchoring is not restricted to the axon, the actin in the AIS still establishes an important vesicle filter, because it enables the halting of cargo that is not supposed to enter the axon. This suggests that the cargo recruitment and/or activation state of myosin-V determines whether the cargo is allowed to pass the AIS. Upon anchoring, the subsequent recruitment of dynein could return the cargo to the cell body. This is consistent with recent work on the dynein regulator NDEL, which was shown to localize to the AIS via an interaction with the scaffolding protein Ankyrin-G and facilite cargo reversal (Kuijpers, van de Willige et al. 2016).

EXPERIMENTAL PROCEDURES

DNA constructs and protein purification

DNA constructs used in this study were cloned in pGW1-CMV and pβactin-16-pl vectors. The pβactin-PEX3-mRFP-FKBP-linker-GID1 construct was made by PCR amplification of the GID1 domain with addition of a linker (SAGGSAGGSAGG), then ligated into the SpeI and NotI sites of the pβactin-PEX3-mRFP vector described previously (Kapitein, Schlager et al. 2010b), followed by PCR amplification of FKBP(1x) and insertion into the EcoRI and SalI sites of the construct. The FKBP encoding fragments were described previously (Kapitein, Schlager et al. 2010b).

pβactin-MyoVb-(amino acid 1-1090)-GFP-FRB was described before (Kapitein, van Bergeijk et al. 2013). MyoVb-(1-1090)-iRFP-FRB (myosin-Vb) was generated by replacing the GFP by iRFP using the EcoRI and SpeI sites. Kif17md-GFP-GAI was generated by insertion of Kif17MD (aa 1-547 of human KIF17) in AscI and SalI sites, GFP in SalI and SpeI sites, and GAI(1-92) in SpeI and NotI sites of pβactin. FKBP-tdTomato-Rab3c was generated by insertion of PCR-amplified tdTomato in Sal and SpeI site, Mouse Rab3c in SpeI and NotI sites and FKBP(1x) in BamHI and SalI sites of the pβactin-16-pl vector.

To visualize actin using single molecule localization microscopy lifeAct-GFP was purified and used as a transient binding probe(Kiuchi, Higuchi et al. 2015). In brief, lifeAct-GS linker -GFP was cloned into a PET28a vector with a C-terminal 6x His sequence and transformed into BL21DE3 bacteria. Bacteria were grown until OD0.6 and induced with 1mM IPTG overnight at 17 °C. Cells were then pelleted and resuspended in resuspension buffer (20 mM HNa2PO4, 300 mM NaCl, 0.5% glycerol, 7% glucose, EDTA-free protease inhibitor (Roche Diagnostics GmbH), 1mM dithiothreitol (DTT), pH 7.4). Cells were lysed by sonication and the soluble and insoluble fraction were separated by centrifugation. Ni-NTA (Roche) beads were washed with resuspension buffer and incubated with the soluble supernatant for 1.5 hours at 4 °C. After incubation, the beads with bound proteins were washed 5 times with wash buffer (10 mM HNa2PO4, 300 mM NaCl, 30 mM imidazole, 1mM DTT, pH7.4). Finally lifeAct-GFP was eluted in Elution Buffer (10 mM HNa2PO4, 300 mM

NaCl, 300 mM imidazole, 1mM DTT, pH 7.4) and snap-frozen at -80°C with 10% glycerol.

Cell cultures and transfection

COS-7 cells were cultured in DMEM/Ham's F10 (1:1) medium containing 10% FCS and penicillin/streptomycin. Cells were plated on 18-mm diameter coverslips 2–4 days before transfection. Cells were transfected with Fugene6 transfection reagent (Roche) according to the manufacturer's protocol and imaged one day after transfection.

Primary hippocampal cultures were prepared from embryonic day 18 (E18) rat brains. Cells were plated on coverslips coated with poly-L-lysine (30 mg ml^{-1}) and laminin (2 mg ml^{-1}). Hippocampal cultures were grown in Neurobasal medium (NB) supplemented with B27 (Invitrogen), 0.5 mM glutamine, 12.5 mM glutamate, and penicillin plus streptomycin. Transfections of hippocampal neurons were performed 48 h before imaging with lipofectamine 2000 (Invitrogen). DNA (1.8 µg per well) was mixed with 3.3 µl lipofectamine 2000 in 200 ml NB, incubated for 30 min, and added to the neurons in NB supplemented with 0.5 mM glutamine at 37 °C in 5% CO_2. After 60-90 min neurons were washed with NB and transferred to the original medium at 37 °C in 5% CO_2 for 2 days. Transport assays in neurons were imaged at day-in-vitro 12-16.

Live-cell imaging

Time-lapse live-cell imaging of peroxisomes in hippocampal neurons was performed on a Nikon Eclipse TE2000E (Nikon) equipped with an incubation chamber (Tokai Hit; INUG2-ZILCS-H2) mounted on a motorized stage (Prior)(Kapitein, van Bergeijk et al. 2013). Coverslips (18 mm) were mounted in metal rings covered with conditioned medium. Cells were imaged every 30 s for 60 min using a 40× objective (Plan Fluor, numerical aperture (NA) 1.3, Nikon) and a Coolsnap HQ2 CCD camera (Photometrics).

Peroxisomes in COS7 and neurons were images using a 40x objective (Plan Fluor, numerical aperture (NA) 1.3, Nikon) in Ringer's solution (10 mM HEPES, 155 mM NaCl, 5 mM KCl, 1 mM $CaCl_2$, 1 mM $MgCl_2$, 2 mM NaH_2PO_4 and 10 mM glucose, pH 7.4) or conditioned culture medium respectively. Rab3 vesicles in neurons were imaged in conditioned medium using a 100× objective (Apo TIRF, 1.49 NA, Nikon). A mercury lamp (Osram) and filter wheel containing ET-GFP (49002), ET-dsRed (49005), ET-mCherry (49008) and ET-GFPmCherry (59022) emission filters (all Chroma) were used for excitation. Rab3 in neurons were imaged on a CoolSNAP MYO CCD camera (Photometrics) and peroxisomes in neurons and COS7 cells with a Coolsnap HQ camera (Photometrics, Tucson, AZ). During imaging, all cells were maintained at 37 °C, as well as 5% CO_2 when using conditioned medium.

Cell-permeable gibberellin (GA3IAM, a gift from Dr. T. Inoue (Miyamoto, DeRose et al. 2012) and Rapalog (AP21967 from Ariad Pharmaceuticals) were added during image acquisition to reach a final concentration of 150-300 nM and 100 nM respectively at the indicated time points. In hippocampal neurons, the axon was identified based on morphology

and Rab3 vesicle enrichment. The proximal axon was defined as the first part of the axon before branching, whereas distal axon refers to axonal segments after at least 2 branch points. To identify the axon in live cell imaging experiments (Figure S1), neurons were stained for extracellular Neurofascin before imaging. Coverslips were placed in cultured medium containing anti-neurofascin (Neuromab, mouse, 1/200) for 10 minutes. Coverslips where then washed 5 times by briefly dipping them in neurobasal. Subsequently, coverslips were incubated with anti-mouse AlexaFluor405 (Life Technologies, anti-mouse, 1/100) for 10 minutes. After 5 additional washes cells were place back into their cultured medium before imaging.

Cell fixation and single molecule localization imaging

Cells transfected with Rab3-TdTomato-FKBP, MyosinVb-HA-FRB and a BFP fill (Fig. 3D-H) were fixed with 4% PFA in PBS for 10 min at 37 °C. Subsequently, cells were washed 2 times with PBS, permeabilized with 0.25% triton in PBS for 10 minutes and washed again 3 times with PBS. After washing, cells were blocked for 45 minutes in blocking solution (2% w/v BSA, 0.2% w/v gelatin, 10 mM glycine, 50 mM NH4Cl in PBS, pH 7.4) and incubated overnight with anti-Ankyrin-G (1/200, mouse, Life technologies). Cells were further incubated with anti-mouse Alexa647 (1/400, Life technologies) and mounted for imaging in mowiol.

To determine the localization of the Rab3 accumulation (Fig. 3) samples were imaged on a Nikon eclipse TI upright microscope with a 40x objective (UPLFLN, NA 1.3). Myosin-Vb localization was imaged on an Olympus BX53 upright microscope with a 60x objective (oil, UPLSAPO, NA1.35).

For simultaneous super-resolution imaging of Rab3 and actin (Fig. 4) cells overexpressing Rab3-TdTomato-FKBP and MyosinVb-HA-FRB (either treated with rapalog or not), were pre-extracted 1 minute with 0.35% glutaraldehyde and 0.25% triton-x in cytoskeleton buffer (Xu, Zhong et al. 2013). Cells were then further fixed with 4% PFA. Subsequently, samples were washed 3x with PBS followed by 10 minutes permeabilization in PBS + 0.25% triton-x. After 3 more 5 minute washes in PBS, samples were blocked in 3% BSA for 45 minutes followed by overnight 4°C staining with anti-AnkG (1/200, mouse, Life technologies) and anti-RFP (1/500, rabbit, Rockland) in blocking buffer. After incubation cells were washed 3 times 10 minutes in PBS and incubated with secondary anti-mouse AlexaFluor488 (1/400, Life Technologies) and anti-rabbit-D2 from the Ultivue-2 super resolution 2-plex kit (1/100, Ultivue) for 1.5 hours at room temperature in blocking buffer. After 3 additional washes samples were mounted in a Lundin chamber in Imaging Buffer (Ultivue). Single-molecule microscopy was performed on a Nikon Ti-E microscope equipped with a 100x Apo TIRF oil immersion objective (NA. 1.49) and Perfect Focus System 3. Excitation was achieved via a custom illumination pathway with a Lighthub-6 (Omicron) containing a 638 nm laser (BrixX 500 mW multimode, Omicron), a 488nm laser (Luxx 200 mW, Omicron), and a 405 nm laser (Luxx 60 mW, Omicron). Emission light was separated

from excitation light with a quad-band polychroic mirror (ZT405/488/561/640rpc, Chroma), a quad-band emission filter (ZET405/488/561/640m, Chroma), and an additional single-band emission filter (ET525/50m for green emission and ET655lp for far-red emission, Chroma). Fluorescence was detected using a sCMOS camera (Hamamatsu Flash 4.0v2). Samples were positioned in the *x*- and y-direction with an M-687 PILine stage (PI).

For super-resolution imaging, first cells expressing Rab3-TdTomato were selected and AnkyrinG was imaged to identify the axon. LifeAct-GFP and Imager strand I2-650 (Ultivue) were diluted so that single molecule binding events could be observed for both channels. Subsequently, the relatively weak AnkyrinG AlexaFluor488 staining was completely bleached and LifeAct based protein-PAINT (Kiuchi, Higuchi et al. 2015)was performed by observing single binding and unbinding effects. Subsequently, DNA-PAINT was performed similarly for Rab3 structures stained with rabbit-D2 and Imager strand I-2. For both channels between 8000 and 15000 frames were acquired with a 100 ms exposure time to reconstruct super resolved images of both actin and Rab3. Images were then reconstructed using our ImageJ plugin called DoM (Detection of Molecules, https://github.com/ekatrukha/DoM_Utrecht) which has previously been described in detail(Yau, van Beuningen et al. 2014, Chazeau, Katrukha et al. 2016).

Image processing and analysis

Images of live cells were processed and analyzed using MetaMorph (Molecular Devices), LabVIEW (National Instruments) software and ImageJ (NIH). Drift correction was applied using the StackReg plugin for ImageJ (Thevenaz, Ruttimann et al. 1998) for time series during which multiple positions were recorded using a motorized stage.

To generate the radial kymograph, pixels that were above the set threshold were inserted into a histogram representing the intensity versus the distance from the center of the cell. This was done for each video frame using the camera pixel size as bin size (Kapitein, Schlager et al. 2010b).

For analysis of redistribution dynamics in COS7 cells, cells were masked to exclude contributions from neighboring cells to the analysis. A threshold was set for all images of a time-lapse recording at ~6-12 times the standard deviation of the background above the background to yield binary images. These thresholds were set manually such that individual peroxisomes were suprathreshold (by a experimenter who was not blind to experimental group). The same thresholds were set for analysis of the $R_{90\%}$ and calculations of the correlation index. To quantify peroxisome redistribution upon recruitment of motor proteins in COS7 cells, the radius required to include 90% of the total intensity of the cell, $R_{90\%}(t)$, was calculated for each frame as described previously (Kapitein, Schlager et al. 2010b). To quantify changes in the dynamics of peroxisomes upon recruitment of (additional) motor proteins, we calculated the time-dependent frame-to-frame correlation index$c_\tau(t)$ as described before (van Bergeijk, Adrian et al. 2015). A value of 1 for $c_\tau(t)$ indicates that particles are completely anchored and

thus their position is unchanged after a time τ, whereas a value of 0 means that all particles moved to locations that were previously unoccupied. For statistical analysis on R90% and correlation index, average values of 10 frames at t=0-4.5min, 25-29.5min and 55-59.5 min were used. Friedman test was performed with Dunn's posthoc test.

To quantify the movement of the peroxisome or Rab3 accumulations formed after recruiting Myosin-V in the proximal axon (Fig. 2E and Fig. 3G), their positions were analyzed between 10 and 25 minutes after the addition of rapalog with 30 seconds interval acquisition. The spots were tracked using the trackmate plugin for ImageJ. For every time point the x-position relative to the initial position was plotted. For these trajectories, mean square displacement analysis was performed using the MSDanalyzer (Tarantino, Tinevez et al. 2014) class for MATLAB, including tracks that were at least 25 time points long (n=26 for 2E and 18 for 3G)).

To analyze Rab3 clustering (Figure 3E-F), the number of bright isolated spots as shown in Fig. 3D were compared between the proximal axon (colocalizing with the AIS marker Ankyrin-G, which marked a segment with visibly identifiable boundaries) and more distal segments (further than the second branch), both in the presence and absence of rapalog. For the quantification of the Rab3 accumulations relative to the AIS, the AIS length was measured manually based on the bright Ankyrin-G staining that defines the AIS. Subsequently, the location of the rab3 accumulation was divided by the measured length of the AIS.

AUTHOR CONTRIBUTIONS

L.C.K. conceived research. P.B., R.O., A.F.J.J designed, created and tested constructs. A.F.J.J. and R.P.T. performed experiments and analyzed data. C.C.H. provided conceptual input and provided neuron cultures. A.F.J.J., R.P.T and L.C.K. wrote the paper with input from all other authors. L.C.K. supervised research.

ACKNOWLEGDMENTS

We are grateful to Dr. T. Inoue for the gift of AM-modified gibberellin. This work was supported by the Netherlands Organisation for Scientific Research (NWO) (NWO-ALW-VICI to C.C.H., NWO-ALW-VIDI to L.C.K.), the Dutch Technology Foundation STW, which is part of the NWO (to C.C.H and L.C.K), and the European Research Council (ERC Starting Grant to L.C.K., ERC Consolidator Grant to C.C.H).

REFERENCES

AL-BASSAM, S., XU, M., WANDLESS, T.J. and ARNOLD, D.B., 2012. Differential trafficking of transport vesicles contributes to the localization of dendritic proteins. *Cell reports,* **2**(1), pp. 89-100.
CHAZEAU, A., KATRUKHA, E.A., HOOGENRAAD, C.C. and KAPITEIN, L.C., 2016. *Studying*

neuronal microtubule organization and microtubule-associated proteins using single molecule localization microscopy.
DERR, N.D., GOODMAN, B.S., JUNGMANN, R., LESCHZINER, A.E., SHIH, W.M. and RECK-PETERSON, S.L., 2012. Tug-of-war in motor protein ensembles revealed with a programmable DNA origami scaffold. *Science (New York, N.Y.),* **338**(6107), pp. 662-665.
GANGULY, A., TANG, Y., WANG, L., LADT, K., LOI, J., DARGENT, B., LETERRIER, C. and ROY, S., 2015. A dynamic formin-dependent deep F-actin network in axons. *The Journal of cell biology,* **210**(3), pp. 401-417.
HUANG, C. and BANKER, G., 2012. The translocation selectivity of the kinesins that mediate neuronal organelle transport. *Traffic,* **13**(4), pp. 549-564.
JUNGMANN, R., AVENDANO, M.S., WOEHRSTEIN, J.B., DAI, M., SHIH, W.M. and YIN, P., 2014. Multiplexed 3D cellular super-resolution imaging with DNA-PAINT and Exchange-PAINT. *Nat Meth,* **11**(3), pp. 313-318.
KAPITEIN, L.C., SCHLAGER, M.A., KUIJPERS, M., WULF, P.S., VAN SPRONSEN, M., MACKINTOSH, F.C. and HOOGENRAAD, C.C., 2010a. Mixed microtubules steer dynein-driven cargo transport into dendrites. *Current Biology,* **20**(4), pp. 290-299.
KAPITEIN, L.C., SCHLAGER, M.A., VAN DER ZWAN, WOUTER A, WULF, P.S., KEIJZER, N. and HOOGENRAAD, C.C., 2010b. Probing intracellular motor protein activity using an inducible cargo trafficking assay. *Biophysical journal,* **99**(7), pp. 2143-2152.
KAPITEIN, L.C., VAN BERGEIJK, P., LIPKA, J., KEIJZER, N., WULF, P.S., KATRUKHA, E.A., AKHMANOVA, A. and HOOGENRAAD, C.C., 2013. Myosin-V opposes microtubule-based cargo transport and drives directional motility on cortical actin. *Current Biology,* **23**(9), pp. 828-834.
KIUCHI, T., HIGUCHI, M., TAKAMURA, A., MARUOKA, M. and WATANABE, N., 2015. Multitarget super-resolution microscopy with high-density labeling by exchangeable probes. *Nat Meth,* **12**(8), pp. 743-746.
KUIJPERS, M., VAN DE WILLIGE, D., FREAL, A., CHAZEAU, A., FRANKER, M., HOFENK, J., RODRIGUES, R.C., KAPITEIN, L., AKHMANOVA, A., JAARSMA, D. and HOOGENRAAD, C., 2016. Dynein Regulator NDEL1 Controls Polarized Cargo Transport at the Axon Initial Segment. *Neuron,* **89**(3), pp. 461-471.
LEWIS, T.L., MAO, T., SVOBODA, K. and ARNOLD, D.B., 2009. Myosin-dependent targeting of transmembrane proteins to neuronal dendrites. *Nature neuroscience,* **12**(5), pp. 568-576.
LIPKA, J., KAPITEIN, L.C., JAWORSKI, J. and HOOGENRAAD, C.C., 2016. Microtubule-binding protein doublecortin-like kinase 1 (DCLK1) guides kinesin-3-mediated cargo transport to dendrites. *The EMBO journal,* , pp. e201592929.
MIYAMOTO, T., DEROSE, R., SUAREZ, A., UENO, T., CHEN, M., SUN, T., WOLFGANG, M.J., MUKHERJEE, C., MEYERS, D.J. and INOUE, T., 2012. Rapid and orthogonal logic gating with a gibberellin-induced dimerization system. *Nature chemical biology,* **8**(5), pp. 465-470.
PETERSEN, J.D., KAECH, S. and BANKER, G., 2014. Selective microtubule-based transport of dendritic membrane proteins arises in concert with axon specification. *The Journal of neuroscience : the official journal of the Society for Neuroscience,* **34**(12), pp. 4135-4147.
SAXTON, M.J. and JACOBSON, K., 1997. Single-particle tracking: applications to membrane dynamics. *Annual Review of Biophysics and Biomolecular Structure,* **26**(1), pp. 373-399.
SONG, A., WANG, D., CHEN, G., LI, Y., LUO, J., DUAN, S. and POO, M., 2009. A selective filter for cytoplasmic transport at the axon initial segment. *Cell,* **136**(6), pp. 1148-1160.
TARANTINO, N., TINEVEZ, J.Y., CROWELL, E.F., BOISSON, B., HENRIQUES, R., MHLANGA, M., AGOU, F., ISRAEL, A. and LAPLANTINE, E., 2014. TNF and IL-1 exhibit distinct ubiquitin requirements for inducing NEMO-IKK supramolecular structures. *The Journal of cell biology,* **204**(2), pp. 231-245.
THEVENAZ, P., RUTTIMANN, U.E. and UNSER, M., 1998. A pyramid approach to subpixel registration based on intensity. *Image Processing, IEEE Transactions on,* **7**(1), pp. 27-41.
VAN BERGEIJK, P., ADRIAN, M., HOOGENRAAD, C.C. and KAPITEIN, L.C., 2015. Optogenetic

control of organelle transport and positioning. *Nature,* .
WATANABE, K., AL-BASSAM, S., MIYAZAKI, Y., WANDLESS, T.J., WEBSTER, P. and ARNOLD, D.B., 2012. Networks of polarized actin filaments in the axon initial segment provide a mechanism for sorting axonal and dendritic proteins. *Cell reports,* **2**(6), pp. 1546-1553.
XU, K., ZHONG, G. and ZHUANG, X., 2013. Actin, spectrin, and associated proteins form a periodic cytoskeletal structure in axons. *Science (New York, N.Y.),* **339**(6118), pp. 452-456.
YAU, K.W., VAN BEUNINGEN, S.F., CUNHA-FERREIRA, I., CLOIN, B.M., VAN BATTUM, E.Y., WILL, L., SCHÄTZLE, P., TAS, R.P., VAN KRUGTEN, J. and KATRUKHA, E.A., 2014. Microtubule minus-end binding protein CAMSAP2 controls axon specification and dendrite development. *Neuron,* **82**(5), pp. 1058-1073.

SUPPLEMENTARY FIGURES

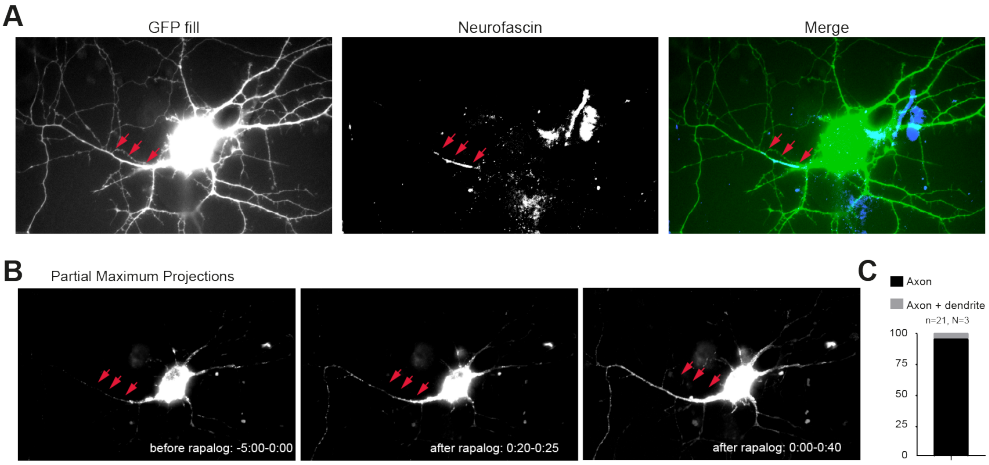

Supplemental figure 1. Corresponds to Fig. 2

A) *GFP fill (left) and live neurofascin staining (middle) of a cell expressing GFP, Pex3-mRFP-FKBP and Kif5-GFP-FRB.*

B) *Partial maximum projections of the peroxisome-redistribution experiment performed on the cell in (A), before (left) and after rapalog addition (right). Red arrows indicate the axon identified by neurofascin.*

C) *Percentage of cells with peroxisome targeting into the axon or both axon and dendrite, after recruitment of kif5-GFP-FRB. In all cases the axon was identified by the live neurofascin staining as in (A,B). n=21*

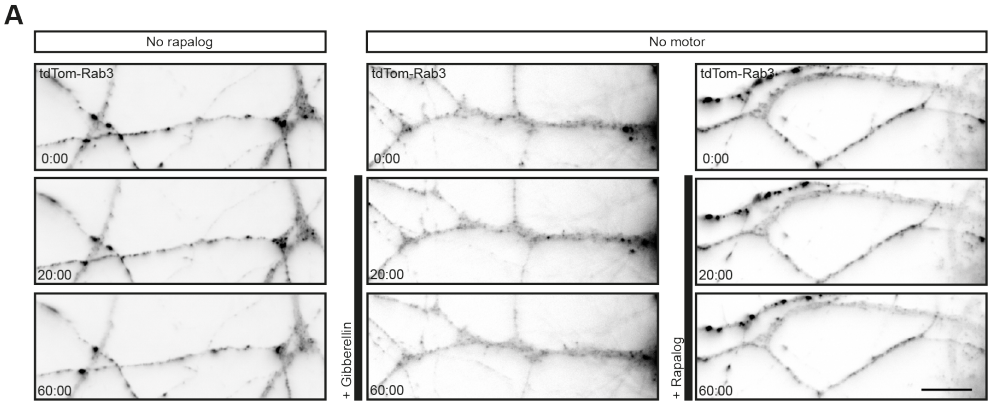

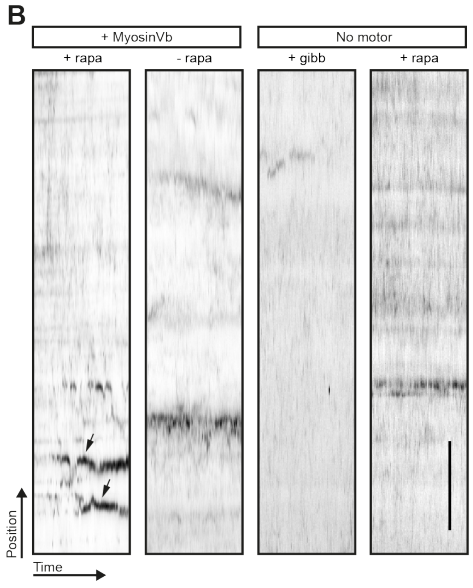

Supplemental figure 2. Corresponds to Fig. 3
A) *Rab3 positive vesicle distribution in the proximal axon of a neuron that co-expressed myosin-Vb, but was not treated with ligands (left panels), or did not express myosinVb and was treated with Gibberellin (middle panels) or rapalog (right panels). In these control conditions Rab3 vesicles do not accumulate in big puncta as seen by selective recruitment of myosinVb. Scale bar, 10 µm.*
B) *Kymographs of Rab3 vesicles in the proximal axon of cells co-expressing myosin-Vb with and without addition of rapalog, or cells without myosinVb and treated with Gibberellin or Rapalog. Timelapse images were acquired with 20 s intervals. Arrows indicate Rab3 accumulations appearing after rapalog addition. Scale bar, 5 µm.*

LEGENDS TO SUPPLEMENTARY VIDEOS

Supplemental video 1: sequential recruitment of kinesin and myosin-V in a COS7 cell
This video corresponds to Figure 1. Anchoring of kinesin propelled cargo by Myosin-V in a COS7 cell. Total time: 60 minutes. Acquired with 30 seconds between frames. 600x sped up.

Supplemental video 2: Myosin-V anchors kinesin-1 propelled peroxisomes in the proximal axon
This video corresponds to Figure 2. Anchoring of kinesin propelled cargo by Myosin-V in a hippocampal neuron. Total time: 60 minutes. Acquired with 30 seconds between frames. 600x sped up.

Supplemental video 3: Myosin-V anchors Rab3 vesicles in the AIS of hippocampal neurons
This video corresponds to Figure 3. Anchoring and clustering of Rab3 vesicles in the proximal axon of hippocampal neurons. Total time: 40 minutes. Acquired with 10 seconds between frames. 200x sped up.

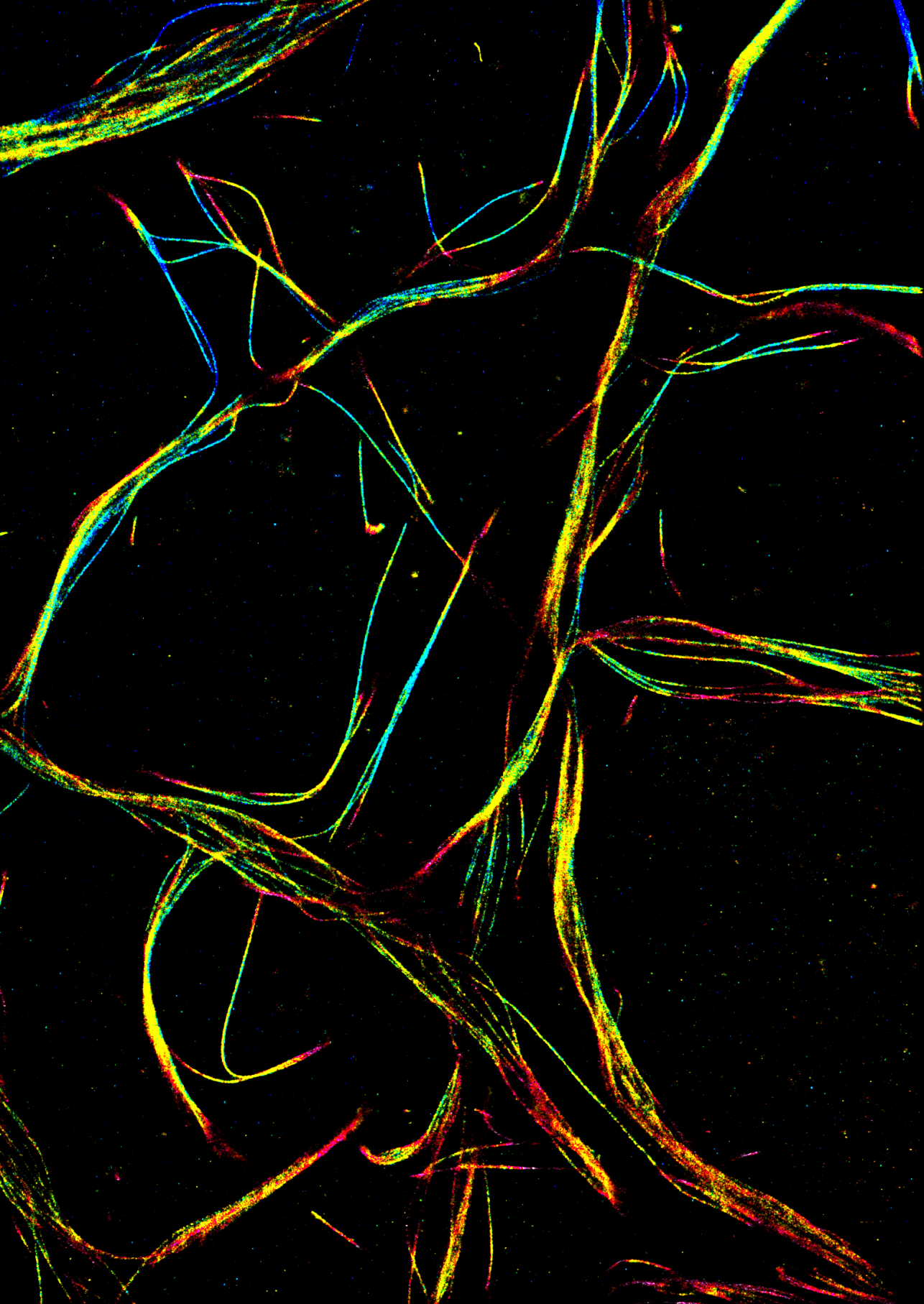

4

Three-Step Model for Polarized Sorting of KIF17 into Dendrites

Mariella A. Franker[1]†, Marta Esteves da Silva[1]†, **Roderick P. Tas[1]†**, Elena Tortosa[1], Yujie Cao, Catia P. Friás, Anne F.J. Janssen[1], Phebe S. Wulf[1], Lukas C. Kapitein[1] and Casper C. Hoogenraad[1]

Current Biology (2016); 26, pp. 1705-1712

[1] Division of Cell Biology, Faculty of Science, Utrecht University, The Netherlands
† Equal Contribution

ABSTRACT

Kinesin and dynein motors drive bidirectional cargo transport along microtubules and have a critical role in polarized cargo trafficking in neurons [1, 2]. The kinesin-2 family protein KIF17 is a dendrite-specific motor protein and has been shown to interact with several dendritic cargoes [3-7]. However, the mechanism underlying the dendritic targeting of KIF17 remains poorly understood [8-11]. Using live cell imaging combined with inducible trafficking assays to directly probe KIF17 motor activity in living neurons, we found that the polarized sorting of KIF17 to dendrites is regulated in multiple steps. First, cargo binding of KIF17 relieves autoinhibition and initiates microtubule-based cargo transport. Second, KIF17 does not autonomously target dendrites, but enters the axon where the actin cytoskeleton at the axon initial segment (AIS) prevents KIF17 vesicles from moving further into the axon. Third, dynein-based motor activity is able to redirect KIF17 coupled cargoes into dendrites. We propose a three-step model for polarized targeting of KIF17, in which the collective function of multiple motor teams is required for proper dendritic sorting.

RESULTS AND DISCUSSION

Full length KIF17 localizes to dendrites and tailless KIF17 targets the axon

Consistent with previous findings [4, 5], we found that endogenous KIF17 and exogenously expressed full length KIF17 (KIF17-FL) localized to the dendritic compartment (MAP2 positive) of mature hippocampal neurons in culture (Figure 1A-E and S1A). Quantification revealed that endogenous KIF17 is localized to dendrites in developing (DIV6) and mature (DIV15) neurons; only ~5% of the cells show accumulations in axon tips and no AIS (NF-186 positive) enrichment is observed (Figure 1A,F). Interestingly, overexpressed KIF17-FL targeted the axon (~85%) in young neurons (DIV6), while in more mature neurons (DIV15) the localization of KIF17-FL was largely dendritic (~10% of neurons with axonal tip accumulation and no AIS accumulation) (Figure 1F and S1B,C). As reported [8-11], a truncated form of KIF17 containing the motor domain and dimerization region (amino acid 1-547) but lacking the tail domain, hereafter referred to as KIF17-MD, targeted the axon and accumulated in axon tips in both young and mature neurons (~80% and ~90%, respectively; Figure 1E-H). Together, these data demonstrate that the motor domain is selective for the axon and the tail region regulates the dendritic targeting of KIF17 in mature neurons.

Cargo binding relieves autoinhibition of full length KIF17

Autoinhibition is a well-described regulatory mechanism for kinesins, in which the tail domain interacts with the motor domain and prevents motor activity [12-16]. It has been suggested that cargo binding may unfold autoinhibited motors to initiate microtubule-based transport. *In vitro* studies have shown that binding kinesin to beads activates the motor [17, 18]. Expression of KIF17-FL in COS7 cells showed a diffuse cytoplasmic pattern without any microtubule labeling (Figure 2A). In contrast, both the KIF17-MD and coiled-coil 2 (CC2) mutant KIF17-G754E, which has no autoinhibition [16], showed a strong microtubule staining in the periphery of the cell (Figure 2A) and displayed fast motility towards the microtubule plus-ends (Figure 2B). The KIF17-G754E mutant showed very fast motility on microtubules with an instantaneous speed of 3.2 ± 0.1 μm/s (Figure 2B). These data suggested that cargo-unbound KIF17-FL is autoinhibited in living cells.

To investigate if cargo binding can directly activate the motor in cells, we chemically induced the binding of KIF17 to peroxisomes using the FRB-FKBP dimerization system (Figure 2C)[11, 19]. We expressed KIF17-GFP-FRB and PEX-RFP-FKBP in COS7 cells and addition of rapalog during live cell imaging induced KIF17 binding to the cargo [20]. As shown by maximum projections, time-coded color plots and kymographs, rapalog treatment allowed KIF17-FL, KIF17-MD and KIF17-G754E to efficiently transport peroxisomes from the cell center to the cell periphery (Figure 2D-E and Movie S1). The data suggested that the cargo binding relieves autoinhibition of KIF17-FL. Interestingly, analysis of displacement curves (Figure 2F,G and S2A-E) showed that the onset of motility of KIF17-FL is markedly

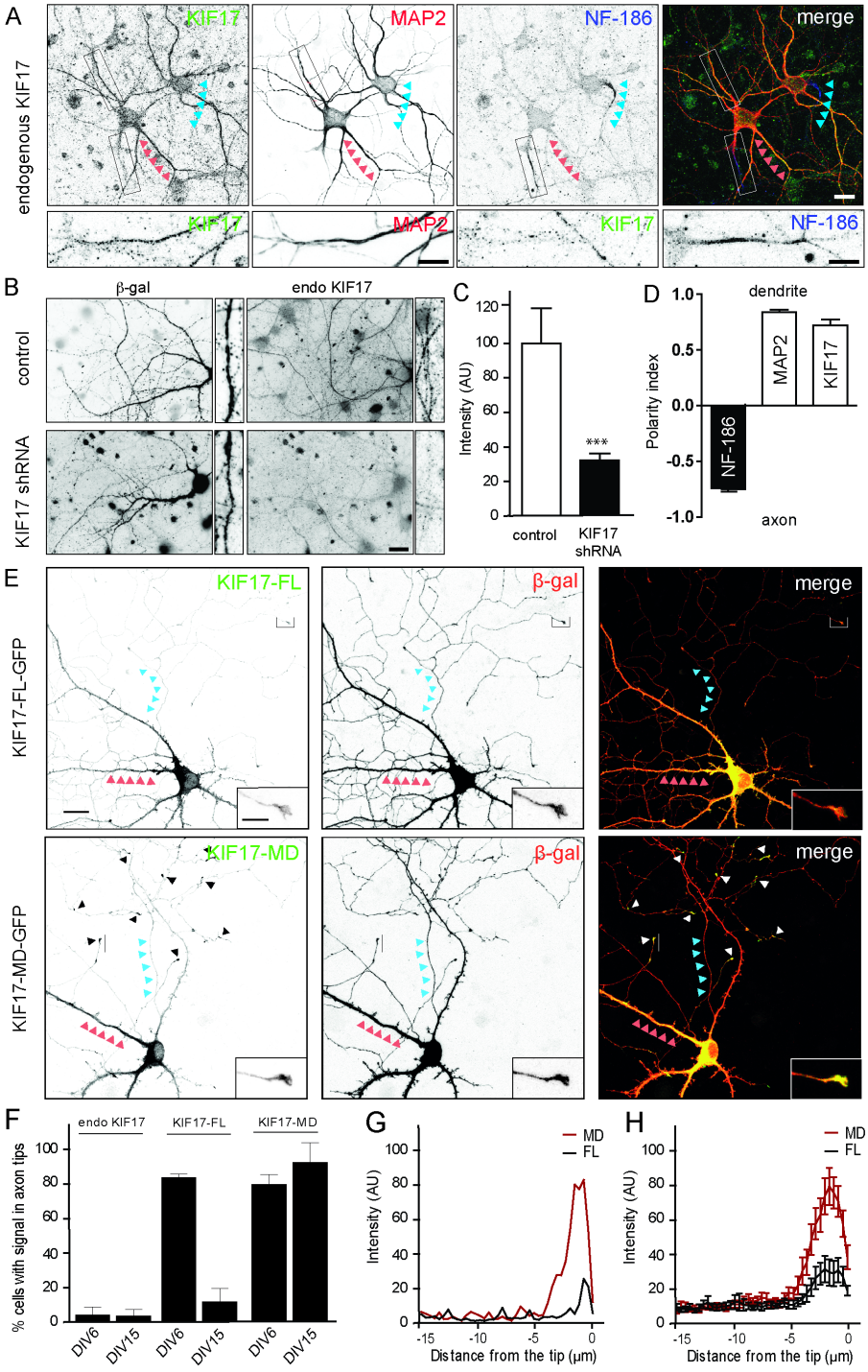
A
endogenous KIF17
KIF17
MAP2
NF-186
merge
B
β-gal
endo KIF17
control
KIF17 shRNA
C
Intensity (AU)
***
control
KIF17 shRNA
D
dendrite
Polarity index
MAP2
KIF17
NF-186
axon
E
KIF17-FL-GFP
KIF17-FL
β-gal
merge
KIF17-MD-GFP
KIF17-MD
F
endo KIF17
KIF17-FL
KIF17-MD
% cells with signal in axon tips
DIV6
DIV15
G
MD
FL
Intensity (AU)
Distance from the tip (μm)
H
MD
FL
Intensity (AU)
Distance from the tip (μm)

Figure 1: Full length and truncated KIF17 constructs localize to different neuronal compartments.
A) *Hippocampal neurons at DIV15 co-stained for endogenous KIF17, dendritic marker MAP2 and axon initial segment marker NF-186.*
B) *Hippocampal neurons at DIV11+3 co-transfected with pSuper control or KIF17 shRNAs and β-galactosidase (β-gal) to highlight neuronal morphology and stained for endogenous KIF17 and β-gal.*
C) *Quantification of KIF17 mean intensity in dendrites of neurons expressing pSuper control or KIF17 shRNAs (n =34-38).*
D) *Polarity index of NF-186, MAP2 and KIF17 in DIV15 neurons (n =12).*
E) *Hippocampal neurons at DIV19+2 co-transfected with β-gal and KIF17-FL-GFP or KIF17-MD-GFP. Inserts show zooms of axon tips.*
F) *Percentage of cells with accumulations in at least 2 axon tips in young (DIV6) and mature (DIV15) neurons with endogenous KIF17 and overexpressed KIF17-FL-GFP and KIF17-MD-GFP (n = 22-30).*
G) *Representative individual fluorescent intensity profile of KIF17-FL-GFP (black) and KIF17-MD-GFP (red) at the tip of the axon.*
H) *Average normalized fluorescent intensity profiles of KIF17-FL-GFP (n =20) and KIF17-MD-GFP (n= 20) at the tip of the axon.*
*Blue arrowheads indicate axons and red arrowheads indicate dendrites. Scale bars: 20 μm (A,B,E), 10 μm (inset A) and 5 μm (inset B,E). Error bars indicate SEM; ***p < 0.001 (Mann Whitney test). See also Figure S1.*

slower (t½ = 10.6 ± 3.0 min) compared to KIF17- G754E (t½ = 5.5 ± 2.9 min) and KIF17-MD (t½ = 4.7 ± 2.2 min). Next, we analyzed the speed of single peroxisomes (Figure 2H). Immobile peroxisomes were excluded from the analysis and only minimum track lengths of 1 μm and 1 second were analyzed. All three KIF17 constructs showed similar single peroxisome behavior with an average velocity around 1 μm/s (mean ± SD: FL = 1.07 ± 0.50; MD = 0.91 ± 0.47; G754E = 1.09 ± 0.46 μm/s) (Figure 2I). These velocities were comparable to previous reports of kinesin-mediated organelle transport in cells (0.5 - 2 μm/s) [4, 21]. These data indicate that the KIF17 motor domain alone and the non-autoinhibited KIF17 mutant quickly initiate cargo transport in living cells. These observations are consistent with the proposed role of the CC2 region in regulating KIF17 activity [16].

Full length KIF17 does not directly target dendrites but is anchored at AIS

To further study the role of the tail region on the dendritic targeting of KIF17, we used the cargo trafficking assay in cultured hippocampal neurons [11]. Without rapalog-induced motor coupling, the peroxisomes are largely immobile in hippocampal neurons (Figure S3A). After coupling KIF17 to peroxisomes, we observed that KIF17-FL was able to transport peroxisomes but did not target the dendrites. Instead, it had a strong preference for the axon, where the peroxisomes anchored at the AIS (Figure 3A-C and Movie S2). In contrast, KIF17-MD efficiently drove transport through the proximal axon. Earlier work established that the actin-rich AIS localized in the beginning of the axon functions as barrier for membrane-bound proteins [22], as well as transported cargoes [9, 23]. It was observed that dendritic cargoes halt and reverse in the AIS, suggesting that the AIS barrier prevents 'unwanted' cargoes from entering the axon [24]. Furthermore, it has been shown that the actin cytoskeleton is

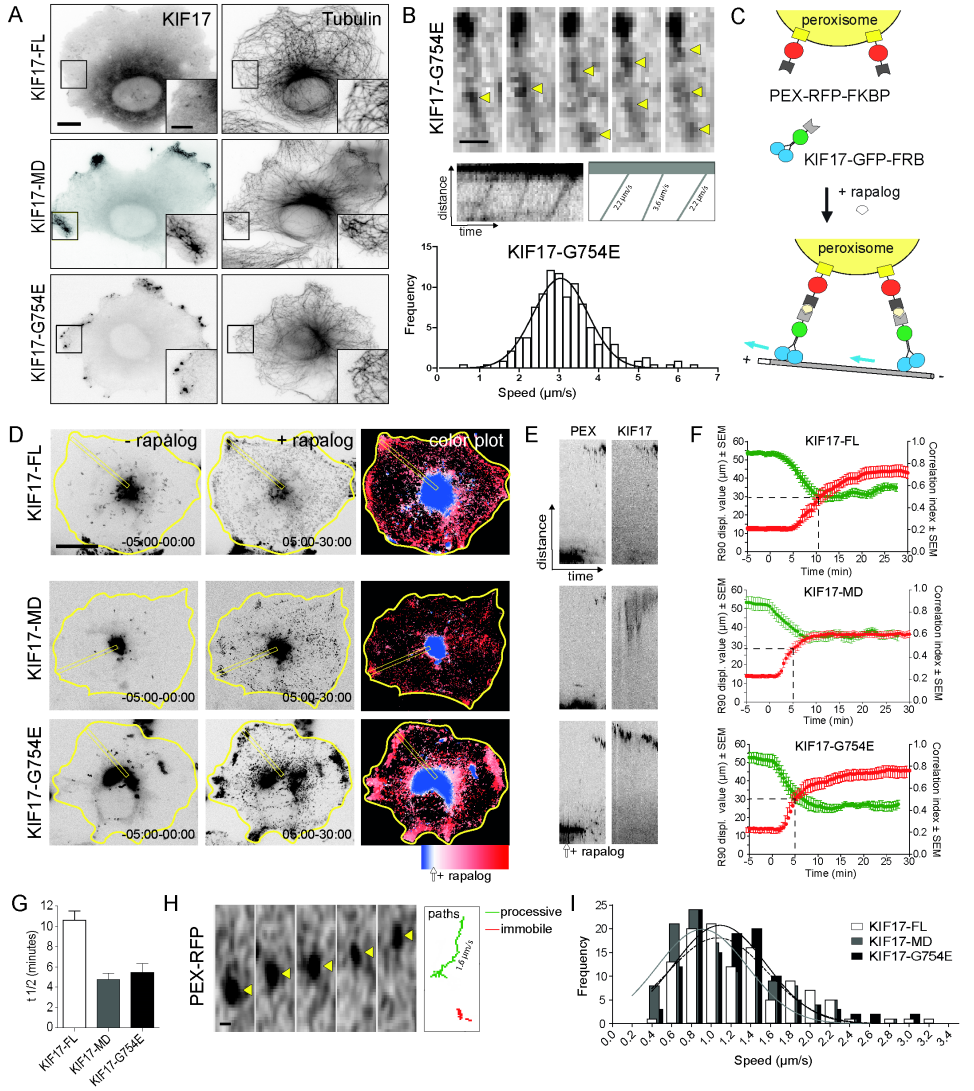

Figure 2: Cargo binding activates full length KIF17

A) *COS7 cells transfected with KIF17-FL-GFP, KIF17-MD-GFP or KIF17-G754E-GFP and stained with tubulin.*

B) *Still frames and kymograph (3.2µm x 5s) of KIF17-G754E-GFP moving towards the tip of a microtubule. Histogram of average speeds of KIF17-G754E-GFP (n=31 tracks) was fitted with a Gaussian function.*

C) *Schematic representation of rapalog-induced coupling of KIF17-GFP-FRB to PEX-RFP-FKBP.*

D) *Cargo transport efficiency of indicated KIF17-GFP-FRB constructs. Left and middle panels show maximum projections of peroxisome motility before and after rapalog. Right panels are time-coded color plots.*

E) *Kymographs (35µm x 30 min) of PEX-RFP-FKBP and KIF17-GFP as indicated in (D; yellow boxes)*

F) *Graphs showing R90 displacement value (red) and correlation index (green) of peroxisomes over time (n=11-13).*

G) *Graph showing t½ of indicated KIF17 constructs (n=11-13).*
H) *Still frames of a single KIF17-FL coupled peroxisome in COS7 cells at 10 fps. Tracked path of a processive nd an immobile peroxisome are indicated.*
I) *Histograms showing the average speeds of processive peroxisomes coupled to KIF17-FL, KIF17-MD and KIF17-G754E (n=113-121 tracks) were fitted with a Gaussian fit.*
Scale bar: 20 µm (A,D), 5 µm (A, inset) and 0.5 µm (B,H). Error bars indicate SEM. See also Figure S2 and Movie S1.

important for the function of the AIS cytosolic barrier [9, 23, 24]. Next, we treated neurons with Latrunculin B (LatB) to depolymerize actin or expressed Ankyrin G (AnkG) shRNA to disrupt the AIS (Figure S1D,E) and analyzed the behavior of KIF17-FL coupled peroxisomes. We observed that disrupting the actin cytoskeleton or the AIS increased cargo motility and allowed axon transport comparable to KIF17-MD (Figure 3C and Movie S3). These data support the existence of an actin-based barrier at the AIS that regulates the entry of specific vesicles into the axon [9, 23]. Since LatB treatment did not affect KIF5- or dynein-coupled peroxisome motility (Figure 3E,F), the actin cytoskeleton is responsible for the specific KIF17-FL-coupled cargo accumulations in the AIS. Next, we generated several truncated KIF17 constructs and found that the tail region (amino acid 846-1015) was required for anchoring at the AIS (Figure 3D). Consistently, the shortest KIF17 construct that anchored at the AIS - KIF17(1-1015) - did not strongly accumulate in axonal tips (Figure S2). Interestingly, rapalog-induced coupling of both truncated KIF5 motors (KIF5-MD-GFP-FRB) and the KIF17-tail region (KIF17(266-1029)-GFP-FRB) to peroxisomes induced cargo stalling in the proximal axon (Figure 3G,H). Moreover, the KIF17-tail region also stalls KIF5-MD-induced Rab3 positive vesicles at the AIS, which can be suppressed by actin depolymerization (Figure S3B-E). Furthermore, expression of the KIF17-tail region (as a dominant negative approach, without coupling to cargo) suppresses KIF17-FL-GFP-induced Rab3 stalling at the AIS (Figure S3F,G). These results indicate that the tail region of KIF17 is responsible for AIS anchoring.

One other possibility is that deactivation of KIF17 motor activity by back folding may cause cargo stalling at the AIS. However our data argue against this option: KIF17-G754E shows strong axonal tip accumulation when overexpressed in neurons but still anchors at the AIS (Figure 3D and S2). However, local deactivation of KIF17 may still be achieved via additional mechanisms, such as inhibiting microtubule binding or ATP hydrolysis of the kinesin motor via local activation of regulatory protein in the AIS.

KIF17 vesicles are redirected into dendrites by cytoplasmic dynein

Next we examined how KIF17 vesicles transported out of the proximal axon and into the dendrites and tested whether other motors present on the same cargo could redirect KIF17 transport. We first determined whether the retrograde motor dynein via recruitment of dynein adaptor BICD2 drives KIF17-bound vesicles out of the axon towards the soma. We expressed KIF17-FL-GFP-FRB, HA-BICD2N-FRB and PEX-RFP-FKBP in neurons. Addition of rapalog recruited both KIF17-FL and BICD2N to peroxisomes and increased retrograde movement

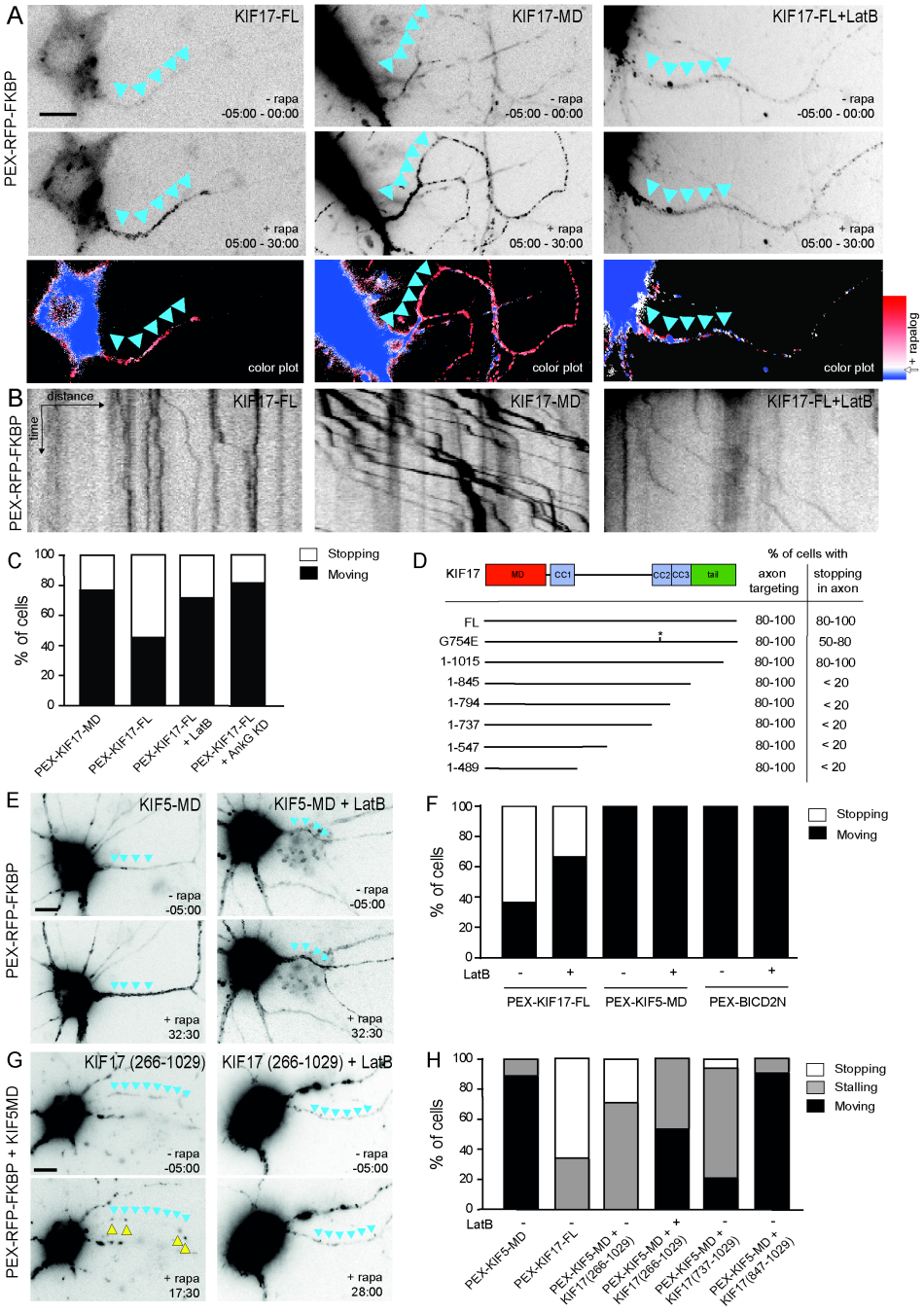
A
KIF17-FL
KIF17-MD
KIF17-FL+LatB
PEX-RFP-FKBP
- rapa
-05:00 - 00:00
+ rapa
05:00 - 30:00
color plot
+ rapalog
B
distance
time
KIF17-FL
KIF17-MD
KIF17-FL+LatB
PEX-RFP-FKBP
C
% of cells
Stopping
Moving
PEX-KIF17-MD
PEX-KIF17-FL
PEX-KIF17-FL + LatB
PEX-KIF17-FL + AmkG KD
D
KIF17
MD
CC1
CC2
CC3
tail
% of cells with
axon targeting
stopping in axon
FL 80-100 80-100
G754E 80-100 50-80
1-1015 80-100 80-100
1-845 80-100 < 20
1-794 80-100 < 20
1-737 80-100 < 20
1-547 80-100 < 20
1-489 80-100 < 20
E
KIF5-MD
KIF5-MD + LatB
PEX-RFP-FKBP
- rapa
-05:00
+ rapa
32:30
F
% of cells
Stopping
Moving
LatB
PEX-KIF17-FL
PEX-KIF5-MD
PEX-BICD2N
G
KIF17 (266-1029)
KIF17 (266-1029) + LatB
PEX-RFP-FKBP + KIF5MD
- rapa
-05:00
+ rapa
17:30
+ rapa
28:00
H
% of cells
Stopping
Stalling
Moving
LatB
PEX-KIF5-MD
PEX-KIF17-FL
PEX-KIF5-MD + KIF17(266-1029)
PEX-KIF5-MD + KIF17(266-1029)
PEX-KIF5-MD + KIF17(737-1029)
PEX-KIF5-MD + KIF17(847-1029)

Figure 3: The KIF17 tail region mediates cargo stalling at the AIS
A) *Hippocampal neurons co-transfected with PEX-RFP-FKBP and KIF17-FL-GFP-FRB or KIF17-MD-GFP-FRB and live stained for AIS marker Neurofascin. Cells expressing KIF17-FL were treated with 10 μM Latrunculin B (LatB) for 1-2 h before imaging. Maximum projections of peroxisomes motility before and after rapalog addition (top panels) and color plots of peroxisome distributions (bottom panels) are shown.*
B) *Kymographs (31μm x 31sec) showing movement of peroxisomes in the proximal axon.*
C) *Percentage of neurons with motile (moving) or non-motile (stopping) peroxisomes in the proximal axon expressing the indicated constructs (n=11-16).*
D) *Behavior of the various KIF17 constructs after peroxisome coupling characterized as percentage of cells with axon targeting and non-motile (stopping) peroxisomes in the proximal axon.*
E) *Hippocampal neurons co-transfected with PEX-RFP-FKBP and KIF5-MD-GFP-FRB before/after rapalog addition, with/without LatB treatment. Images show maximum projections.*
F) *Percentage of neurons with moving or stopping peroxisomes in the proximal axon after rapalog-induced coupling with KIF17-FL-GFP-FRB, KIF5-MD-GFP-FRB or BICD2N-GFP-FRB, with/without LatB treatment (n= 11-16).*
G) *Hippocampal neurons co-transfected with PEX-RFP-FKBP, KIF5-MD-GFP-FRB and KIF17(266-1029)-GFP-FRB before and after rapalog addition, with/without LatB treatment.*
H) *Percentage of neurons with moving, stalling or stopping peroxisomes in the proximal axon after rapalog-induced coupling of KIF5-MD-GFP-FRB together with indicated KIF17 constructs (n=12-30).*
Scale bars: 10 μm (A,E,G). See also Figure S3 and Movie S2 and S3.

of peroxisomes in the proximal axon (Figure 4A-C) from ~20% in neurons with KIF17-FL alone to ~50% in cells with KIF17-FL and BICD2N (Figure 4G). We next determined whether dynein also redirects KIF17 bound vesicles into dendrites. Addition of rapalog simultaneously recruited KIF17-FL and BICD2N to peroxisomes and quickly redistributed cargoes from the soma into the dendrites (Figure 4D-F and Movie S4, S5). Under these conditions, all neurons showed dendrite localization of KIF17-FL, while in the absence of BICD2N dendrite targeting is rare (Figure 4H). These results demonstrate that KIF17 vesicles can be redirected into dendrites by dynein motor activity.

Previous studies have analyzed the movements of KIF17 bound vesicles in neurons and therefore concluded that KIF17 actively transports cargoes into dendrites [3, 4]. Since various motor types (dynein, kinesin and myosin) can simultaneously bind to cargo, it is challenging to interpret endogenous vesicle motility in neurons. Particularly in dendrites, where the microtubule cytoskeleton has opposite polarity orientations [25]. Moreover, motors attached to cargo can exist in active and inactive states and many regulators can influence their local motor activity [26]. By directly probing KIF17-mediated cargo movements, we found that full length KIF17 does not target dendrites but steers cargo into the axon, where it anchors at the AIS. We also demonstrate that dynein can drive KIF17-bound vesicles out of the axon and redirect them into the dendrites. These data fit well with the basic model for polarized transport where most kinesins are responsible for transport into axons and dynein motors are responsible for transport into dendrites [1, 2]. Thus, the dendrite specific localization of KIF17 is not due to active KIF17 transport from the soma to the dendrite but to decreased axonal entry and the use of dynein activity to target dendrites. What is the role of KIF17 in dendrite specific cargo trafficking? First of all, in contrast to many other

kinesin family members, KIF17 is a unique plus-end directed motor that prevents cargoes from entering the axon by AIS anchoring. The decreased axonal targeting emphasizes the importance of the actin-rich AIS in preventing 'unwanted' cargoes from entering the axon and setting up the polarized distribution of somatodendritic proteins. Second, dynein helps to bring KIF17 into dendrites. However, once the more distal dendrites are reached, KIF17 may take over from dynein and deliver cargo towards the more distal dendritic regions. This idea is consistent with the observed motility of KIF17-bound cargoes within dendritic branches [11, 27]. Moreover, our data is in line with previous studies on polarized channel trafficking showing that KIF17 is required for K+ channel Kv4.2 transport in dendrites but does not, by itself, specify dendritic localization of the channel [5]. However additional studies are needed to determine whether the transport kinetics of KIF17-attached peroxisomes can be compared to a bona fide KIF17 cargo. Within dendrites, KIF17 may play a role in the spatial and temporal fine-tuning of receptor and/or channel trafficking to synapses [27-29]. Together, the data suggest that cooperativity between different motors is an important part of the polarized sorting mechanism. However, it remains an open question how coupling between KIF17 and dynein is regulated. Several studies have shown that interaction between different motor types occurs via adaptor proteins, which act as a 'switch' between two motors to mediate trafficking [26, 30]. Future research will have to clarify how KIF17 and dynein interact with adaptors and which regulators are involved to achieve targeted trafficking.

EXPERIMENTAL PROCEDURES

Animals and Ethics Statement

All animal experiments were performed in compliance with the guidelines for the welfare

Figure 4: Dynein redirects KIF17 to dendrites

A) *Schematic representation of rapalog-induced co-coupling of KIF17-FL-GFP-FRB and dynein adaptor HA-BICD2N-FRB to PEX-RFP-FKBP.*

B) *Still frames of retrograde peroxisome movement in the proximal axon at 30s interval after simultaneous recruitment of HA-BICD2N-FRB and KIF17-FL-GFP-FRB.*

C) *Kymographs (25µm x 45 min) show increased retrograde movement of KIF17-FL-coupled peroxisomes in proximal axon in the presence of BICD2N-FRB. Illustrations of manually traced cargo displacements are indicated.*

D) *Maximum projections of KIF17-FL-GFP and peroxisomes movements in neurons expressing PEX-RFP-FKBP, HA-BICD2N-FRB and KIF17-FL-GFP-FRB before and after rapalog addition.*

E-F) *Maximum projections before and after rapalog of dendrites of neurons expressing PEX-RFP-FKBP and KIF17-FL-GFP-FRB with and without HA-BICD2N-FRB.*

G) *Percentage of neurons with retrograde and anterograde movement in proximal axon expressing the indicated constructs.*

H) *Percentage of neurons with KIF17-FL positive peroxisomes in dendrites expressing the indicated constructs.*

Scale bars: 20 µm (D), 5 µm (E,F) and 3 µm (B). See also Movie S4 and S5.

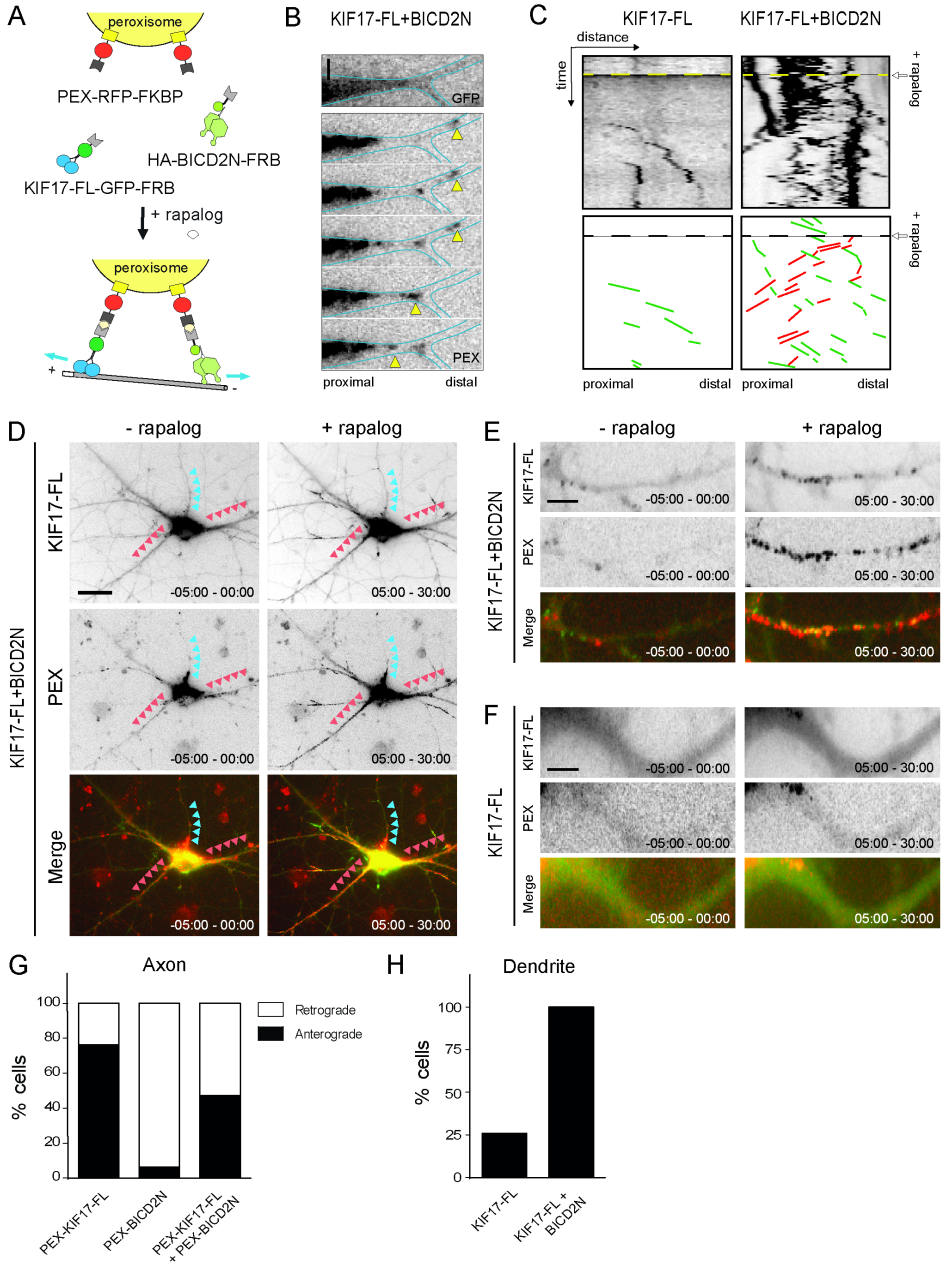
A
peroxisome
PEX-RFP-FKBP
HA-BICD2N-FRB
KIF17-FL-GFP-FRB
+ rapalog
peroxisome
B
KIF17-FL+BICD2N
GFP
PEX
proximal
distal
C
KIF17-FL
KIF17-FL+BICD2N
distance
time
+ rapalog
+ rapalog
proximal
distal
proximal
distal
D
- rapalog
+ rapalog
KIF17-FL+BICD2N
KIF17-FL
PEX
Merge
-05:00 - 00:00
05:00 - 30:00
E
- rapalog
+ rapalog
KIF17-FL+BICD2N
KIF17-FL
PEX
Merge
-05:00 - 00:00
05:00 - 30:00
F
KIF17-FL
KIF17-FL
PEX
Merge
-05:00 - 00:00
05:00 - 30:00
G
Axon
% cells
100
80
60
40
20
0
Retrograde
Anterograde
PEX-KIF17-FL
PEX-BICD2N
PEX-KIF17-FL + PEX-BICD2N
H
Dendrite
% cells
100
75
50
25
0
KIF17-FL
KIF17-FL + BICD2N

of experimental animals issued by the federal government of the Netherlands. All animal experiments were approved by the Animal Ethical Review Committee (DEC) of Utrecht University.

DNA Constructs, shRNA sequences and Antibodies

The KIF17 expression constructs were generated by a PCR-based strategy using the human KIF17 cDNA (accession NM_020816; IMAGE clone 6171598). The shRNA sequences used in this study are rat KIF17 shRNA1 (5'-GCCACCAAGATTAACCTGT-3'), rat KIF17 shRNA2 (5'-GACAGGACAAAGCTCAACA-3'), rat KIF17 shRNA3 (5'-CCATCAACATCGAGATCTA-3') and AnkyrinG shRNA (5'-GAGTTGTGCTGATGACAAG-3'). Details about the FRB/FKB constructs can be found in [11]. The following antibodies were used: rabbit-anti-KIF17 (K3638, Sigma and H-280, Santa Cruz) and mouse-anti-AnkyrinG (Invitrogen). See the Supplemental Experimental Procedures.

Cell culture, Transfections and Live Cell Imaging

Primary hippocampal neurons were harvested from rat E18 embryos, cultured on poly-L-lysine (35 μg/ ml) and laminin (5 μg/ml) coated coverslips in neurobasal medium (NB) supplemented with B27, 0.5 mM glutamine, 12.5 μM glutamate and Pen/Strep and transfected with Lipofectamine 2000 (Invitrogen). Imaging experiments were performed on Nikon Eclipse TE2000E microscope equipped with 40x oil objective, Coolsnap CCD camera (Photometrics), perfect-focus system and imaging chamber. Imaging chamber was maintained at 37°C and 5% CO2 during acquisition. See the Supplemental Experimental Procedures.

AUTHOR CONTRIBUTIONS

MAF, MEdS and RPT designed and performed the live cell imaging experiments and analyzed the results; ET performed ICC experiments and analysed the data; YC, CPF, AJ, PSW cloned constructs; LCK supervised the research; CCH supervised the research, coordinated the study and wrote the manuscript with input from all authors.

ACKNOWLEDGEMENTS

This work was supported by the Netherlands Organization for Scientific Research (NOW-ALW-VIDI: LCK, NWO-ALW-VICI: CCH), the Foundation for Fundamental Research on Matter ((FOM): LCK and CCH), which is part of the NWO, the Netherlands Organization for Health Research and Development (ZonMW-TOP: CCH), the European Research Council (ERC) (ERC-starting: LCK, ERC-consolidator: CCH). MEdS is supported by Fundação para a Ciência e Tecnologia (FCT-Portugal, grant SFRH/BD/68642/2010) and YC is part of the

China Scholarship Council - Utrecht University (CSC-UU) PhD-program.

REFERENCES

1. Kapitein, L.C., and Hoogenraad, C.C. (2011). Which way to go? Cytoskeletal organization and polarized transport in neurons. Molecular and cellular neurosciences *46*, 9-20.
2. Rolls, M.M. (2011). Neuronal polarity in Drosophila: sorting out axons and dendrites. Developmental neurobiology *71*, 419-429.
3. Setou, M., Nakagawa, T., Seog, D.H., and Hirokawa, N. (2000). Kinesin superfamily motor protein KIF17 and mLin-10 in NMDA receptor-containing vesicle transport. Science (New York, N.Y.) *288*, 1796-1802.
4. Guillaud, L., Setou, M., and Hirokawa, N. (2003). KIF17 dynamics and regulation of NR2B trafficking in hippocampal neurons. The Journal of neuroscience : the official journal of the Society for Neuroscience *23*, 131-140.
5. Chu, P.J., Rivera, J.F., and Arnold, D.B. (2006). A role for Kif17 in transport of Kv4.2. The Journal of biological chemistry *281*, 365-373.
6. Irla, M., Saade, M., Fernandez, C., Chasson, L., Victorero, G., Dahmane, N., Chazal, G., and Nguyen, C. (2007). Neuronal distribution of spatial in the developing cerebellum and hippocampus and its somatodendritic association with the kinesin motor KIF17. Experimental cell research *313*, 4107-4119.
7. Kayadjanian, N., Lee, H.S., Pina-Crespo, J., and Heinemann, S.F. (2007). Localization of glutamate receptors to distal dendrites depends on subunit composition and the kinesin motor protein KIF17. Molecular and cellular neurosciences *34*, 219-230.
8. Nakata, T., and Hirokawa, N. (2003). Microtubules provide directional cues for polarized axonal transport through interaction with kinesin motor head. The Journal of cell biology *162*, 1045-1055.
9. Song, A.H., Wang, D., Chen, G., Li, Y., Luo, J., Duan, S., and Poo, M.M. (2009). A selective filter for cytoplasmic transport at the axon initial segment. Cell *136*, 1148-1160.
10. Huang, C.F., and Banker, G. (2012). The translocation selectivity of the kinesins that mediate neuronal organelle transport. Traffic (Copenhagen, Denmark) *13*, 549-564.
11. Kapitein, L.C., Schlager, M.A., Kuijpers, M., Wulf, P.S., van Spronsen, M., MacKintosh, F.C., and Hoogenraad, C.C. (2010). Mixed microtubules steer dynein-driven cargo transport into dendrites. Current biology : CB *20*, 290-299.
12. Blasius, T.L., Cai, D., Jih, G.T., Toret, C.P., and Verhey, K.J. (2007). Two binding partners cooperate to activate the molecular motor Kinesin-1. The Journal of cell biology *176*, 11-17.
13. Hackney, D.D., and Stock, M.F. (2000). Kinesin's IAK tail domain inhibits initial microtubule-stimulated ADP release. Nature cell biology *2*, 257-260.
14. Yamada, K.H., Hanada, T., and Chishti, A.H. (2007). The effector domain of human Dlg tumor suppressor acts as a switch that relieves autoinhibition of kinesin-3 motor GAKIN/KIF13B. Biochemistry *46*, 10039-10045.
15. van der Vaart, B., van Riel, W.E., Doodhi, H., Kevenaar, J.T., Katrukha, E.A., Gumy, L., Bouchet, B.P., Grigoriev, I., Spangler, S.A., Yu, K.L., et al. (2013). CFEOM1-associated kinesin KIF21A is a cortical microtubule growth inhibitor. Developmental cell *27*, 145-160.
16. Hammond, J.W., Blasius, T.L., Soppina, V., Cai, D., and Verhey, K.J. (2010). Autoinhibition of the kinesin-2 motor KIF17 via dual intramolecular mechanisms. The Journal of cell biology *189*, 1013-1025.
17. Coy, D.L., Hancock, W.O., Wagenbach, M., and Howard, J. (1999). Kinesin's tail domain is an inhibitory regulator of the motor domain. Nature cell biology *1*, 288-292.
18. Imanishi, M., Endres, N.F., Gennerich, A., and Vale, R.D. (2006). Autoinhibition regulates the motility of the C. elegans intraflagellar transport motor OSM-3. The Journal of cell biology *174*, 931-937.

19. Hoogenraad, C.C., Wulf, P., Schiefermeier, N., Stepanova, T., Galjart, N., Small, J.V., Grosveld, F., de Zeeuw, C.I., and Akhmanova, A. (2003). Bicaudal D induces selective dynein-mediated microtubule minus end-directed transport. The EMBO journal *22*, 6004-6015.
20. Kapitein, L.C., Schlager, M.A., van der Zwan, W.A., Wulf, P.S., Keijzer, N., and Hoogenraad, C.C. (2010). Probing intracellular motor protein activity using an inducible cargo trafficking assay. Biophysical journal *99*, 2143-2152.
21. Soppina, V., Rai, A.K., Ramaiya, A.J., Barak, P., and Mallik, R. (2009). Tug-of-war between dissimilar teams of microtubule motors regulates transport and fission of endosomes. Proceedings of the National Academy of Sciences of the United States of America *106*, 19381-19386.
22. Winckler, B., Forscher, P., and Mellman, I. (1999). A diffusion barrier maintains distribution of membrane proteins in polarized neurons. Nature *397*, 698-701.
23. Al-Bassam, S., Xu, M., Wandless, T.J., and Arnold, D.B. (2012). Differential trafficking of transport vesicles contributes to the localization of dendritic proteins. Cell reports *2*, 89-100.
24. Petersen, J.D., Kaech, S., and Banker, G. (2014). Selective microtubule-based transport of dendritic membrane proteins arises in concert with axon specification. The Journal of neuroscience : the official journal of the Society for Neuroscience *34*, 4135-4147.
25. Baas, P.W., Deitch, J.S., Black, M.M., and Banker, G.A. (1988). Polarity orientation of microtubules in hippocampal neurons: uniformity in the axon and nonuniformity in the dendrite. Proceedings of the National Academy of Sciences of the United States of America *85*, 8335-8339.
26. Fu, M.M., and Holzbaur, E.L. (2014). Integrated regulation of motor-driven organelle transport by scaffolding proteins. Trends in cell biology *24*, 564-574.
27. Yin, X., Feng, X., Takei, Y., and Hirokawa, N. (2012). Regulation of NMDA receptor transport: a KIF17-cargo binding/releasing underlies synaptic plasticity and memory in vivo. The Journal of neuroscience : the official journal of the Society for Neuroscience *32*, 5486-5499.
28. Wong, R.W., Setou, M., Teng, J., Takei, Y., and Hirokawa, N. (2002). Overexpression of motor protein KIF17 enhances spatial and working memory in transgenic mice. Proceedings of the National Academy of Sciences of the United States of America *99*, 14500-14505.
29. Yin, X., Takei, Y., Kido, M.A., and Hirokawa, N. (2011). Molecular motor KIF17 is fundamental for memory and learning via differential support of synaptic NR2A/2B levels. Neuron *70*, 310-325.
30. Maeder, C.I., Shen, K., and Hoogenraad, C.C. (2014). Axon and dendritic trafficking. Current opinion in neurobiology *27*, 165-170.

SUPLEMENTAL EXPERIMENTAL PROCEDURES

DNA and shRNA constructs

KIF17 constructs were generated by PCR-based strategy using human KIF17 cDNA sequence (accession NM_020816). PEX-RFP-FKBP construct contains human peroxisomes membrane-targeting sequence (accession NM_003630). HA-BICD2N-FRB construct was generated using BICD2N(1-594) from mouse cDNA (accession AJ250106). Further details about the motor constructs and the FRB/FKBP system can be found in [S1-S4]. KIF17tail(266-1029)-GFP-FRB, KIF17tail(737-1029)-GFP-FRB and KIF17(847-1029)-GFP-FRB were AscI/SalI subcloned into pβactin-GFP-FRB. FKBP-tdTomato-Rab3c was generated by insertion of PCR-amplified tdTomato in Sal and SpeI site, mouse Rab3c [S5] in SpeI and NotI sites and FKBP(1x) in BamHI and SalI sites of the pβactin-16-pl vector [S1]. The following shRNAs were cloned in pSuper [S6] and used in this study: rat KIF17 shRNA1 (5'-GCCACCAAGATTAACCTGT-3'), rat KIF17 shRNA2 (5'-GACAGGACAAAGCTCAACA-3'), rat KIF17

shRNA3 (5'-CCATCAACATCGAGATCTA-3') and AnkG shRNA (5'-GAGTTGTGCTGATGACAAG-3').

Antibodies and reagents

The following antibodies were used: mouse-anti-tubulin alpha (Sigma), mouse-anti-β-galactosidase (Promega), chicken anti-β-Galactosidase (BGL-1040, Aves Labs), mouse-anti-AnkyrinG (Invitrogen), mouse anti-pan-Nav (clone K58/35, S8809, Sigma), rabbit-anti-GFP (Sanbio), rabbit-anti-KIF17 (K3638, Sigma used in figure 1A-C), rabbit-anti-KIF17 (H-280, Santa Cruz used in Figure S1A) mouse-anti-MAP2 (Sigma), chicken anti-MAP2 (ab5392, Abcam), mouse-anti-Neurofascin-pan (NF-186, Neuromab) for fixed samples and mouse-anti-Neurofascin-pan Extracellular (Neuromab) for live experiments, mouse-anti-tau (Chemicon) and Alexa405-, Alexa488-, Alexa568- and Alexa647- conjugated secondary antibodies (Life Technologies).

Cell culture and transfections

Primary hippocampal neurons were harvested from rat E18 embryos and cultured on poly-L-lysine (35 μg/ ml) and laminin (5 μg/ml) coated coverslips in neurobasal medium (NB) supplemented with B27, 0.5 mM glutamine, 12.5 μM glutamate and Pen/Strep [S2]. Mature neurons (>DIV14) were used for all experiments unless otherwise indicated. Cells were transfected with Lipofectamine 2000 (Invitrogen) and fixed with 4% PFA+sucrose or ice-cold 100% methanol / 1 mM EGTA / 4% PFA+sucrose after 2-3 day expression. COS7 cells were cultured in DMEM/Ham's F10 medium (50/50%) with 10% FCS and 1% pen/strep. Cells were transfected with Fugene6 (Roche) and imaged after 1 day.

Immunofluorescence staining

After fixation, cells were washed three times for 5 min in PBS and incubated with primary antibodies in GDB buffer (0.2% BSA, 0.8 M NaCl, 0.5% Triton X-100, and 30 mM phosphate buffer, pH 7.4) overnight at 4°C [S1]. Neurons were then washed three times in PBS for 5 min at room temperature and incubated with secondary antibodies in GDB buffer for 1 h at room temperature. After three washes in PBS, coverslips were mounted in Vectashield (Vector Laboratories). Images were acquired using a wide-field fluorescence microscope (Eclipse 80i; Nikon) or a LSM510 confocal laser-scanning microscope (Zeiss) with 40x or 63x oil objectives. For fluorescence intensity comparison, settings were kept the same for all conditions. Quantifications were performed using Image J.

Live cell imaging

Live cell imaging experiments were performed on Nikon Eclipse TE2000E microscope equipped with 40x oil objective, Coolsnap CCD camera (Photometrics), perfect focus system

and imaging chamber [S2]. Imaging chamber was maintained at 37°C and 5% CO2 during acquisition. Neurons were imaged in conditioned medium (NB + B27 + P/S) and COS7 were imaged in Ringer's medium. 100 nM rapalog was added during imaging at t = 00:00 (mm:ss). Cells were imaged at 30s intervals for 30-45 minutes. Movement of single peroxisomes and fast motility of KIF17-G754E were imaged at 10 fps and 20 fps respectively using total internal reflection (TIRF) on a Nikon Eclipse TE2000E microscope equipped with 100x oil objective and Evolve EMCCD camera (Photometrics).

Image processing and analyses

Where necessary, stage drift was corrected with FIJI plugin StackReg (translation) prior to analysis. Kymographs were made using FIJI plugin Multiple kymograph, line width = 3 pixels. Average values are stated in the text as mean ± SEM unless otherwise indicated.

Quantification of induced peroxisome transport in COS-7 cells. Image analysis of peroxisome trafficking assay has been described before [S4,S7]. Images of live cells were processed using MetaMorph (Molecular Devices) or LabVIEW (National Instruments) software. The R90 displacement value is calculated by measuring the diameter of a circle to enclose 90% of all intensity relative to the cell center. The average dispersion speed does not reflect the actual velocity of KIF17 but is the average speed with which KIF17 translocates cargo from cell center to cell periphery. t½ is the time needed for the peroxisomes to reach halfway to the periphery of the cell. Correlation index shows the correlation between consecutive frames (CI ≈ 1: high correlation between frames; CI ≈ 0: low correlation between frames).

Quantification of induced peroxisome transport in neurons. Percentage of neurons with moving, stopping (non-motile) or stalling (irregular, slowly moving) peroxisomes in the proximal axon. Kymographs were drawn along the first 20-30 μm of the axon and peroxisome movement at 30s interval was analysed. We would like to emphasize that that not all KIF17-FL coupled peroxisomes accumulate at the AIS and stay in this axonal region. Some KIF17-coupled peroxisomes escape AIS stalling; they stop in the proximal axon and are released after some time, while others only slow down and move through the AIS. The peroxisomes that make it to the more distal axons are usually motile and are most likely driven by KIF17 motor activity.

Polarity index. Polarity index was calculated using the average dendrite intensity (Id) and average axonal intensity (Ia), using PI=(Id-Ia)/(Id+Ia) [S7]. For non-polarized proteins Id=Ia (PI=0), whereas PI>0 or PI<0 indicates polarization towards dendrites or axons, respectively.

Analysis of KIF17 and AnkG knockdown. DIV11 hippocampal neurons were transfected with either pSuper control or a mix of three shRNAs for KIF17 or AnkG shRNA, together with a fill (GFP or β-galactosidase). Neurons were fixed 72 h after transfection and stained for KIF17 or AnkG. Mean intensities of KIF17 or AnkG signals were quantified in dendrites or the axon initial segment, respectively, of control and depleted neurons using ImageJ software.

Analysis of KIF17 distribution in neurons. Plot profiles were created from segmented lines

traced in axonal tips or from the soma along the axon using Image J. Data processing and statistical analysis were done in Excel and GraphPad Prism (GraphPad Software).

SUPPLEMENTARY FIGURES

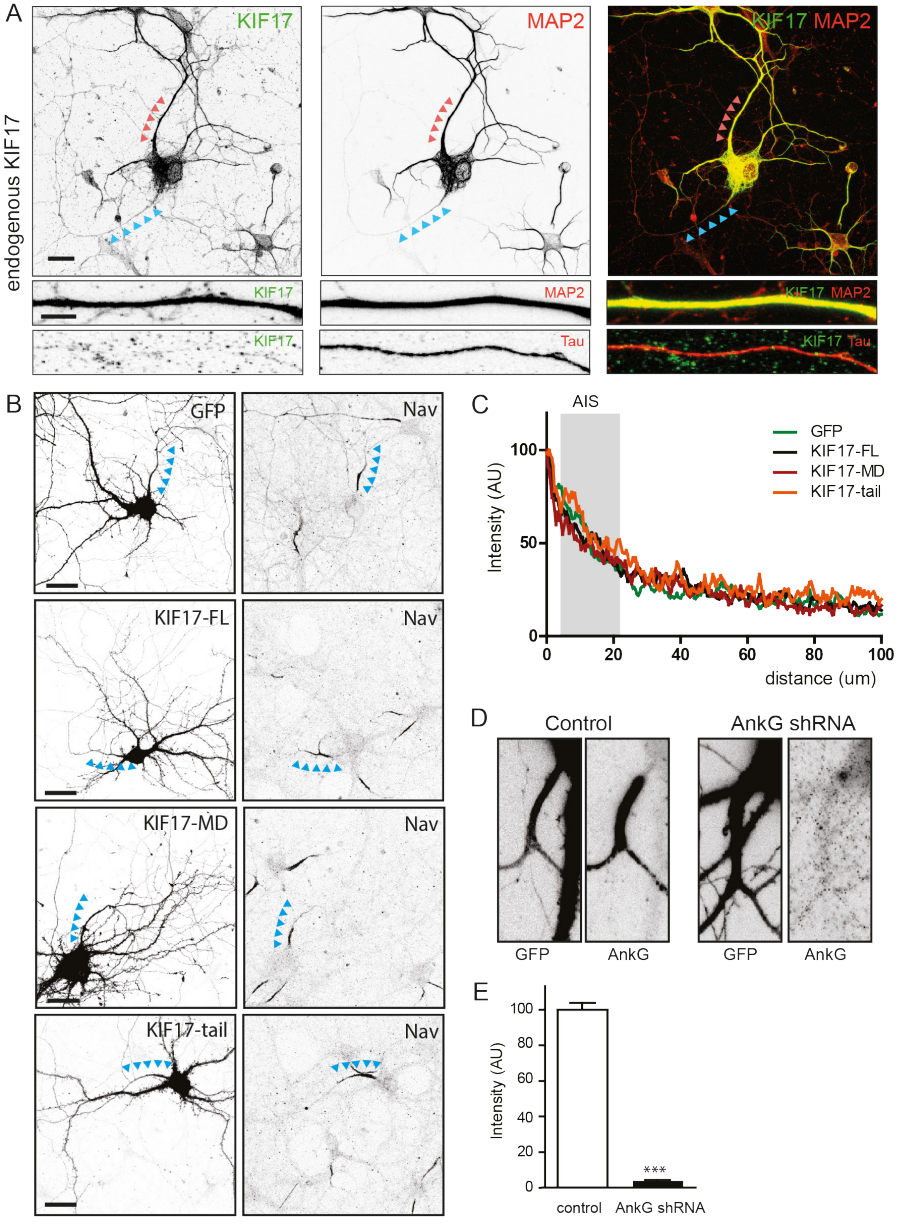

Figure S1, related to Figure 1. Exogenous KIF17 constructs (without inducible cargo attachment) do not accumulate at the AIS

A) *Cultured hippocampal neurons at DIV6 stained for endogenous KIF17 in combination with MAP2 and Tau. Axon is indicated with blue arrows, dendrite with red arrows. Bottom two panels show zooms of a MAP2 positive dendrite and Tau positive axon. Scale bars are 20 μm (top panels) and 5 μm (bottom two panels).*

B) *DIV15 hippocampal neurons transfected with GFP, KIF17-FL-GFP, KIF17-MD-GFP and KIF17-tail and stained for voltage-gated Na+ channels (NaV), as marker for the axon initial segment. Axons are indicated with blue arrow. Scale bars are 20 μm.*

C) *Average normalized fluorescent intensity profiles in the proximal axon of diffuse cytosolic GFP (n=21), KIF17-FL-GFP (n=23), KIF17-MD-GFP (n=22) and KIF17-tail (n=11). Grey area indicates the localization of the axon initial segment, calculated from an average of fluorescent intensity profiles of NaV staining (n=21).*

D) *Zoom of the proximal axon of hippocampal neurons transfected with pSuper control or AnkG shRNA, together with GFP, and stained for AnkG. Scale bars are 5 μm.*

E) *Quantification of AnkG mean intensity in proximal axons of neurons expressing pSuper control (n =27) or AnkG shRNA (n=27). Error bars indicate SEM; ***p < 0.001 (unpaired t-test)*

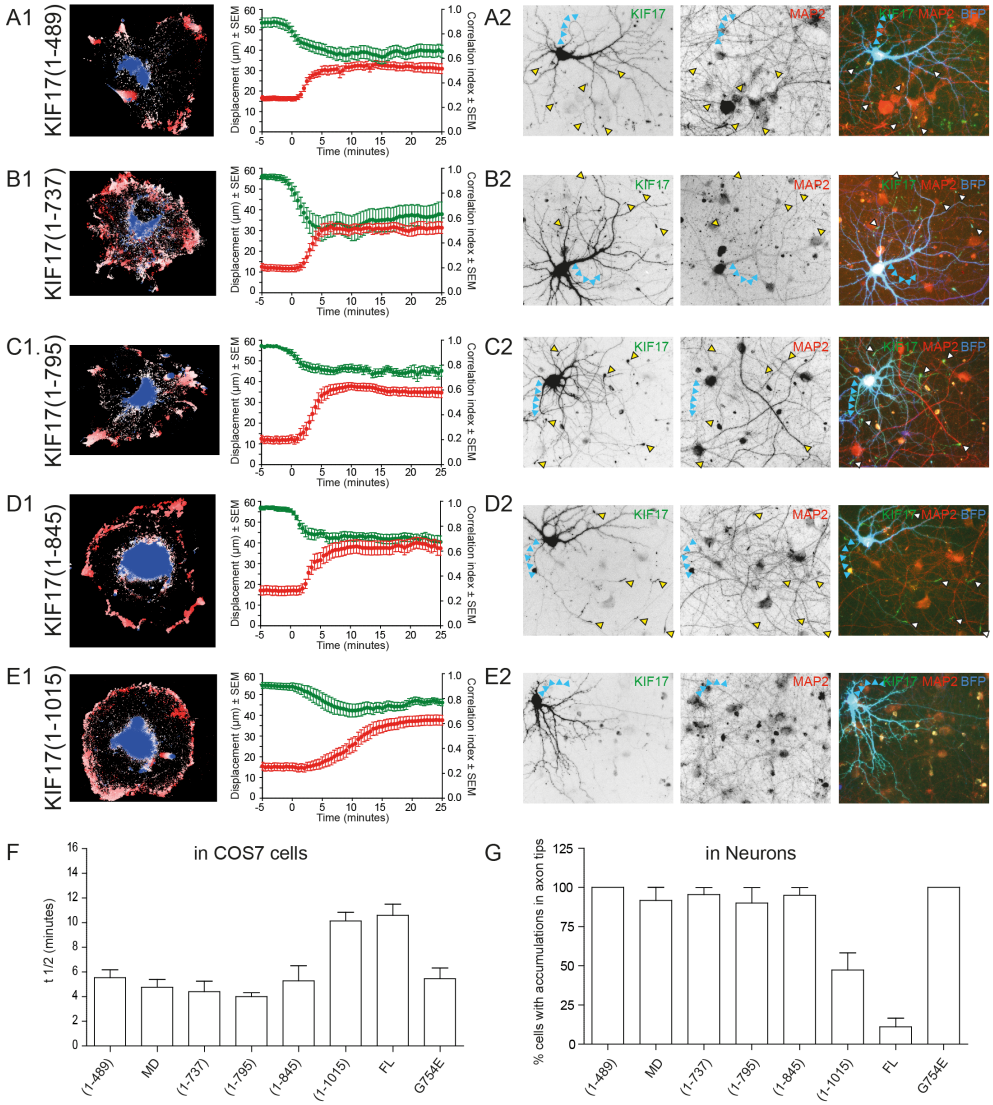

Figure S2, related to Figure 2. Behavior of KIF17 constructs in COS7 cells and neurons

A1-E1) *Analysis of the inducible peroxisome trafficking assay in COS7 cells for full length KIF17 and various KIF17 deletion constructs. Color plots (left panel) show displacement of peroxisomes over time and graph (right panel) indicates peroxisome displacement (R90, red curve) and Correlative index (CI analysis, green curve).*

A2-E2) *Expression of various KIF17 constructs in hippocampal neurons and stained for MAP2. Blue arrows indicate axon, yellow arrows indicate accumulation of KIF17 in tips.*

F) *t½ as measured in COS7 cells (n=11–13 cells from 2 independent experiments).*

G) *Percentage of cells with accumulations in axon tips in hippocampal neurons (n=18-23 cells from 2 independent experiments).*

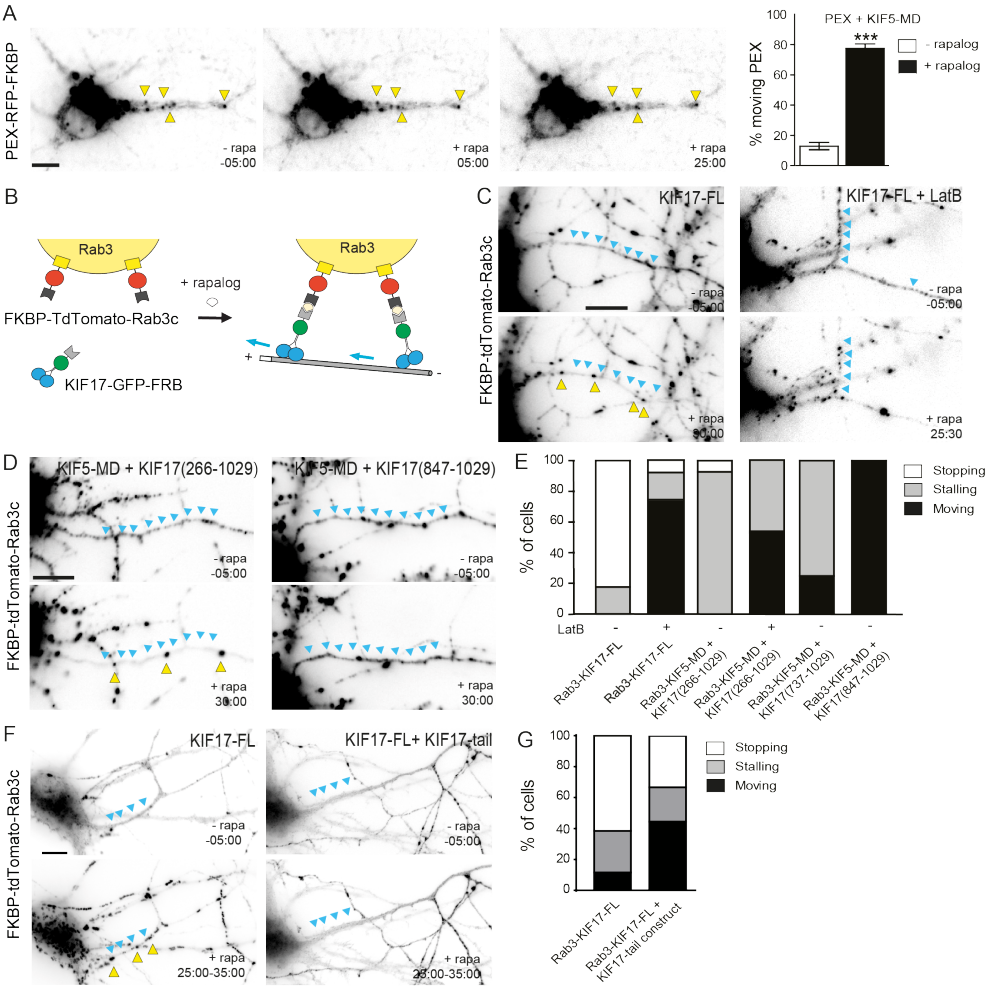

Figure S3, related to Figure 3. KIF17-tail region stalls KIF5-MD-induced Rab3 vesicles at the AIS

A) *Left panels. Typical example of a cultured hippocampal neuron expressing PEX-RFP-FKBP (without exogenous motor constructs). Note that the peroxisome distribution before and after rapalog addition is very similar, indicating that peroxisomes are largely immobile in hippocampal neurons. Scale bar is 10µm. Right panel. Quantification of percentage of moving peroxisomes (PEX-RFP-FKBP) in the axon before and after recruitment of KIF5-MD (now with exogenous motor constructs) using rapalog (N=2, n=11 cells). 5 minute intervals were analyzed for each condition. Note that the peroxisome distribution after rapalog addition (KIF5-MD recruitments) is strongly increased (from ~15% to ~75% mobility). The results without rapalog again show that peroxisomes are largely immobile in hippocampal neurons without exogenous motor attachment. Graph represents mean ± SEM. Statistical significance was determined using an unpaired t-test with*
*Mann-Whitney correction (*** p<0,001)*

B) *Schematic diagram showing the coupling of KIF17-GFP-FRB to FKBP-TdTomato-Rab3c vesicles upon rapalog addition.*

C) *Hippocampal neurons were transfected with KIF17-FL-GFP-FRB and FKBP-TdTomato-Rab3c and imaged and analyzed after 2 days. Images show stills from neurons expressing KIF17-FL-GFP-FRB and FKBP-TdTomato-Rab3c before and after rapalog addition. Most KIF17-FL-coupled cargos stop in the proximal axon (yellow arrowheads). In parallel experiments, neurons were treated with 10μM latrunculin B for 1-2 h before imaging. Depletion of actin allows KIF17-FL-coupled cargos to move through the proximal axon. Scale bar is 10μm.*
D) *Images show stills from hippocampal neurons expressing KIF5-MD-GFP-FRB, KIF17 (266-1029)-GFP-FRB and FKBP-TdTomato-Rab3c before and after rapalog addition. Rapalog-induced coupling of Rab3c to KIF5-MD-GFP-FRB and KIF17(266-1029)-GFP-FRB induces stalling (also indicated as delayed KIF5-MD-induced cargo movements) of vesicles in the axon (top panel). Coupling of KIF17(847-1029)-GFP-FRB does not stall or stop KIF5-MD induced Rab3c vesicle movement. Scale bar is 10μm.*
E) *Percentage of neurons with moving, stalling or stopping Rab3c vesicles along the axon, when coupled to KIF5-MD-GFP-FRB and the indicated KIF17 truncations (n=11–17 cells from at least 2 independent experiments).*
F) *Coupling of Rab3c vesicles to KIF17-FL-GFP-FRB in the presence or absence of KIF17 tail domain (KIF17(266-1029)-GFP; note that this construct contains the FRB domain). Images show maximum projections of the timelapse acquired for 10 minutes. The KIF17 tail domain acts as a dominant negative construct and prevents the accumulation and stopping of KIF17-FL-GFP-FRB coupled Rab3 vesicles in the proximal axon. Scale bar is 10μm.*
G) *Percentage of neurons with moving, stalling or stopping Rab3c vesicles along the axon in the presence or absence of the KIF17 tail domain (KIF17(266-1029)-GFP) after rapalog-induced coupling of KIF17-FL-GFP-FRB (n=26-27 neurons from at least 2 independent experiments).*

LEGENDS TO SUPPLEMENTARY VIDEOS

Supplementary Video 1. Related To Figures 2D and 2E.
KIF17-FL Transports Peroxisomes to the Periphery of COS7 Cells after Rapalog Addition. COS7 cells were transfected with PEX-RFP-FKBP and KIF17-FL-GFP-FRB and imaged after 1 day overexpression. 100 nM rapalog was added during acquisition to induce coupling of KIF17-FL motors to peroxisomes. Images were taken at 30 s interval. Movie playback is 10 fps. Scale bar is 10 μm.

Supplementary Video 2. Related To Figures 3A-C.
KIF17-FL Does Not Directly Target Dendrites but Is Anchored at AIS. Adult hippocampal neuron with zoom of the proximal axon. Neurons were transfected with PEX-RFP-FKBP (red) and KIF17-FL-GFP-FRB (green) and imaged after 2 day overexpression. 100 nM rapalog was added during acquisition. Images were taken at 30 s interval. Movie playback is 10 fps. Stalling peroxisomes are indicated with red arrows. Scale bars are 10 μm in full image and 5 μm in zoom.

Supplementary Video 3. Related To Figures 3C.
Disrupting the AIS by AnkG KD Eliminates Stalling of KIF17-FL-Coupled Peroxisomes. Zooms of the proximal axon of neurons transfected with PEX-RFP-FKBP and KIF17-MD-GFP-FRB or KIF17-FL-GFP-BRF with or without AnkG shRNA. Neurons were imaged after 2 day overexpression and 100 nM rapalog was added during acquisition. Images were taken at 30 s interval. Movie playback is 10 fps. Scale bar is 5 μm.

Supplementary Video 4. Related To Figures 4A, 4D and 4E.
KIF17-FL Vesicles Are Redirected into Dendrites by Dynein. Neuron were transfected with PEX-RFP-FKBP (red), HA-BICD2N-FRB and KIF17-FL-GFP-FRB (green). Neurons were imaged after 2 day overexpression and 100 nM rapalog was added during acquisition to induce simultaneous coupling of KIF17-FL and dynein motors to peroxisomes. Images were taken at 30 s interval. Movie playback is 10 fps. Scale bar is 10 µm.

Supplementary Video 2. Related To Figures 4A, 4D and 4E.
KIF17-FL Colocalizes with Peroxisomes in Dendrites after Coupling to BICD2N. Zoom of the proximal dendrite of a neurons transfected with PEX-RFP-FKBP (red), HA-BICD2N-FRB and KIF17-FL-GFP-FRB (green). Neurons were imaged after 2 day overexpression and 100 nM rapalog was added during acquisition. Images were taken at 30 s interval. Movie playback is 10 fps. Scale bar is 5 µm.

SUPPLEMENTAL REFENCES

S1. Hoogenraad, C.C., Milstein, A.D., Ethell, I.M., Henkemeyer, M., and Sheng, M. (2005). GRIP1 controls dendrite morphogenesis by regulating EphB receptor trafficking. Nature neuroscience 8, 906-915.

S2. Kapitein, L.C., Yau, K.W., and Hoogenraad, C.C. (2010). Microtubule dynamics in dendritic spines. Methods in cell biology 97, 111-132.

S3. Kapitein, L.C., Schlager, M.A., Kuijpers, M., Wulf, P.S., van Spronsen, M., MacKintosh, F.C., and Hoogenraad, C.C. (2010). Mixed microtubules steer dynein-driven cargo transport into dendrites. Current biology 20, 290-299.

S4. Kapitein, L.C., Schlager, M.A., van der Zwan, W.A., Wulf, P.S., Keijzer, N., and Hoogenraad, C.C. (2010). Probing intracellular motor protein activity using an inducible cargo trafficking assay. Biophysical journal 99, 2143-2152.

S5. van Vlijmen, T., Vleugel, M., Evers, M., Mohammed, S., Wulf, P.S., Heck, A.J., Hoogenraad, C.C., and van der Sluijs, P. (2008). A unique residue in rab3c determines the interaction with novel binding protein Zwint-1. FEBS letters 582, 2838-2842.

S6. Brummelkamp, T.R., Bernards, R., and Agami, R. (2002). A system for stable expression of short interfering RNAs in mammalian cells. Science 296, 550-553

S7. Lipka J, Kapitein LC, Jaworski J, Hoogenraad CC. (2016). Microtubule-binding protein doublecortin-like kinase 1 (DCLK1) guides kinesin-3-mediated cargo transport to dendrites. EMBO J. 35, 302-18.

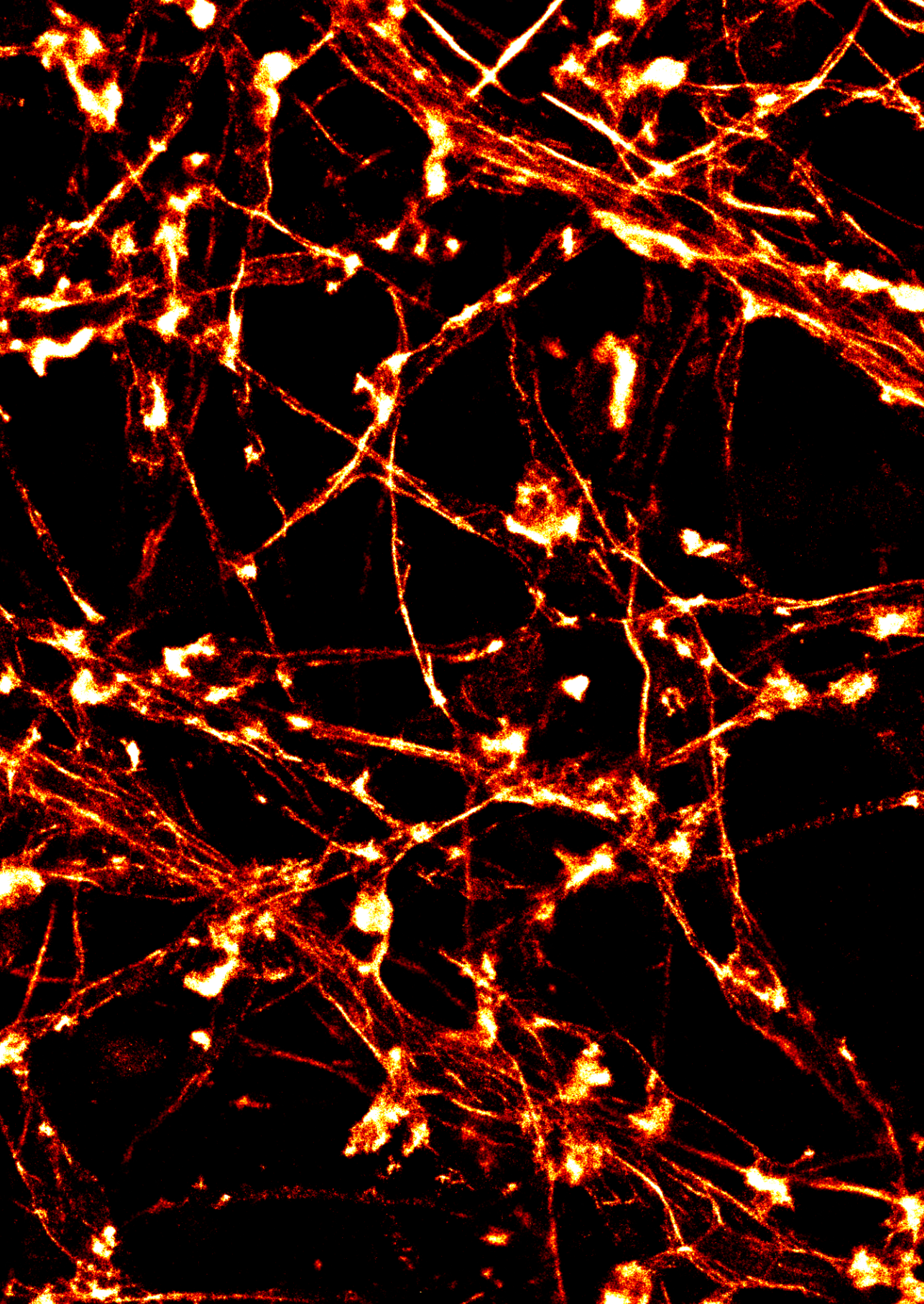

5

Activity-Dependent Actin Remodeling at the Base of Dendritic Spines Promotes Microtubule Entry

Philipp Schätzle[1], Marta Esteves da Silva[1], **Roderick P. Tas[1]**, Eugene A. Katrukha[1], Hai Yin Hui[1], Corette J. Wieringa[1], Lukas C. Kapitein[1] and Casper C. Hoogenraad[1]

Current Biology (2018); 28, pp. 2081-2091

[1] Division of Cell Biology, Faculty of Science, Utrecht University, The Netherlands

ABSTRACT

In neurons, microtubules form dense bundles and run along the length of axons and dendrites. Occasionally, dendritic microtubules can grow from the shaft directly into dendritic spines. Microtubules target dendritic spines that are undergoing activity-dependent changes, but the mechanism by which microtubules enter spines has remained poorly understood. Using live-cell imaging, high-resolution microscopy and local glutamate uncaging, we show that local actin remodeling at the base of a spine promotes microtubule spine targeting. Microtubule spine entry is triggered by activation of NMDA receptors and calcium influx, and requires dynamic actin remodelling. Activity-dependent translocation of the actin remodelling protein cortactin out of the spine correlates with increased microtubule targeting at a single spine level. Our data shows that the structural changes in the actin cytoskeleton at the base of the spine are directly involved in microtubule entry, and emphasize the importance of actin-microtubule crosstalk in orchestrating synapse function and plasticity.

INTRODUCTION

Microtubules are critical structures for stable neuronal morphology. They can serve as tracks for cargo transport, provide dynamic and mechanical functions, and control local signaling events [1]. In dendrites, microtubules polymerize from their plus ends along the length of the dendrite in both anterograde and retrograde directions [2]. Equal numbers of opposing microtubule orientations throughout the dendritic processes have been reported *in vitro* and *in vivo* [3]. Occasionally, microtubules can polymerize from the dendritic shaft directly into dendritic spines [4, 5]. Even though microtubules enter spines spontaneously, subsequent studies have shown that these microtubule invasions of spines are regulated by synaptic activity. Recent work has shown that microtubule invasion frequency increases after induction of chemical long-term potentiation (cLTP) [6]. In contrast, applying a paradigm that induces chemical long-term depression (cLTD) results in a loss of microtubule dynamics in dendritic spines [7]. However, the mechanistic link between neuronal activity and microtubule entry into spines remains largely unclear.

Dynamic microtubule entry in dendritic spines has been thought to contribute to processes related to synaptic maintenance and plasticity. For instance, recent data showed that microtubules entering dendritic spines provide a direct route for microtubule-based motor-driven transport of selective synaptic cargo into spines [8]. Under basal conditions, the frequency of microtubule-spine invasions is relatively low, making actin-based transport a more generic way of driving cargo trafficking in spines. For example, it has been shown that endoplasmic reticulum and recycling endosomes use myosin V motors to enter spines [9-11]. However, kinesin-3 family proteins (KIF1A and KIF1C) can act as microtubule-base motors that transport cargo along newly polymerized microtubules directly into spines [8, 12]. The mechanism by which microtubules enter dendritic spines has remained poorly understood. In this study we investigate which processes regulate microtubule entry into spines.

RESULTS

Microtubules enter dendritic spines in cultured neurons and organotypic slices

The invasion of dendritic spines by dynamic microtubules was recently shown in developing neuron culture systems [4-6, 13]. Using a lentivirus-based inducible expression system we demonstrate microtubule entry in spines in mature rat dissociated hippocampal neuron cultures (up to DIV45) and in dentate gyrus granule cells of organotypic mouse hippocampal slice cultures (Figure 1A). We observed frequent microtubule invasions in spines in both culture types and at different stages of maturation, indicating that this phenomenon is not limited to a transient phase during development (Figure 1B). The average spine entry frequency in slices was about half of the observed value for dissociated neuron cultures (Figure 1B), which is partially explained by a higher spine density compared to the number

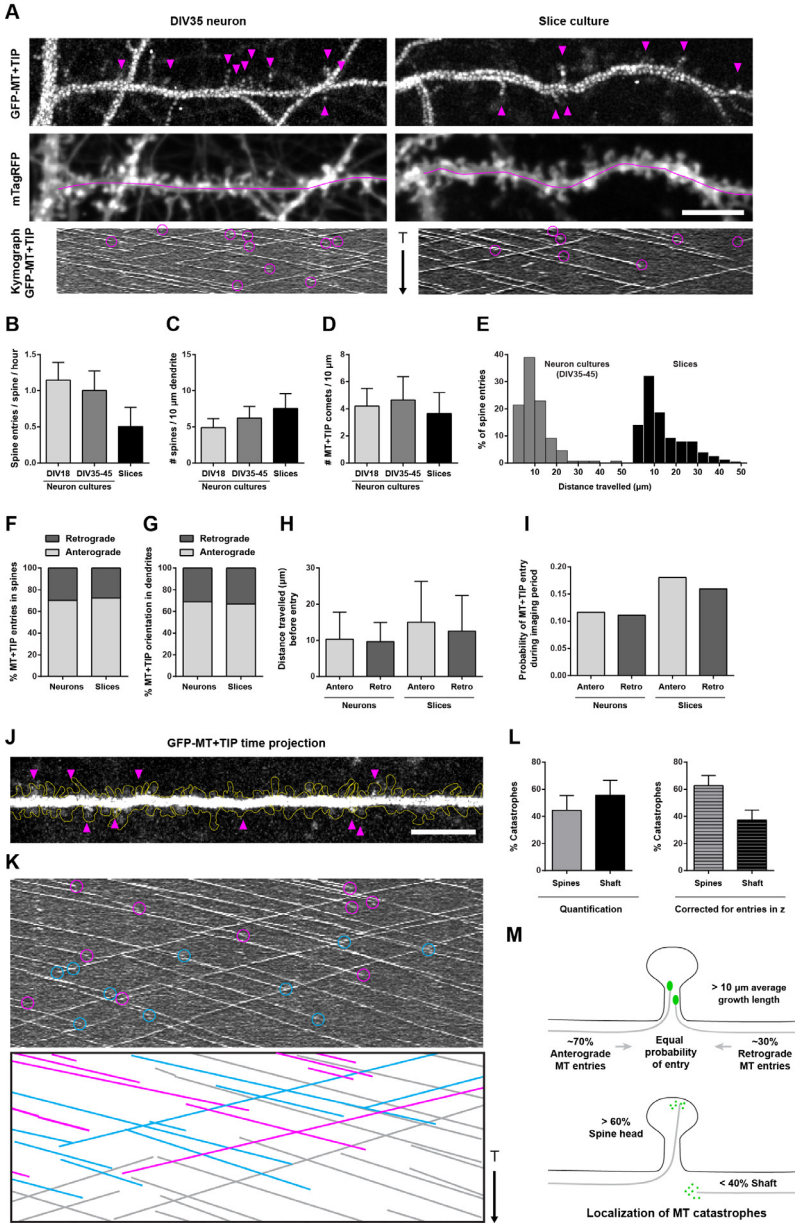

Figure 1. Microtubules invade spines in mature cultured neuron and organotypic slice

A) *Dendrites from lentiviral-transduced hippocampal dissociated neurons (rat) and dentate gyrus granule cells of a hippocampal slice culture (mouse) expressing a marker for dynamic microtubules (MT+TIP, top) and cellular morphology (mTagRFP, middle). The top panel shows maximum projections of average-subtracted time-lapse recordings of MT+TIP comets (6 min). Arrowheads highlight examples of microtubules entering spines. The middle panel shows average projections of the full time-lapse and the line displays the dendritic sections used for kymographs. Bottom panels show kymographs of the MT+TIP comets from the top panels. Magenta circles indicate microtubules invading spines.*

B) *Quantification of spine entry frequency in cultured neurons and slice cultures. Cultured neurons DIV18: n = 10, DIV35-45: n = 25, slices: n = 37 analyzed neurons.*
C) *Quantification of spine number per 10 µm dendrite (n = identical to B).*
D) *Density of MT+TIP comets per 10 µm dendrite.*
E) *Histogram of distance travelled by MT+TIP comets entering a spine in neuron (left graph) and slice cultures (right graph). Bin size = 5 µm, neurons: n = 131 comets, slices: n = 149 comets.*
F) *Orientation of microtubules invading spines (n = identical to E).*
G) *Distribution of anterograde and retrograde oriented MT+TIP comets in neurons and slice cultures. DIV35-45: n = 1140 comets, slices: n = 859 comets.*
H) *Average distance MT+TIP comets travelled before entering a spine.*
I) *Probability of MT+TIP comets entering a spine relative to its orientation (pooled data).*
D-I Make use of the same dataset. Cultured neurons DIV18: n = 14 dendrites from 2 preparations, DIV35-45: n = 25 dendrites from 2 preparations, slices: n = 21 dendrites from 6 preparations.
J) *Maximum intensity projection of MT+TIP comets time-lapse recording in slices. The spine outline was generated from mTagRFP signal. Arrowheads indicate microtubule entries in spines.*
K) *Kymograph of the MT+TIP comets shown in J. Microtubule catastrophes within spines are highlighted by magenta circles, catastrophes without detectable spine entries (shaft) by cyan circles. Bottom graph shows a drawing of the kymograph using the same color code. Gray lines represent microtubule traces without observable catastrophes. The scale and time lapse length is identical to J.*
L) *Localization of microtubule catastrophes in dendrites of slice cultures. Right graph is corrected for false positive shaft catastrophes resulting from limited z-resolution. n = 203 comets of 12 dendrites from 10 slices of 4 preparations.*
M) *Summary of findings: Spine targeting is not selective for microtubule polarity but the higher number of anterograde growing microtubules results in a more frequent targeting of this orientation. Spines represent preferred localizations for microtubule growth termination.*
Scale bars, 10 µm. Vertical arrows, 4 min. Bars diagrams show mean + s.d.

of dynamic microtubules in granule cells (Figure 1C and 1D). We found that microtubules grew over remarkable distances before entering a spine (Figure 1E). This was even more pronounced in slice cultures, where 25% of all spine entries were preceded by growth episodes of 20-50 microns. Furthermore, a considerable number of comet traces crossed the acquisition borders in time and/or space, which means that the actual length of many comets was actually underestimated. This observation is in conflict with a recent publication where it is reported that microtubules travel short distances before spine invasions [14]. This discrepancy could be explained by the limited z-resolution of TIRF microscopy used in the aforementioned study. The bidirectional polarity of growing microtubules in dendrites [3] could entail that one orientation is preferential for spine entries. However, the polarity of microtubules entering spines (Figure 1F) was identical to the orientation of the total dynamic microtubule population (Figure 1G). Consistently, microtubules of opposed polarity did not show differences for the covered distances before spine entries (Figure 1H) and spine entry probabilities (Figure 1I). These data demonstrate that the polarity of microtubules is not a determinant factor for the targeting of dendritic spines (Figure 1M).

Spines are hotspots of microtubule catastrophes in mature dendrites

The growth and shrinkage of microtubules is controlled by a variety of regulatory proteins that interact with the plus-tip or the microtubule lattice [15]. In slice cultures the majority of microtubule catastrophes were not followed by a microtubule rescue event (see for instance the kymograph in Figure 1K). As spine entries always result in a microtubule catastrophe, we asked to which extent this scenario accounts for the termination of microtubule growth in the dendrite. Based on kymographs, we identified microtubule catastrophes in slices and analyzed if these occur within the dendrite or in spines (Figure 1J and 1K). Surprisingly, more than 40% of the microtubule catastrophes could directly be associated with entries in spines (magenta circles in Figure 1K). However, this number reflects only spine entries identified in x,y dimensions because we limited imaging to one z-plane to capture the rapid dynamics. We therefore applied a z-correction factor that was determined by the assumption that spine entries cannot be resolved if the spine is more than ± 60 degrees out of the imaging plane. This correction increased the proportion of catastrophes occurring in spines to more than 60% (Figure 1L), suggesting that spine entries may represent the default pathway of terminating the growth of dynamic microtubules in mature neurons.

Increasing dendritic calcium levels increase microtubule entries in spines

Previous studies in dissociated neurons suggest a regulatory effect of synaptic activation on spine invasions by microtubules [6, 7, 14]. To verify this in slices, we applied pharmacological treatments that modulate the pattern of synaptic activation in hippocampal slice cultures and analyzed microtubule dynamics in spines. While decreasing (TTX) or increasing (PTX) network activity did not affect spine entry frequencies in slices, we observed a small but significant decrease using low concentrations of DHPG, known to induce chemical LTD in slices (Figure 2A). The most striking effect was found after application of the muscarinic agonist methacholine (MCh). Cholinergic stimulation has been used by several groups to induce LTP in hippocampal slice cultures and acute slices via G protein-coupled release of calcium from IP_3-sensitive stores [16, 17]. Following methacholine stimulation we observed a doubling of spine entry events compared to control conditions (Figure 2A-C; Video S1). Interestingly, TTX-induced blocking of action potentials did not abolish the potentiating effect of methacholine, suggesting that the MCh-induced increase of intracellular calcium is sufficient to increase microtubule invasions in spines (Figure 2A and 2C). We did not observe a significant change in microtubule dynamics and density as a result of the MCh stimulation protocol (Figure 2D and 2E). Our data is in agreement with a recent study demonstrating an increase of microtubule invasions in spines of dissociated cultures after stimulation with a glycine-based chemical LTP protocol [14]. To confirm the role of dendritic calcium levels in this process, we applied brief local application of NMDA on TTX-silenced neuron cultures (Figure 2F). Quantifications of spine entry frequencies before and after application revealed a significant increase following NMDA-induced increase in calcium levels (Figure 2G).

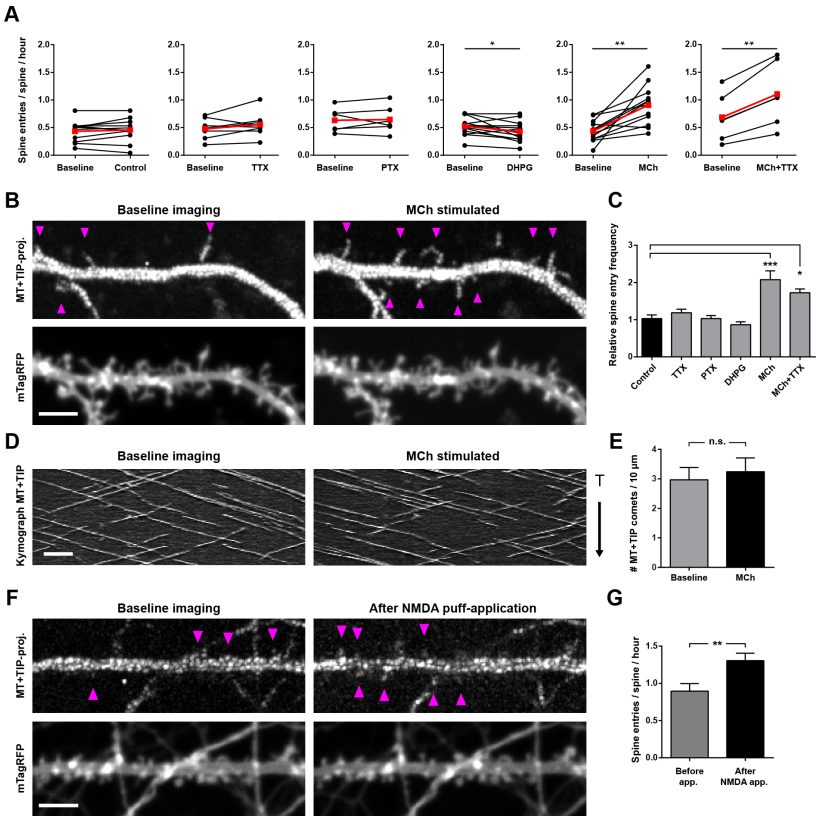

Figure 2. Specific synaptic activation modulates microtubule invasions in spines
*(A) Synaptic activation in slice cultures was altered by indicated pharmacological treatments. Cultures were transduced with lentivirus expressing GFP-tagged MT+TIP marker and mTagRFP. Red points represent the mean values of the dataset. *p<0.05, **p<0.01, paired t-test; control: n = 11, TTX: n = 8, PTX: n = 6, DHPG: n = 13, methacholine (MCh): n = 12, MCh+TTX: n = 6 dendrites.*
(B) Example of MCh-stimulated dendrite showing projections of MT+TIP comets (upper panel) and dendrite morphology (lower panel), before and after stimulation in slice cultures. Arrowheads indicate examples of MT-+TIP entries in spines. See also Video S1.
*(C) Relative change of spine entry frequency in slice cultures (stimulation/baseline) for each treatment in a. *p<0.05, ***p<0.0001, one-way ANOVA with posthoc Dunnett's test.*
(D) Kymographs of the MT+TIP comets shown in B before and after MCh stimulation (both 8:15 min recordings).
(E) Quantification of MT+TIP comet density per 10 µm dendrite in slice cultures. n.s. = not significant, paired t-test; n = 15 dendrites.
(F) Neuron culture infected with virus expressing MT+TIP marker and mTagRFP. Dendrite recorded 4 min before and after local puff-application of NMDA. Panels are arranged as in B.
*(G) Quantification of spine entry frequency before and after local NMDA application. **p<0.01, paired t-test; n = 12 dendrites.*
Scale bars, 5 µm. Bars diagrams show mean + s.e.m. See also Video S1.

Together, these experiments suggest that intracellular calcium is involved in the regulation of spine targeting by microtubules.

Regulation of spine targeting on the level of single synapses

To our knowledge, all previous studies addressing the effects of synaptic activity on microtubule dynamics in spines were performed using global stimulation protocols. The above-described local NMDA applications were our first attempts to target individual synapses. However, recordings of calcium dynamics showed that the majority of synapses within the field of view became activated and NMDA stimulation evoked calcium waves extending throughout the dendrite. To activate only a small population of synapses along a dendrite, we performed glutamate uncaging on cultured neurons. Two-photon uncaging in slice cultures is associated

Figure 3. NMDA receptor activation triggers microtubule entry in spines

A) *Still frames of a dissociated neuron expressing mTagRFP. The first and last images represent time points before and after single-photon glutamate uncaging. Uncaging intervals were 0.5 Hz starting from 0 sec for 1 min. The white/yellow line marks the uncaging spot; arrowhead indicates a targeted spine and the arrows point to examples of spines that do not respond by size changes.*

B) *The targeted spine in A at higher magnification. Spine outline was traced and the last image shows an overlay of the before and after uncaging situation.*

C) *Quantification of the change in spine head size in response to the uncaging stimulus over time. Targeted spines lay in close proximity to the uncaging spot, while control spines were chosen with a maximum possible distance to this position. Left graph shows the results of the standard uncaging protocol (targeted: n = 21, control: n = 26 spines). Middle graph represents a control condition in which the light pulse is applied in the absence of caged glutamate (targeted: n = 9, control: n = 9 spines) and right graph shows the uncaging experiment in the presence of the NMDA-receptor blocker APV (targeted: n = 10, control: n = 11 spines). Error bars indicates s.e.m.*

D) *Dendrite morphology before (left) and during glutamate uncaging (middle). Based on the morphological response to the stimulation, spines were classified as "activated" (white box) and "non-activated" (dashed box). White/yellow line marks the uncaging spot and the circles indicate the distance to the center of the uncaging region. See also Video S2.*

E) *Maximum projection of the MT+TIP comets time-lapse recorded after the uncaging session. Magenta arrowheads show MT-+TIP spine entries in activated spines, white arrowheads in a non-activated spine. See also Video S2.*

F) *Quantification of spine entries following glutamate uncaging. Entry frequencies for activated and non-activated distant spines are shown separately, while this separation was not made for APV experiments. Right graph shows the individual experiments, where each point represents the mean spine entry frequency of an uncaged dendrite. ***p<0.0001, one-way ANOVA with posthoc Tukey's test; uncaged: n = 25, APV silenced: n = 17 dendrites.*

G) *Average spine numbers of the analyzed experiments and the fraction considered activated.*

H) *Histogram showing the relative frequency of spine entries in relation to the localization of spines to the uncaging region. Microtubule dynamics were recorded for 8 min after uncaging. Invaded and non-invaded spines were quantified together with their distance to the uncaging region. Data is presented in bins of 3 µm intervals for uncaged control and APV treated dendrites (uncaged: n = 20, APV: n = 17 dendrites).*

I) *Histogram showing the relative spine entries frequency relative to the time point of microtubule entry. Spines previously identified as activated are compared to APV silenced spines (activated: n = 39 dendrites with 153 entries, APV: n = 17 dendrites with 103 entries).*

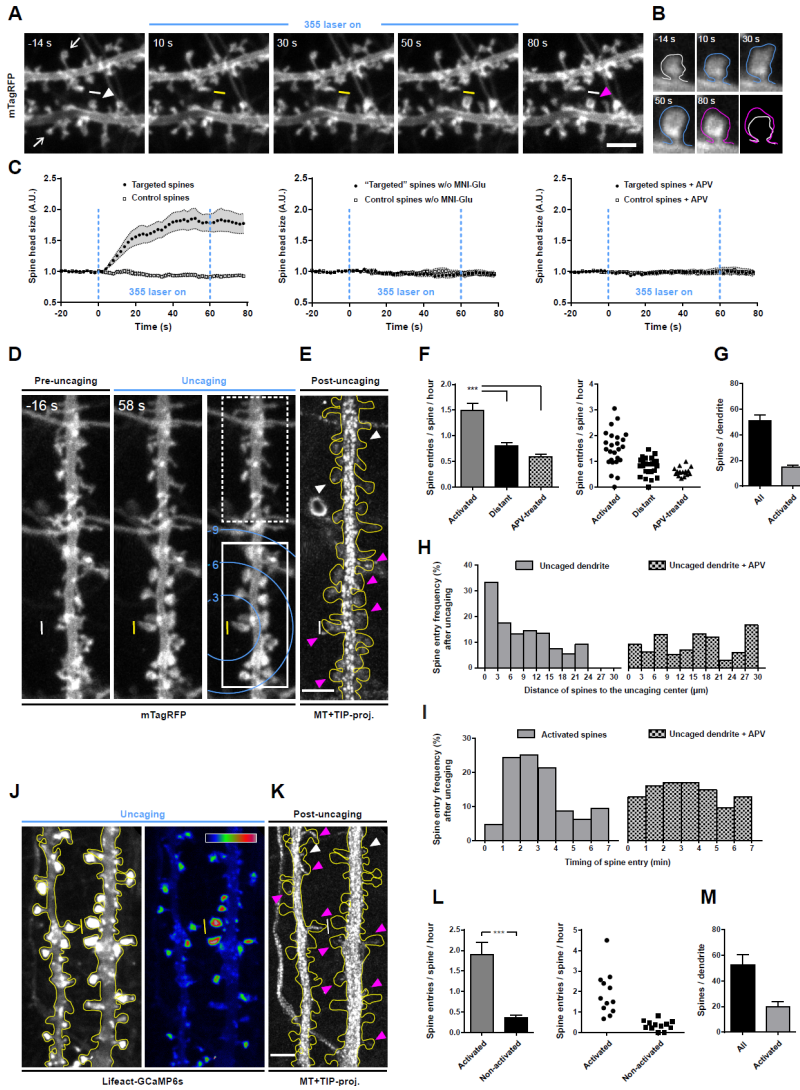

J) *Maximum projection of a Lifeact-GCaMP6s time-lapse acquired during uncaging of glutamate. The levels are strongly enhanced to identify all spines on the dendrite (left). The color coded sum projection allows the identification of activated spines (right). Yellow line marks the uncaging region, insert in top right corner shows lookup table for the color code. See also Video S3.*

K) *Projection of MT+TIP comets time-lapse recorded after the uncaging session. Microtubule entries in activated spines are highlighted with magenta arrowheads, entries in non-activated spines with white arrowheads. See also Video S3.*

L) *Quantification of spine entry frequency following glutamate uncaging. Activated and non-activated spines are identified on their GCaMP6s signal. ***p<0.0001, Mann Whitney test; n = 12 dendrites. The scatter plot on the right shows the results of the individual experiments.*

M) *Average total and activated spine numbers of the analyzed experiments.*

Scale bars, 3 µm. Bars diagrams show mean + s.e.m.

with an NMDA-dependent increase in spine size [18, 19]. We used spine growth as read-out of successful single-photon glutamate uncaging in our neuronal cultures. Spines close to the uncaging region showed an almost 2-fold increase in size while distant control spines were unchanged (Figure 3A-D). Additional control experiments demonstrated that the spine size changes were not a direct result of the 355 nm laser excitation but depended on the activation of NMDA receptors (Figure 3C). Next, we combined the uncaging protocol with subsequent recording of microtubule dynamics (Figure 3D and 3E; Video S2). Quantifications of microtubule invasions showed that the MT entry frequency on activated spines was almost two-fold increased when compared to distant spines (Figure 3F). Uncaging in the presence of APV resulted in a lower invasion frequency, which was similar to distant spines. As an alternative quantification, we determined the spine entry frequency relative to the distance to the uncaging center, which confirmed that spines in close proximity to the uncaging region were more frequently targeted than more distant spines (Figure 3H). This effect was absent when APV was applied. The spine entry promoting effect could be observed starting from 1 min after the end of the uncaging stimulus and lasted for about 3 min (Figure 3I). Although these uncaging experiments strongly suggest that local activation induces local targeting, our approach could not indisputably resolve the activation state of individual spines. To overcome this we combined the uncaging experiments with a read-out of the NMDA-evoked calcium transients. A fusion construct of Lifeact and GCaMP6s resulted in a highly specific indicator for calcium signals in spines. The combined recording of calcium signals and microtubule dynamics (Figure 3J and 3K; Video S3), showed a strong correlation between activated spines and microtubule targeting events in the uncaging experiments (Figure 3L). Both approaches to identify activated spines showed similar numbers (Figure 3G and 3M). In summary, the activation of a small number of dendritic spines using glutamate uncaging yielded direct evidence for a coupling between synaptic activation and increased probability of targeting by dynamic microtubules on the level of single spines.

Microtubule targeting in spines depends on actin remodeling

The actin cytoskeleton in spines is a major downstream target of activity-induced plastic changes at synapses [20]. To determine whether actin plays a role in microtubule entries in spines, we pharmacologically interfered with actin dynamics. We monitored spine size and actin in neuron cultures expressing the actin marker Lifeact in control conditions and after incubation with the actin stabilizing drug jasplakinolide. The treatment did not increase spine size but reduced actin-based motility of the spine heads [21] (Figure 4A). Interestingly, microtubule entries in spines were strongly increased by jasplakinolide, while the total number of comets remained stable but the relative comet density decreased (Figure 4A, 4B and S2A-C). In contrast, disruption of actin structures with latrunculin B induced a significant decrease of spine entry frequency in dissociated neurons (Figure 4B). We found similar results in slice cultures, in which jasplakinolide also increased spine entry frequency

(Figure 4C). Remarkably, the methacholine-induced potentiating effect on spine entry in slices (Figure 2A) was completely abolished in the presence of latrunculin B (Figure 4C). These data demonstrate a clear involvement of actin in the microtubule invasion of spines.

The localization of endoplasmic reticulum (ER) in spines is another actin-dependent process [11] that is affected by synaptic activity [22], reminiscent of our microtubule spine invasions. As microtubule plus-tips can interact with the ER [23] we wondered if growing microtubules were guided into spines by following previously established ER-structures. To address this possibility, we overexpressed a dominant negative MyosinVa construct in dissociated neuron cultures to disrupt spine targeting of ER. Although we noticed a more than 5 times reduction of ER positive spines in these experiments, there was no effect on the microtubule spine entry frequency (Figure S1), indicating that microtubule invasions occur independent of ER in spines.

End-binding proteins (EBs) recognize growing microtubule plus-tips and could be involved in the microtubule spine targeting process through specific protein interactions via their acidic C-terminal tail region [15]. We therefore tested if only disrupting these EB3-interactions would interfere with microtubule spine invasions. We observed full rescue of spine targeting after endogenous EB3 depletion and expression of EB3-CΔAC (Figure 4D), putting forward the idea that microtubule-actin interlinking proteins are not directly required in this process. Control experiments with co-expression of EB3 shRNA and the MT+TIP marker did not allow recording of microtubule comets, indicating strong depletion of endogenous EB3. Next, we investigated if the knockdown of specific actin interacting/regulating proteins affects the targeting of spines by microtubules. Cortactin, MARCKS and MyosinIIb represent important regulators of actin dynamics in spines [24-26], while Drebrin and MACF2 were chosen due to their ability to directly interact with actin and growing microtubule plus-ends [27, 28]. Lentiviral induced RNAi of the actin-interacting candidate proteins differentially affected spine morphology and density (Figure 4E and S2E). Interestingly, only the knockdown of Cortactin resulted in a significant effect on microtubule spine entry frequency in dissociated neuron cultures (Figure 4F). To exclude potential off-target effects of the used Cortactin-shRNA, we performed rescue experiments using a knockdown-resistant version of Cortactin, which resulted in a comparable spine entry frequency as in control conditions (Figure 4G). Pharmacological blockade of the Cortactin downstream target Arp2/3 complex (CK-666), as well as inhibition of upstream Src kinase (PP2) resulted in a significant decrease of spine targeting by microtubules (Figure 4H) [29]. The involvement of the actin regulator Cortactin suggests that the actin cytoskeleton *per se* may facilitate microtubule spine targeting and that actin-microtubule interactions may be of less importance. An activity-dependent redistribution of Cortactin and/or the underlying actin remodelling [24, 29, 30] may be linked to a role for Cortactin in activity-dependent targeting of microtubules to spines. Using glutamate uncaging in combination with Cortactin knockdown, we found a significant reduction of microtubule spine targeting confirming the

importance of Cortactin regulated actin dynamics in promoting spine entries (Figure 4I and 4J). While overexpression of exogenous Cortactin alters spine morphology, microtubule spine targeting and cortactin redistribution after glutamate uncaging is observed (Videos S4, S5)

Actin remodelling at the base of the spine

Actin dynamics have been extensively studied in the spine head but relatively little data exists about actin remodelling at the base of the spine. Electron microscopy has demonstrated a branched actin network at the base of the spine, which often overlapped with microtubules at the intersection between the spine neck and dendritic shaft [31]. We reasoned that the base of the spine is an important area for guiding microtubule entry into spines and we analysed actin dynamics at single spine level in greater detail. Glutamate uncaging-induced stimulation of spines in control neurons markedly increased actin fluorescence intensities (Lifeact) in spine heads and at the spine base (Figure 5A). Interestingly, the knockdown of Cortactin significantly blocked the actin increase at the spine head and spine base in response to stimulation (Figure 5A-C and S3; Video S6). These data suggest that the reduction of microtubule entries in spines observed after knockdown of Cortactin (Figure 4E and 4F) may result from disturbed actin dynamics at the spine base. To test if microtubule entries in spines correlate with actin dynamics at the base of the spine, we recorded actin dynamics in neuron cultures under baseline conditions. We frequently observed increased actin dynamics at the base of spines that were invaded by microtubules in the analysed time-lapses (Figure 5D and 5E; Video S6). Analysis of the signal intensities for actin and dynamic microtubules confirmed these observations (Figure 5F and 5G). Quantifications of the live-imaging data demonstrated that 77% of the invaded spines exhibit increased actin dynamics at the spine

Figure 4. Actin is important for mediating microtubule entries in spines

A) *Dendrite of a dissociated neuron before and after treatment with jasplakinolide. Neurons were infected with virus co-expressing MT+TIP marker and Lifeact. Top panel shows the projection of the MT+TIP comets, middle panel is a still frame of the Lifeact signal and bottom panel is a projection of the standard deviation of the complete Lifeact time-lapse recording. Note that following jasplakinolide treatment there is a reduction in the number of MT+TIP comets and spine head dynamics but no increase in spine size.*

B) *Effects on spine entry frequency in neuron cultures treated with DMSO (left) or actin targeting drugs jasplakinolide (middle) and latrunculin B (right). Red points represent the mean values of the dataset. ***p<0.001, n.s. = not significant, paired t-test; Jasp.: n = 16, Lat B: n= 14 dendrites.*

C) *Slice culture experiments with either Jasp. (left) or a combination of MCh and Lat B (right). *p< 0.05, paired t-test; Jasp.: n = 9, MCh+Lat B: n = 12 dendrites.*

D) *Neuron cultures coinfected with EB3 shRNA virus and either the full-length GFP-EB3-rescue or GFP-EB3-CΔAC virus. Not significant, unpaired t-test; EB3-rescue: n = 21, EB3-CΔAC: n = 22 dendrites.*

E) *Representative examples of dendritic morphology after lentivirus-mediated depletion of indicated target proteins in cultured neurons. Neurons were coinfected with virus expressing indicated shRNAs and virus expressing mTagRFP and the MT+TIP marker.*

F) *Quantification of microtubule invasion frequencies in knockdown conditions. ***p<0.001, one-way ANOVA with posthoc Dunnett's test; scrambled: n = 45, Drebrin: n = 21, MACF2: n = 7, Cortactin: n = 20, MARCKS: n = 15, Myosin IIb: n = 17 dendrites.*

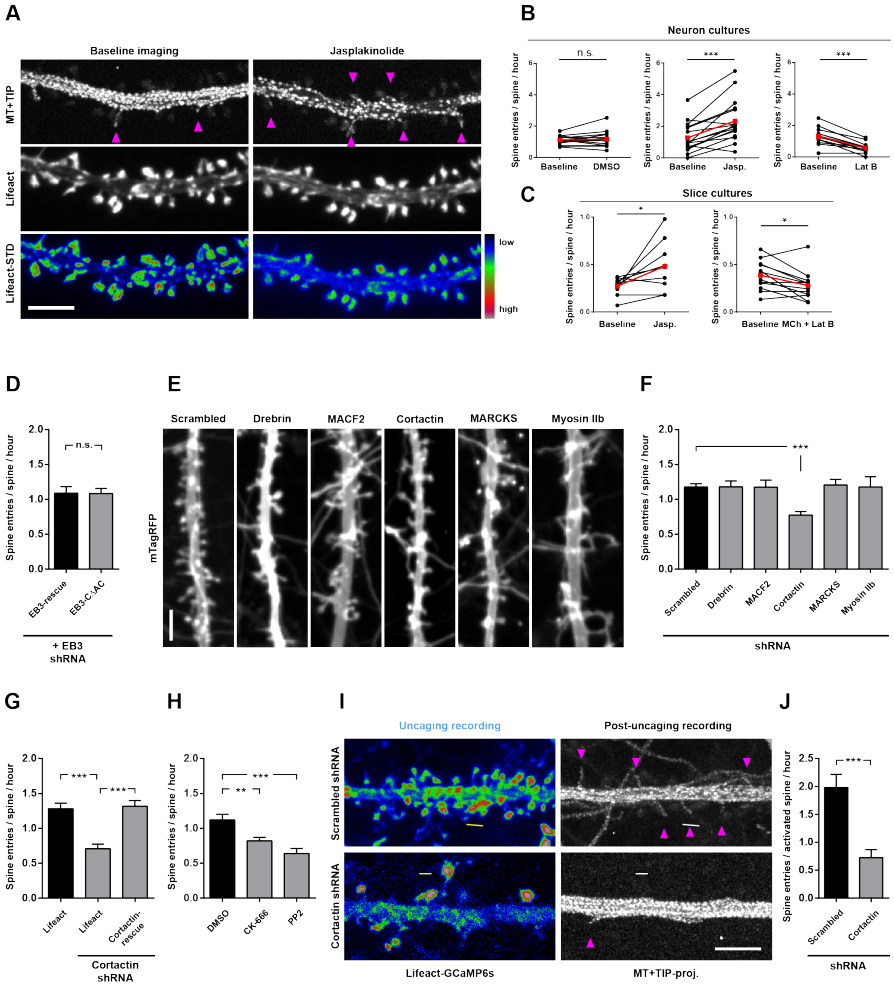

G) *Quantification of MT+TIP spine entries in baseline, Cortactin-knockdown or Cortactin-rescue conditions. Neurons were depleted for endogenous Cortactin with lentivirus and spines identified based on the Lifeact or the shRNA-resistant Cortactin signals. ***p < 0.0001, one-way ANOVA with posthoc Tukey's test; Lifeact: n = 17, Lifeact+shRNA: n = 13, Cortactin-rescue+shRNA: n = 14 dendrites.*

H) *Quantification of MT+TIP spine entries in control conditions (DMSO), with Arp2/3 complex inhibitory drug CK-666, and Src inhibitory drug PP2. **p<0.01, ***p<0.001, one-way ANOVA with posthoc Dunnett's test; DMSO: n = 14, CK-666: n =18, PP2: n = 15 dendrites.*

I) *Glutamate uncaging experiment in control (upper) and Cortactin-knockdown (lower) neuron cultures. Neuron cultures were coinfected with the Cortactin-shRNA virus and virus expressing the MT+TIP marker and Lifeact-GCaMP6s. Left panel shows a sum projection of the Lifeact-GCaMP6s signal recorded during the glutamate uncaging protocol (yellow/white line marks uncaging region). The majority of spines within the field of view were activated because of a slightly stronger uncaging stimulation as in previous experiments (same color coding as in A. Right panel shows a projection of MT+TIP comets acquired after the uncaging session. Magenta arrowheads indicate microtubule entries in spines.*

J) *Spine entry frequency after uncaging of glutamate for control and Cortactin knockdown neurons. ***p<0.0001, unpaired t-test; scrambled: n = 15, Cortactin: n = 16 dendrites.*

Scale bars, 5 µm. Bars diagrams show mean + s.e.m. See also Figure S1 and S2; Video S4 and S5.

base (Figure 5H). Using the same quantification criteria, we found that 40% of all spines showed actin dynamics at the spine base (Figure 5I). By combining both quantifications, we found a significant association between microtubule entries and actin dynamics at the spine base (*p<0.001, Fisher's exact test).

Consistent with the live-imaging data, single molecule reconstructions of endogenous actin, using purified Lifeact, revealed actin structures and cables at the base of a subset of spines [32, 33] (Figure 6A). These structures could also be observed with dSTORM imaging of labelled Lifeact-Myc after expression in neuronal cultures (Figure S4A). To further investigate if Cortactin can potentially influence actin dynamics by directly localizing to the spine base, two color super resolution was performed. This revealed that expressed Cortactin frequently colocalizes with the observed actin structures at the spine base and in the spine head (Figure 6B and S4B). Together, our results suggest that increasing the dynamics and remodeling of a specialized actin organization at the base of the spine enables microtubule entry into spines.

DISCUSSION

Here we have identified a mechanism by which synaptic activity locally regulates microtubule entry into spines. We found that microtubule-spine entry is regulated by NMDA receptor activation and calcium influx and that actin remodeling is directly involved in microtubule entry. Our data demonstrate that structural changes in the actin cytoskeleton at the base of the spine allows for microtubule entry.

Figure 5. Actin dynamics at the spine base

A) *Glutamate uncaging in neuron cultures expressing virus delivered Lifeact and either scrambled or Cortactin shRNAs. First two columns show still frames before and after uncaging and the yellow line indicates uncaging region. Next, subtraction of the pre- from the post-uncaging Lifeact signals to visualize the increases in fluorescence intensity. Right column is a projection of the Lifeact signal s.d. over the full 5 min recording to visualize hot spots of actin dynamics. Arrowheads point to the same position at the base of the spine. Scale bar, 1 μm. Full length recordings of these and additional examples are shown in Video S6.*

B) *Quantification of Lifeact average intensities at the spine head in response to glutamate uncaging. Relative signals for activated spines in control or Cortactin knockdown conditions and non-activated spines in control conditions are plotted over time. Data points represent mean ± s.e.m.; ***p<0.001, two-way ANOVA with posthoc Bonferroni test; scrambled activated: n = 20 spines, Cortactin activated: n = 19 spines, scrambled non-activated: n = 22 spines. Spines from each condition were imaged from ≥ 15 dendrites of two independent cultures.*

C) *Same dataset representation as in B showing quantified intensities for the corresponding spine bases. *p<0.05, two-way ANOVA with posthoc Bonferroni test*

D) *Still frames of two example neurons expressing MT+TIP and Lifeact. The moment of spine entries are indicated by a cyan arrow in the upper rows. Arrowheads indicate actin dynamics at the spine base. Note that time intervals change within the panel as indicated. Full time-lapse recordings of both examples can be found in Video S6.*

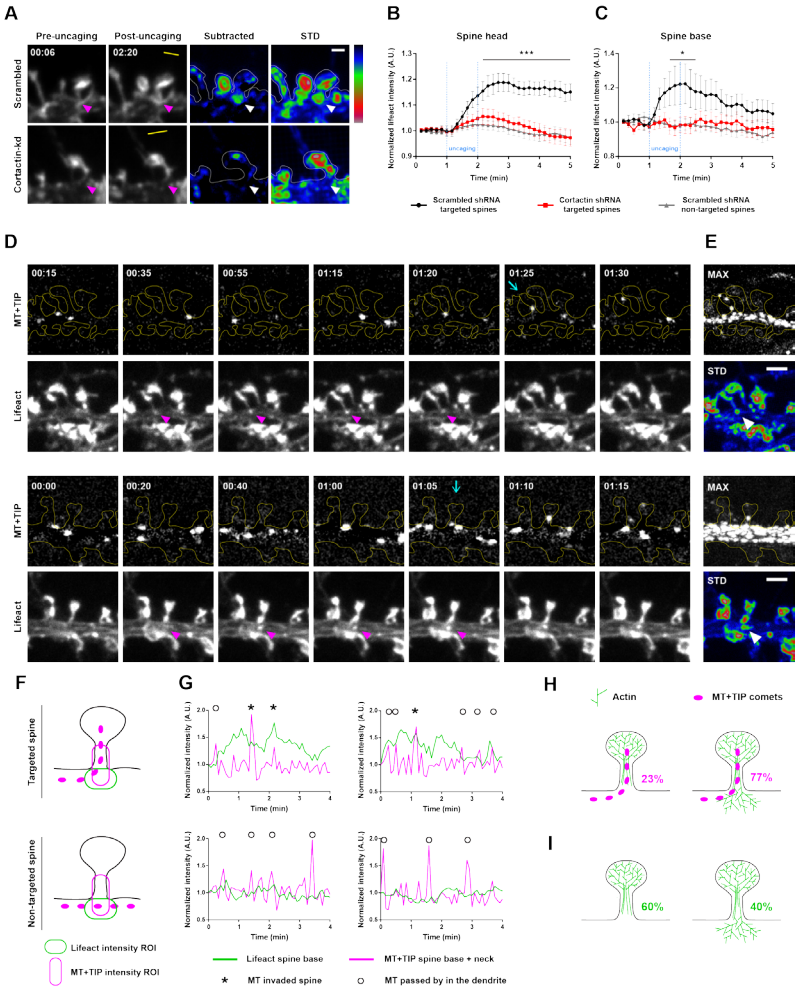

E) *Maximum projection of the MT+TIP channel (upper) and a projection of the s. d. of the Lifeact signal to highlight actin dynamics (bottom). Scale bar, 2 µm.*
F) *Schematic representation of the regions of interest (ROIs) used in the quantification of actin and MT+TIP comets signals (left).*
G) *Measurements of actin and MT+TIP signals of two targeted (examples from D) and two non-targeted spines. Curves represent the mean signal intensities measured in the ROIs at the spine base or spine base and neck. Asterisks indicate microtubules entering spines, while circles depict comets that passed by in the shaft.*
H) *Manual quantification of actin dynamics in spines targeted by microtubules. Correlation was considered positive when actin dynamics at the spine base coincide in a window of 1 min before the microtubule enters the spine. In 21 dendrites we analyzed 43 invaded spines of which 33 showed actin dynamics at the spine base.*
I) *The same dendrites were classified for actin dynamics independent of microtubule invasions. All spines were analyzed for actin dynamics at the spine base within the same 1 min time window as in the previous analysis. Spines: n = 217 positive and n=323 negative for actin dynamics. See also Figure S3.*

Microtubule spine entry is triggered by activation of NMDA receptor and calcium influx

We used a lentivirus-based inducible expression system of fluorescently labeled microtubule plus-ends combined with fast live cell imaging to examine microtubule entry in dendritic spines in mature neurons in dissociated cultures and in organotypic hippocampal slices. Our findings demonstrate that microtubule entry into spines not only occurs in a transient episode during neuronal development, but that it is very common and perhaps even the default pathway for terminating dendritic microtubule growth in adult neurons. We found that at least 40% of the microtubule catastrophes is directly associated with entries in spines under baseline conditions. Anterograde or retrograde growing microtubules did not show differences in spine entry probabilities, indicating that the polarity of microtubules in dendrites is not a determinant factor for the targeting of dendritic spines. Previous studies in dissociated neurons suggest a regulatory effect of synaptic activity on microtubule spine entry [6, 7, 14]. To investigate whether synaptic activity correlates with microtubule spine entry at the level of individual spines, we applied pharmacological treatments that modulate the pattern of synaptic activation in hippocampal slice cultures and analyzed microtubule dynamics in spines. We found that microtubule spine entry frequency was strongly increased following cLTP protocols which increase intracellular calcium levels. In addition, using glutamate uncaging in neuron cultures we showed direct evidence for a coupling between NMDA-dependent synaptic activation and increased microtubule targeting on the level of single spines. Together, these data indicate that dynamic microtubules preferentially target dendritic spines that have recently experienced NMDAR-mediated calcium increase.

Local actin remodeling links synaptic activity and microtubule spine entry

Calcium influx through NMDA receptors has been shown to alter the actin dynamics within dendritic spines [20]. Previous findings suggested that the microtubule plus-end binding protein EB3 through the interaction of microtubule actin-associated protein Drebrin is involved in dendritic spine entries [14]. These conclusions are largely based on Drebrin overexpression experiments, where increased levels of Drebrin promote microtubule invasion frequency and the number of spines invaded by microtubules [14]. Super resolution microscopy imaging revealed that actin filaments at the spine base extend throughout the dendritic shaft. Consistent with microtubule-actin cooperation in various other cellular processes [34], it is possible that the actin filaments directly guide the entry of microtubules in dendritic spines. Our data also indicate that EB3 knockdown can be rescued by an EB3 construct lacking the C-terminal SxIP binding site. These results indicate that SxIP-mediated interactions between microtubule plus-ends and components of the actin cytoskeleton are not required for microtubule spine targeting. Therefore, we propose a model in which structural changes in the actin cytoskeleton at the base of the spine are through steric interactions, rather than specific protein-protein interactions involved with microtubule entry (Figure 6C). In this way, activity-dependent remodeling of the actin cytoskeleton at the base of the spine may

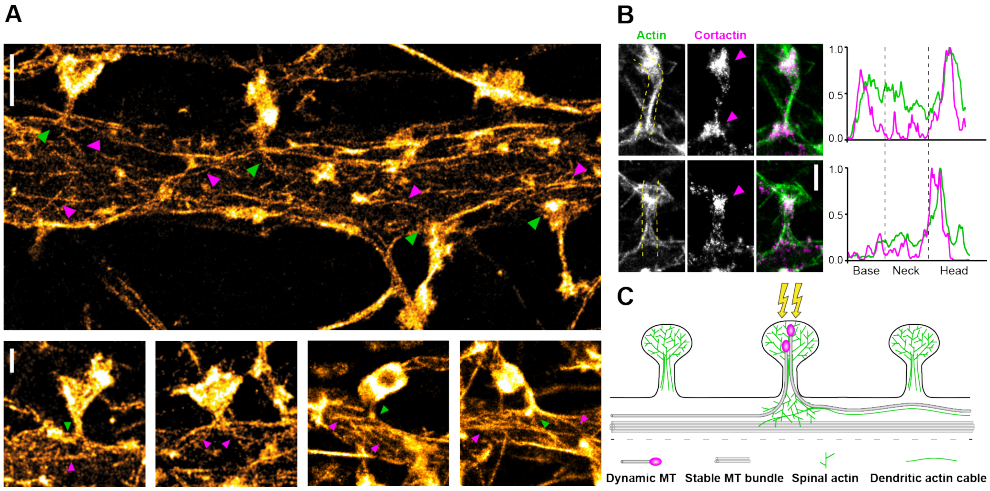

Figure 6. Super-resolution imaging of actin in dendrites
A) *Untreated neuron cultures were fixed and imaged through transient binding of purified Lifeact-GFP or Lifeact-mNeonGreen. Regions of interest were identified through sparse labelling with Phalloidin 568. Top panel shows a super-resolved reconstruction of the dendritic shaft and spines. Bottom panels show more examples of actin structures in individual spines. Green arrowheads indicate examples of actin structures at the spine base; Magenta arrowheads indicate actin cables.*
Scale bar: overview 1 µm, zooms 0.5 µm
B) *2-color super-resolution images of actin and cortactin in spines of DIV18+ neurons transfected with Cortactin-dsRed. Magenta arrowheads indicate cortactin in the spine head or at the base. Corresponding linescans along both structures are shown for the area indicated in the middle panel. Scale bar: 0.5 µm*
C) *Model illustrating potential mechanisms of microtubule entries in spines. Dynamic microtubules can interact with bundles of stable microtubules and/or dendritic actin cables. Synaptic stimulation enhances actin structures at the base of the spine, thereby connecting to stable microtubules and/or actin cables and leading to increased chances of microtubule targeting. See also Figure S4.*

allow for regulated microtubule targeting. Obviously, actin-binding proteins remodeling the actin cytoskeleton are indirectly involved. An increase in actin dynamics at the spine base has also been observed using glutamate uncaging combined with actin photoactivation [35]. In approximately half of the stimulated spines, an outflow of actin and release of actin filaments from the spine head into the dendritic shaft was observed [35]. These data are consistent with an activity-dependent redistribution of Cortactin [24, 29, 30] and the interpretation that local actin remodelling facilitates microtubule spine entries. Together our data show that dynamic microtubules preferentially target spines that are undergoing actin reorganization in an activity-regulated manner.

ACKNOWLEDGEMENT

P.S. was supported by postdoctoral fellowships from the Marie-Curie Program (grant 326425)

and the Swiss National Science Foundation (PBZHP3_147307). M.E.d.S. is supported by Fundação para a Ciência e Tecnologia (FCT, Portugal; grant SFRH/BD/68642/2010). This work was further supported by the Netherlands Organization for Scientific Research (NWO-ALW-VICI, CCH; NWO ZonMW-VIDI, CJW and HYH), the Netherlands Organization for Health Research and Development (ZonMW-TOP, CCH), the European Research Council (ERC) (ERC-consolidator, CCH).

AUTHOR CONTRIBUTIONS

P.S. designed and performed the live cell imaging experiments and analyzed the data; M.E.d.S. performed lentiviral transduction of neuronal cultures and live cell imaging experiments; R.P.T purified Lifeact-GFP and Lifeact-mNeonGreen and performed super resolution of actin structures in the dendrites; E.A.K wrote automated comet analysis routine; H.Y.H. assisted with the uncaging experiments; C.J.W. and L.C.K. provided critical input for experimental design and data analysis; P.S. and C.C.H wrote the manuscript with comments by all other authors. C.C.H. supervised the project and coordinated the study.

REFERENCES

1. Kapitein, L.C., and Hoogenraad, C.C. (2015). Building the Neuronal Microtubule Cytoskeleton. Neuron *87*, 492-506.
2. Stepanova, T., Slemmer, J., Hoogenraad, C.C., Lansbergen, G., Dortland, B., De Zeeuw, C.I., Grosveld, F., van Cappellen, G., Akhmanova, A., and Galjart, N. (2003). Visualization of microtubule growth in cultured neurons via the use of EB3-GFP (end-binding protein 3-green fluorescent protein). J Neurosci *23*, 2655-2664.
3. Yau, K.W., Schatzle, P., Tortosa, E., Pages, S., Holtmaat, A., Kapitein, L.C., and Hoogenraad, C.C. (2016). Dendrites In Vitro and In Vivo Contain Microtubules of Opposite Polarity and Axon Formation Correlates with Uniform Plus-End-Out Microtubule Orientation. J Neurosci *36*, 1071-1085.
4. Jaworski, J., Kapitein, L.C., Gouveia, S.M., Dortland, B.R., Wulf, P.S., Grigoriev, I., Camera, P., Spangler, S.A., Di Stefano, P., Demmers, J., et al. (2009). Dynamic microtubules regulate dendritic spine morphology and synaptic plasticity. Neuron *61*, 85-100.
5. Hu, X., Viesselmann, C., Nam, S., Merriam, E., and Dent, E.W. (2008). Activity-dependent dynamic microtubule invasion of dendritic spines. The Journal of neuroscience : the official journal of the Society for Neuroscience *28*, 13094-13105.
6. Merriam, E.B., Lumbard, D.C., Viesselmann, C., Ballweg, J., Stevenson, M., Pietila, L., Hu, X., and Dent, E.W. (2011). Dynamic microtubules promote synaptic NMDA receptor-dependent spine enlargement. PLoS One *6*, e27688.
7. Kapitein, L.C., Yau, K.W., Gouveia, S.M., van der Zwan, W.A., Wulf, P.S., Keijzer, N., Demmers, J., Jaworski, J., Akhmanova, A., and Hoogenraad, C.C. (2011). NMDA receptor activation suppresses microtubule growth and spine entry. J Neurosci *31*, 8194-8209.
8. Esteves da Silva, M., Adrian, M., Schatzle, P., Lipka, J., Watanabe, T., Cho, S., Futai, K., Wierenga, C.J., Kapitein, L.C., and Hoogenraad, C.C. (2015). Positioning of AMPA Receptor-Containing Endosomes Regulates Synapse Architecture. Cell reports *13*, 933-943.
9. Correia, S.S., Bassani, S., Brown, T.C., Lise, M.F., Backos, D.S., El-Husseini, A., Passafaro, M., and Esteban, J.A. (2008). Motor protein-dependent transport of AMPA receptors into spines

during long-term potentiation. Nature neuroscience *11*, 457-466.
10. Wang, Z., Edwards, J.G., Riley, N., Provance, D.W., Jr., Karcher, R., Li, X.D., Davison, I.G., Ikebe, M., Mercer, J.A., Kauer, J.A., et al. (2008). Myosin Vb mobilizes recycling endosomes and AMPA receptors for postsynaptic plasticity. Cell *135*, 535-548.
11. Wagner, W., Brenowitz, S.D., and Hammer, J.A., 3rd (2011). Myosin-Va transports the endoplasmic reticulum into the dendritic spines of Purkinje neurons. Nature cell biology *13*, 40-48.
12. McVicker, D.P., Awe, A.M., Richters, K.E., Wilson, R.L., Cowdrey, D.A., Hu, X., Chapman, E.R., and Dent, E.W. (2016). Transport of a kinesin-cargo pair along microtubules into dendritic spines undergoing synaptic plasticity. Nature communications *7*, 12741.
13. Hu, X., Ballo, L., Pietila, L., Viesselmann, C., Ballweg, J., Lumbard, D., Stevenson, M., Merriam, E., and Dent, E.W. (2011). BDNF-induced increase of PSD-95 in dendritic spines requires dynamic microtubule invasions. The Journal of neuroscience : the official journal of the Society for Neuroscience *31*, 15597-15603.
14. Merriam, E.B., Millette, M., Lumbard, D.C., Saengsawang, W., Fothergill, T., Hu, X., Ferhat, L., and Dent, E.W. (2013). Synaptic regulation of microtubule dynamics in dendritic spines by calcium, F-actin, and drebrin. J Neurosci *33*, 16471-16482.
15. Akhmanova, A., and Steinmetz, M.O. (2008). Tracking the ends: a dynamic protein network controls the fate of microtubule tips. Nat Rev Mol Cell Biol *9*, 309-322.
16. De Roo, M., Klauser, P., and Muller, D. (2008). LTP promotes a selective long-term stabilization and clustering of dendritic spines. PLoS Biol *6*, e219.
17. Fernandez de Sevilla, D., Nunez, A., Borde, M., Malinow, R., and Buno, W. (2008). Cholinergic-mediated IP3-receptor activation induces long-lasting synaptic enhancement in CA1 pyramidal neurons. J Neurosci *28*, 1469-1478.
18. Matsuzaki, M., Honkura, N., Ellis-Davies, G.C., and Kasai, H. (2004). Structural basis of long-term potentiation in single dendritic spines. Nature *429*, 761-766.
19. Ross, W.N. (2012). Understanding calcium waves and sparks in central neurons. Nat Rev Neurosci *13*, 157-168.
20. Hotulainen, P., and Hoogenraad, C.C. (2010). Actin in dendritic spines: connecting dynamics to function. The Journal of cell biology *189*, 619-629.
21. Fischer, M., Kaech, S., Knutti, D., and Matus, A. (1998). Rapid actin-based plasticity in dendritic spines. Neuron *20*, 847-854.
22. Holbro, N., Grunditz, A., and Oertner, T.G. (2009). Differential distribution of endoplasmic reticulum controls metabotropic signaling and plasticity at hippocampal synapses. Proc Natl Acad Sci U S A *106*, 15055-15060.
23. Grigoriev, I., Gouveia, S.M., van der Vaart, B., Demmers, J., Smyth, J.T., Honnappa, S., Splinter, D., Steinmetz, M.O., Putney, J.W., Jr., Hoogenraad, C.C., et al. (2008). STIM1 is a MT-plus-end-tracking protein involved in remodeling of the ER. Curr Biol *18*, 177-182.
24. Hering, H., and Sheng, M. (2003). Activity-dependent redistribution and essential role of cortactin in dendritic spine morphogenesis. J Neurosci *23*, 11759-11769.
25. Calabrese, B., and Halpain, S. (2005). Essential role for the PKC target MARCKS in maintaining dendritic spine morphology. Neuron *48*, 77-90.
26. Rex, C.S., Gavin, C.F., Rubio, M.D., Kramar, E.A., Chen, L.Y., Jia, Y., Huganir, R.L., Muzyczka, N., Gall, C.M., Miller, C.A., et al. (2010). Myosin IIb regulates actin dynamics during synaptic plasticity and memory formation. Neuron *67*, 603-617.
27. Geraldo, S., Khanzada, U.K., Parsons, M., Chilton, J.K., and Gordon-Weeks, P.R. (2008). Targeting of the F-actin-binding protein drebrin by the microtubule plus-tip protein EB3 is required for neuritogenesis. Nature cell biology *10*, 1181-1189.
28. Leung, C.L., Sun, D., Zheng, M., Knowles, D.R., and Liem, R.K. (1999). Microtubule actin cross-linking factor (MACF): a hybrid of dystonin and dystrophin that can interact with the actin and microtubule cytoskeletons. J Cell Biol *147*, 1275-1286.

29. Iki, J., Inoue, A., Bito, H., and Okabe, S. (2005). Bi-directional regulation of postsynaptic cortactin distribution by BDNF and NMDA receptor activity. Eur J Neurosci *22*, 2985-2994.
30. Seese, R.R., Babayan, A.H., Katz, A.M., Cox, C.D., Lauterborn, J.C., Lynch, G., and Gall, C.M. (2012). LTP induction translocates cortactin at distant synapses in wild-type but not Fmr1 knock-out mice. J Neurosci *32*, 7403-7413.
31. Korobova, F., and Svitkina, T. (2010). Molecular architecture of synaptic actin cytoskeleton in hippocampal neurons reveals a mechanism of dendritic spine morphogenesis. Mol Biol Cell *21*, 165-176.
32. Kiuchi, T., Higuchi, M., Takamura, A., Maruoka, M., and Watanabe, N. (2015). Multitarget super-resolution microscopy with high-density labeling by exchangeable probes. Nature methods *12*, 743-746.
33. Tas, R.P., Bos, T., and Kapitein, L.C. (2018). Purification and Application of a Small Actin Probe for Single-Molecule Localization Microscopy. Methods Mol Biol *1665*, 155-171.
34. Rodriguez, O.C., Schaefer, A.W., Mandato, C.A., Forscher, P., Bement, W.M., and Waterman-Storer, C.M. (2003). Conserved microtubule-actin interactions in cell movement and morphogenesis. Nature cell biology *5*, 599-609.
35. Honkura, N., Matsuzaki, M., Noguchi, J., Ellis-Davies, G.C., and Kasai, H. (2008). The subspine organization of actin fibers regulates the structure and plasticity of dendritic spines. Neuron *57*, 719-729.
36. Schatzle, P., Kapitein, L.C., and Hoogenraad, C.C. (2016). Live imaging of microtubule dynamics in organotypic hippocampal slice cultures. Methods Cell Biol *131*, 107-126.
37. Riedl, J., Crevenna, A.H., Kessenbrock, K., Yu, J.H., Neukirchen, D., Bista, M., Bradke, F., Jenne, D., Holak, T.A., Werb, Z., et al. (2008). Lifeact: a versatile marker to visualize F-actin. Nat Methods *5*, 605-607.
38. MacGillavry, H.D., Kerr, J.M., Kassner, J., Frost, N.A., and Blanpied, T.A. (2016). Shank-cortactin interactions control actin dynamics to maintain flexibility of neuronal spines and synapses. Eur J Neurosci *43*, 179-193.
39. Szymczak-Workman, A.L., Vignali, K.M., and Vignali, D.A. (2012). Design and construction of 2A peptide-linked multicistronic vectors. Cold Spring Harb Protoc *2012*, 199-204.
40. Komarova, Y., Lansbergen, G., Galjart, N., Grosveld, F., Borisy, G.G., and Akhmanova, A. (2005). EB1 and EB3 control CLIP dissociation from the ends of growing microtubules. Mol Biol Cell *16*, 5334-5345.
41. Yau, K.W., van Beuningen, S.F., Cunha-Ferreira, I., Cloin, B.M., van Battum, E.Y., Will, L., Schatzle, P., Tas, R.P., van Krugten, J., Katrukha, E.A., et al. (2014). Microtubule minus-end binding protein CAMSAP2 controls axon specification and dendrite development. Neuron *82*, 1058-1073.
42. van Beuningen, S.F., Will, L., Harterink, M., Chazeau, A., van Battum, E.Y., Frias, C.P., Franker, M.A., Katrukha, E.A., Stucchi, R., Vocking, K., et al. (2015). TRIM46 Controls Neuronal Polarity and Axon Specification by Driving the Formation of Parallel Microtubule Arrays. Neuron *88*, 1208-1226.
43. Mikhaylova, M., Cloin, B.M., Finan, K., van den Berg, R., Teeuw, J., Kijanka, M.M., Sokolowski, M., Katrukha, E.A., Maidorn, M., Opazo, F., et al. (2015). Resolving bundled microtubules using anti-tubulin nanobodies. Nat Commun *6*, 7933.

SUPLEMENTAL EXPERIMENTAL PROCEDURES

Animals

All experiments were approved by the DEC (Dutch Experimental Review Committee),

performed in line with institutional guidelines of the University Utrecht and were conducted in agreement with Dutch law (Wet op de Dierproeven, 1996) and European regulations (Guideline 86/609/EEC). Female pregnant Wistar rats were delivered from Janvier, aged at least 10 weeks at the time of delivery. Female pregnant C57BL/6 mice were delivered from Janvier, aged at least 15 weeks at the time of delivery. Upon delivery, animals were kept at SPF facilities in a controlled 12 h light-dark cycle with a temperature of 22±1°C and given access to food pellets and water *ad libitum*. The animals were housed in small groups in transparent plexiglass cages with wood-chip bedding and paper tissue for nest building.

Primary neuron culture and viral transduction/transfection

Hippocampal neuron cultures were prepared from embryonic day 18 rat brains [3] (Wistar, both genders). Cells were plated on coverslips coated with poly-L-lysine (37.5 mg/mL) and laminin (1.25 mg/mL) at a density of 100,000/well and cultured at 37°C in 5% CO_2. Cultures were fed weekly by replacing 1/3 of the medium with fresh Neurobasal medium (NB) supplemented with 2% B27, 0.5 mM glutamine, and 1% penicillin/streptomycin. Experiments were performed with mature rat neuron cultures ranging from DIV 25-45, except for the analysis of spine entry frequencies in DIV18 neurons. Lentiviral infections were carried out 8-14 days before experiments. Inducible expression systems were triggered 2-4 days prior imaging by application of 500 ng/mL doxycycline. All infections with shRNA containing virus were carried out 8-9 days before experiments. Dendrites in knockdown experiments were routinely checked for clear mEBFP2 signals, confirming the infection with shRNA virus, before starting the actual experiments. Transfections were only applied for Video S4. Briefly, 0.9 µg GW2_Lifeact-GFP and 0.9 µg βactin_Cortactin-dsRed-exp vector were mixed with 3.3 µl Lipofectamine 2000 (Invitrogen) and incubated for 30 min. The mixture was added to coverslips placed in fresh NB and incubated for 45 min. Finally, neurons were washed in NB and translocated back into the original culture medium.

Primary tissue culture

Hippocampal organotypic interface slice cultures were generated from P5-6 mice pups (C57BL/6, both genders). Dissected hippocampi were cut in 350 µm sections and positioned on FHLC membrane patches (Millipore, FHLC01300) laying on Millicell culture inserts (Millipore, PICM0RG50). Viral infection was carried out within 2 hours after platting. Slices were fed every 2-3 days with culture medium containing 47.75% MEM, 25% HBSS, 25% horse serum, 1.25% 1M HEPES, 1% 3M D-glucose, pH 7.2 and osmolality of 310-320 mOsm. Detailed information about slice preparation and viral transduction has been published recently [36]. Experiments were made with slices kept for 2-4 weeks in culture.

DNA plasmids and lentivirus

Fluorescently tagged constructs were generated for subsequent subcloning in a bicistronic

expression cassette. Membrane-targeted TagRFP-T (mTagRFP, generated from N-terminal first 41 amino acids of MARCKS) and the microtubule plus-tip marker (MT+TIP) GFP-MACF18 have been described previously [36]. Tomato-MACF18 is identical to GFP-MAC18 except for the replacement of GFP by tandem dimer Tomato (also called MT+TIP). Lifeact-TagRFP-Myc was PCR generated by cloning the 17 amino acid (aa) Lifeact sequence [37] linked by a 7 aa linker (GDPPVAT) to the N-terminus of TagRFP-T (Evrogen). The TagRFP-T stop codon was replaced by a 4 aa linker (SSGS) followed by the 10 aa Myc sequence. Lifeact-GCaMP6s was based on the pGP-CMV-GCaMP6s (addgene #40753) vector. The start codon within this construct was replaced by the Lifeact sequence by a PCR based strategy. The TagRFP-ER construct is composed of the 17 amino acid rat calreticulin signal sequence fused to the N-term of TagRFP-T and a C-terminally located ER retention signal (KDEL). GFP-EB3-ΔAc and GFP-EB3-rescue constructs are identical to our previous publication [4]. Membrane-targeted EBFP2-HA was generated with a cryptic splice site corrected version of EBFP2 containing a C-terminal HA-tag. Cortactin-dsRed [38] was made shRNA resistant by introducing silent mutations in the target sequence using a PCR based strategy (GCATTGCTCTCAGGTGGAT).

Lifeact-GFP for super-resolution microscopy was generated using a bacteria codon optimized Lifeact fragment that was N-terminally inserted by PCR into a pET28a vector containing an EcoRI/XhoI flanked GFP or mNeonGreen sequence. The full vector was amplified with the LifeAct fragment and the template was digested with DPN1. The resulting construct was transformed into competent bacteria and sequenced.

Bicistronic expression constructs were generated based on the attenuated IRES site, derived from pIRES (Clonetech). This design allows high expression of the coding sequence upstream of the IRES site and relative low expression of the inserted downstream construct. The following plasmids were generated by conventional cloning strategies: mTagRFP_IRES_GFP-MACF18, mTagRFP_IRES_GFP-EB3-rescue, mTagRFP_IRES_GFP-EB3-ΔAc, Lifeact-TagRFP-Myc_IRES_GFP-MACF18, Lifeact-GCaMP6s_IRES_Tomato-MACF18, TagRFP-ER_IRES_GFP-MACF18, Cortactin-dsRed_IRES_GFP-MACF18. Equal expression of two constructs was achieved in the mEBFP2-HA_P2A_Myc-MyoVa-tail construct by using the 2A sequence of the porcine teschovirus-1 [39].

Lentiviral transfer vectors are based on the pSIN-TRE-MCS-Synapsin-rtTA2 plasmid [36]. The bicistronic expression cassettes described above were subcloned in the multiple cloning site resulting in a TET-On inducible expression of the target proteins. Full sequence information of all constructs can be provided on request.

RNAi-induced knockdown of target genes by lentivirus was based on a modified pLVTHM (addgene #12247) transfer vector, named pLVTHPS-mEBFP2-HA_shRNA. The original EF-1α promotor and GFP sequences were replaced by a central polypurine tract/central termination sequence (cPPT/CTS), followed by a short 0.5kb Synapsin promoter and mEBFP2-HA. Individual shRNA sequences were subcloned from the original pSuper

vectors via BamHI and ClaI sites. Following shRNA target sequences were used: scrambled GGTTTATATCGCGGTTATT, Cortactin GCACTGCTCACAAGTGGAC [24], Drebrin GAGAACCAGAAAGTGATGTAC[27]e></EndNote>,EB3 ACTATGATGGAAAGGATTAC [40], MACF2 GCCGTGGTCAGAGTTGCTGAT , MARCKS CTGTACCAGTCAGTAATTA [25], Myosin IIb GATCAAAGTTGGCCGAGAT [26].
Lentiviral particles were generated by transfecting the transfer plasmid together with the packaging plasmids p.MDG2 (addgene #12259) and psPAX2 (addgene #12260) in HEK293T cells. The supernatant was collected two days after transfection and concentrated using tangential flow filtration (Amicon Ultra spin filters, Millipore #UFC910024). Detailed information about the lentivirus production has been described elsewhere [36].

LifeAct-GFP purification

LifeAct-GFP-6xHis was purified using standard His-tag purification methods. *E. coli* BL21DE3 were induced at OD 0.6 for overnight expression at 20 degrees. After pelleting the cells were lysed through sonication in the presence of lysozyme and a protease inhibitor cocktail (Roche). The soluble fraction was filtered and bound to a His-Trap HP 1 mL column (GE healthcare). Elution was performed on an AKTAxpress (GE healthcare). After buffer exchange to PBS the pure protein sample was frozen in 10% glycerol.

Pharmacological treatments

The 1st control imaging session in neuron cultures was performed in the original culture medium. Jasplakinolide (10 µM) or latrunculin B (1 µM) were diluted in 100 µL preconditioned culture medium, transferred into the recording chamber and incubated for 30 min before the 2nd recording session was started. For Cortactin inhibition experiments, neurons were preincubated in either DMSO (1:1000) for 30 min or 3 hours, CK-666 (100 µM) for 30 min, or PP2 (25 µM) for 3 hours. Next, neurons were transferred to the recording chamber and imaged in the presence of the drug.
The 1st control recordings of organotypic slice cultures were acquired in ACSF composed of 126 mM NaCl, 3 mM KCl, 2.5 mM $CaCl_2$, 1.3 mM $MgCl_2$, 1.25 mM Na_2HPO_4, 26 mM $NaHCO_3$, 20 mM glucose, and 1 mM Trolox (Sigma, 238813). For slice experiments, all drugs were diluted in ACSF and applied as continuous perfusion of the imaging chamber using a peristaltic pump. Following application pattern have been used. Control application: 0.1% DMSO incubated for 30min before start of 2nd recording session; TTX: 1 µM tetrodotoxin incubated for 30 min before 2nd recording; PTX: 100 µM picrotoxin incubated for 30 min before 2nd recording; DHPG: 50 µM dihydroxyphenylglycine incubated for 5 min + 5 min washout with ACSF before 2nd recording was started; MCh: 25 µM methacholine incubated for 15 min + 15 min washout before 2nd recording started; MCh + TTX: 10 min preincubation of 1 µM TTX then application of 25 µM MCh & 1 µM TTX incubated for 15 min + 15 min washout => 2nd recording started; MCh + LatB: 15 min preincubation of 10 µM latrunculin

B then application of 25 µM MCh & 10 µM LatB incubated for 15 min + washout in the presence of LatB + 15 min incubation in ACSF => 2nd recording started; Jasp: 10 µM jasplakinolide incubated for 20 min => 2nd recording. Drugs were purchased from Abcam (TTX), Bio-Connect (latrunculin B), Sigma (Methacholine, NMDA), Tocris (APV, CK-666, DHPG, jasplakinolide, MNI-Glutamate, Picrotoxin, PP2).

Live-cell imaging

Spinning-disk confocal microscopy was performed on an inverted Nikon Eclipse Ti with a Perfect Focus System. Glutamate uncaging experiments were imaged with a S Fluor 100×, 0.5–1.3 NA oil, all other neuron cultures with Plan Fluor 40×, 1.3 NA oil-immersion objective; slice cultures with a CFI Apo Lambda S LWD 40×, 1.15 NA water-immersion objective (all Nikon). The Yokogawa spinning disk confocal scanning unit (CSU-X1-A1NeE) is equipped with a triple-band dichroic mirror (z405/488/568trans-pc; Chroma) and a filter wheel (CSU-X1-FW-06P-01; Yokogawa) containing ET-BFP2 (49021), ET-GFP (49002), ET-mCherry (49008) emission filters from Chroma. Excitation is based on Vortran Stradus 405 nm (100 mW), Cobolt Calypso 491 nm (100 mW) and Cobolt Jive 561 nm (100 mW) lasers, photoactivation on a Teem Photonics 355 nm Q-switched pulsed laser. The UV laser light is controlled by the Ilas-2 system (Roper Scientific, France) and is tunable in intensity via an AOTF filter. Images were acquired in sequential mode with a Photometrics Evolve 512 EMCCD camera equipped with an additional 2.0× lens (Edmund Optics) resulting in a final resolution of 66 nm/pixel. Neuron and slice cultures were imaged in the type 1 Ludin chamber (LIS, Switzerland), positioned in a Tokai Hit Stage Top Incubator (INUBG2E-ZILCS), which is mounted on a ASI motorized stage MS-2000-XYZ enabling multi-position imaging. Slice cultures were positioned upside down on an empty coverslip and kept in place by a ring of platinum laying on the edge of the FHLC membrane patch. The camera, lasers and all motorized parts are controlled by MetaMorph software.

Imaging of microtubule entries in spines and actin dynamics was performed with following parameters. Neuron cultures were imaged in full conditioned medium at 37°C and 5% CO_2 with 5 sec intervals and z-stacks of 0.7 µm step sizes (4-7 depending on the z orientation of the dendrite). Slices were recorded with the same settings except for a continuous perfusion with ACSF (oxygenated with 95% O_2, 5% CO_2).

For local NMDA applications, dissociated neurons were silenced with 1 µM TTX for 14-18 hours prior recording. MT+TIP comets were recorded for 4 min at 5 sec intervals and mTagRFP only every 5th frame in the original culture medium. Puff-applications of 10 mM NMDA through a patch pipette were applied for 2x 50 ms (with a 10 sec break) using a Picospritzer III (Parker). The second imaging session was started 1 min after application with the same settings as in the first recording.

Single photon glutamate uncaging of neuron cultures was performed in modified Tyrod's buffer composed of 119 mM NaCl, 5 mM KCl, 2 mM $CaCl_2$, 10 mM HEPES, 10 mM glucose,

1 µM TTX; pH 7.25 and osmolarity of 0.265 mOsm. MNI-glutamate was added in 100 µL buffer to the darkened recording chamber on the microscope stage to a final concentration of 0.5 mM. Uncaging regions were defined as lines with about 2 µm in length and a distance of 1-1.5 µm to the spine head. The stimulation time-lapse recording contained several time points before and after the uncaging session, in which images were taken in 2 sec intervals with 4×0.8 µm z-stacks. The 355 nm uncaging pulse (0.5 Hz for 1 min) lasted for 3-4 ms and preceded the recording of mTagRFP/GCaMP6. The laser power was adjusted to activate around 30% of the imaged spines, except for the uncaging experiments in combination with Cortactin knockdown (Figure 4I and 4J), where a slightly stronger activation stimulus was used. The subsequent imaging of MT+TIP and mTagRFP/GCaMP6 was recorded at 5 sec intervals with the same stack size as before.

We want to point out that successive imaging of different neurons/dendrites on the same coverslip sometimes varied in the cellular response to the uncaging stimulus (based on mTagRFP/GCaMP6 readout). We believe that this most likely represent artefacts of the single-photon uncaging, as for instance light scattering by optical dense structures in the light path. For this reason, suspicious recordings with unusual mTagRFP/GCaMP6 dynamics were excluded from the quantification of microtubule dynamics. The intensity of the uncaging laser is sufficient to bleach mTagRFP signals within a few frames if the uncaging region is directly targeted on the spine head (data not shown). Since we never observed spine bleaching in our uncaging experiments, we conclude together with our control experiments in Figure 3C that the observed morphological changes of spines were not an artifact of light stress. The dependence on NMDA receptor activation was tested by uncaging glutamate in the presence of 150 µM DL-2-amino-5-phosphonopentanoic acid (APV).

Super resolution imaging

For dSTORM imaging of lentiviral infected neurons expressing Lifact-TagRFP-Myc, DIV18+ neurons were fixed with 4% PFA. After fixation cells were washed and permeabilized with 0.25% triton-X in PBS. After 3 washes the samples were blocked for 1 hour at RT in PBS with 2% BSA, 0.2% gelatin, 10mM glycin, 50mM NH_4Cl; pH 7.4. Cells were incubated overnight at 4°C with a combination of two mouse anti-myc primary antibodies (Santa Cruz; 9E10 and Oncogene; AB-1 both diluted 1:400). After three more washes in PBS the cells were incubated with secondary anti-mouse Alexa647 for 1 hour at room temperature and washed 3 more times. Super resolution imaging was performed in buffer optimal for Alexa647 as described before [41, 42].

To perform super resolution of actin by transient binding of diffusing Lifeact-GFP [33] or Lifeact-mNeonGreen, cells were first extracted in 0.35% triton-x and 0.15% glutaraldehyde in CB (10 mM MES, 150 mM NaCl, 5mM $MgCl_2$, 5mM EGTA, 5mM Glucose; pH 6.1) for 1 minute at 37 degrees. Cells were fixed in 4% PFA in CB at 37°C, washed 3 times and blocked in 3% BSA for 30 min. To visualize regions for imaging, cells were mildly stained with Phalloidin

568 (Life Technologies, 1/1000). After 3 thorough washes in PBS cells were mounted in PBS supplemented with low concentrations of Lifeact-GFP or Lifeact-mNeonGreen. In this way, transient single molecule binding could be observed with 60-100 ms exposure time. For 2 color-imaging of actin and cortactin, cells transfected with Cortactin-dsRed were fixed, blocked and stained with anti-RFP (1:400, rabbit, Rockland, 600-401-379) overnight at 4°C. Next, neurons were washed 3x in PBS and stained with secondary anti-rabbit-D2 (Ultivue). After 3 more washes coverslips were mounted and supplemented with Lifeact-mNeonGreen and I2-560 imager strand (Ultivue) so that single molecule binding events could be observed with 60-100 ms exposure. Regions of interest could be identified based on the dsRed signal of cortactin. Images were reconstructed using DoM Utrecht (Detection of Molecules, https://github.com/ekatrukha/DoM_Utrecht) [43].

Image analysis and quantification

Image processing

The four dimensional time-lapse data was reduced in complexity by generating average z-stack projections before additional image processing and quantifications were performed in FIJI. Time-lapse recordings were corrected for *x-y* drifts using the MultiStackReg plugin whenever required. Curved dendrites in Figure 1J, 3D, 3I and Video S2 were straightened because of space limitations or for better illustration using the FIJI "Straighten" plugin.

Quantification of microtubule spine entries

Time-lapse recordings of MT+TIP comets were processed with a moving average subtraction and additional low pass filtering to amplify comet signals [36]. Spine entries were manually identified based on maximum intensity projections of the processed data and visually confirmed in the videos. Spine entry frequency is presented as "Spine entries / spine / hour" in order to compensate for variations in recording time and spine density between dendrites. Multiple targeting of the same spine within short time intervals is often caused by alternating catastrophe and rescue events of the same microtubule. Because we here rather focused on the microtubule targeting mechanism than on the functional consequences for the spines, we counted multiple spine targeting as a single event if the imaging data did not clearly confirm independent microtubules as the source of multiple invasions.

Quantification of MT+TIP comet properties

Kymographs were generated from average subtracted and low pass filtered MT+TIP recordings using the FIJI "KymoResliceWide" plugin. The FIJI "Cell Counter" plugin was used to label the start and end points of individual microtubule traces. All coordinates were exported to Matlab and used to calculate microtubule density, orientation and length. It is important to state that a substantial proportion of microtubule traces crossed the observation limits in space or time. Therefore, our analysis underestimates the actual length of some of the microtubule traces before entering a spine, which should be kept in mind for a correct interpretation of the results presented in Figure 1E and 1H.

Correlation study of spine entries and catastrophes

Time-lapse recordings were processed as in the previous section with the exception that curved dendrites were additionally straightened using the corresponding function in FIJI. All endings of microtubule traces in the kymograph were visually verified in the videos for coincidental spine entries.

Spine size changes following glutamate uncaging

Recordings of mTagRFP were bleach corrected (exponential fit method) and thresholded (percentile method) using corresponding FIJI plugins. ROIs were defined around the heads of activated and distant non-activated spines. Areas corresponding to the spine head sizes were quantified over time using the "Analyze Particles" function. Data was normalized to the average spine size of the first 10 time points representing baseline conditions.

Spine head and base actin quantifications

Mean intensities of the Lifeact signals over time were quantified in manually defined regions of interest (ROI) at the spine base and head. Resulting mean intensities were adjusted for bleaching based on the mean Lifeact signals of the full image over time and then normalized to the first time point in the time-lapse. The graph in Figure 5B and 5C presents averaged signals from 10 sec intervals (5 time points) for a better visual arrangement, while Figure S3C shows the raw data of all quantified ROIs.

Visualization of actin and MT+TIP signals at the spine base/neck

ROIs covering the spine base (Lifeact) or spine base and neck (MT+TIP) of the same spine were defined and mean intensities quantified (scheme in Figure 5F). The same method for bleach correction and normalization was used for both channels as described in the previous section. Peaks in the MT+TIP intensities were rechecked in the time-lapse recordings whether they represent spine entries or passing microtubule comets.

Correlation of actin dynamics at the spine base with MT entries

Moving average subtraction and low pass filtering were applied to the MT+TIP recordings to improve comet signals. Spine entries were identified by the maximum intensity projections of the improved time lapses. Using the MT comets trajectory and the position of the spine head and neck structures, we verified that the recorded z-stack included the presumed position of the spine base within the dendrite. We further excluded dendritic sections with high spine densities that did not allow to clearly identifying the spine base of an individual spine. In combination, this excluded a considerable number of spine targeting events for this analysis. In 21 dendrites we found 43 spines being targeted by microtubules which met the above criteria. Next, we visually inspected the corresponding spine base for increased actin dynamics within a time window of 1 min before the microtubule entered the spine.

As control we analyzed all 540 spines of the 21 dendrites for comparable actin dynamics at the spine base. For each dendrite we choose the time point of a spine invasion and analyzed for 1 min in reverse.

QUANTIFICATION AND STATISTICAL ANALYSIS

Data processing, statistical analysis and diagrams were done in Excel and Prism (GraphPad) software. The assumption of normality was tested with D'Agostino-Pearson omnibus normality test. All statistical details of experiments, including the definitions, exact values of n, and statistical tests performed, can be found in the corresponding figure legends. The experiments were independently repeated three or more times to ensure consistency and reproducibility. No specific strategy for randomization and/or stratification was employed. The studies were blind in data analysis. No samples were excluded from analysis if not stated explicitly in the corresponding analysis section.

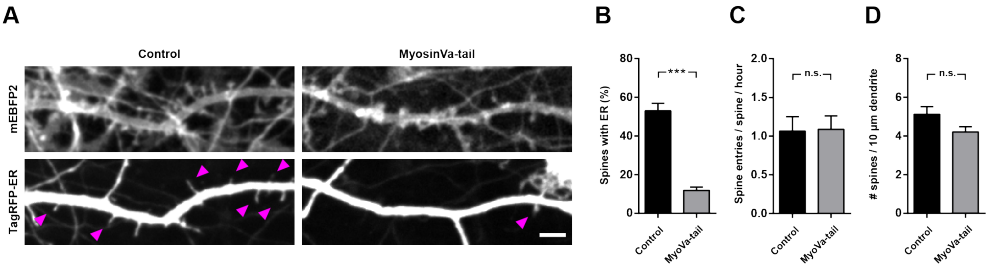

Figure S1. ER structures do not guide microtubules into spines. Related to Figure 4.
A) *Neuron cultures were double infected with virus expressing a TagRFP-ER and MT+TIP, as well as mEBFP2 (control) or mEBFP2 and MyosinVa-tail (dominant negative construct).*
B) *Quantification of ER positive spines for both conditions.*
C) *Spine entry frequencies were quantified based on MT+TIP signals.*
D) *Spine density quantification.*
****p<0.0001 all others not significant, unpaired t-test; control: n = 12, MyosinVa-tail: n = 15 dendrites. Scale bars, 5 µm. Bars diagrams show mean + s.e.m.*

Figure S2. Interfering with actin dynamics. Related to Figure 4.
A) *Kymographs of MT+TIP comets recorded before and after jasplakinolide treatment in neuron cultures.*
B) *Quantification of absolute MT+TIP comets number in the same dendrite section before and after jasplakinolide treatment, n.s. = not significant, paired t-test.*
C) *Relative MT+TIP comet density per 10 µm dendrite quantified from the same dataset as in B. Red points represent the mean values of the dataset.***p<0.0001 paired t-test.*
D) *Spine entry frequencies after depletion of candidate proteins potentially mediating microtubule invasions in spines. Each data point shows the spine entries for an individual recorded dendrite. Average values for each condition are identical to the bar diagram shown in Fig 4F.*
E) *Effects of the depletion of actin interactors on spine density. *p<0.05, **p<0.01, ***p<0.001, n.s. = not significant, one-way ANOVA with posthoc Dunnett's test.*

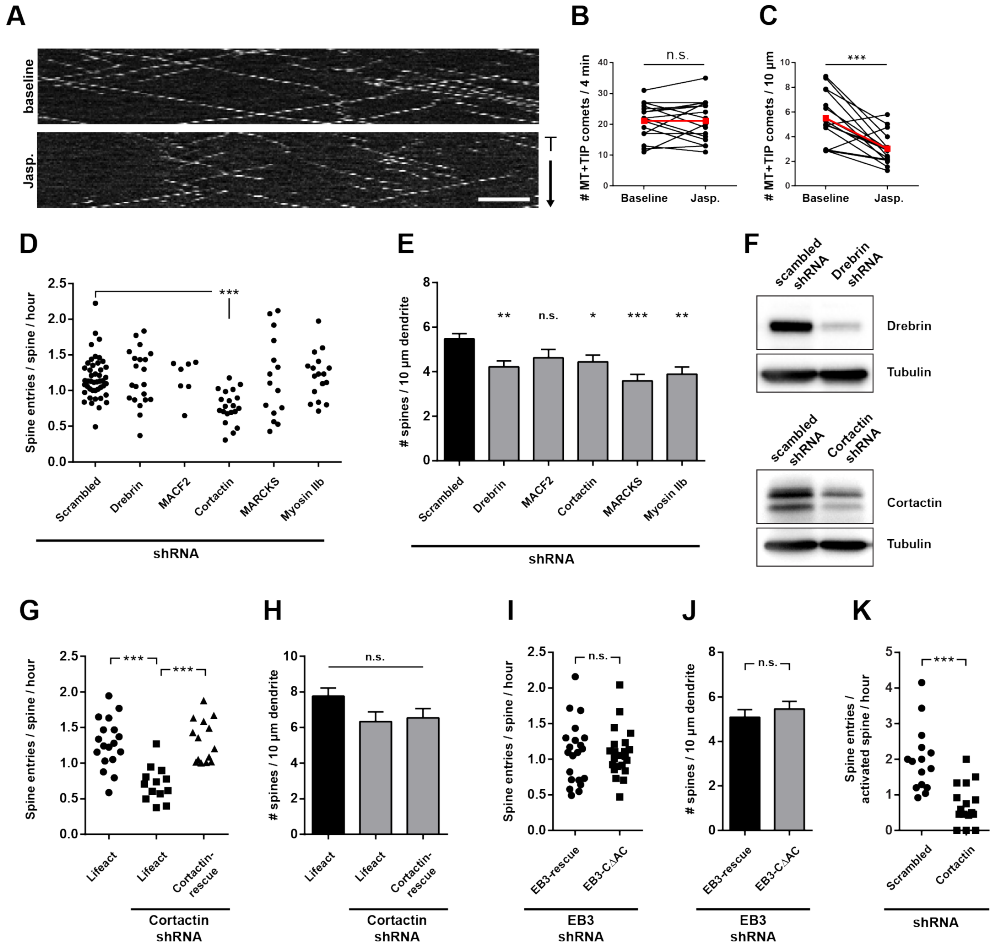

F) *Efficiency of lentivirus induced shRNA knockdown for Drebrin (upper) and Cortactin (lower) by Western Blot. The reduction of signal intensities compared to controls and normalized to the Tubulin signals were as follows: Drebrin: 15% and Cortactin: 47% remaining signal after 8 days.*
G) *Individual experiments for the Cortactin-rescue experiments from Fig. 4G.*
H) *Quantification of spine density in control, knockdown and Cortactin-rescue conditions (8 days of kd). While the expression of Cortactin-rescue restores microtubule entries in spines it does not recover the loss in spine numbers. One-way ANOVA.*
I) *Individual experiments for the EB3-rescue experiments from Fig. 4D.*
J) *Spine density does not vary between the used EB3-rescue constructs. Unpaired t-test.*
K) *Individual experiments for the uncaging experiment in control and Cortactin knock down conditions. Each data point represents the mean spine entry frequency for an individual dendrite. ***p<0.0001, unpaired t-test; scrambled: n = 15, Cortactin: n = 16 dendrites.*
Scale bar, 5 µm. Bars diagrams show mean + s.e.m.

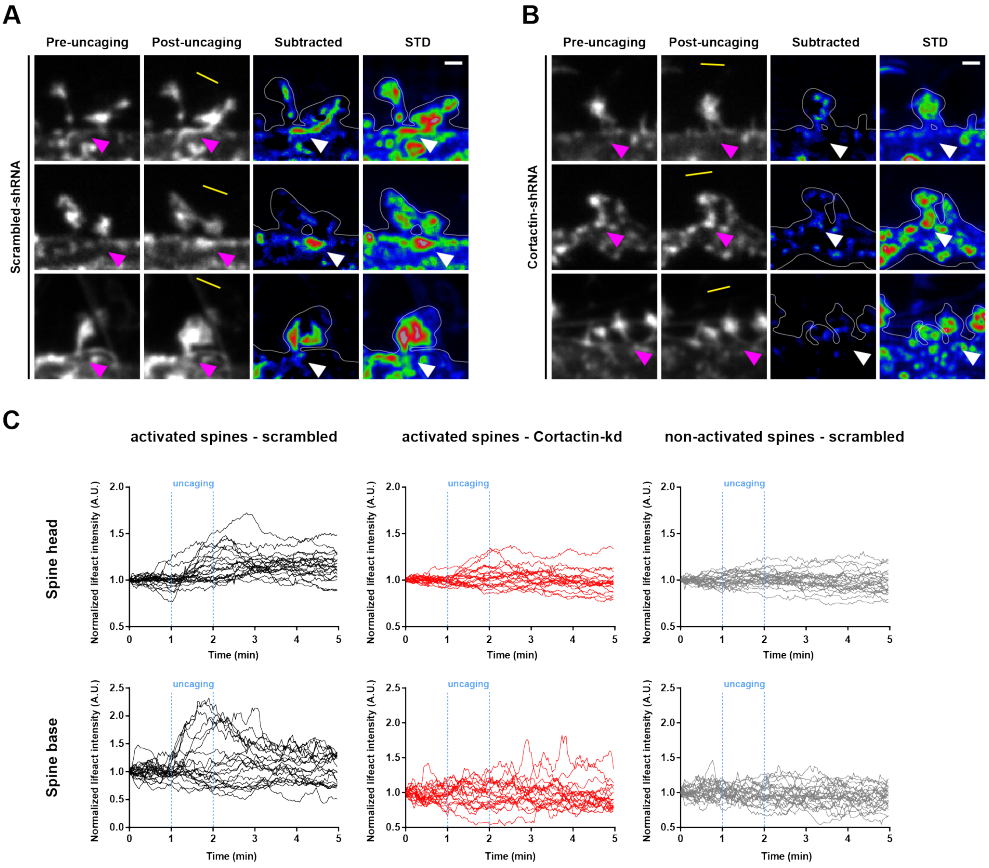

Figure S3. Actin dynamics at the spine base. Related to Figure 5.

A, B) *Additional examples of glutamate uncaging-induced actin dynamics in spines for control (A) and Cortactin knockdown (B). The first two columns show still frames before and after uncaging. Next, subtraction of the pre- from the post-uncaging Lifeact signals to visualize the increases in fluorescence intensity. Right column is a projection of the Lifeact signal s.d. over the full 5 min recording to visualize hot spots of actin dynamics. Arrowheads point on the same position at the base of a spine. Scale bar, 1 µm. Full length movies of these and the example in Fig. 5A are shown in Movie S6.*

C) *Single traces of mean intensities in spine heads (upper panel) and base (lower panel) for all quantified spines. Scrambled activated: n = 20 spines, Cortactin activated: n = 19 spines, scrambled non-activated: n = 22 spines.*

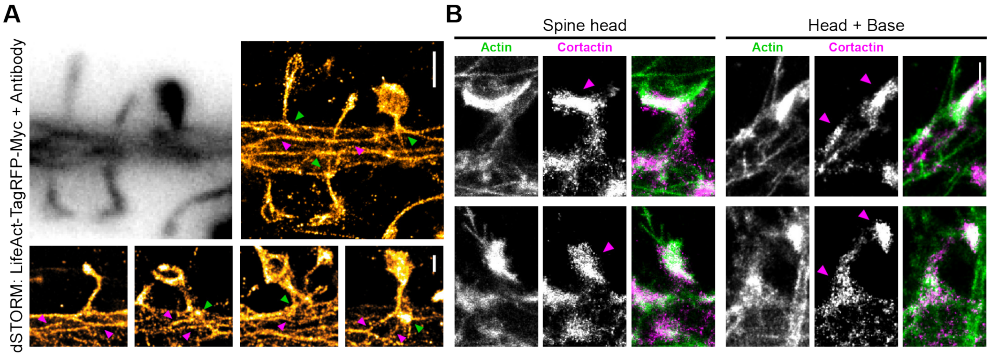

Figure S4. Super-resolution imaging of actin in dendrites. Related to Figure 6.
A) *Lentiviral infected neurons expressing Lifeact-TagRFP-Myc were fixed and stained against the Myc-tag with a primary and a secondary Alexa647 antibody. Top panel shows a diffraction limited and a dSTORM reconstruction of the dendritic shaft and spines. Bottom panels shows additional examples of actin structures in individual spines. Green arrowheads indicate examples of actin structures at the spine base; magenta arrowheads indicate actin cables. Scale bar: top: 1 µm, bottom 0.5 µm.*
B) *Additional examples of dendritic spines where Cortactin is colocalized with actin in the spine head only or to the spine head and base. Arrowheads indicate Cortactin structures. Scale bar: 0.5 µm.*

SUPPLEMENTAL FIGURES
LEGENDS TO SUPPLEMENTARY VIDEOS

Video S1. Methacholine stimulation in slice cultures, Related to Figure 2

Time-lapse recording of MT+TIP marker and mTagRFP in a hippocampal organotypic slice culture. The granule cell was infected with lentivirus and the same neuron is shown before and after stimulation with methacholine. MT+TIP comets were imaged with 5 sec intervals (middle), while mTagRFP was recorded only for every 5th frame (right). The left side shows a maximum projection of the MT+TIP recording to better localize spine entries. Dashed box marks the dendritic region shown in Figure 2B. Time runs as indicated with 20 fps. Spine entry frequency strongly increased after stimulation with methacholine.

Video S2. Local spine stimulation with glutamate uncaging increases spine targeting by microtubules, Related to Figure 3

Example dendrite of a dissociated neuron expressing mTagRFP during photoactivation. The uncaging laser was targeted to the white line and is active with appearance of the asterisk. Spines in close proximity to the uncaging region respond with morphological changes, while more distant spines are not affected. Time-lapse was recorded at 2 s intervals and is identical to the example shown in Figure 3D. After a break of 30 sec the same dendrite was recorded for MT+TIP and mTagRFP at 5 sec intervals. Arrowheads highlight spines targeted by dynamic microtubules.

Video S3. Glutamate uncaging combined with calcium imaging, Related to Figure 3
Two dendrites from the same dissociated neuron expressing Lifeact-GCaMP6s and MT+TIP. While recording for Lifeact-GCaMP6s in 2 sec intervals the uncaging was triggered at the white line with appearance of the asterisk (left). The center image represents the sum projection of the recorded GCaMP6s signals shown in Figure 3J. After a break of 30 sec, the same dendrite was recorded for MT+TIP in 5 sec intervals (right). Comet signals were improved using a running average subtraction and low-pass filtering. Dendritic outline was drawn based on a maximum projection of the calcium signals during uncaging. Spines receiving microtubule entries and being classified as activated were labeled with magenta arrowheads, while white arrowheads indicate non-activated spines.

Video S4. Combined movement of Cortactin and actin to the spine base after glutamate uncaging, Related to Figure 4
Dual imaging of Lifeact-GFP and Cortactin-dsRed in transfected DIV 19 neuron culture. The moment of glutamate uncaging is shown next to the white line representing the uncaging region. The white framed inserts shows a magnification of the targeted spine for each channel. The uncaging induced a simultaneous translocation of Cortactin and actin towards the spine base. The overexpression of Cortactin seems to boost the overall high actin dynamics in these relatively young neuron cultures.

Video S5. Recording of microtubule and Cortactin dynamics, Related to Figure 4
Example of a transduced DIV 39 neuron expressing MT+TIP marker and Cortactin-dsRed in baseline conditions. Arrowheads point to spines that are targeted by microtubules while an asterisk indicates the time point of microtubule invasion. Arrows point to regions of Cortactin dynamics at the base of targeted spines.

Video S6. Actin dynamics at the base of the spine, Related to Figure 5
Part1: Actin dynamics induced by synaptic activation. Individual spines expressing Lifeact-TagRFP were recorded during uncaging of glutamate in neuron cultures co-expressing scrambled shRNA (upper panel) or Cortactin shRNA (lower panel). First spines on the left side represent the examples shown in Figure 5A.The appearance of asterisks indicate the time of uncaging and white lines mark the regions of photoactivation. Spines were imaged with 2 sec intervals in the presence of TTX. The transient increase of actin dynamics in spine head and base is considerably reduced in Cortactin knockdown conditions.
Part2: Actin dynamics in spines invaded by microtubules. Full time sequences of the MT+TIP and Lifeact imaging shown in Figure 5D. The orange asterisks in the Lifeact channel appear 1 min before a microtubule comet enters the spine and turn red during the invasion period. Images were acquired at 5 sec intervals in sequential mode. Increased actin dynamics at the base of the spines precede the invasion of microtubules in spines.

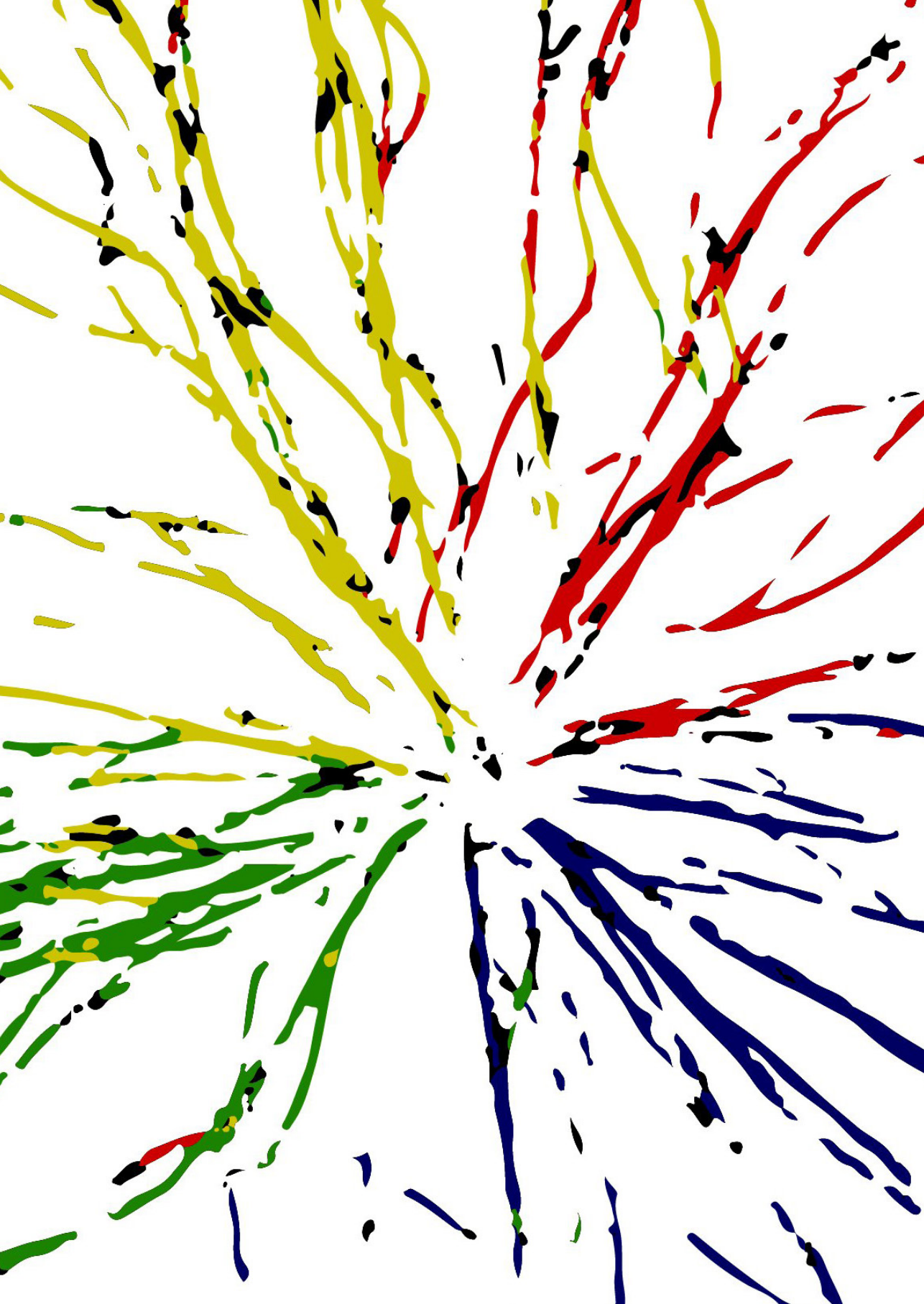

6

Differentiation between Oppositely Oriented Microtubules Controls Polarized Neuronal Transport

Roderick P. Tas[1], Anaël Chazeau[1], Bas M.C. Cloin[1], Maaike L.A. Lambers[1], Casper C. Hoogenraad[1] and Lukas C. Kapitein[1]

Neuron (2017); 96, pp. 1264-1271

[1] Division of Cell Biology, Faculty of Science, Utrecht University, The Netherlands

ABSTRACT

Microtubules are essential for polarized transport in neurons, but how their organization guides motor proteins to axons or dendrites is unclear. Because different motors recognize distinct microtubule properties, we used optical nanoscopy to examine the relation between microtubule orientations, stability and modifications. Nanometric tracking of motors to super-resolve microtubules and determine their polarity revealed that in dendrites, stable and acetylated microtubules are mostly oriented minus-end out, while dynamic and tyrosinated microtubules are oriented oppositely. In addition, microtubules with similar orientations and modifications form bundles that bias transport. Importantly, because the plus-end directed Kinesin-1 selectively interacts with acetylated microtubules, this organization guides this motor out of dendrites and into axons. In contrast, Kinesin-3 prefers tyrosinated microtubules and can enter both axons and dendrites. This separation of distinct microtubule subsets into oppositely oriented bundles constitutes a key architectural principle of the neuronal microtubule cytoskeleton that enables selective sorting by different motor proteins.

INTRODUCTION

The polarized organization of neurons depends on the selective targetting of cargoes to either axons or dendrites, driven by motor proteins that move selectively towards either the plus or minus end of microtubules (Bentley and Banker, 2016; Britt et al., 2016; Hirokawa et al., 2010; Kapitein and Hoogenraad, 2011; Stiess and Bradke, 2011; Vale, 2003). For some axonal cargoes selective targeting is established by non-selective transport to axons and dendrites, followed by selective endocytosis in dendrites, while other cargoes are directly targeted to axons and do not enter dendrites (Bentley and Banker, 2016; Sampo et al., 2003; Wisco et al., 2003). In lower organisms, such as *Drosophila* or *C. elegans*, microtubule orientations in dendrites and axons are both uniform, but of opposite orientation (Kapitein and Hoogenraad, 2015; Maniar et al., 2012; Rolls, 2011). Here, plus-end outward oriented microtubules in axons enable kinesin-driven anterograde transport, whereas transport into dendrites depends on minus-end directed motors because the microtubule orientations are reversed (Harterink et al., 2016; Rolls, 2011). In contrast, in dendrites of mammalian neurons microtubules are equally mixed between both orientations (Baas et al., 1988; Kleele et al., 2014; Yau et al., 2016). Remarkably, several plus-end directed motor proteins can nevertheless selectively enter axons, while others target both axons and dendrites (Huang and Banker, 2011; Jacobson et al., 2006; Kapitein et al., 2010a; Lipka et al., 2016; Nakata and Hirokawa, 2003). While it is widely assumed that these fundamental differences in selectivity are encoded by the neuronal microtubule network (Janke, 2014; Verhey and Gaertig, 2007), the design principles that ensure axon-selective transport have remained unresolved (Bentley and Banker, 2016; Britt et al., 2016; Kapitein and Hoogenraad, 2011; Stiess and Bradke, 2011).

It has been reported that certain members of the kinesin superfamily can preferentially interact with microtubule subsets that carry specific chemical modifications or associated proteins (Atherton et al., 2013; Cai et al., 2009; Konishi and Setou, 2009; Sirajuddin et al., 2014). For example, the axon-selective Kinesin-1 has been shown to prefer stable microtubules marked by acetylation and detyrosination (Cai et al., 2009; Konishi and Setou, 2009), while the non-selective Kinesin-3 has been suggested to preferentially bind to tyrosinated microtubules (Guardia et al., 2016; Lipka et al., 2016). Nevertheless, these properties alone cannot explain the axon-selectivity of Kinesin-1, given that acetylated and detyrosinated microtubules are also abundantly present in dendrites (Hammond et al., 2010). The mild enrichment of these microtubules in proximal axons versus proximal dendrites (Hammond et al., 2010) is insufficient to explain why Kinesin-1 exclusively enters axons and fails to enter dendrites (Kapitein et al., 2010a). Thus, despite the accumulating evidence for and understanding of the selective binding of motors to specific subsets of microtubules, the link between selective microtubule binding and selective axonal entry has remained unclear.

The axon selectivity of the plus-end directed Kinesin-1 could be explained if the

microtubules preferred by this motor would be largely oriented minus-end out in dendrites. Likewise, if the microtubule subset preferred by non-selective motors would be oriented plus-end out, this would explain why these motors can drive anterograde transport in dendrites. To test this, we here use novel optical nanoscopy techniques to dissect the relation between microtubule orientations, stability and modifications in neurons. Using nanometric tracking of motor proteins running over an extracted cytoskeleton to super-resolve microtubules and determine their polarity, we find that dendritic microtubules are organized in polarized bundles that locally bias transport. In dendrites, these polarized bundles with opposite orientations differ in overall stability and composition, with minus-end out microtubules being more stable and more acetylated. We also show that Kinesin-1 selectively binds to these minus-end out oriented microtubules, which explains why this plus-end directed motor cannot drive cargo transport into dendrites. In addition, we find that Kinesin-3 preferentially binds to microtubules that are mostly oriented plus-end out, which explains why this motor can enter dendrites. Thus, the separation of distinct microtubule subsets into oppositely oriented bundles constitutes a key architectural principle of the neuronal microtubule cytoskeleton that enables selective sorting by different motor proteins.

RESULTS

Motor-PAINT: super-resolution imaging of microtubules and their orientation

To test whether axon-selective kinesins only interact with the subset of microtubules that is oriented minus-end out in dendrites, we set out to explore the relation between microtubule orientations, stability and modifications in neurons. Super-resolution microscopy (Hell, 2007; Huang et al., 2009; Molle et al., 2016; Patterson et al., 2010) enables resolving individual microtubules in dense networks (Mikhaylova et al., 2015) and can also detect specific microtubule modifications, but robust detection of microtubule orientations has not yet been demonstrated. We reasoned that using nanometric tracking of plus-end directed motor proteins would super-resolve microtubules and also reveal their polarity. Because this approach requires detecting thousands of single-molecule events over the course of several minutes and any concurrent microtubule rearrangement would blur the final image, we tested whether motor proteins could still move over microtubules after chemical fixation of the cytoskeleton (Brawley and Rock, 2009; Sivaramakrishnan and Spudich, 2009) (Fig.

Figure 1: motor-PAINT: super-resolution imaging of microtubules and their orientation
A) *Assay: after extraction and fixation, purified and fluorescently labeled motors are added and map out the microtubule array by unidirectional runs. See also Figure S1 - S2*
B) *Super-resolved image of an extracted U2OS cell obtained by subpixel localization of thousands of motor binding events.*
C) *Left: Super-resolution reconstruction of the same cell with all microtubule segments colored according to their absolute orientation. Legend arrows point in the direction of the plus end. Right: Zooms showing free microtubule plus and minus end. See also Figure S2*

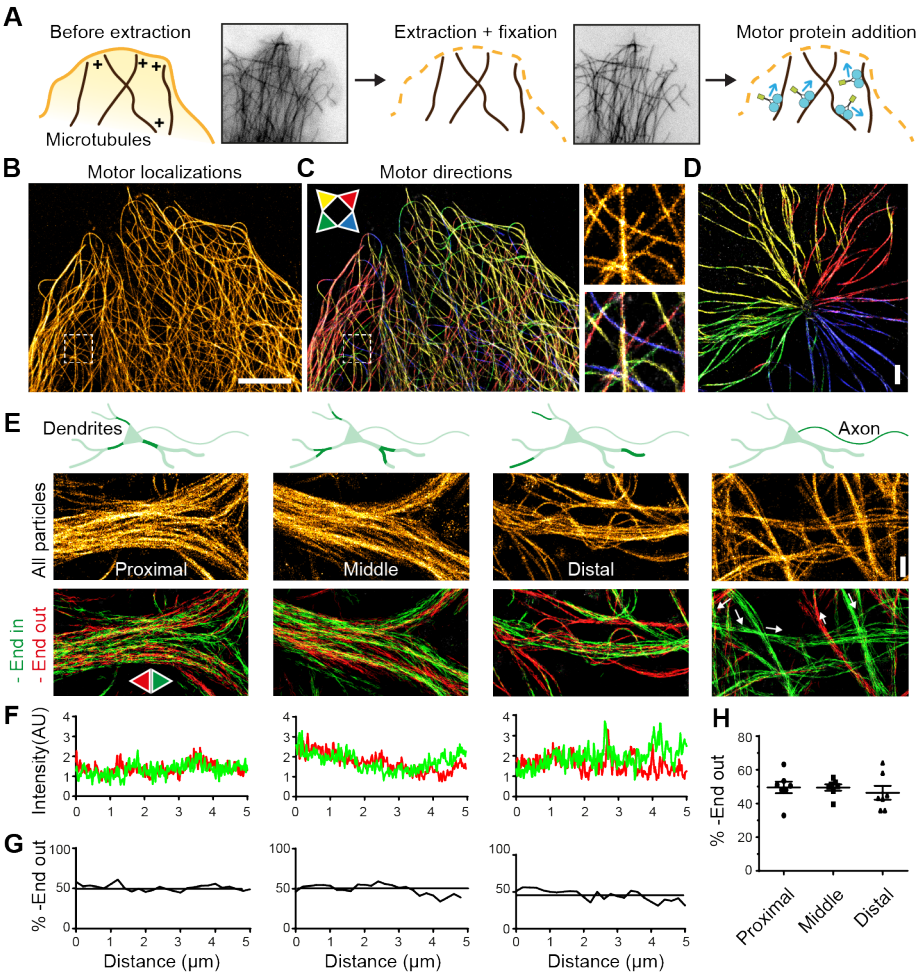

D) *Orientation mapping of a centrosomal microtubule array obtained after nocodazole washout in a COS7 cell.*
E) *Motor-based super-resolution reconstruction of microtubules in dendrites and axons of cultured rat hippocampal neurons (DIV 16-17). Top images are based on all binding events (> 42405 events per image). Bottom images are color coded for absolute orientation. Track interpolation was used for all run-based images.*
F) *Quantification of inward and outward moving kinesins in 5 µm long proximal, middle and distal dendritic segments, reflecting the number minus-end outward and inward oriented microtubules, respectively.*
G) *Percentage of minus-end out oriented microtubules in proximal, middle and distal dendritic segments, based on the graphs shown in F.*
H) *Average percentage of minus-end out oriented microtubules in proximal, middle and distal dendritic segments (Mean ±SEM, n= 7 segments from 7 neurons for every category).*
Scale bars: 5 µm (B); 1 µm (D,E).

1A). COS7 or U2OS cells were permeabilized using detergent, extracted, and fixed using paraformaldehyde and real-time imaging was used to carefully optimize buffer conditions for extraction and fixation (Fig. S1). This resulted in a procedure to successfully preserve microtubule organization without any noticeable rearrangements or depolymerization (Fig. 1A, Fig. S1-2, Supplemental Video 1). Subsequent addition of purified and fluorescently labeled kinesin molecules (DmKHC-GFP) resulted in numerous transient events of motors binding to the microtubule and running over it for hundreds of nanometers with a speed of 7.5 ± 3.0 · 10^2 nm/s (average±SD) (Fig. 1A, Fig. S2, Supplemental Video 2). Thus, motor proteins can still move over a chemically fixed cytoskeleton to report microtubule orientations.

Next, we analyzed these binding events using single-molecule localization and tracking algorithms to construct a diffraction-unlimited image of the microtubule array in which the absolute orientation of each microtubule is known along the entire microtubule lattice (Fig. 1B-D, Fig. S2). Line scans across individual microtubules revealed a full width at half maximum (FWHM) of 52 ± 5 nm (mean±SD for n=30 profiles, Fig. S2), suggesting a lateral resolution of the same magnitude, because microtubule FWHM is a good predictor of lateral resolution in case of sufficient labeling density (Mikhaylova et al., 2015). To validate the motors trajectories as reliable readout of microtubule polarity, we treated cells with the microtubule destabilizing agent nocodazole. Subsequent washout induced rapid regrowth of microtubules nucleated by the centrosome, resulting in a well-defined radial array of microtubules with all plus ends oriented outward. Indeed, the motor-based super-resolution image obtained for these cells unambiguously confirmed this organization, with 100% of centrosome-associated microtubules attached with their minus end (Fig. 1D; 141 microtubules in 3 cells). Thus, motors moving over an extracted cytoskeleton reliably report the polarity of microtubules and can be used to reconstruct a super-resolved image. Because our method is conceptually related to transient binding approaches that can be classified as PAINT variants (point-accumulation-for-imaging-in-nanoscale-topography) (Giannone et al., 2010; Jungmann et al., 2014; Kiuchi et al., 2015; Molle et al., 2016; Sharonov and Hochstrasser, 2006), we termed it motor-PAINT.

Dendritic microtubule arrays form bundles of preferred polarity

We next used our methodology to explore the microtubule organization in the dendrites and axons of rat hippocampal neurons. Consistent with earlier reports (Baas et al., 1988; Stepanova et al., 2003; Yau et al., 2016), microtubules in axons were uniformly oriented, whereas microtubules in dendrites were oriented both ways (Fig.1E; Movie S3). Comparing the number of outward and inward runs in 5-mm stretches in proximal, middle and distal regions of dendrites revealed that 50% of the microtubules were oriented minus-end out throughout the dendrite (Fig.1E-H). Interestingly, the separate images created for minus-end outward and minus-end inward oriented microtubules were not identical. Often, spatially separated bundles of microtubules in dendrites would be enriched for one orientation, indicating local

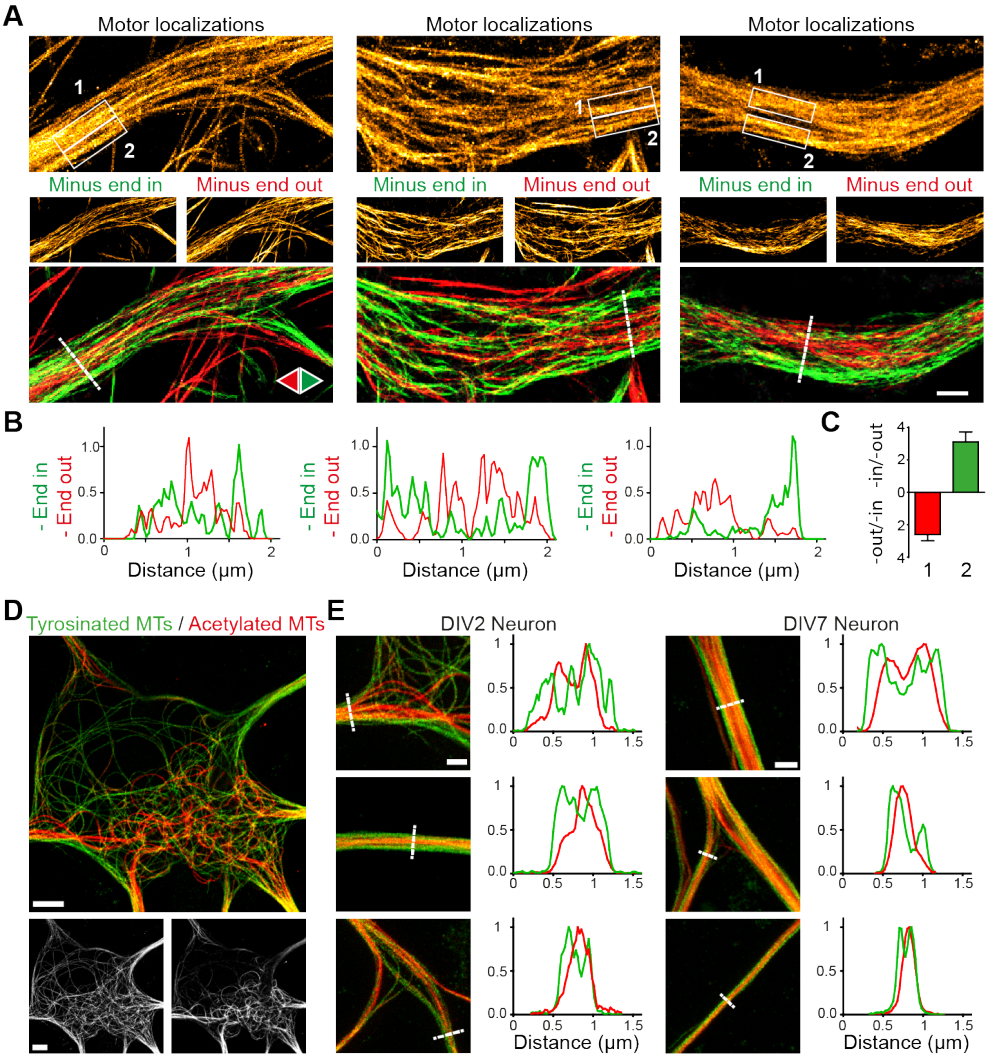

Figure 2: Dendritic microtubule arrays spatially segregate by orientation and modification

A) *Three examples of dendrites demonstrating bundles of preferred polarity (left-right). Motor-based super-resolution reconstructions, based on either all binding events (top), inward runs (middle right), outward runs (middle left) or runs of both directions (bottom). Track interpolation was used for the run-based images.*

B) *Intensity profiles for inward and outward pointing microtubules along the lines indicated in A. See also Figure S3.*

C) *Ratio between outward and inward runs or inverse for regions marked with 1 or 2 in A. Mean ±SEM.*

D) *STED image from the soma of a DIV2 neuron immunostained for tyrosinated and acetylated MTs (top) and the individual tyrosinated (bottom left) and acetylated channel (bottom right).*

E) *Zooms from DIV2 and DIV7 neurites highlighting spatial segregation between tyrosinated and acetylated MTs. Corresponding intensity profiles along the indicated line is shown next to the image on the right. See also Figure S4.*

Scale bars: 1 µm (A,E); 5 µm (D)

orientational order (Fig.2A-B). Spatial correlation analysis and intensity quantification (Fig. S3, see Methods) revealed that at lateral length scales below 600 nm dendritic microtubules are enriched 2-4 fold for a specific orientation, suggesting a 66/33% - 80/20% ratio between microtubules of opposing orientations (Fig. 2C). Thus, the dendritic microtubule array is comprised of bundles of preferred polarity, while overall both orientations are equally abundant.

Minus-end-out-oriented microtubules are more stable and more acetylated

To explore the relation between microtubule modifications and orientations, we first performed nanoscopy of markers for different microtubule subsets. Immunolabeling of tyrosinated tubulin reveals freshly polymerized microtubules in which most α-tubulins have not yet lost their C-terminal tyrosine nor their penultimate glutamate, whereas staining for acetylated tubulin or D2-tubulin (detecting loss of the C-terminal tyrosine and glutamate) labels stable microtubules (Janke, 2014). STED (stimulated emission depletion) microscopy (Fig. 2D-E) and localization microscopy (Fig. S4) revealed that acetylated microtubules and tyrosinated microtubules form spatially separated subsets both in the cell soma and within dendrites. In addition, tyrosinated microtubules did not overlap with D2-tubulin, while the EB1-positive stretches that label growing microtubules were enriched in regions with strong tyrosinated tubulin signals (Fig. S4). These results demonstrate that dendritic microtubules spatially segregate into bundles with either dynamic or stable microtubules.

So far, motor-PAINT revealed bundles enriched for plus or minus-end out microtubules, while immunolabeling revealed bundles enriched for stable or dynamic microtubules. To resolve the connection between these different bundles and directly explore whether stable microtubules have a preferred orientation, we treated neurons with 4 μM nocodazole for 2.5 hours to selectively preserve stable microtubules and subsequently performed motor-PAINT microscopy. Immunolabeling confirmed the loss of tyrosinated microtubules, while the acetylated microtubule network was still intact (Fig. 3A-B). Motor-PAINT microscopy on the remaining network of stable microtubules revealed that minus-end out microtubules were approximately twice as abundant as plus-end out microtubules (66% versus 34% for plus and minus end out, respectively, Fig. 3C-E). In addition, to explore the link between microtubule stability and orientation without microtubule destabilization, motor-PAINT microscopy on unperturbed networks was followed by immunolabeling of acetylated tubulin, which revealed that acetylated microtubules predominantly overlapped with minus-end out oriented microtubules (Fig. 3F-G, Fig. S5). Together, these results demonstrate that the spatially segregated stable and dynamic microtubules networks are enriched in minus-end out and plus-end out oriented microtubules, respectively.

Kinesin-1 and Kinesin-3 prefer different microtubule subsets in neurons

Kinesin-1 has been shown to prefer stable microtubules marked by acetylation and

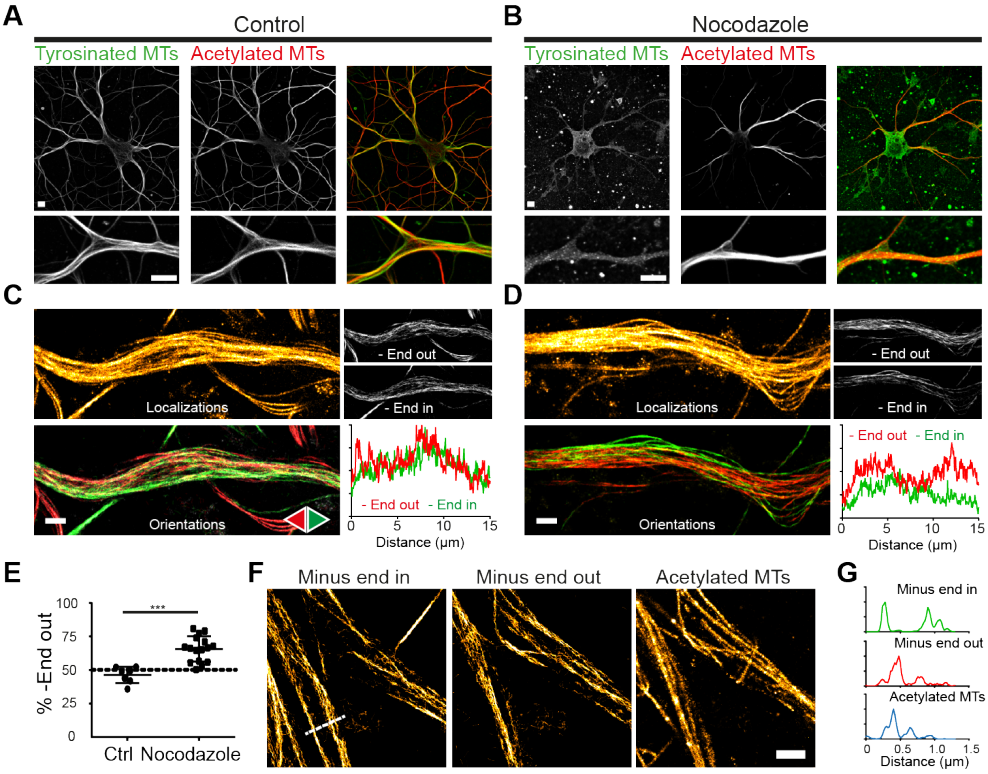

Figure 3: Minus-end out oriented microtubules are more stable and more acetylated
A,B) *Overview and zoom of DIV9 neurons immunostained for tyrosinated and acetylated microtubules in control conditions (A) or following 2.5 hours incubation with 4 uM nocodazole (B).*
C,D) *motor-PAINT performed on a dendritic segment in control conditions (C) or after nocodazole treatment (D).*
E) *Percentage of minus-end out oriented microtubules in dendritic segments in control and nocodazole-treated neurons. Mean ±SD, control: n=7, nocodazole: n=16 acquired in 3 independent experiments. T-test: ***, P<0.001.*
F) *Correlative reconstructed images of minus-end in (left), minus-end out (middle) and acetylated microtubules (right) of a dendritic segment. See also Figure S5*
G) *Intensity profiles measured for both microtubule orientations and the acetylated tubulin channel. Scale bars: 5 µm (A,B); 1 µm (C,D,F).*

detyrosination (Cai et al., 2009; Konishi and Setou, 2009), while the non-selective Kinesin-3 has been suggested to preferentially bind to tyrosinated microtubules (Guardia et al., 2016; Lipka et al., 2016). Together with our findings that stable and dynamic microtubules are predominantly oriented minus-end outward and plus-end outward, respectively, this would explain why Kinesin-1 cannot enter dendrites, while Kinesin-3 enters dendrites and accumulates at their tips. Nevertheless, the exact binding bias of Kinesin-1 and Kinesin-3 in neurons has not yet been determined. To measure this, we overexpressed a rigor mutant of

Kinesin-1 (Kif5a-rigor), which can bind to microtubules but not walk nor detach (Farias et al., 2015). Kinesin-1 showed a very dramatic colocalization with acetylated tubulin, whereas staining for tyrosinated tubulin highlighted a microtubule network that was completely devoid of Kinesin-1 (Fig. 4A-B, Fig. S6). At moderate over-expression levels, the motor was largely bound to acetylated/non-tyrosinated microtubules in the cell body and near the axon entry, whereas at very high levels it was also present in dendrites, but still selective for acetylated/non-tyrosinated microtubules (Fig. 4A-B). Thus, Kinesin-1 selectively binds to those dendritic microtubules whose plus ends are mostly oriented towards the cell body, which prevents entry into dendrites and ensures axon selectivity.

For Kinesin-3, we found that a rigor construct (Kif1a-Rigor-GFP) (Guardia et al., 2016) was about 1.5- to 2-fold enriched on tyrosinated microtubules versus acetylated microtubules in COS7 cells (Fig. S6D-F). Because this motor is not completely excluded

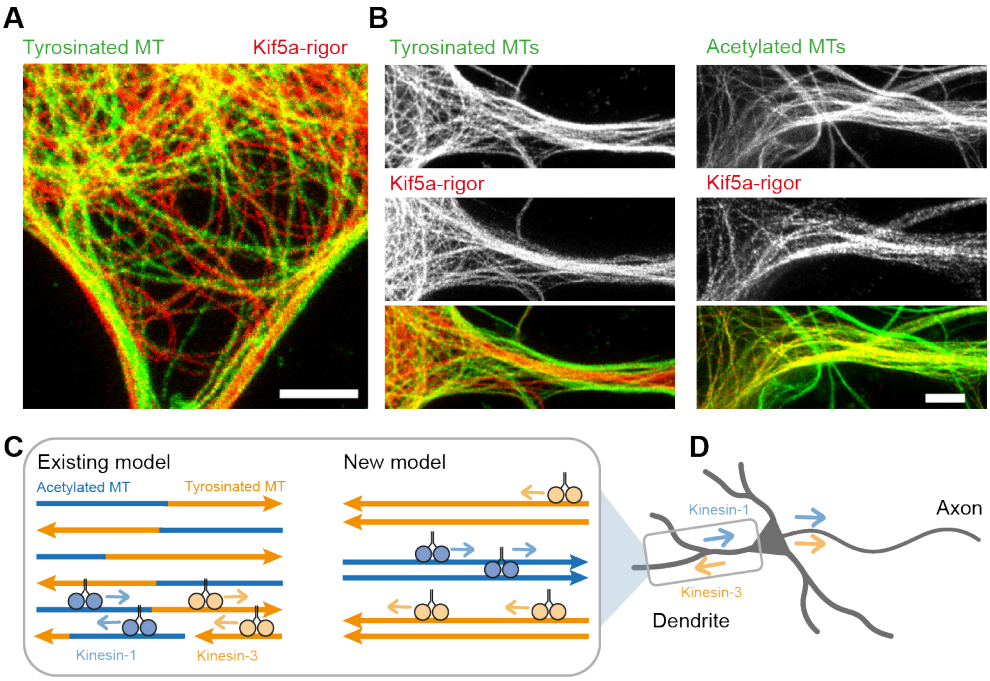

Figure 4: Kinesin-1 prefers stable, acetylated microtubules in neuronal axon and dendrites
A,B) *STED images of DIV4 polarized neuronal soma (A) or neurites (B) after 1 day expression of GFP-kif5a rigor stained for GFP and acetylated-tubulin or GFP and tyrosinated-tubulin. See also Figure S6.*
C) *Cartoon illustrating the existing and new model for dendritic microtubule organization. Arrow heads on microtubules depict plus ends. Kinesin-1 and Kinesin-3 preferentially move over stable/acetylated and dynamic/tyrosinated microtubules, respectively.*
D) *The new model can explain the selective entry of Kinesin-1 into axons. Arrows depict bias in transport directionality (see also Fig. S7).*
Scale bars: 2 µm (A,B)

from acetylated microtubules, assessing preferential binding in neurons was challenging, given the high density of microtubules. However, in somatic regions where tyrosinated and acetylated microtubules were clearly separated, we could analyze the binding preference and again found a nearly twofold enrichment on tyrosinated microtubules (Fig. S6G-H). Given that tyrosinated microtubules are preferentially oriented plus-end out, this enrichment is sufficient to bias transport to the distal end (Fig. S6I). As shown in Figure S7, even a small difference in inward versus outward runs (e.g. $p_+ = 0.55\text{-}0.6$) will already direct most motors to the distal end of the dendrite (Fig. S7).

DISCUSSION

Existing models of the dendritic microtubule array suggest that microtubules of different orientations are randomly distributed and have a similar composition, often consisting of a stable, chemically modified segment followed by a dynamic, tyrosinated end (Fig. 4C) (Baas et al., 2016; Conde and Caceres, 2009; Nirschl et al., 2017). We here used novel optical nanoscopy techniques to dissect the relation between microtubule orientations, stability and modifications in neurons (Balabanian et al., 2017). This revealed unanticipated local orientational order in dendrites where microtubules are organized in multiple polarized bundles, whose properties depend on their absolute orientation. Minus-end out oriented microtubules are more stable and more modified, while the plus-end out microtubule are more dynamic.

The finding that the microtubules preferred by Kinesin-1 are predominantly oriented minus-end out in dendrites solves how this motor can be axons-selective, while the microtubules it prefers are also found in dendrites (Fig. 4C-D). In addition, the finding that dynamic microtubules are largely oriented plus-end out explains why motors that interact with these microtubules, such as Kinesin-3, not only enter dendrites (Jacobson et al., 2006; Kapitein et al., 2010a; Nakata and Hirokawa, 2003), but also accumulate at dendrite tips (Huang and Banker, 2011; Jacobson et al., 2006; Lipka et al., 2016) (Fig. 4C-D). Our results thus support the tubulin-code hypothesis by showing that microtubules with different modifications and associated proteins have different functional roles (Janke, 2014; Verhey and Gaertig, 2007).

In addition, for motors without a preference for specific microtubule subsets, the bundles of uniform polarity that we identified promote persistent motility in a certain direction, because once moving within a bundle, motility will be biased despite potential switching between different microtubules within a bundle. Mathematical modeling revealed that even a small asymmetry will create a directional bias for motors (Kapitein et al., 2010a) (Fig. S7). For example, when plus-end out microtubules are twofold enriched, 50% of kinesin-driven cargoes would accumulate in the last 20% or 9% of the bundle for a bundle length of 20 or 50 mm, respectively (Fig. S7).

Given that dendrite-entering motors can also enter axons, additional mechanisms

are required to prevent axonal entry of dendritic cargoes, which are most likely mediated by the minus-end directed microtubule motor dynein and by myosin motors that can oppose microtubule-based transport (Arnold and Gallo, 2014; Kapitein et al., 2010a; Kapitein et al., 2013; Kuijpers et al., 2016; Watanabe et al., 2012), possibly augmented by specific filtering properties of the Axon Initial Segment (Leterrier and Dargent, 2014; Rasband, 2010; Song et al., 2009). Furthermore, how motors selectively recognize specific microtubule subsets remains poorly understood. Current models implicate direct effects of different modifications or important roles for different microtubule-associated proteins (MAPs) in loading motors to specific microtubules (Atherton et al., 2013; Bentley and Banker, 2016; Janke, 2014; Lipka et al., 2016). In addition, the mechanisms by which the sophisticated organization of dendritic microtubules is established are unknown, but they likely depend on a multitude of MAPs and microtubule-organizing motors that collectively phase separate and polarity sort different microtubule populations (Kapitein and Hoogenraad, 2015). Regardless the mechanisms, our finding that microtubules with opposite orientations differ in stability and chemical composition constitutes a key architectural principle of the neuronal microtubule cytoskeleton that enables selective sorting by different motor proteins.

AUTHOR CONTRIBUTIONS

LCK conceived research and supervised the project. RPT optimized motor-PAINT procedures, purified motors, designed and performed experiments, wrote motor-PAINT analysis code and analyzed data. AC optimized procedures for discriminating stable and dynamic microtubules and performed STED and SMLM experiments. BMCC performed additional experiments and analyzed data. MLAL created and analyzed the Kif1A-Rigor under supervision of RPT. CCH provided neuronal cultures and gave advice during the project. RPT and LCK wrote the paper with input from all other authors.

ACKNOWLEDGEMENTS

We thank Anna Akhmanova for advice and Marina Mikhaylova for establishing initial experiments. This research was supported by the Netherlands Organization for Scientific Research (NWO) (NWO-ALW-VICI to C.C.H., NWO-ALW-VIDI to L.C.K.), the Dutch Technology Foundation STW, which is part of the NWO (NWO-NANO to C.C.H and L.C.K), and the European Research Council (ERC Starting Grant to L.C.K., ERC Consolidator Grant to C.C.H, Marie Curie fellowship to A.C.).

REFERENCES

Arnold, D.B., and Gallo, G. (2014). Structure meets function: actin filaments and myosin motors in the axon. J Neurochem 129, 213-220.

Atherton, J., Houdusse, A., and Moores, C. (2013). MAPping out distribution routes for kinesin couriers. Biology of the cell / under the auspices of the European Cell Biology Organization 105, 465-487.
Baas, P.W., Deitch, J.S., Black, M.M., and Banker, G.A. (1988). Polarity orientation of microtubules in hippocampal neurons: uniformity in the axon and nonuniformity in the dendrite. Proc Natl Acad Sci U S A 85, 8335-8339.
Baas, P.W., Rao, A.N., Matamoros, A.J., and Leo, L. (2016). Stability properties of neuronal microtubules. Cytoskeleton (Hoboken) 73, 442-460.
Balabanian, L., Berger, C.L., and Hendricks, A.G. (2017). Acetylated Microtubules Are Preferentially Bundled Leading to Enhanced Kinesin-1 Motility. Biophys J 113, 1551-1560.
Bentley, M., and Banker, G. (2016). The cellular mechanisms that maintain neuronal polarity. Nat Rev Neurosci 17, 611-622.
Brawley, C.M., and Rock, R.S. (2009). Unconventional myosin traffic in cells reveals a selective actin cytoskeleton. Proc Natl Acad Sci U S A 106, 9685-9690.
Britt, D.J., Farias, G.G., Guardia, C.M., and Bonifacino, J.S. (2016). Mechanisms of Polarized Organelle Distribution in Neurons. Frontiers in cellular neuroscience 10, 88.
Cai, D., McEwen, D.P., Martens, J.R., Meyhofer, E., and Verhey, K.J. (2009). Single molecule imaging reveals differences in microtubule track selection between Kinesin motors. PLoS Biol 7, e1000216.
Chazeau, A., Katrukha, E.A., Hoogenraad, C.C., and Kapitein, L.C. (2016). Studying neuronal microtubule organization and microtubule-associated proteins using single molecule localization microscopy. Methods Cell Biol 131, 127-149.
Conde, C., and Caceres, A. (2009). Microtubule assembly, organization and dynamics in axons and dendrites. Nat Rev Neurosci 10, 319-332.
Edelstein, A., Amodaj, N., Hoover, K., Vale, R., and Stuurman, N. (2010). Computer control of microscopes using microManager. Current protocols in molecular biology / edited by Frederick M Ausubel [et al] Chapter 14, Unit14 20.
Farias, G.G., Guardia, C.M., Britt, D.J., Guo, X., and Bonifacino, J.S. (2015). Sorting of Dendritic and Axonal Vesicles at the Pre-axonal Exclusion Zone. Cell reports 13, 1221-1232.
Giannone, G., Hosy, E., Levet, F., Constals, A., Schulze, K., Sobolevsky, A.I., Rosconi, M.P., Gouaux, E., Tampe, R., Choquet, D., and Cognet, L. (2010). Dynamic superresolution imaging of endogenous proteins on living cells at ultra-high density. Biophys J 99, 1303-1310.
Guardia, C.M., Farias, G.G., Jia, R., Pu, J., and Bonifacino, J.S. (2016). BORC Functions Upstream of Kinesins 1 and 3 to Coordinate Regional Movement of Lysosomes along Different Microtubule Tracks. Cell reports 17, 1950-1961.
Hammond, J.W., Huang, C.F., Kaech, S., Jacobson, C., Banker, G., and Verhey, K.J. (2010). Posttranslational modifications of tubulin and the polarized transport of kinesin-1 in neurons. Mol Biol Cell 21, 572-583.
Harterink, M., van Bergeijk, P., Allier, C., de Haan, B., van den Heuvel, S., Hoogenraad, C.C., and Kapitein, L.C. (2016). Light-controlled intracellular transport in Caenorhabditis elegans. Curr Biol 26, R153-154.
Hell, S.W. (2007). Far-field optical nanoscopy. Science 316, 1153-1158.
Hirokawa, N., Niwa, S., and Tanaka, Y. (2010). Molecular motors in neurons: transport mechanisms and roles in brain function, development, and disease. Neuron 68, 610-638.
Huang, B., Bates, M., and Zhuang, X. (2009). Super-resolution fluorescence microscopy. Annu Rev Biochem 78, 993-1016.
Huang, C.F., and Banker, G. (2011). The Translocation Selectivity of the Kinesins that Mediate Neuronal Organelle Transport. Traffic 4, 549-564.
Jacobson, C., Schnapp, B., and Banker, G.A. (2006). A change in the selective translocation of the Kinesin-1 motor domain marks the initial specification of the axon. Neuron 49, 797-804.
Janke, C. (2014). The tubulin code: molecular components, readout mechanisms, and functions. J Cell Biol 206, 461-472.
Jungmann, R., Avendano, M.S., Woehrstein, J.B., Dai, M., Shih, W.M., and Yin, P. (2014). Multiplexed 3D cellular super-resolution imaging with DNA-PAINT and Exchange-PAINT. Nat Methods 11, 313-

318.
Kapitein, L.C., and Hoogenraad, C.C. (2011). Which way to go? Cytoskeletal organization and polarized transport in neurons. Mol Cell Neurosci 46, 9-20.
Kapitein, L.C., and Hoogenraad, C.C. (2015). Building the Neuronal Microtubule Cytoskeleton. Neuron 87, 492-506.
Kapitein, L.C., Schlager, M.A., Kuijpers, M., Wulf, P.S., van Spronsen, M., MacKintosh, F.C., and Hoogenraad, C.C. (2010a). Mixed microtubules steer dynein-driven cargo transport into dendrites. Curr Biol 20, 290-299.
Kapitein, L.C., van Bergeijk, P., Lipka, J., Keijzer, N., Wulf, P.S., Katrukha, E.A., Akhmanova, A., and Hoogenraad, C.C. (2013). Myosin-V opposes microtubule-based cargo transport and drives directional motility on cortical actin. Curr Biol 23, 828-834.
Kapitein, L.C., Yau, K.W., and Hoogenraad, C.C. (2010b). Microtubule dynamics in dendritic spines. In Methods Cell Biol, pp. 111-132.
Kiuchi, T., Higuchi, M., Takamura, A., Maruoka, M., and Watanabe, N. (2015). Multitarget super-resolution microscopy with high-density labeling by exchangeable probes. Nat Methods 12, 743-746.
Kleele, T., Marinkovic, P., Williams, P.R., Stern, S., Weigand, E.E., Engerer, P., Naumann, R., Hartmann, J., Karl, R.M., Bradke, F., et al. (2014). An assay to image neuronal microtubule dynamics in mice. Nature communications 5, 4827.
Konishi, Y., and Setou, M. (2009). Tubulin tyrosination navigates the kinesin-1 motor domain to axons. Nat Neurosci 12, 559-567.
Kuijpers, M., van de Willige, D., Freal, A., Chazeau, A., Franker, M.A., Hofenk, J., Rodrigues, R.J., Kapitein, L.C., Akhmanova, A., Jaarsma, D., and Hoogenraad, C.C. (2016). Dynein Regulator NDEL1 Controls Polarized Cargo Transport at the Axon Initial Segment. Neuron 89, 461-471.
Leterrier, C., and Dargent, B. (2014). No Pasaran! Role of the axon initial segment in the regulation of protein transport and the maintenance of axonal identity. Seminars in cell & developmental biology 27, 44-51.
Lipka, J., Kapitein, L.C., Jaworski, J., and Hoogenraad, C.C. (2016). Microtubule-binding protein doublecortin-like kinase 1 (DCLK1) guides kinesin-3-mediated cargo transport to dendrites. EMBO J 35, 302-318.
Maniar, T.A., Kaplan, M., Wang, G.J., Shen, K., Wei, L., Shaw, J.E., Koushika, S.P., and Bargmann, C.I. (2012). UNC-33 (CRMP) and ankyrin organize microtubules and localize kinesin to polarize axon-dendrite sorting. Nat Neurosci 15, 48-56.
Mikhaylova, M., Cloin, B.M., Finan, K., van den Berg, R., Teeuw, J., Kijanka, M.M., Sokolowski, M., Katrukha, E.A., Maidorn, M., Opazo, F., et al. (2015). Resolving bundled microtubules using anti-tubulin nanobodies. Nature communications 6, 7933.
Molle, J., Raab, M., Holzmeister, S., Schmitt-Monreal, D., Grohmann, D., He, Z., and Tinnefeld, P. (2016). Superresolution microscopy with transient binding. Curr Opin Biotechnol 39, 8-16.
Nakata, T., and Hirokawa, N. (2003). Microtubules provide directional cues for polarized axonal transport through interaction with kinesin motor head. J Cell Biol 162, 1045-1055.
Nirschl, J.J., Ghiretti, A.E., and Holzbaur, E.L.F. (2017). The impact of cytoskeletal organization on the local regulation of neuronal transport. Nat Rev Neurosci 18, 585-597.
Patterson, G., Davidson, M., Manley, S., and Lippincott-Schwartz, J. (2010). Superresolution imaging using single-molecule localization. Annu Rev Phys Chem 61, 345-367.
Rasband, M.N. (2010). The axon initial segment and the maintenance of neuronal polarity. Nat Rev Neurosci 11, 552-562.
Rolls, M.M. (2011). Neuronal polarity in Drosophila: sorting out axons and dendrites. Developmental neurobiology 71, 419-429.
Sampo, B., Kaech, S., Kunz, S., and Banker, G. (2003). Two distinct mechanisms target membrane proteins to the axonal surface. Neuron 37, 611-624.
Sharma, A., Aher, A., Dynes, N.J., Frey, D., Katrukha, E.A., Jaussi, R., Grigoriev, I., Croisier, M., Kammerer, R.A., Akhmanova, A., et al. (2016). Centriolar CPAP/SAS-4 Imparts Slow Processive

Microtubule Growth. Dev Cell 37, 362-376.
Sharonov, A., and Hochstrasser, R.M. (2006). Wide-field subdiffraction imaging by accumulated binding of diffusing probes. Proc Natl Acad Sci U S A 103, 18911-18916.
Sirajuddin, M., Rice, L.M., and Vale, R.D. (2014). Regulation of microtubule motors by tubulin isotypes and post-translational modifications. Nat Cell Biol 16, 335-344.
Sivaramakrishnan, S., and Spudich, J.A. (2009). Coupled myosin VI motors facilitate unidirectional movement on an F-actin network. J Cell Biol 187, 53-60.
Song, A.H., Wang, D., Chen, G., Li, Y., Luo, J., Duan, S., and Poo, M.M. (2009). A selective filter for cytoplasmic transport at the axon initial segment. Cell 136, 1148-1160.
Stepanova, T., Slemmer, J., Hoogenraad, C.C., Lansbergen, G., Dortland, B., De Zeeuw, C.I., Grosveld, F., van Cappellen, G., Akhmanova, A., and Galjart, N. (2003). Visualization of microtubule growth in cultured neurons via the use of EB3-GFP (end-binding protein 3-green fluorescent protein). J Neurosci 23, 2655-2664.
Stiess, M., and Bradke, F. (2011). Neuronal polarization: the cytoskeleton leads the way. Developmental neurobiology 71, 430-444.
Vale, R.D. (2003). The molecular motor toolbox for intracellular transport. Cell 112, 467-480.
Verhey, K.J., and Gaertig, J. (2007). The tubulin code. Cell Cycle 6, 2152-2160.
Watanabe, K., Al-Bassam, S., Miyazaki, Y., Wandless, T.J., Webster, P., and Arnold, D.B. (2012). Networks of polarized actin filaments in the axon initial segment provide a mechanism for sorting axonal and dendritic proteins. Cell reports 2, 1546-1553.
Wisco, D., Anderson, E.D., Chang, M.C., Norden, C., Boiko, T., Folsch, H., and Winckler, B. (2003). Uncovering multiple axonal targeting pathways in hippocampal neurons. J Cell Biol 162, 1317-1328.
Yau, K.W., Schatzle, P., Tortosa, E., Pages, S., Holtmaat, A., Kapitein, L.C., and Hoogenraad, C.C. (2016). Dendrites In Vitro and In Vivo Contain Microtubules of Opposite Polarity and Axon Formation Correlates with Uniform Plus-End-Out Microtubule Orientation. J Neurosci 36, 1071-1085.
Yau, K.W., van Beuningen, S.F., Cunha-Ferreira, I., Cloin, B.M., van Battum, E.Y., Will, L., Schatzle, P., Tas, R.P., van Krugten, J., Katrukha, E.A., et al. (2014). Microtubule minus-end binding protein CAMSAP2 controls axon specification and dendrite development. Neuron 82, 1058-1073.

SUPLEMENTAL EXPERIMENTAL PROCEDURES

Cell Lines and Tissue Culture

COS7 cells were cultured in DMEM/Ham's F10 (1:1) medium containing 10% FCS and penicillin/streptomycin.

Primary hippocampal cultures were prepared from embryonic day 18 (E18) rat brains (Kapitein et al., 2010b). Cells were plated on coverslips coated with poly-L-lysine (37.5 μg ml^{-1}) and laminin (1.25 μg ml^{-1}). Hippocampal cultures were grown in Neurobasal medium (NB) supplemented with 2% B27 (Invitrogen), 0.5 mM glutamine, 15.6 μM glutamate, and 1% penicillin plus streptomycin.

The sex of cells was not determined.

DNA constructs and Protein purification

To generate DmKHC(1-421)-GFP-6xHis, amino acids 1-421 of the *Drosophila* kinesin heavy chain were inserted in a pET28a-GFP-6xHis expression vector in the NcoI and EcoRI site. GFP was previously inserted between the EcoRI and XhoI sites. The construct was verified by

sequencing and transformed in the BL21DE3 bacterial strain. The GFP-Rigor-KIF5A cloned into a peGFP vector was a gift from Ginny Farías (Farias et al., 2015). pβactin-Kif1a-FRB was described previously (Lipka et al., 2016). Kif1a-Rigor-GFP-FRB was cloned by PCR of the N-terminus (AA1-253) and the fused C-terminus (AA253-383-GFP) of Kif1a, substituting glutamic acid to lysine at amino acid 253. Both fractions were fused through Gibson assembly (addgene) and ligated into pβactin restricted with AscI/SpeI.

To express the DmKHC(1-421)-GFP-6xHis, a 2L culture was grown until OD0.6. Expression was induced with 1mM of IPTG and cells were grown for 0.5 hours at 37 ºC and 3.5 hours at 20 ºC. Cells were then pelleted by centrifugation and resuspended on ice in resuspension buffer (20mM Pipes, 150mM NaCL, 4 mM $MgSO_4$, pH7.0) supplemented with lysozyme and protease inhibitor cocktail (Roche). Subsequently, cells were lysed through 5 rounds of 30 seconds sonication. The soluble fraction containing the expressed protein was separated through 40 minutes centrifugation at 20000g and incubated with NiNTA beads (Roche) for 1 hour at 4 ºC.

Beads were washed 3 times in resuspension buffer supplemented with 50 μM ATP and in the last wash 60mM imidazole was added. Recombinant protein was eluted for 15 minutes in Elution buffer (80mM Pipes, 4mM $MgSO_4$, 300mM imidazole, 50μM ATP, pH7.0). The supernatant was concentrated to 0.5 ml and recombinant protein was further purified and buffer exchanged through gel filtration on a superdex75 column (GE Healthcare, Superdex 75 10/300) equilibrated with PEM80 buffer (80 mM Pipes, 4mM MgCl2, 1 mM EGTA). Fractions containing DmKHC(1-421)-GFP-6xHis were identified by SDS-page, collected and stored at -80 ºC in 10% glycerol after snap-freezing in liquid nitrogen.

Cell transfection

COS7 and U2OS cells were plated on 18-mm diameter coverslips 2–4 days before transfection. Cells were transfected with Fugene6 transfection reagent (Roche) according to the manufacturer's protocol and imaged one day after transfection.

Transfections of hippocampal neurons were performed 24 h before imaging with lipofectamine 2000 (Invitrogen). DNA (1.8 μg per well) was mixed with 3.3 μl lipofectamine 2000 in 200 ml NB, incubated for 30 min, and added to the neurons in NB supplemented with 0.5 mM glutamine at 37 °C in 5% CO_2. After 60-90 min neurons were washed with NB and transferred to the original medium at 37 °C in 5% CO_2 for 1 day.

Kinesin motility assay

To prepare cellular microtubule cytoskeletons for the kinesin motility assays, the cytoplasm of COS7-cells or hippocampal neurons was extracted for 1 minute in extraction buffer (1M sucrose + 0.15% Triton-X in PEM80) at 37 ºC. Subsequently, an equal amount of fixation buffer (2% PFA in PEM80 at 37 ºC) was added and the solution was gently mixed by pipetting for 1 minute. The extraction and fixation buffer were then replaced by washing solution

(PEM80 + 100nM Paclitaxel 37 ºC) for 1 minute. After three more 1-minute washes imaging buffer (1.7% w/v glucose, 185 µg/ml glucose oxidase, 40 µg/ml catalase, 5mM ATP, 1mM DTT, 100mM Paclitaxel in PEM80 buffer at 37 ºC) was added.

mCherry-tubulin expressing cells were selected for imaging and after a conventional preacquisition of cherry-tubulin, 1 µl of approximately 30nM DmKHC(1-421)-GFP-His was added above the location of acquisition and 10000-20000 frames were acquired at 10 Hz using stream acquisition. Because the concentration of visible kinesins at the selected position gradually decreased because of diffusion and photobleaching, recombinant kinesin was supplemented during imaging to increase the number of localizations of motile kinesins.

For the Nocodazole washout experiments (Figure 1D), COS7 cells were treated with 10 µM nocodazole (M1404, Sigma-Aldrich) for 1 hour at 37 ºC followed by 1 hour incubation at 4 ºC. Samples were washed 6x times with cold culturing medium. Subsequently, microtubules were allowed to polymerize for ~6 minutes at 37 ºC. Finally, extracted microtubule cytoskeletons were prepared as described earlier. Nocodazole treatments in neurons were performed by using 4 µM nocodazole in the culture medium for 2.5 hours.

Most samples were imaged on a Nikon Ti-E microscope equipped with a 100x Apo TIRF oil immersion objective (NA. 1.49) and Perfect Focus System 3. Excitation was achieved with a mercury lamp or via a custom illumination pathway starting with a Lighthub-6 (Omicron) containing a 638 nm laser (BrixX 500 mW multimode, Omicron), a 488nm laser (Luxx 200 mW, Omicron) and using an optical configuration that allowed tuning the angle of incidence. In most instances, total internal reflection or highly inclined laser illumination was used. Emission light was separated from excitation light with a quad-band polychroic mirror (ZT405/488/561/640rpc, Chroma), a quad-band emission filter (ZET405/488/561/640m, Chroma), and an additional single-band emission filter (ET525/50m for GFP emission, Chroma), and detected using a sCMOS camera (Hamamatsu Flash 4.0v2). In some cases, a very similar microscope that has been previously described (Chazeau et al., 2016) was used in the same configuration (see section "Immunocytochemistry, (correlative) SMLM, confocal and gSTED). All components were controlled by Micromanager software (Chazeau et al., 2016).

Immunocytochemistry, (correlative) SMLM, confocal and gSTED imaging

Extraction, fixation and immunocytochemistry (ICC) were performed as previously described (Chazeau et al., 2016). Briefly, cells were incubated for 90 seconds in a extraction buffer preheated at 37 °C (80 mM pipes, 2 mM MgCl2, 1 mM EGTA, 0.3% Triton® X100 and 0.25% glutaraldehyde, pH 6.9), followed by incubation with 4% PFA preheated at 37 °C for 10 minutes. Neurons were further permeabilized with 0.25% Triton® X100 and blocking was performed with 2% w/v bovine serum albumin (BSA), 0.2% gelatin, 10 mM glycine, 50 mM NH4Cl in PBS, pH 7.4. Primary and secondary antibodies were incubated for 1h at room temperature in blocking buffer. For SMLM (single-molecule localization microscopy), samples

were post-fixed in 2% PFA for 10 minutes. Primary and secondary antibodies used in this study are the following: rat monoclonal anti tyrosinated tubulin (Abcam, [YL1/2], ab6160), mouse monoclonal anti acetylated tubulin (Sigma, [6-11B-1], T7451), rabbit polyclonal anti Δ2 tubulin (Millipore, AB3203), mouse monoclonal anti EB1 (BD Bioscience, [clone 5], 610535), Rabbit polyclonal anti GFP (MBL Sanbio, 598),Alexa Fluor® 647 Goat Anti-Rat IgG (H+L) (Molecular Probes®, Life Technologies™ A21247), Alexa Fluor® 488 Goat Anti-Rat IgG (H+L) (Molecular Probes®, Life Technologies™ A11006), Alexa Fluor® 647 Goat Anti-Mouse IgG (H+L) (Molecular Probes®, Life Technologies™ A21236), Alexa Fluor® 594 Goat Anti-Mouse IgG (H+L) (Molecular Probes®, Life Technologies™ A11032), Alexa Fluor® 568 Goat Anti-Mouse IgG (H+L) (Molecular Probes®, Life Technologies™ A11031), Alexa Fluor® 568 Goat Anti-Rabbit IgG (H+L) (Molecular Probes®, Life Technologies™ A11036), Alexa Fluor® 594 Goat Anti-Rabbit IgG (H+L) (Molecular Probes®, Life Technologies™ A11032).

Gated STED (gSTED) imaging of acetylated and tyrosinated MTs (Figure 2) was performed with a Leica TCS SP8 STED 3X microscope using a HC PL APO 100x/1.4 oil STED WHITE objective. For excitation of Alexa647 and Alexa594, a pulsed white laser (80MHz) was used at 641 nm and 594 nm, respectively, whereas a 775 nm pulsed laser was used for depletion. Images were acquired in 2D STED mode with the vortex phase mask. Depletion laser power was equal to 35% and 70% of maximum power for Alexa647 and Alexa594, respectively. We used an internal Leica GaAsP HyD hybrid detector with a time gate (tg) of $0.3 \leq tg \leq 6$ ns and $0.8 \leq tg \leq 8$ ns for Alexa647 and Alexa594, respectively. Confocal two color imaging was performed on the same setup using the same white laser excitation and emission settings from LAS X controlling software library. Alternatively, for Figure S4C,D confocal images were acquired using a LSM 700 confocal laser-scanning microscope (Zeiss) with a 63×1.4 N.A. oil objective.

To correlate microtubule orientations and acetylated tubulin using SMLM, motor-PAINT was performed as described above on DIV9/DIV10 neurons. Subsequently the imaged positions were saved and the sample was removed from the microscope but kept in the imaging chamber. To remove the motors from the microtubule lattice the sample was washed two times in PEM80 supplemented with 100 nM paclitaxel and 5 mM ATP. Cells were fixed in 0.3% Glutaraldehyde, 2% PFA and 100 nM paclitaxel in PEM80 for three minutes. After fixation the sample was washed three times in wash buffer (PEM80 with 100 nM paclitaxel) followed by a 30 minute block in blocking buffer (3% BSA, 100 nM paclitaxel in PEM80). Cells were then incubated for one hour with 1/400 mouse anti-acetylated antibody in blocking buffer. After incubation cells were washed three times in washing buffer and incubated for one hour with secondary anti-mouse AlexaFluor647 1/400 in blocking buffer. After three more washes in wash buffer, the buffer was exchanged for imaging buffer (50-100mM MEA, 5% w/v glucose, 700 μg/ml glucose oxidase, 40 μg/ml catalase in PEM80). The sample in the imaging chamber was placed back on the microscope in exactly the same position and the regions where motor-PAINT was performed were imaged by SMLM as described below for

Alexa647.

Two color SMLM imaging (Fig. S4A,B) was performed as previously described (Chazeau et al., 2016) on a Nikon Ti microscope equipped with a 100x Apo TIRF oil objective (NA. 1.49), a Perfect Focus System and an additional 2.5x Optovar to achieve an effective pixel size of 64 nm. Oblique laser illumination was achieved using a custom illumination pathway with a 15 mW 405 nm diode laser (Power Technology), a 50mW 491 nm DPSS laser (Cobolt Calypso) and a 40 mW 640 nm diode laser (Power Technology). Fluorescence was detected using a water-cooled Andor DU-897D EMCDD camera and ET series Cy5 filter (Chroma Technology). All components were controlled by Micromanager software (Edelstein et al., 2010). The composition of the imaging buffer was 100mM MEA, 5% w/v glucose, 700 μg/ml glucose oxidase, 40 μg/ml catalase in PBS buffer. Alexa Fluor 647 and Alexa Fluor A488 were imaged sequentially, using continuous illumination with 640 nm and 491 nm light, respectively. During acquisition, the sample was illuminated with 405 nm light at increasing intensity to keep the number of fluorophores in the fluorescent state constant. Between 10000 and 20000 frames were recorded per acquisition with exposure time of 30/40 ms.

Antibody combinations

	Primary Antibodies	Secondary Antibodies	Technique/Microscope
Figure 2D-E	Rat anti tyrosinated tubulin Mouse anti acetylated tubulin	Anti Rat Alexa 647 Anti Mouse Alexa 594	Confocal and gSTED/ Leica TCS SP8
Figure 3A-B	Rat anti tyrosinated tubulin Mouse anti acetylated tubulin	Anti Rat Alexa 488 Anti Mouse Alexa 568	Confocal/ Zeiss LSM 700
Figures 3F and Figure S5	Mouse anti acetylated tubulin	Anti Mouse Alexa 647	SMLM/ Nikon Ti
Figure S4	Rat anti tyrosinated tubulin Mouse anti acetylated tubulin	Anti Rat Alexa 488 Anti Mouse Alexa 647	SMLM/ Nikon Ti
Figure S4C	Rat anti tyrosinated tubulin Rabbit anti Δ2 tubulin	Anti Rat Alexa 488 Anti Rabbit Alexa 568	Confocal/ Zeiss LSM 700
Figure S4D	Rat anti tyrosinated tubulin Mouse anti EB1	Anti Rat Alexa 488 Anti Mouse Alexa 568	Confocal/ Zeiss LSM 700

Figure 4B and Figure S6B	Mouse anti acetylated Rabbit anti GFP	Anti mouse Alexa 647 Anti rabbit Alexa 594	gSTED/ Leica TCS SP8
Figure 4A-B and Figure S6C	Rat anti tyrosinated tubulin Rabbit anti GFP	Anti Rat Alexa 647 Anti rabbit Alexa 594	gSTED/ Leica TCS SP8
Figure S6A	Mouse anti tubulin Rabbit anti GFP	Anti mouse Alexa 647 Anti rabbit alexa 594	gSTED/ Leica TCS SP8
Figure S6D-H	Rat anti tyrosinated tubulin Mouse anti acetylated Rabbit anti GFP	Anti Rat Alexa 594 Anti Mouse Alexa 647 Anti rabbit Alexa 488	gSTED/ Leica TCS SP8

Simulations

Simulations of motors on microtubule orientations with different ratios of plus and minus end out oriented microtubules were performed as described previously (Kapitein et al., 2010a). In the same reference, we also derived the mathematical expression for the distributions of kinesin-propelled cargoes on different arrays as a function of the fractional orientation probabilities p_+ and p_- and the average run length before switching microtubules l:

$$c(x) = c_0 e^{\alpha x}, \text{ with } \alpha = \frac{p_+ - p_-}{l}$$

Integrating this to calculate the number of particles n at x_n gives

$$n = \frac{1}{\alpha}\left(e^{\alpha x_n} - 1\right)$$

From this, the dendritic coordinate $L_{50\%}$ at which the number of particles before that position equals the number of particles beyond that position can be found by solving

$$\frac{1}{\alpha}\left(e^{\alpha L_{50\%}} - 1\right) = \frac{1}{2\alpha}\left(e^{\alpha L_{dendrite}} - 1\right), \text{ which gives}$$

$$L_{50\%} / L_{dendrite} = \frac{1}{\alpha} \ln\left(\frac{1}{2} e^{\alpha L_{dendrite}} + \frac{1}{2}\right) / L_{dendrite}$$

Single molecule localization and track orientation analysis

Images were analyzed using our custom ImageJ plugin called DoM (Detection of Molecules, https://github.com/ekatrukha/DoM_Utrecht), which has been described in detail previously (Chazeau et al., 2016; Yau et al., 2014). Briefly, each image in an acquired stack was convoluted with a two dimensional Mexican hat-type kernel that matches the microscope's point spread function (PSF) size. Spots were detected by thresholding the images and their sub-pixel positions were determined by fitting a 2D Gaussian function using unweighted nonlinear least squares fitting with the Levenberg-Marquardt algorithm. Drift correction was applied by calculating the spatial cross-correlation function between intermediate super-resolved reconstructions.

To link localizations into motor trajectories, the linking function of DoM was used as described previously (Sharma et al., 2016). Briefly, linking was performed using a nearest neighbor algorithm were the maximum permitted distance between detected molecules in two subsequent frames, was 3 pixels (~192 nm). No frame gap was permitted within a track. Only individual tracks that could be observed for at least 3 subsequent frames were included for further analysis. In addition, trajectories in which the angle between two segments was larger than 75 degrees were discarded.

Next, trajectories were separated into different tables based on their direction. For non-neuronal cells, localizations belonging to validated tracks were separated into four different particle tables defined by four criteria for the total displacement in x and y coordinates of the track (i.e. $\Delta x>0 \wedge \Delta y>0$; $\Delta x>0 \wedge \Delta y<0$; $\Delta x<0 \wedge \Delta y>0$; $\Delta x<0 \wedge \Delta y<0$). For neuronal cells, particle tables were separated into two particle tables corresponding to the axis of the dendrite. The resulting particle tables were subsequently reconstructed using DoM into different super-resolved images that represented all microtubules with similar orientations.

Because the average frame-to-frame displacement of motors was 75 ± 30 nm, tracks appeared as a series of dots when rendered at small pixel sizes. To better visualize these tracks, additional localizations were inserted with a spacing of 15 nm by interpolating between two subsequent localizations within tracks. The localization precision was set as the average of the two observed localizations. Nevertheless, to avoid potential artefacts, all quantifications were performed on the non-interpolated data sets and images.

Correlation analysis

To determine the degree of overlap between images obtained from the retrograde and anterograde runs, the correlation coefficient $C_{in/out}$ was calculated as

$$C_{in/out} = \frac{\sum_{x=1}^{X}\sum_{y=1}^{Y} i_{in}(x,y)\, i_{out}(x,y)}{\sqrt{\sum_{x=1}^{X} i_{in}^2(x,y) \sum_{y=1}^{Y} i_{out}^2(x,y)}}$$

Where i_{in}(x,y) and i_{out}(x,y) are the intensities of the images based on anterograde and retrograde runs at pixel (x,y), respectively. Similarly, the correlation coefficient Codd/even was calculated from the intensities i_{odd}(x,y) and i_{even}(x,y) of the images based on odd and even localizations within tracks (see Fig. S2). The curves of C against different pixel sizes were fitted in Graphpad Prism 5 using the functions described in the legends.

Ratio analysis

Ratios of minus-end out versus minus-end in microtubules were determined based on the intensity of the localizations in either direction. Every detected motor localization in a valid track was normalized to an intensity of 1, so that for both orientations the sum value per image reflected the number of localizations in a specific direction. Subsequently a 5µm segment of a dendrite was selected. These sum values could be presented as arbitrary values along the segment (e.g. Fig. 1F) or the total intensity in the minus-end out versus minus-end in was plotted against each other (e.g. Fig. 1G) or the ratio of each trace was averaged and used as a single data point (e.g. Fig. 1H).

Statistical parameters are included in the figures or corresponding legends. The number of measured segments from different cells is indicated. All quantified data is obtained from at least 3 independent experiments from neurons cultured from different batches. ***, P <0.001 as tested by a T-test or non-parametric Mann-Whitney test.

SUPPLEMENTARY FIGURES

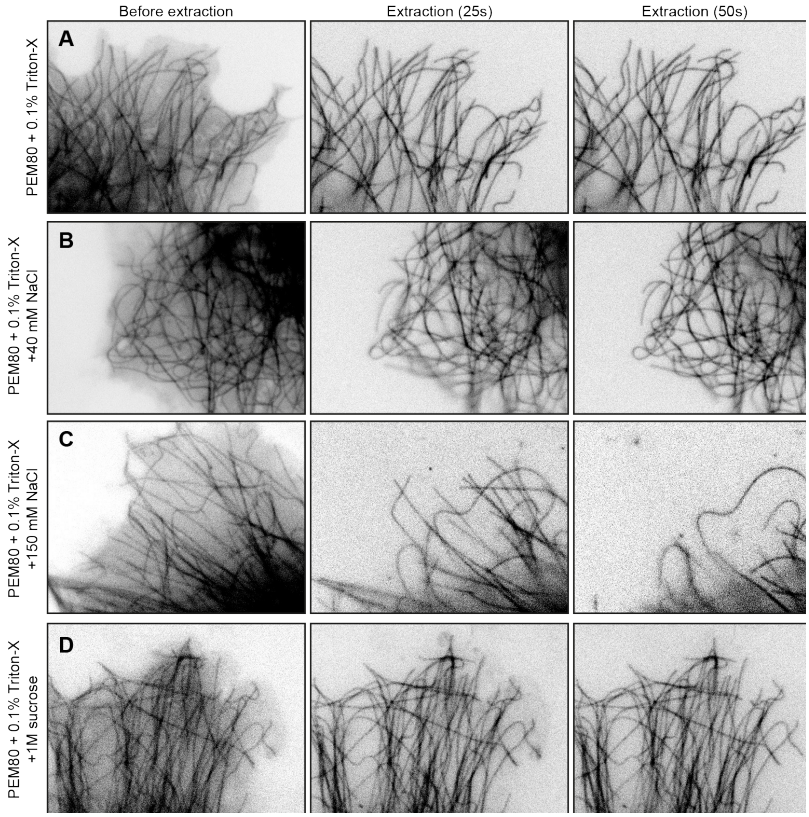

Figure S1 (related to Figure 1): Preservation of the microtubule cytoskeleton during extraction
Optimization of the extraction protocol to preserve microtubule organization in COS7 cells expressing cherry-tubulin. Images shown were obtained before extraction (left), 25 seconds after extraction (middle), or 50 seconds after extraction and before fixation (right). Extraction was performed in the presence of 0.1-0.15% Triton-X in PEM80 buffer (A), supplemented with NaCl (B,C) or sucrose (D). The conditions in d were used for all subsequent experiments.
Scale bar: 2 µm

Figure S2 (related to Figure 1): Super-resolution imaging of microtubules and their orientations
A) *COS7 cell expressing mCherry-tubulin shown before extraction (left), during extraction (middle) and after fixation (right). Zoom indicates the region of interest for which the microtubule orientations are determined in b.*
B) *Three subsequent frames from a 10.000 frame recording of the zoom region in a.*
C) *Median-filtered (0.3 pixel size) standard deviation projection of the complete 10.000 frame recording of the zoom region in A (also see Supplemental Video 1).*
D) *FWHM of cross sections of microtubule imaged by motor tracking (mean±s.d.: 52±1 nm, n=30 profiles).*
E) *Zoom of cell shown in A expressing mCherry-tubulin (left) and corresponding super-resolved image obtained by subpixel localization of thousands of motor binding events (middle, 255466 localizations).*

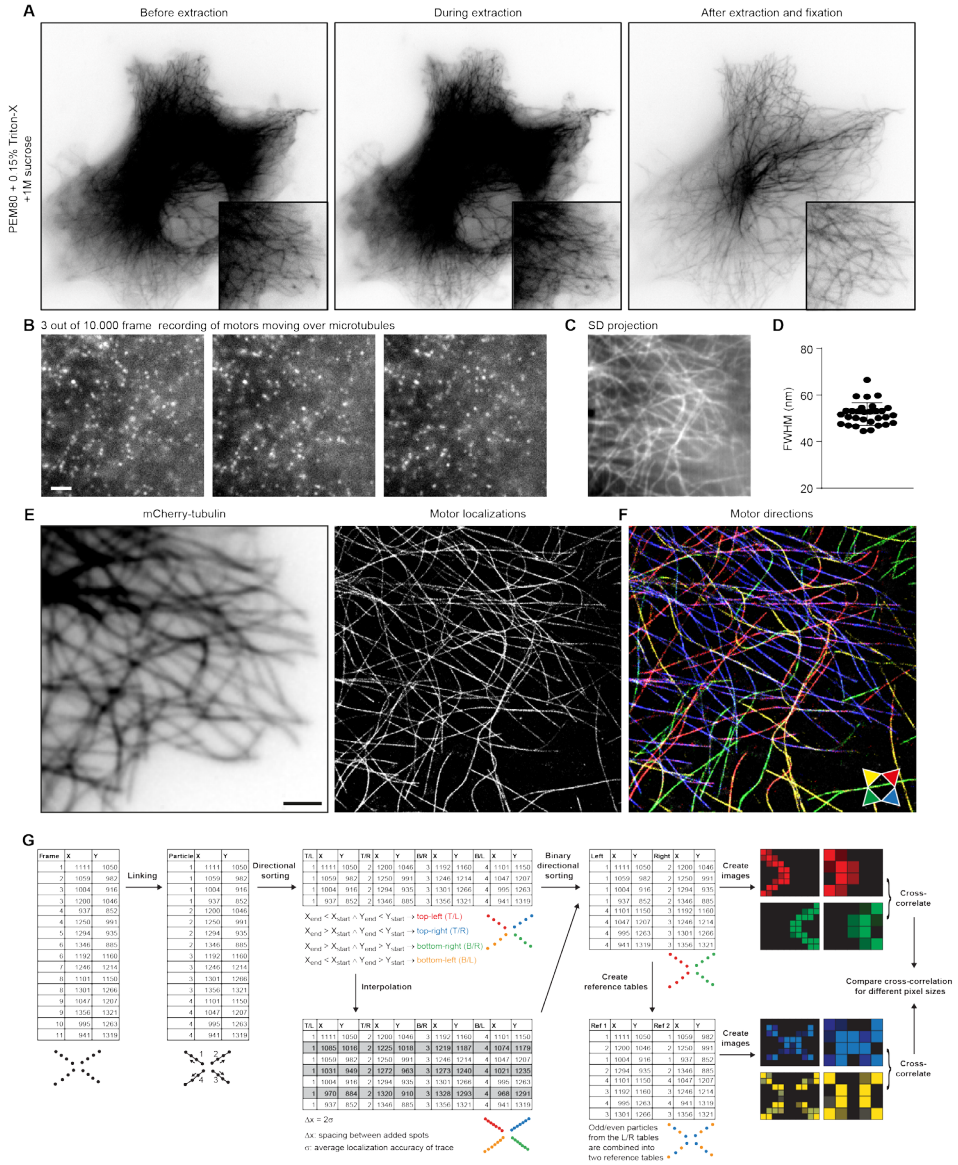

F) *Super-resolution reconstruction with all microtubule segments colored according to their absolute orientation. Legend arrows point in the direction of the plus end. Directional image obtained from 19511 motor trajectories with 72846 localizations and created using track interpolation (see methods).*
G) *Particle tables containing single molecule information are linked to generate tracks and the resulting tracks are sorted based on the orientation. Optionally, tracks are interpolated to enhance visualization. For neuronal acquisitions tracks are sorted in two bidirectional tables. To analyze the overlap, control particle tables are created by sorting even and odd localizations, irrespective of orientations. Subsequently, the correlation coefficient is calculated for the orientation images or the reference images. (related to Figure 1,2,3,4).*
Scale bar: 2 µm

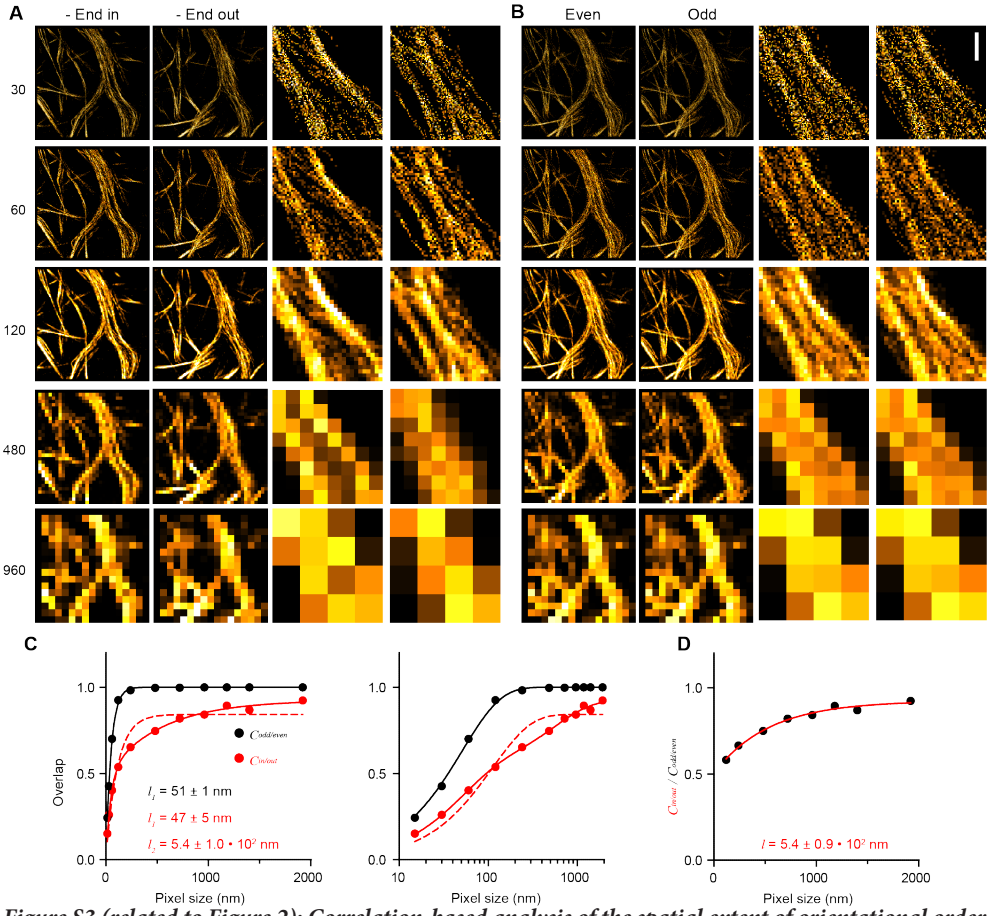

Figure S3 (related to Figure 2): Correlation-based analysis of the spatial extent of orientational order

A) *Motor-based super-resolution reconstructions of a dendritic segment, based on inward runs (left and left zoom) or outward runs (right and right zoom) and rendered at different pixel sizes.*

B) *Motor-based super-resolution reconstructions of the same segment, based on all even (left and left zoom) or odd (right and right zoom) localizations, irrespective of direction, and rendered at different pixel sizes.*

C) *Degree of overlap as a function of reconstruction pixel size, obtained by calculating the correlation coefficient between reconstructions of minus-end in and minus-end out tracks ($C_{in/out}$), or reconstructions of even and odd localizations, irrespective of direction ($C_{odd/even}$). Solid black and dotted red lines are fits of* $C = A(1-\exp(p/l))$ *, whereas the solid red line is a fit with* $C = A(1 - B\exp(p/l_1) - (1-B)\exp(p/l_$ *. Error bars of SE fall within symbol size.*

D) *Ratio between $C_{in/out}$ and $C_{odd/even}$ for pixel sizes >100 nm and fitted with* $C = A(1-\exp(p/l))$ *. Error bars of SE fall within symbol size.*

Scale bar: 1 µm

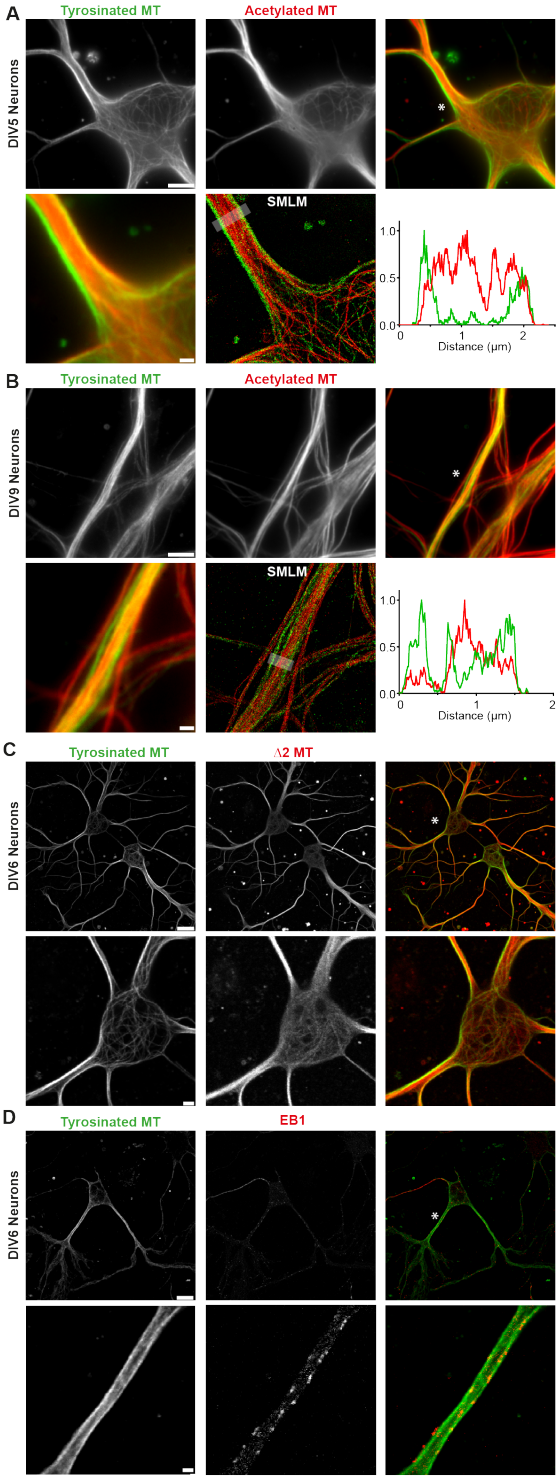

Figure S4 (related to Figure 2): Imaging of tyrosinated, acetylated, Δ2-positive and EB1 decorated MTs in dendrites

A) DIV5 neurons immunostained for tyrosinated (top left) and acetylated (top middle) tubulin. Top right: merge. A zoom from the merged image (bottom left) is compared to the merged SMLM reconstruction (bottom middle). Bottom right: Intensity profiles from tyrosinated and acetylated MT along the line indicated in the SMLM image.

***B)** Similar to a, but for DIV9 neurons.*

***C)** DIV6 neurons immunostained for tyrosinated (left) and Δ2 (middle) tubulin. Right: merge.*

***D)** DIV6 neurons immunostained for tyrosinated tubulin (left) and EB1 (middle). Right: merge.*

Scale bar: 5 µm (A), 1 µm (B), 10 µm (C), 2 µm (D)

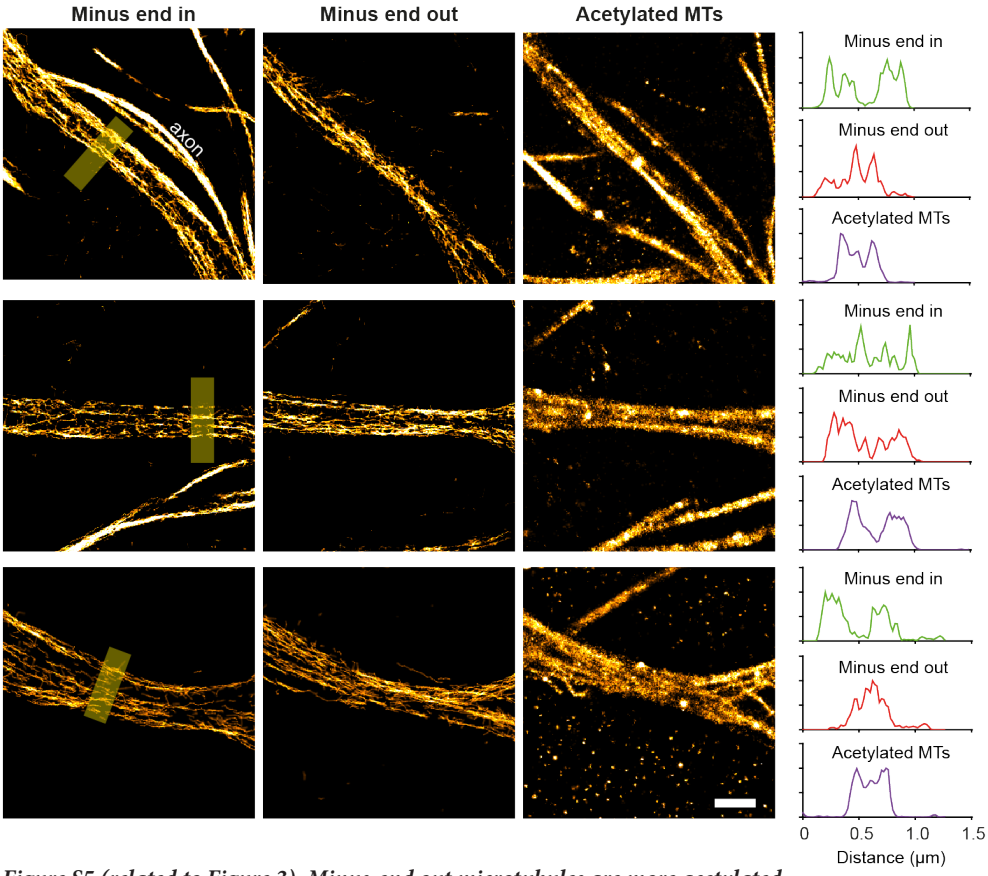

Figure S5 (related to Figure 3). Minus-end out microtubules are more acetylated
A) *Three additional examples showing correlative motor-PAINT and SMLM for acetylated tubulin. After motor-PAINT cells were stained for acetylated tubulin.*
B) *Line scans corresponding to each individual channel in A.*
Scale bar: 1 µm

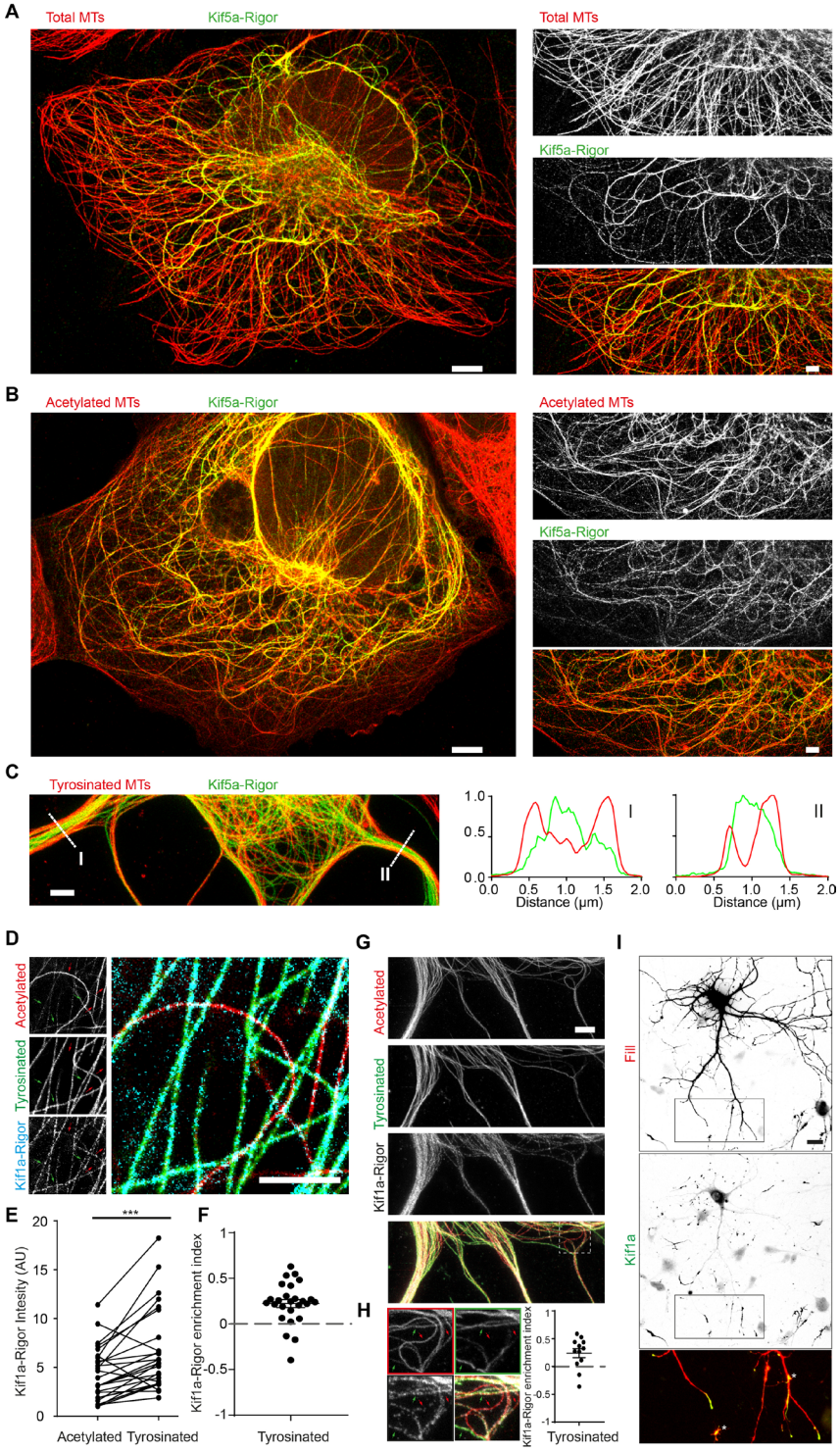
A
Total MTs
Kif5a-Rigor
Total MTs
Kif5a-Rigor
B
Acetylated MTs
Kif5a-Rigor
Acetylated MTs
Kif5a-Rigor
C
Tyrosinated MTs
Kif5a-Rigor
I
II
1.0
0.5
0.0
0.0 0.5 1.0 1.5 2.0
Distance (μm)
D
Acetylated
Tyrosinated
Kif1a-Rigor
E
***
Kif1a-Rigor Intesity (AU)
20
15
10
5
0
Acetylated Tyrosinated
F
Kif1a-Rigor enrichment index
1
0.5
0
-0.5
-1
Tyrosinated
G
Acetylated
Tyrosinated
Kif1a-Rigor
H
Kif1a-Rigor enrichment index
1
0.5
0
-0.5
-1
Tyrosinated
I
Fill
Kif1a

Figure S6 (related to Figure 4): Kinesin-1 and Kinesin-3 prefer different microtubule subsets
A,B) *STED imaging of COS7 cells after 1 day expression of GFP-kif5a rigor stained for GFP and acetylated-tubulin (A) or GFP and acetylated-tubulin (B). Cellular overview (left) and Zooms of (right) are shown.*
C) *Linescans across the minor neurite (I) and longest neurite (II) for the segments shown in Fig. 4A for tyrosinated-tubulin and the kif5a rigor.*
D) *STED imaging of COS7 cells after 1 day, low-level, expression of Kif1a-Rigor-GFP stained for GFP, acetylated- and tyrosinated-tubulin. Predominantly acetylated microtubules are indicated by red arrows, tyrosinated microtubules by green arrows.*
E) *Paired Kif1a-Rigor intensities on neighboring microtubules that are predominantly tyrosinated compared to acetylated microtubules, within the same imaged region. n= 26 pairs, N= 2, Paired Wilcoxon non-parametric test: ***, p<0.001*
F) *Kif1a-Rigor enrichment index in Cos7 cells for Tyrosinated microtubules calculated for data in (E). Calculated by substracting the Kif1a-Rigor intensity on acetylated microtubules from tyrosinated microtubules subsequently divided by the total signal on both populations. Positive values mean enrichment on tyrosinated-tubulin, negative values on acetylated microtubules, Mean ±SEM. Mean = 0.223 corresponding to a 1.58 fold enrichment on tyrosinated microtubules.*
G) *STED imaging of DIV 3 neurons after 1 day expression of kif1a Rigor-GFP stained for GFP, acetylated- and tyrosinated-tubulin.*
H) *Zoom of region in (G) and corresponding quantification of Kif1a-Rigor microtubule preference. Red arrows indicate exclusively acetylated microtubules, green arrows indicate tyrosinated microtubules. Quantification as in (F) but measured on individual tyrosinated, acetylated microtubule pairs in neurons. Mean ±SEM, n= 12 pairs, N= 2, paired T-test performed on the raw paired intensities (as in (E)) shows p = 0.0062 confirming statistical significance of Kif1a-Rigor preference in neurons. Mean = 0.223 corresponding to a 1.63 fold enrichment on tyrosinated microtubules.*
I) *DIV 10 neuron overexpressing a mCherry fill and Kif1a-GFP to assess Kif1a localization. Asterisks in zoom indicate axonal tips.*
Scale bars: 20 µm (I); 5 µm (A,B overview); 2 µm (A,B,C zooms and D,G)

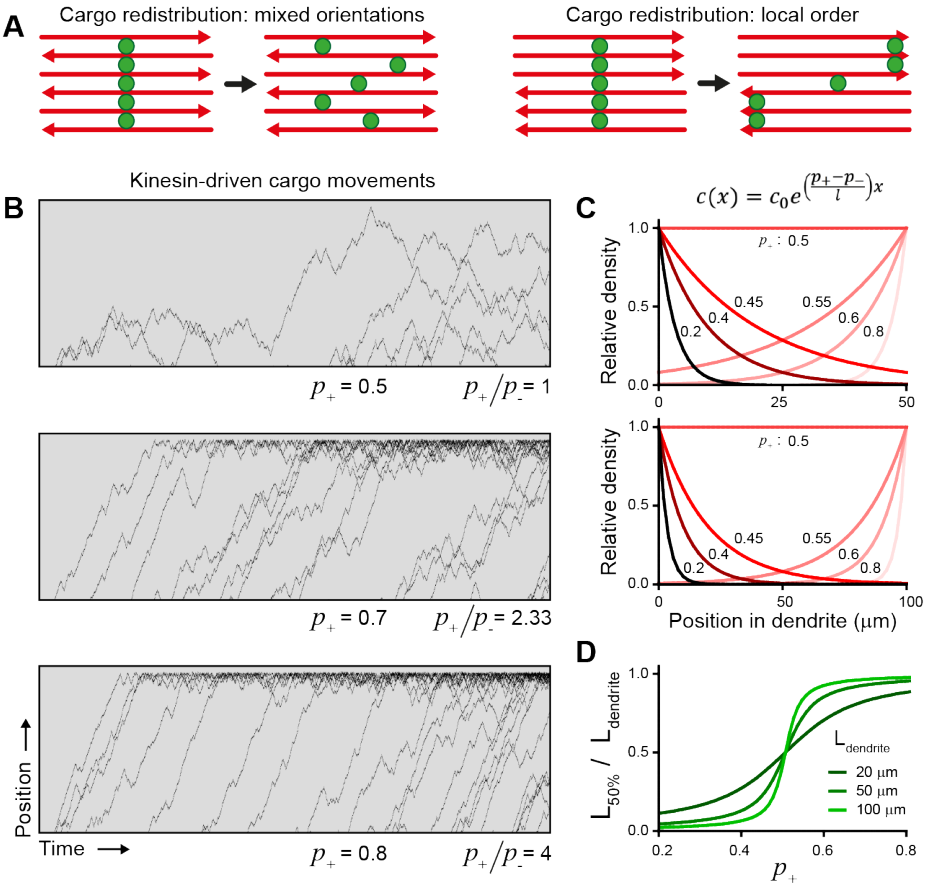

Figure S7 (related to Figure 4). Orientational order and directional transport

A) *Illustration depicting the influence of microtubule organization on directional transport.*

B) *Simulated kymographs of kinesin-driven transport on microtubules arrays with different fractions of plus-end out oriented microtubules p_+, as indicated. A small asymmetry in orientations results in a strong directional bias. Total dendrite length $L_{dendrite}$ is 100 µm and average run length l before selecting a new direction is 2 µm.*

C) *Expected distributions of kinesin-driven cargoes for different fractions of plus-end out oriented microtubules p_+ and for three different dendrite length (20, 50, 100 µm). Distributions follow the stated equation and are normalized to maximum density. Numbers indicated in the graph denote the specific p_+ for each curve.*

D) *Graph of the relative dendritic coordinate, $L_{50\%}/L_{dendrite}$, at which the number of particles before that position equals the number of particles beyond that position. $L_{50\%}/L_{dendrite}$ is shown against p_+ for three dendritic lengths. Except for p_+=0.5, where $L_{50\%}/L_{dendrite}$ = 0.5, the functional form plotted is*

$$L_{50\%}/L_{dendrite} = \frac{1}{\alpha}\ln\left(\frac{1}{2}e^{\alpha L_{dendrite}} + \frac{1}{2}\right)/L_{dendrite}, \text{ with } \alpha = \frac{p_+ - p_-}{l}$$

LEGENDS TO SUPPLEMENTARY VIDEOS

Supplementary Video 1. Related to Figure 1.
Video demonstrating the real-time extraction and fixation of a COS7 cell expressing mCherry-tubulin.

Supplementary Video 2, Related to Figure S2.
Video demonstrating motor movements on the extracted microtubule cytoskeleton of the zoom of the cell indicated in Fig. S2. This video corresponds to Fig. S2. Imaged at 10 frames per seconds, total time is 16 seconds. Scale bar is 1 µm. 4 x sped up.

Supplementary Video 3, Related to Figure 1E.
Video demonstrating motor movements on the extracted dendritic microtubule cytoskeleton of a hippocampal neuron. This video corresponds to Figure 1E. Imaged at 10 frames per seconds, total time is 16 seconds. Scale bar is 1 µm. 4x sped up.

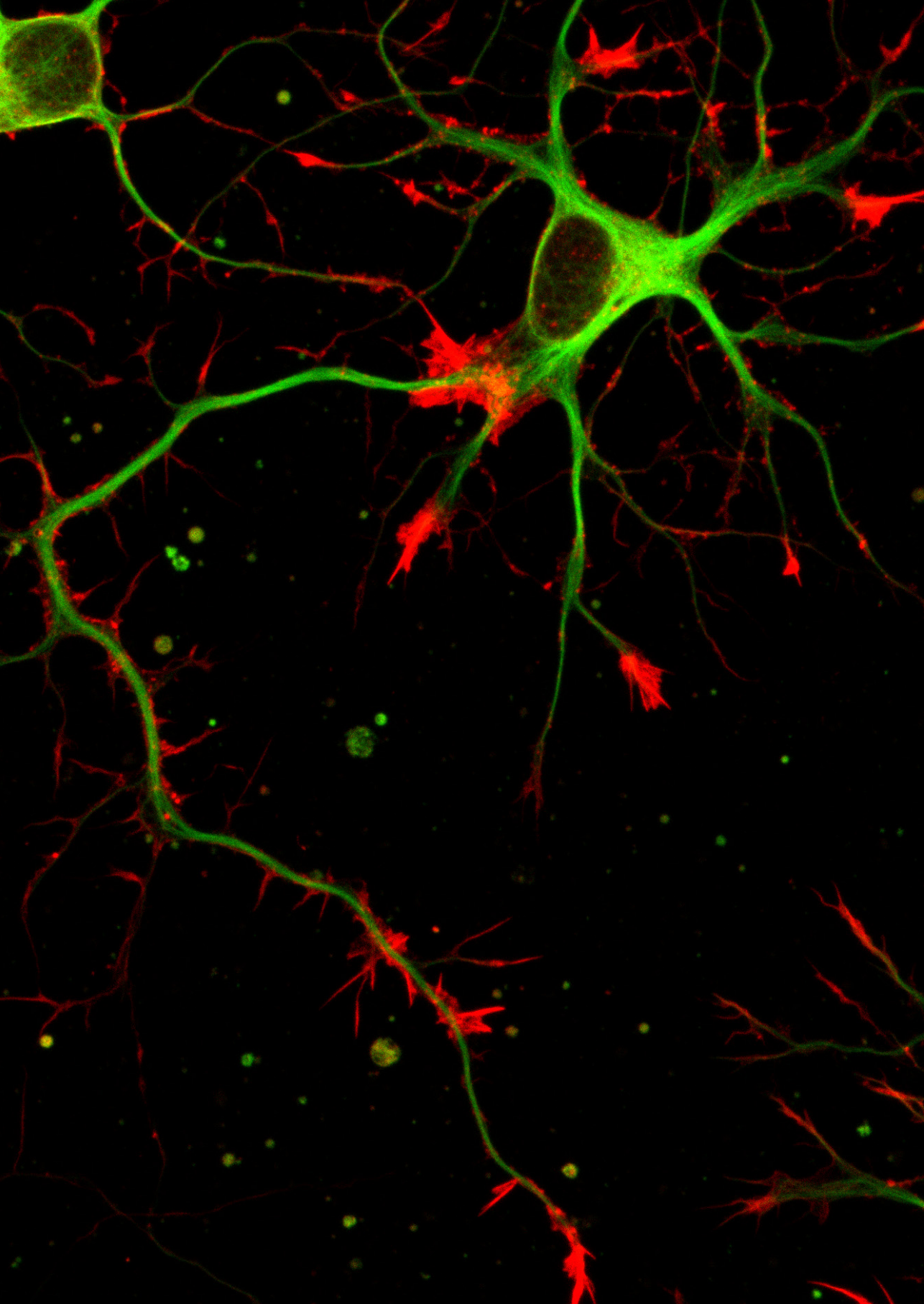

7

Exploring Cytoskeletal Diversity in Neurons

Roderick P. Tas[1] and Lukas C. Kapitein[1]

Science (2018); 361, pp. 231-232

[1] Division of Cell Biology, Faculty of Science, Utrecht University, The Netherlands

MAIN TEXT

Often in biology, form follows function. For example, the ability of a neuron to receive, process and transmit information depends on its polarized organization into axons and dendrites. The cytoskeleton and associated motor proteins shape cells and establish spatial organization. Microtubules (MTs) and actin are core components of the cytoskeleton and are assembled by head-to-tail polymerization of α- and β-tubulin heterodimers and actin monomers, respectively, resulting in asymmetric, polarized polymers with two different ends, called plus and minus ends. The spatially regulated polymerization of MTs and actin can drive morphological transitions, such as local protrusion of the plasma membrane to drive cell migration or the development of specialized extensions, such as axons or dendrites and their branches. In addition, the structural asymmetry of MTs and actin enables cytoskeletal motor proteins (myosin, kinesin and dynein) to walk towards a specific end of the fibers. Given the extreme dimensions and functional compartmentalization of neurons, such active transport is critical to sort and distribute cellular cargoes. Recently, several studies have used advanced microscopy to reveal how the cytoskeleton takes many different forms to facilitate local functions in neurons.

Actin is strongly enriched in the tip of growing axons, termed growth cones, during development or regeneration and in the small protrusions along dendrites, called spines, that harbor most excitatory synapses. Therefore, research often focused on exploring actin organization and function in relation to axon outgrowth and synaptic organization and plasticity. More recently, techniques that enable diffraction-unlimited microscopy have provided surprising new insights into the organization of the axonal actin cytoskeleton in neurons. Most notably, this revealed a periodic matrix of actin and its cross-linking partner spectrin, alternating in ~190 nm spaced rings along the entire axon of hippocampal neurons (1). Similar structures have been reported in the cell body and dendrites of different neuronal subtypes (2) and it has been shown that they provide mechanical support, maintain axon diameter and can serve as a diffusion barrier for membrane proteins (2).

Other actin-based structures, such as actin-rich patches or 'hot spots', have also been identified in axons of hippocampal neurons (2-4). Different actin nucleators have been implicated in their formation (3, 4) and further away from the cell body, they often form around stationary endosomes (intercellular sorting vesicles) (4). Interestingly, more elongated and dynamic actin filaments, termed actin trails, emerge from these distal actin patches (4). How these different actin structures contribute to intracellular transport is not fully understood. Myosin-V motor proteins can oppose axonal transport by tethering cargoes onto proximal actin patches, thus serving as a filter for axonal transport (3, 5). Whether myosins can drive directional transport on actin trails is not known. Furthermore, little is known about the exact organization of actin at the pre-synapse, the site where neurotransmitter-containing vesicles are released for interneuronal signaling. More work is needed to further resolve the nano-architecture of the neuronal actin cytoskeleton, including the polarity of filaments, which determines the direction of motor proteins, and the distribution of

actin-binding proteins that can nucleate, stabilize, bundle or destabilize actin to create functional diversity among different actin networks.

MTs are often much longer than actin filaments and facilitate long-range transport driven by the kinesin and dynein motor proteins (6). Even though each MT is composed of α- and β-tubulin heterodimers, diversity can be generated by the incorporation of different tubulin isotypes, the recruitment of MT associated proteins (MAPs), and by posttranslational modifications (PTMs), such as detyrosination, polyglutamylation and acetylation (6). Indeed, the neuronal MT cytoskeleton is heterogeneous and features dynamic MTs that are turned over as well as stable MTs that are highly modified. This has led to the tubulin code hypothesis, which proposes that the genetic and chemical diversity of tubulin regulates MT properties and functioning (6). For example, PTMs can change the mechanical properties of MTs (7) or alter the binding of MAPs (6, 8), which can in turn affect MT stability or activate specific motor proteins. Consequently, by recruiting motor proteins that prefer specific MT subsets, cargoes could ensure delivery to the proper compartment, such as axons, dendrites, dendritic spines or growth cones. Moreover, dynamic MTs recruit specific proteins to their growing plus end that can establish local signaling networks that promote actin remodeling and result in outgrowth or branching (6). Nevertheless, in most cases the exact functions of different MT populations are still unknown. In addition, how MTs with different properties emerge and co-exist is unclear.

In many cell types, MTs are generated by a MT organizing center (MTOC), such as the centrosome, where γ-tubulin ring complexes (γ-TuRCs) and other MAPs nucleate tube-like structures that then quickly elongate through polymerization at the plus end. This results in a radial array with most MTs pointing towards the cell periphery. In such cells, minus-end directed dynein drives retrograde transport towards the cell center, whereas outward, anterograde transport is driven by the mostly plus-end directed kinesin family members. Nonetheless, in developing neurons the centrosome quickly loses its role as MTOC, suggesting that most MTs are nucleated throughout the whole cell (9). Local MT formation requires mechanisms to stabilize labile minus ends, which could be achieved by nucleating MTs from structures to which they remain anchored. For example, Golgi outposts have been proposed as potential sites of non-centrosomal nucleation in fruitfly (*Drosophila melanogaster*) neurons, although active mispositioning of these structures did not alter MT organization (10). Understanding the birth and fate of neuronal MTs requires dissecting the frequency, spatial distribution and mechanisms of local MT nucleation. In systems with small numbers of MTs, such as axons in the nematode worm, *Caenorhabditis elegans*, careful analysis of intensity patterns, recently used to determine MT density and length, might also reveal nucleation events (11). However, for more dense MT arrays, the development of live-cell markers that highlight nucleation is needed.

Local nucleation also requires additional mechanisms to control the proper orientation of newly formed MTs within the existing cytoskeleton. Because MT orientation determines motor protein directionality, one would assume that efficient long-range transport requires that most MTs in a cellular compartment have similar orientations. Indeed, MTs are largely uniformly

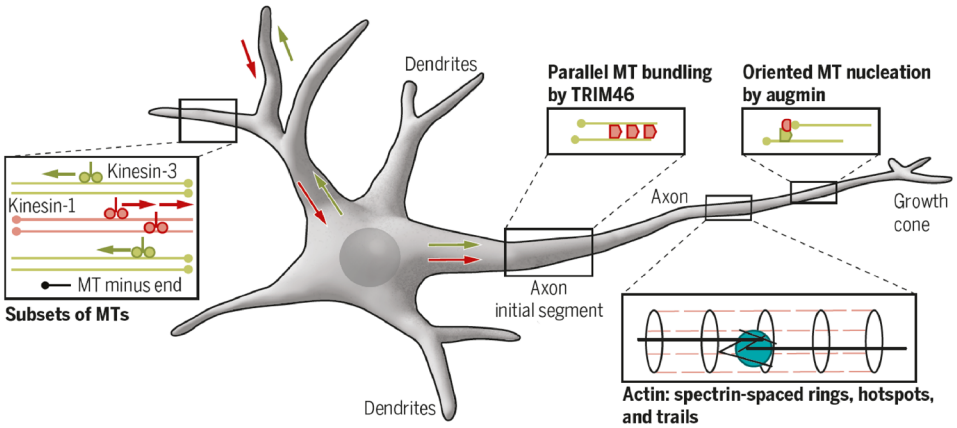

Examples of Cytoskeletal network diversification in a neuron.
Oppositely oriented microtubules in dendrites have different properties and recruit different plus-end directed motor proteins. Parallel MT organization in the axon is established through parallel bunding by TRIM46 in the axon initial segment and by Augmin-mediated oriented nucleation. Actin in the axon is organized in rings that provide mechanical support, as well as (endosome-associated) patches or hot spots and longer trails that might contribute to arresting or promoting directional transport.

oriented plus-end outward in the axons, ensuring that kinesin activation results in anterograde cargo transport, whereas retrograde transport is driven by dynein. Recent work has shown that this uniform organization depends on the Augmin complex, which can position γ-TuRCs along existing MTs so that newly nucleated MTs have the same orientation (12). In addition, TRIM46 (tripartite motif 46) is important for generating parallel MT bundles near the axon initial segment (AIS), a specialized zone involved in the generation of action potentials and filtering of membrane proteins and intracellular cargoes (13).

In fruitflies and worms, also dendrites have a uniform MT array, but oriented oppositely relative to the axon. In such systems, kinesins drive axon-selective transport, whereas dynein drives transport into dendrites (14). Remarkably, in dendrites of mammalian cells MTs have mixed orientations. How do motor proteins navigate such a network to still ensure directional transport? Recent work has addressed this question by introducing a new super-resolution technique, called motor-PAINT (point accumulation for imaging in nanoscale topography), that enabled mapping both MT orientations and PTMs (15). This revealed that although overall both orientations are equally abundant, MTs locally cluster into bundles with a more uniform orientation. This ensures that motor proteins will mostly persist in the direction dictated by the bundle orientation, even when they occasionally switch to neighboring MTs. In addition, stable and modified MTs were predominantly oriented minus-end outward, whereas dynamic MTs were mostly oriented plus-end out (15). Because these MT subsets facilitate transport by distinct kinesins, this creates an overall inward or outward bias for different plus-end directed kinesins. Whereas kinesin-1 would mostly move inward over stable MTs, kinesin-3 would move outward over dynamic MTs. These findings explain why some kinesins only transport cargoes to axons, whereas others target both

axons and dendrites.

Despite these important insights, why certain motor proteins selectively interact with specific MTs remains unresolved. Motor proteins could recognize specific combinations of PTMs and/or MAPs or particular features of the MT lattice. Recent progress in the purification of tubulin isotypes and the reconstitution of different PTMs now allows for teasing out the differential effects of PTMs and MAPs on MT dynamics, mechanics and MT-based transport (7, 8, 16). Such controlled in vitro reconstitution experiments will hopefully lead to a structural understanding of motor protein selectivity. Similar experiments might also provide hints towards the mechanisms through which MT heterogeneity is established. Why do some MTs become modified and stabilized and others not? How can MTs with different chemical properties have opposite orientations? Resolving these questions will also require visualization of the developmental dynamics of different MT subsets, both at the time scale of single MT turnover (minutes to hours) as well as the time scale of dendrite differentiation (several days). Here, developing markers for live-cell imaging of different subsets would provide exciting new opportunities.

Although frequently studied independently, actin and MTs often are functionally connected and also interconnect with other cytoskeletal structures, such as neurofilaments and septins, the functions of which are much less explored. In addition, these cytoskeletal components often interact with different organelles, including endosomes, the Golgi apparatus and the endoplasmic reticulum. How such interactions contribute to the compartment-specific shaping of the heterogenous neuronal cytoskeleton or the communication between organelles is an important topic for future studies. Although mammalian cytoskeletal studies have largely focused on cultured, dissociated neurons, it will be important to explore cytoskeletal form and function in more intact model systems in vivo. This might also enable unraveling the mechanisms by which cytoskeletal organization and intracellular transport are affected during neuronal degeneration and suggest avenues for modulation.

REFERENCES

1. K. Xu et al., Science 339, 452 (2013).
2. C. Leterrier et al., Nat. Rev. Neurosci. 18, 713 (2017).
3. V. Balasanyan et al., Cell Rep. 21, 2696 (2017).
4. A. Ganguly et al., J. Cell Biol. 210, 401 (2015).
5. A. F. J. Janssen et al., Front. Cell Neurosci. 11, 260 (2017).
6. L. C. Kapitein et al., Neuron 87, 492 (2015).
7. Z. Xu et al., Science 356, 328 (2017).
8. M. L. Valenstein et al., Cell 164, 911 (2016).
9. M. Stiess et al., Science 327, 704 (2010).
10. M. M. Nguyen et al., Mol. Biol. Cell 25, 2039 (2014).
11. S. Yogev et al., Neuron 92, 449 (2016).
12. C. Sanchez-Huertas et al., Nat. Commun. 7, 12187 (2016).
13. S. F. B. van Beuningen et al., Neuron 88, 1208 (2015).
14. M. Harterink et al., Curr. Biol. 26, R153 (2016).
15. R. P. Tas et al., Neuron 96, 1264 e1265 (2017).
16. B.Y. Monroy et al., Nat. Commun. 9, 1487 (2018).

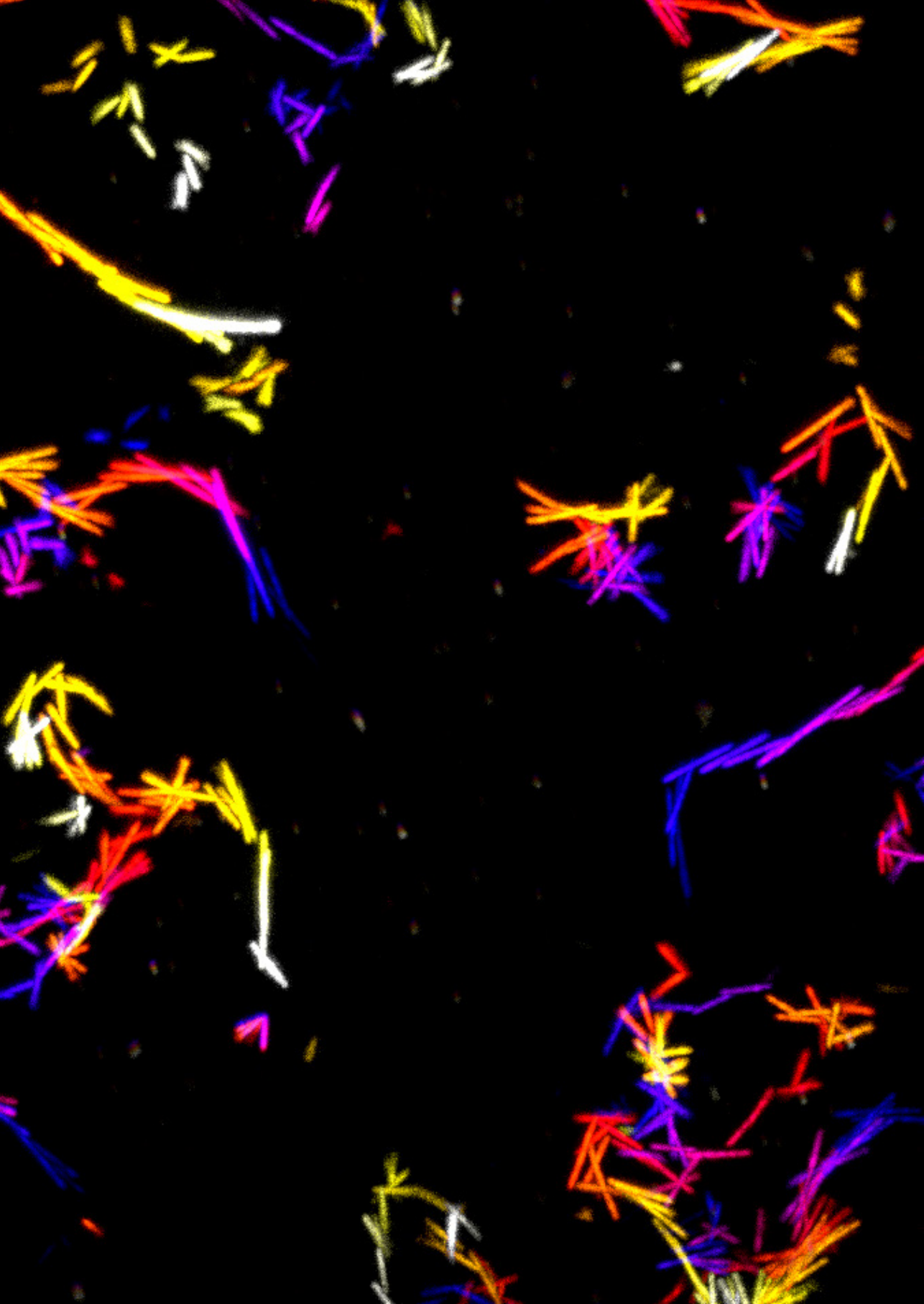

8

Guided by Light: Optical Control of Microtubule Gliding Assays

Roderick P. Tas[1†], Chiung-Yi Chen[1†], Eugene A. Katrukha[1], Mathijs Vleugel[2], Maurits Kok[2], Marileen Dogterom[2], Anna Akhmanova[1] and Lukas C. Kapitein[1]

Nano Letters (2018); 18, pp. 7524-7528

[1] Division of Cell Biology, Faculty of Science, Utrecht University, The Netherlands
[2] Department of Bionanoscience, Kavli Institute of Nanoscience, Delft University of Technology, The Netherlands
[†] Equal Contribution

ABSTRACT

Force generation by molecular motors drives biological processes such as asymmetric cell division and cell migration. Microtubule gliding assays, in which surface-immobilized motor proteins drive microtubule propulsion, are widely used to study basic motor properties as well as the collective behavior of active self-organized systems. Additionally, these assays can be employed for nanotechnological applications such as analyte detection, bio-computation and mechanical sensing. While such assays allow tight control over the experimental conditions, spatiotemporal control of force generation has remained underdeveloped. Here we use light-inducible protein-protein interactions to recruit molecular motors to the surface to control microtubule gliding activity *in vitro*. We show that using these light-inducible interactions, proteins can be recruited to the surface in patterns, reaching a ~5-fold enrichment within 6 seconds upon illumination. Subsequently, proteins are released with a half-life of 13 seconds when the illumination is stopped. We furthermore demonstrate that light-controlled kinesin recruitment results in reversible activation of microtubule gliding along the surface, enabling efficient control over local microtubule motility. Our approach to locally control force generation offers a way to study the effects of non-uniform pulling forces on different microtubule arrays and also provides novel strategies for local control in nanotechnological applications.

MAIN TEXT

Force generation by molecular motors on the microtubule cytoskeleton drives biological processes such as asymmetric cell division and cell migration. To better understand these processes, *in vitro* reconstitution assays are often used to decipher the underlying interactions and principles[1-3]. Microtubule gliding assays, in which motor proteins are immobilized on the surface to propel microtubules, are a widely used example of such experiments. Applications of these assays range from studying basic properties of motor proteins to exploring collective and swarming behavior of self-organized systems[4-8]. Additionally, microtubule gliding assays are being developed for a variety of nanotechnological applications such as analyte detection, bio-computation and mechanical sensing[9-11]. These assays have been shown to be very robust and sensitive enough to detect and analyze very small molecular fluctuations. Controlling these assays with both spatial and temporal precision has however remained a longstanding challenge. Previous studies used microfabricated or pre-patterned surfaces to spatially confine, guide, and steer microtubules[12-16]. Furthermore, temporal control to activate microtubule gliding on pre-defined structures has been achieved through electric field manipulation[17] and heat responsive polymer tracks[18-19], while slow light-controlled gliding (10-20 nm/s) of actin filaments has been achieved using engineered myosin motors[20]. Additionally, control of microtubule gliding has been achieved using a light-to-heat converting layer in combination with heat-responsive polymers that compact upon heating and allow access of microtubules to surface-attached motors[21]. Furthermore, azobenzene switches fused to inhibitory peptides have been used to control kinesin-dependent motility with light[22-23]. However, the majority of these approaches requires extensive surface modifications or complicated molecular engineering, leaving simultaneous spatial and temporal control of force generation on non-predefined patterns underdeveloped.

Here we report local activation of microtubule gliding by direct light-inducible recruitment of kinesins to the surface (Fig. 1). Previously, it has been shown that tunable, light-controlled interacting protein tags (TULIPs) can be efficiently used for light-induced heterodimerization to control intracellular protein recruitment and intracellular transport[24-25]. The interaction is based on the unfolding of the Jα-helix from the LOVpep core to interact with an engineered PDZ (ePDZ) domain upon blue light illumination[24, 26]. We argued that light-inducible interactions based on TULIPs can be used to reversibly control local protein recruitment *in vitro*. Therefore, we generated recombinant proteins fused to TULIPs to induce local heterodimerization under the control of blue light (Fig. 1). We demonstrate that purified recombinant ePDZ-tagged proteins can be recruited to the coverslip with high spatiotemporal precision. Furthermore, upon recruitment of kinesin-ePDZ, microtubule gliding could be reversibly induced. This approach allows for spatiotemporal control of microtubule gliding on homogeneously coated surfaces providing an adaptive platform to manipulate microtubule motility.

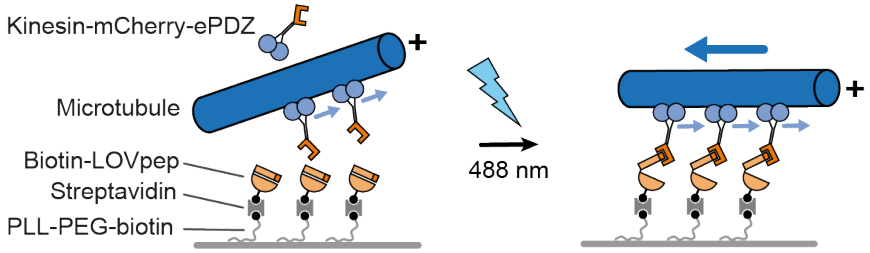

Figure 1: Schematic representation of the experimental assay for light-controlled microtubule propulsion. The LOVpep domain undergoes a conformational change upon illumination with blue light, which facilitates the binding of Kinesin-mCherry-ePDZ and induces controlled microtubule gliding.

First, to test whether the TULIP based interactions are sufficient for spatiotemporal control of protein recruitment *in vitro*, we designed an optical readout of ePDZ recruitment to the surface. We purified the LOVpep fused to biotin, which was immobilized on a microscopy coverslip functionalized with PLL-PEG-biotin and streptavidin. Subsequently, local blue light application was used to recruit purified ePDZ-mCherry from solution (Fig. 2A). Indeed, when a small square region was briefly exposed to blue laser light, we observed a ~5-fold enrichment of ePDZ-mCherry in that region, compared to a ~1.2-fold increase in a region 15 mm away from the activation light. Upon arrest of illumination, complete dissociation of ePDZ-mCherry was observed (Movie S1, Fig. 2B, D). This could be efficiently repeated for multiple cycles where maximum recruitment was reached within ~6 seconds and dissociation rapidly occurred with a half-life of ~13 seconds in the illuminated area (Fig. 2C,D). Furthermore, protein recruitment was not limited to a single shape but could be structured into a variety of patterns (Fig. 2E, F). Thus, these light-induced interactions allow for sequential, reversible and custom patterning *in situ* with high contrast and precision.

Next, we tested whether we could efficiently induce microtubule gliding activity by recruitment of an ePDZ domain fused to kinesin (Fig. 1). After immobilization of biotin-LOVpep to the coverslip, rhodamine labelled microtubules and kinesins were added to the reaction solution. Total internal reflection fluorescence (TIRF) imaging was then used to image the microtubules close to the surface in the absence and presence of a global 200 ms blue light pulse between each frame (Movie S2, Fig. 3A,B). In the absence of blue light, microtubules displayed non-directional movement near the coverslip with only occasional directional events. The strong microtubule enrichment near the coverslip was due to the presence of methylcellulose[27] (Figure S1), while the directional events were presumably due to dark-state activation or nonspecific adsorption of the motors to the surface. In contrast, upon global recruitment of kinesins to the coverslip with blue light, microtubules began to move in long directional runs along the coverslip (Fig. 3A,B). Activation was reversible and induction of microtubule gliding could be repeated multiple times in the same region (Fig. 3A,B). Processive microtubule gliding readily increased and decreased upon the start and stop of blue light illumination. However, complete mobilization or immobilization was observed

on average after 50-100 seconds (Fig. S1B). Determination of the fold-increase of DmKHC-mCherry-ePDZ during such illumination periods showed a gradual increase and decrease of the motor at the coverslip upon illumination or in the dark. On average a ~2 fold-increase was observed and sufficient to efficiently propel microtubules (Fig. S1C,D).

To better understand the dynamics of the system, we traced individual microtubules for a more detailed analysis of light activated microtubule motility. Activation of microtubule gliding led to an increase of the average velocity from ~150 to ~450 nanometer per second, which decreased again when blue light illumination was stopped (Fig. 3C). Importantly, without blue light illumination the motility of most microtubules lacked an overall directionality, because their frame-to-frame displacement did not have consistent direction in subsequent frames. This was revealed by an analysis of the mean squared displacement (MSD), which reports the squared displacement as a function of time interval. The power dependence α of the MSD with increasing time intervals τ, MSD $\propto t^{\alpha}$, is the anomalous diffusion exponent and indicates whether motility is completely random ($\alpha \approx 1$, diffusive), directed ($1 < \alpha \leq 2$, superdiffusive), or confined ($0 < \alpha < 1$, subdiffusive)[28]. Indeed, a log-log plot of MSD(τ) averaged over all traced microtubules of the represented movie revealed that the average slope for non-illuminated microtubules ($\alpha = 1.43$) increased after activation ($\alpha = 1.89$) (Fig. 3D). We also calculated the MSD(τ) for individual microtubules of three independent experiments and fitted the curve to MSD $\propto t^{\alpha}$, which revealed a significant increase in the value of α in

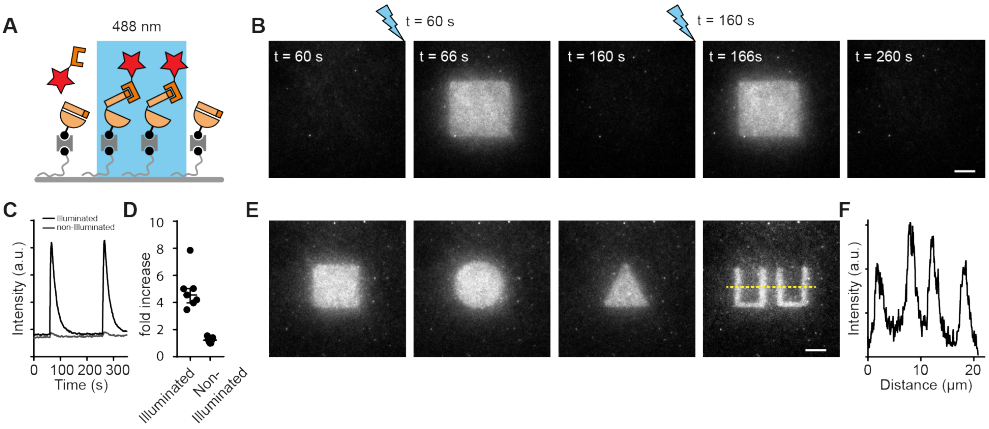

Figure 2: Spatiotemporal control of protein recruitment through light-induced heterodimerization. *A) Schematic representation of the experimental setup to recruit ePDZ-mCherry to the coverslip. B) Locality and reversibility of ePDZ-mCherry surface binding using patterned blue light. C) Background-corrected average intensity traces for a similar movie as shown in B. Intensities over time were measured in the illumintated square (black line) and in the non-illuminated corner of the field of view ~20µm apart (grey line). Single light pulses were given after 60 and 260 seconds. D) Fold-increase of ePDZ-mCherry upon illumination in the illuminated center and the non-illuminated corner of the field of view of 7 traces of 3 independent experiments. Median:IQR. E) Repetitive ePDZ-mCherry recruitment in different patterns during the same acquisition. See also Movie S1. F) Background corrected line scan along the yellow line indicated in D. Scale bars: 5 µm.*

the presence of light (Median:IQR 1.91: 1.72-1.97) compared to the dark state (1.44: 1.04-1.78).These results are consistent with an increase in directed microtubule displacement upon illumination (Fig. 3E,F).

Finally, we tested whether our experimental setup does not only allow for temporal control but can also provide spatial control of microtubule propulsion. We used a lower magnification epifluorescence microscope equipped with a digital mirror device (DMD). In contrast to local illumination by scanning with a FRAP module, a DMD device is able to achieve fast patterned episcopic illumination, compatible with any magnification. This results in local optical control over a large field of view with low light intensities[29]. We designed an experiment where global microtubule gliding was followed by two episodes of local activation

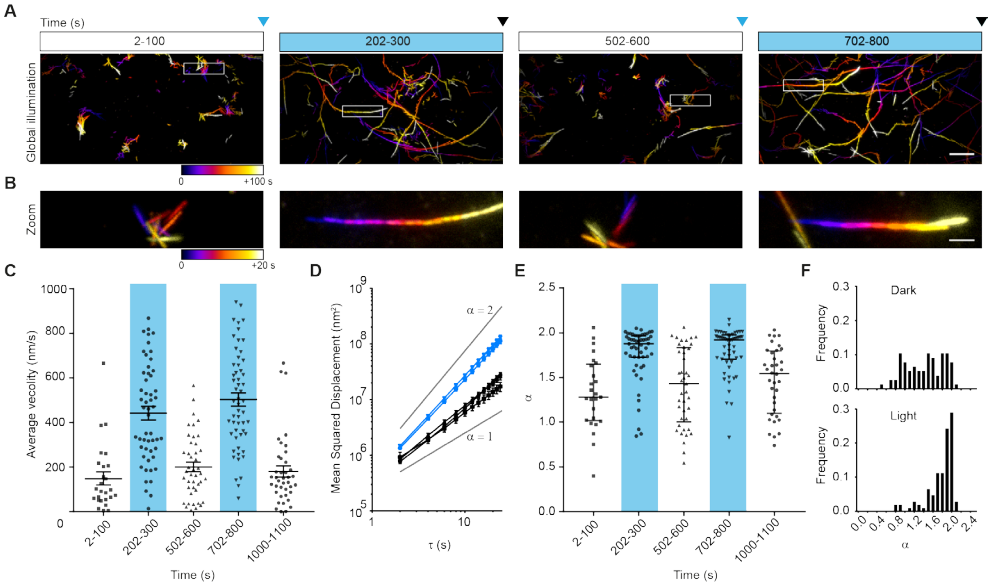

Figure 3: Global reversible control of microtubule gliding assays by blue light *A) Temporal color coded maximum projections of 100 1-second interval frames in the absence (white box) and presence (blue box) of light. Arrowheads indicate start (blue) and stop (black) of blue light illumination. See also Movie S2. B) Zooms of representative 20-second tracks from the regions marked by the white boxes (A). C) Average velocity of microtubules in A in the absence and presence (blue boxes) of light. Average ± s.e.m. For the five subsequent time windows 26, 53, 43, 55 and 40 microtubule tracks were analyzed, respectively. D) Mean squared displacement (MSD) of microtubules in (A) in the absence (black lines) or presence (blue lines) of light. Grey lines depict lines with slopes α of 1 and 2, indicative of diffusive/non-directional or linear/directional movement. Average ± s.e.m. E) Fitted values of α for all individual microtubule tracks (≥ 16 consecutive frames) between the indicated timepoints. For the five subsequent time windows in the graph 25, 52, 41, 55 and 36 microtubule tracks of 3 independent experiments were analyzed, respectively. median:IQR F) Frequency distribution of pooled values of α in the absence or presence of blue light. 102 (dark) and 107 (light) microtubule tracks of 3 independent experiments were analyzed. Scale bars: A – 10 µm; B – 2 µm.*

at different locations. Again efficient gliding of microtubules was observed upon global activation (Movie S3, Fig. 4A, left panel). Because of the episcopic illumination, signal-to-noise levels were reduced compared to the previous global gliding assays imaged in TIRF at higher magnification. Therefore, to visualize and better understand microtubule motion, we developed an automated method to detect microtubules based on cross-correlation with microtubule templates of different orientations (Fig. 4A, right panel, Fig S2, Movie S4). This automated detection resulted in an accurate representation of the microtubule positions and enabled microtubule tracking (Fig. 4B).

To measure the efficiency of light-induced gliding within the assay, directional and non-directional motility were categorized into separate groups and represented by different colors, green and red respectively (Figure 4C, Fig S2, Movie S4). Microtubule movement was classified as directional when the velocity was higher than 250 nm/s and when two consecutive velocity vectors were oriented with an angle whose cosine was larger than 0.6 (Fig. 4C). The other microtubules were classified as non-directional and include slow directional and diffusive, non-directional movement. This analysis allowed us to discriminate microtubule motion under different illumination schemes where the surface was first globally illuminated with blue light and subsequently the left and right area were illuminated to induce local gliding (Figure 4D). During global illumination, the majority of microtubules was moving directionally across the entire field of view (75-85% directional runs). Conversely, upon local illumination, confined microtubule gliding was observed in the activated areas. Quantification

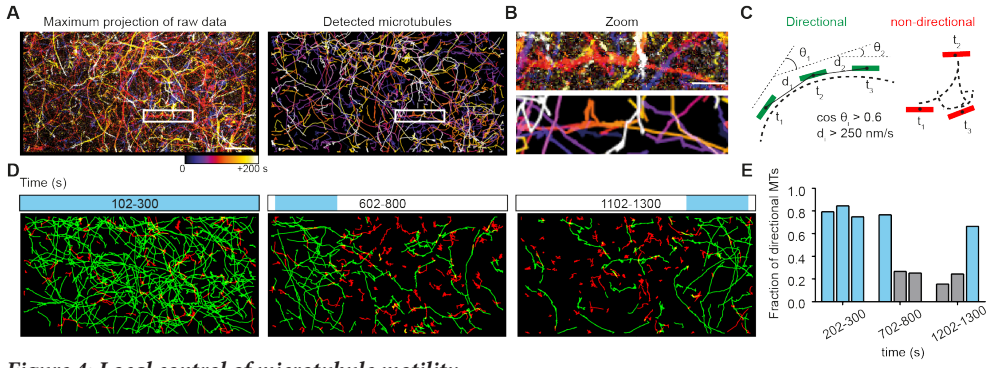

Figure 4: Local control of microtubule motility

A) Temporal color-coded maximum projection of gliding microtubules after global activation. Raw data (left panel) and detected microtubules (right panel) over a time period of 200 seconds as indicated by the color-coded scale bar. See also Movie S3.

B) Zooms of the indicated regions in (A).

C) Rules for motion classification of gliding microtubules.

D) Maximum projections of classified tracks upon global and local illumination over 200 seconds Directional microtubule tracks are depicted in green, and non-directional tracks in red. The blue box on top shows the illuminated area during different episodes.

E) Fraction of processive microtubules in illuminated (blue) and non-illuminated (grey) areas during each illumination episode. 234, 165 and 150 tracks were analyzed during the global, left and right illumination episode respectively. Scale bars: A - 20 µm; B – 5 µm.

of the fraction of processive microtubules showed that during local activation, 77 and 67% of the microtubules were gliding directionally in the left and right area, respectively (Fig. 4D,E). Furthermore, during the local illumination episodes, less than 27% of microtubules were processive in the non-illuminated regions. Our results show that the use of light-inducible protein interactions provides robust spatiotemporal control of microtubule gliding assays.

Here we have developed light-inducible motor patterning on a homogeneously coated surface to directly control microtubule gliding . This approach allows for both spatial and temporal control of microtubule gliding activity within minutes on micrometer length scales with high efficiency. First, we showed that proteins fused to an ePDZ domain can be reliably coupled to surface immobilized LOVpep. Using an ePDZ-kinesin fusion, motors could be recruited to the coverslip upon activation with light to propel microtubules along the surface. Furthermore, kinesins could be locally recruited to achieve spatial control of microtubule gliding without the need for a pre-patterned surface. While previous studies mostly focused on either spatial or temporal control[12-15, 17-19], our adaptive platform now offers simultaneous optical control of both, opening up new possibilities for microtubule gliding assays. Our approach is complementary to a previously developed approach in which a light-to-heat converting layer was used in combination with heat-responsive polymers that compact upon heating and allow access of microtubules to surface-attached motors[21]. However, the current approach requires less surface modifications and does not induce local temperature changes. Compared to previous developments that have used custom-engineered myosin motors to achieve slow (10-20 nm/s) light-controlled gliding of actin filaments, the use of a generic heterodimerization approach makes our approach readily applicable to a variety of different motor proteins[20].

Our approach can be used to reconstitute and understand biological processes that rely on asymmetric forces on complex microtubule arrays. For example, light-inducible control of forces can be used to locally impose forces on reconstituted spindle-like structures or confined microtubule networks to guide the formation of complex microtubule arrays or to study cortical pulling forces[30-31]. Furthermore, light-inducible force generation could directly influence collective motion of microtubules serving as an experimental model for collective and swarming behavior. Future work could explore different light sensitive modules to improve the level of control. For example, phytochrome-based protein interactions enable red-light sensitivity[29, 32] and bidirectional control, which could help to improve both temporal and spatial precision. The use of light inducible interactions to control microtubule gliding assays therefore provides exciting new possibilities for reconstituting and understanding complex biophysical and biological processes.

ACKNOWLEDGEMENTS

This work is supported by the Netherlands Organisation for Scientific Research (NWO)

(NWO-ALW-VIDI 864.12.008 to L.C.K.) and the European Research Council (ERC Starting Grant 336291 to L.C.K., ERC Synergy Grant 609822 to A.A. and M.D.).

AUTHOR CONTRIBUTIONS

LCK conceived research and supervised the study. RPT created constructs and purified proteins with help and input of MV and CYC. CYC performed experiments with help and input from RPT. RPT, CYC and EAK analyzed data. MK, MD and AA provided valuable suggestions and input. RPT, CYC and LCK wrote the paper with input from all other authors.

REFERENCES

1. Nedelec, F. J.; Surrey, T.; Maggs, A. C.; Leibler, S., Nature 1997, 389 (6648), 305-8.
2. Akhmanova, A.; Steinmetz, M. O., Nature Reviews Molecular Cell Biology 2015, 16, 711.
3. Kerssemakers, J. W. J.; Laura Munteanu, E.; Laan, L.; Noetzel, T. L.; Janson, M. E.; Dogterom, M., Nature 2006, 442, 709.
4. Howard, J.; Hudspeth, A. J.; Vale, R. D., Nature 1989, 342, 154.
5. Sumino, Y.; Nagai, K. H.; Shitaka, Y.; Tanaka, D.; Yoshikawa, K.; Chate, H.; Oiwa, K., Nature 2012, 483 (7390), 448-52.
6. Lam, A. T.; Tsitkov, S.; Zhang, Y.; Hess, H., Nano Lett 2018, 18 (2), 1530-1534.
7. Nitzsche, B.; Bormuth, V.; Bräuer, C.; Howard, J.; Ionov, L.; Kerssemakers, J.; Korten, T.; Leduc, C.; Ruhnow, F.; Diez, S., Chapter 14 - Studying Kinesin Motors by Optical 3D-Nanometry in Gliding Motility Assays. In Methods in Cell Biology, Wilson, L.; Correia, J. J., Eds. Academic Press: 2010; Vol. 95, pp 247-271.
8. Keya, J. J.; Suzuki, R.; Kabir, A. M. R.; Inoue, D.; Asanuma, H.; Sada, K.; Hess, H.; Kuzuya, A.; Kakugo, A., Nat Commun 2018, 9 (1), 453.
9. Chaudhuri, S.; Korten, T.; Korten, S.; Milani, G.; Lana, T.; Te Kronnie, G.; Diez, S., Nano Lett 2018, 18 (1), 117-123.
10. Nicolau, D. V., Jr.; Lard, M.; Korten, T.; van Delft, F. C.; Persson, M.; Bengtsson, E.; Mansson, A.; Diez, S.; Linke, H.; Nicolau, D. V., Proc Natl Acad Sci U S A 2016, 113 (10), 2591-6.
11. Inoue, D.; Nitta, T.; Kabir, A. M.; Sada, K.; Gong, J. P.; Konagaya, A.; Kakugo, A., Nat Commun 2016, 7, 12557.
12. van den Heuvel, M. G.; Butcher, C. T.; Smeets, R. M.; Diez, S.; Dekker, C., Nano Lett 2005, 5 (6), 1117-22.
13. Clemmens, J.; Hess, H.; Lipscomb, R.; Hanein, Y.; Bohringer, K. F.; Matzke, C. M.; Bachand, G. D.; Bunker, B. C.; Vogel, V., Langmuir 2003, 19 (26), 10967-10974.
14. Hess, H.; Matzke, C. M.; Doot, R. K.; Clemmens, J.; Bachand, G. D.; Bunker, B. C.; Vogel, V., Nano Letters 2003, 3 (12), 1651-1655.
15. Reuther, C.; Mittasch, M.; Naganathan, S. R.; Grill, S. W.; Diez, S., Nano Lett 2017, 17 (9), 5699-5705.
16. Bhagawati, M.; Ghosh, S.; Reichel, A.; Froehner, K.; Surrey, T.; Piehler, J., Angew Chem Int Ed Engl 2009, 48 (48), 9188-91.
17. van den Heuvel, M. G.; de Graaff, M. P.; Dekker, C., Science 2006, 312 (5775), 910-4.
18. Ramsey, L.; Schroeder, V.; van Zalinge, H.; Berndt, M.; Korten, T.; Diez, S.; Nicolau, D. V., Biomed Microdevices 2014, 16 (3), 459-63.
19. Schroeder, V.; Korten, T.; Linke, H.; Diez, S.; Maximov, I., Nano Lett 2013, 13 (7), 3434-8.
20. Nakamura, M.; Chen, L.; Howes, S. C.; Schindler, T. D.; Nogales, E.; Bryant, Z., Nature

Nanotechnology 2014, 9, 693.
21. Reuther, C.; Tucker, R.; Ionov, L.; Diez, S., Nano Lett 2014, 14 (7), 4050-7.
22. Rahim, M. K. A.; Fukaminato, T.; Kamei, T.; Tamaoki, N., Langmuir 2011, 27 (17), 10347-10350.
23. Kumar, K. R. S.; Kamei, T.; Fukaminato, T.; Tamaoki, N., ACS Nano 2014, 8 (5), 4157-4165.
24. Strickland, D.; Lin, Y.; Wagner, E.; Hope, C. M.; Zayner, J.; Antoniou, C.; Sosnick, T. R.; Weiss, E. L.; Glotzer, M., Nat Methods 2012, 9 (4), 379-84.
25. van Bergeijk, P.; Adrian, M.; Hoogenraad, C. C.; Kapitein, L. C., Nature 2015, 518 (7537), 111-114.
26. Harper, S. M.; Neil, L. C.; Gardner, K. H., Science 2003, 301 (5639), 1541-4.
27. Uyeda, T. Q. P.; Kron, S. J.; Spudich, J. A., Journal of Molecular Biology 1990, 214 (3), 699-710.
28. Saxton, M. J.; Jacobson, K., Annu Rev Biophys Biomol Struct 1997, 26, 373-99.
29. Adrian, M.; Nijenhuis, W.; Hoogstraaten, R. I.; Willems, J.; Kapitein, L. C., ACS Synth Biol 2017, 6 (7), 1248-1256.
30. Heald, R.; Tournebize, R.; Blank, T.; Sandaltzopoulos, R.; Becker, P.; Hyman, A.; Karsenti, E., Nature 1996, 382 (6590), 420-5.
31. Laan, L.; Pavin, N.; Husson, J.; Romet-Lemonne, G.; van Duijn, M.; Lopez, M. P.; Vale, R. D.; Julicher, F.; Reck-Peterson, S. L.; Dogterom, M., Cell 2012, 148 (3), 502-14.
32. Levskaya, A.; Weiner, O. D.; Lim, W. A.; Voigt, C. A., Nature 2009, 461 (7266), 997-1001.

SUPPLEMENTAL EXPERIMENTAL PROCEDURES

Plasmids

GST-ePDZ-mCherry, GST-aviTag-LOVpep, GST-DmKHC-mCherry-ePDZ were cloned into a pGEX-6p-1 vector linearized with BamHI and XhoI restriction enzymes for GST-PreScission purification. GST-ePDZ-mCherry and GST-aviTag-LOVpep were cloned by PCR amplification of the individual domains, restriction digestion and ligation into the vector. A HindIII restriction site was amplified between inserts. GST-DmKHC-mCherry-ePDZ was cloned by PCR amplification of DmKHC (AA1-421), mCherry and ePDZ were ligated via Gibson assembly.

Protein expression and purification.

Protein purification was performed in BL21 DE3 cells. For GST-ePDZ-mCherry and GST-aviTag-LOVpep, bacteria were induced at OD0.6 with 1mM IPTG and grown overnight at 20 degrees Celsius in dark conditions. For purification of GST-aviTag-LOVpep, the bacterial culture was supplemented with 50μM D-biotin. All subsequent purification steps were performed under red light-only in order to prevent activating the LOVpep. After induction, bacteria were pelleted by centrifugation. The supernatant was discarded and bacteria were resuspended in 5ml/gram lysis buffer (PBS supplemented with 10 mM EGTA, 10 mM EDTA, 250 mM NaCl, 1 tablet/50 mL Complete Protease Inhibitor and 0.2 mg/ml lysozyme to compromise the bacterial cell wall). After ~15 minutes incubation cells were sonicated 5 times for 45 seconds with 1-minute intervals, followed by addition of DTT (dithiolthreitol) to a final concentration of 1mM and centrifugation of the extract at 20.000 x g for 45

minutes and the supernatant was incubated for 1.5-2 hours with Glutathione Sepharose 4B GST-tagged beads (GE healthcare) that had been washed 3x in lysis buffer. Next, beads were washed 5x with PreScission Cleavage buffer (50 mM Tris-HCl, 150mM NaCl, 1mM EDTA, 1mM DTT, pH 7.0). The washed beads were incubated overnight at 4 degrees Celcius with PreScission Protease to allow full cleavage of the PreScission sequence. Finally, the beads were spun down and the supernatant was snap-frozen with 10% glycerol. Expression and purification of GST-DmKHC-mCherry-ePDZ was performed with a different lysis buffer (20mM Pipes, 150mM NaCl, 4 mM $MgSO_4$, pH 7.0, supplemented with lysozyme and Complete protease inhibitors) and cleavage buffer (BRB80: 80 mM Pipes, 4mM $MgCl_2$, 1 mM EGTA, 1mM DTT, 50μM ATP, pH 6.8). The final protein concentrations in the purified samples were 11μM, 22μM and 20μM for aviTag-LOVpep, ePDZ-mCherry and DmKHC-mCherry-ePDZ, respectively, as determined by standard BCA assay (ThermoFisher).

Light-inducible patterning and gliding assays

After activation of the coverslips with a plasma cleaner (Harrick), flow chambers were sequentially functionalized with 0.2 mg ml^{-1} PLL-PEG-biotin (Susos AG, Switzerland), 1 mg ml^{-1} streptavidin (Thermo Fisher) and 2 wash-ins of biotin-LOVpep. Flow chambers were further blocked with 1 mg ml^{-1} κ-casein. For light-inducible patterning of ePDZ-mCherry, the reaction mix with purified proteins (BRB80 buffer supplemented with 1μM ePDZ-mCherry, 100 μM imidazole, 0.2 mg ml^{-1}κ-casein, 0.1% methylcellulose and oxygen scavenger mix (50 mM glucose, 400 μg ml^{-1} glucose oxidase, 200 μg ml^{-1}catalase and 4 mM DTT)) was added to the flow chamber after centrifugation. Alternatively, for light inducible-gliding assays the reaction mix composed of 1-3 μM DmKHC-mCherry-ePDZ, 0.1-0.15% methylcellulose, 2 mM ATP, 100 μM imidazole, 0.2 mg ml^{-1} κ-casein and oxygen scavenger mix. Higher concentrations of DmKHC-mCherry-ePDZ and methylcellulose were used for local activation in gliding assay. Microtubules were polymerized using 20 μM unlabeled tubulin, 13% rhodamine-tubulin (Cytoskeleton) and 1 mM GMPCPP (Jena Bioscience). The microtubules were included after centrifugation of the reaction mix.

Imaging

The flow chamber was sealed with vacuum grease and imaged at 30 °C. For the protein patterning assay and the global gliding assay, total internal reflection fluorescence (TIRF) microscopy was performed on an inverted microscope (Eclipse Ti, Nikon) equipped with a 100X oil objective (Apo, NA 1.49, Nikon), an Evolve 512 EMCCD (Photometrics) and a CoolSNAP HQ2 CCD camera (Photometrics). ET-GFP(49002) and ET-mCherry (49008) filter cubes (all Chroma) were used. For TIRF imaging of rhodamine microtubules, a 561 nm laser was used at 2 s intervals and a 488 nm laser was used for activation with 200 ms exposure. To perform local recruitment experiments, images were acquired on a different inverted microscope (Eclipse Ti, Nikon) equipped with 40X oil-immersion objective (Plan

Fluor, NA 1.3, Nikon, CoolSNAP HQ2 CCD cameras (Photometrics), ET-GFP(49002) and ET-mCherry(49008) filter cubes (Chroma). This microscope was equipped with a Polygon 2000 digital mirror device (DMD) as described previously[1]. Rhodamine microtubules were imaged using a mercury lamp (Osram) at 2 s intervals. Global or local illumination to recruit motors was achieved with the DMD at 10% 470nm LED (Mightex) power with 200 ms exposure time.

Data analysis

To assess the fold-increase of ePDZ-mCherry after a single light pulse with the FRAP unit, average intensities over time were measured in the illuminated area and the non-illuminated area. The background intensity of free ePDZ-mCherry was determined by measuring the intensity in the absence of biotin-LOVpep. The intensity traces in the presence of LOVpep could then be subjected to background subtraction and the fold-enrichment after illumination could be determined in the illuminated area versus the non-illuminated area. Similarly the fold-increase of DmKHC-mCherry-ePDZ was measured however, as in the gliding assay, global activation over a longer period using the TIRF laser was used.

To track microtubules that were imaged with TIRF illumination for global activation assays (Fig. 3), FIESTA was used as described previously[2]. Parameters were set such that only filaments were tracked that could be observed for at least 3 consecutive frames with a maximum velocity of 2500 nm/s. Gaps in the tracks were not allowed. Subsequently, the tracks were checked and corrected manually in the FIESTA software if necessary. The output was then restructured for further analysis with the 'msdanalyzer' Matlab class[3]. To analyze the mean square displacement (MSD), only microtubules that were observed for more than 16 frames were included.

The detection of moving microtubules image using conventional illumination (Fig. 4) was performed using template matching with a custom written ImageJ/FIJI macro [4]. Raw image files first were subjected to background subtraction using the FIJI "Subtract Background" command with a rolling ball radius of 50 pixels (8 μm). We generated template images, corresponding to microtubules in different orientations (with different tilt angles). For that, we drew a set of lines of average microtubule length (25 pixels, 5 μm) with rotation angle between 0 and 150 degrees with a step of 30 degrees. Each line image further was convoluted with a 2D Gaussian kernel having the size of microscope's point spread function (1.2 pixels or 193 nm). For each orientation of the template, we calculated the normalized cross-correlation map with a frame of the background subtracted movie using the "Template matching" plugin by Qingzong Tseng[5]. In the next step, the macro was looking for the pixel with a maximum of the cross-correlation value, corresponding to the most probable line position. Coordinates of the pixel, its correlation value and template rotation angle were stored in a results table. To prevent repetitive detections, an area in the shape of the line in the current orientation was set to zero

in the cross-correlation image map at this position. The same area was marked in an additional "detection map" image with a unique identifier, corresponding to the detection. The procedure continued iteratively as long as the next maximum correlation value exceeded the threshold value of average plus four standard deviations of the cross-correlation image map. At each newly detected position, the macro was checking the "detection map" for previous detections with different orientations. If there was a conflict, the detection with higher cross-correlation value was kept and the other one was marked as a "false" detection. Linking of detections to tracks was performed in Matlab using a modified version of the Simple Tracker package by Jean-Yves Tinevez, implementing nearest neighbor linking [https://nl.mathworks.com/matlabcentral/fileexchange/34040-simple-tracker]. To calculate a Euclidean distance between two detections, we introduced rod's rotation angle in degrees as a z coordinate, in addition to the x,y coordinates. For the z distance calculation, we took into account the periodicity of the degrees axis and applied the empirically estimated weight of 0.3. Tracks were composed using the nearest neighbor algorithm with the distance of 22 pixels and frame closing gap of 1. Subsequently, manual correction of the automatically assigned tracks was performed in MTrackJ. This was mainly done to connect split trajectories, which often occurred upon crossing of two microtubules. To find segments of directional runs we used the previously described "strict directional filtering" algorithm[6]. In short, it imposes a threshold on change of the velocity vector angle within a specified time interval to locate a segment with a directional run. In this case, we used the value of 100 degrees (cone looking forward) and a time interval of two frames (4 s). Additional filtering criteria for directional runs were a minimum of ten frames (20 s) and at least 0.25 μm total displacement. Visualization of tracks was performed using MTrackJ plugin[7]. ImageJ/FIJI macro and Matlab code used for analysis are available at [https://github.com/ekatrukha/rods-detection-in-noisy-images/]. Temporal-color coded projection to visualize microtubule trajectories were made with the ImageJ plugin [https://imagej.net/Temporal-Color_Code]. Statistics and graphs were generated using Graphpad prism 7.

SUPPLEMENTARY FIGURES

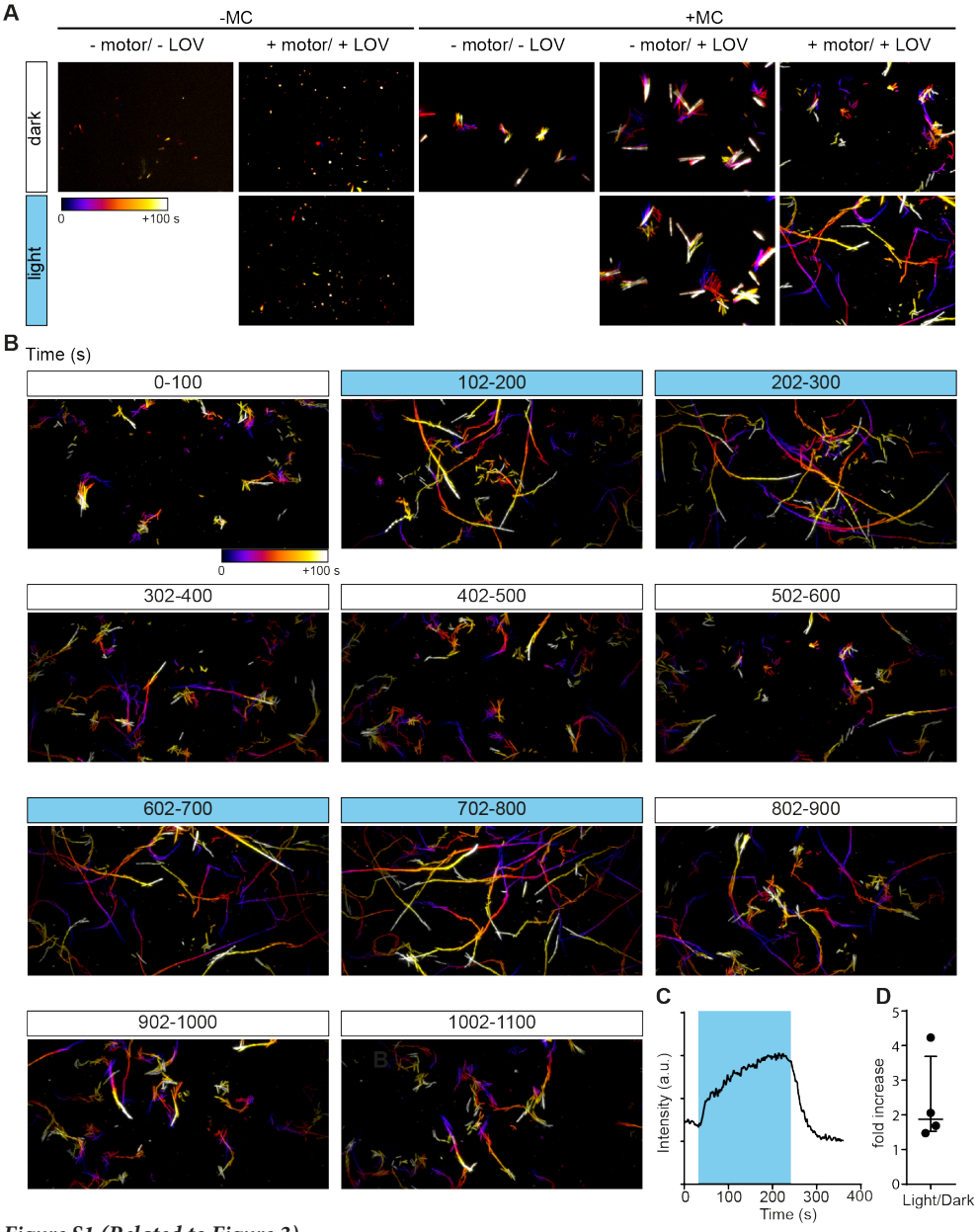

Figure S1 (Related to Figure 3)

A) *Color-coded projection of the light-induced gliding assay in the presence or absence of Methylcellulose, DmKHC-mCherry-ePDZ and LOVpep in the presence and absence of light.*

B) *Global reversible control of microtubule gliding by blue light. Temporal color coded maximum projections of 100 seconds intervals in the absence (white box) and presence (blue box) of light. See also Movie S2.*

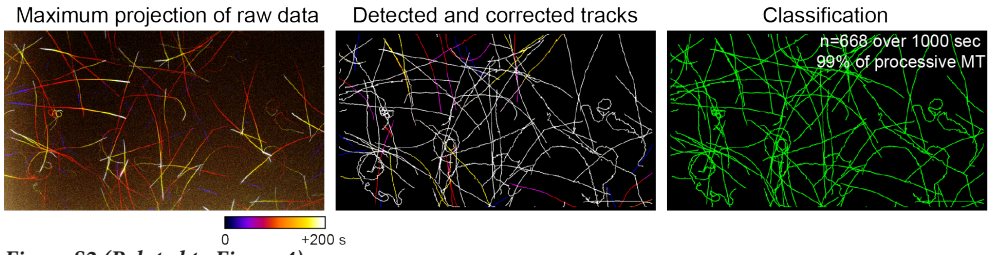

Figure S2 (Related to Figure 4)
Conventional gliding assay with constitutively attached motors to benchmark the tracking software. Raw, tracked/corrected traces and classified traces are shown.

C) *Background-corrected average intensity trace over time for DmKHC-mCherry-ePDZ in the absence or presence of global illumination with blue light (blue box).*
D) *Maximum fold-increase of DmKHC-mCherry-ePDZ after illumination with blue light. N=4, Median:IQR. Scale bar: 10µm*

LEGENDS TO SUPPLEMENTARY VIDEOS

Supplemental movie 1:
This video corresponds to Figure 2D. Sequential light-induced recruitment of ePDZ-mCherry in different patterns. Total time: 500 seconds. Acquired with 2 seconds between frames. 30 fps. (AVI, 11 Mb)

Supplemental movie 2:
This video corresponds to Figure 3. Global reversible control of microtubule gliding assays by blue light. Total time: 1100 seconds. Acquired with 2 seconds between frames. 60 fps. (AVI, 8 Mb)

Supplemental movie 3:
This video corresponds to Figure 4. Local control of microtubule motility. Total time: 1600 seconds. Acquired with 2 seconds between frames. 60 fps. (AVI, 42 Mb)

Supplemental movie 4:
This video corresponds to Figure 4 and Supplemental Figure 2. Conventional gliding assay with constitutively attached motors to benchmark the tracking software. Total time: 1000 seconds. Acquired with 2 seconds between frames. 60 fps. (AVI, 85 Mb)

SUPPLEMENTAL REFERENCES

1. Adrian, M.; Nijenhuis, W.; Hoogstraaten, R. I.; Willems, J.; Kapitein, L. C., *ACS Synth Biol* **2017,** *6* (7), 1248-1256.
2. Ruhnow, F.; Zwicker, D.; Diez, S., *Biophys J* **2011,** *100* (11), 2820-8.
3. Tarantino, N.; Tinevez, J. Y.; Crowell, E. F.; Boisson, B.; Henriques, R.; Mhlanga, M.; Agou, F.; Israel, A.; Laplantine, E., *J Cell Biol* **2014,** *204* (2), 231-45.
4. Schindelin, J.; Arganda-Carreras, I.; Frise, E.; Kaynig, V.; Longair, M.; Pietzsch, T.; Preibisch, S.; Rueden, C.; Saalfeld, S.; Schmid, B.; Tinevez, J. Y.; White, D. J.; Hartenstein, V.; Eliceiri, K.; Tomancak, P.; Cardona, A., *Nat Methods* **2012,** *9* (7), 676-82.
5. Tseng, Q.; Wang, I.; Duchemin-Pelletier, E.; Azioune, A.; Carpi, N.; Gao, J.; Filhol, O.; Piel, M.; Thery, M.; Balland, M., *Lab Chip* **2011,** *11* (13), 2231-40.
6. Katrukha, E. A.; Mikhaylova, M.; van Brakel, H. X.; van Bergen En Henegouwen, P. M.; Akhmanova, A.; Hoogenraad, C. C.; Kapitein, L. C., *Nat Commun* **2017,** *8*, 14772.
7. Meijering, E.; Dzyubachyk, O.; Smal, I., *Methods Enzymol* **2012,** *504*, 183-200.

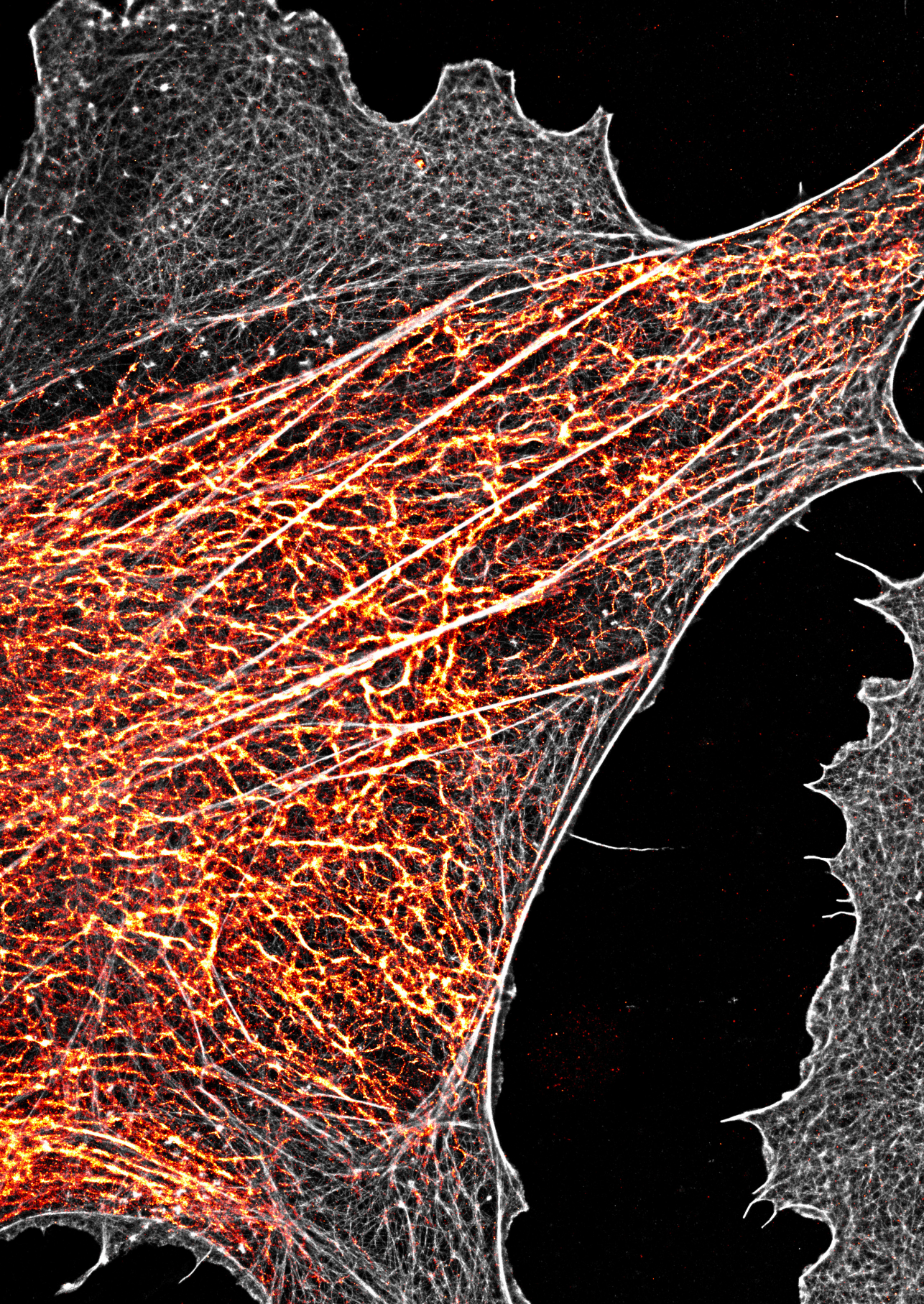

9

General Discussion

Roderick P. Tas[1]

[1] Division of Cell Biology, Faculty of Science, Utrecht University, The Netherlands

GENERAL DISCUSSION

The cytoskeleton and its molecular motors are crucial in the maintenance of cellular polarity and functioning. Especially in neurons, cargoes need to be selectively transported to either the axon or the dendrites. However, how kinesins from different superfamilies can distinguish between these different subcompartments remains poorly understood. The aim of this thesis was to increase our understanding of the relation between cytoskeleton architecture and selective transport by molecular motors. We have used a combination of advanced SMLM techniques and live-cell imaging approaches to explore how cytoskeletal organization affects cargo transport. Importantly, by developing motor-PAINT, we could directly probe neuronal microtubule orientations and correlate their properties with nanometer accuracy. This has revealed new organizational features and provided valuable insights into the traffic rules that facilitate selective targeting into the axon or dendrites by different kinesins. In this chapter I will discuss the main findings and provide a perspective for future studies.

PROBING CYTOSKELETON ARCHITECTURE

High-resolution microscopy is necessary to provide a cellular roadmap of the microtubule and actin tracks within the cell. However, because of their density it had remained challenging to resolve individual filaments and structures within neurons. For example, microtubules are reported to be spaced ~30 to 60 nanometers apart in the axon and dendrites, respectively [1]. To resolve such microtubules, we used diffraction-unlimited super-resolution techniques. Because STED and SIM only provide resolutions up to 50 nanometers, we mostly focused on a variety single-molecule localization microscopy (SMLM) techniques that can resolve structures 10-30 nanometer accuracy [2]. More specifically, our work focused on improving, developing and combining SMLM probes to provide new insights into cytoskeleton architecture.

Optimized purification and labelling of lifeAct to probe the actin cytoskeleton

High resolution SMLM reconstructions are often directly dependent on the photophysics of the fluorophores and the specificity of the probes. While high photon counts are always essential for high accuracy localizations, different imaging strategies require additional fluorophore properties or targeting mechanisms for imaging. For example, in dSTORM the structure of interest is homogeneously labelled, requiring stochastic cycling of fluorophores between a dark state and fluorescent state to detect single molecules. Alternatively, in PAINT-like approaches observation of single-molecules can be achieved by the transient binding of fluorophore-labeled interaction partners to the structure of interest. The importance of selective probes and fluorophore selection in super-resolution microscopy is highlighted by numerous studies that focus on highly selective, small probes as well as new generations of

fluorophores with improved photophysics. Recently, isolated lifeAct coupled to a fluorophore has been introduced as an SMLM probe that transiently labels actin [3]. Similar to DNA-PAINT, the transient interaction of labelled lifeAct results in constant recycling of the probe from the large soluble pool. However, commercial synthesis of this probe is relatively expensive and limited by the fluorophores and labelling techniques supplied by companies. To overcome these pitfalls, we have designed an *E.coli* based expression system of recombinant lifeAct described in **Chapter 2**. We coupled lifeAct to a cysteine followed by a proteolytic cleavage site and a fluorescent protein. This resulted in a cheap, easy to perform strategy to purify the lifeAct fragment at high yields that can easily be extended to other protein fragments. The major advantage of this purification strategy is that the fluorescent probe attached to lifeAct can be easily exchanged. The cysteine can be coupled to any maleimide-containing organic dye followed by on-bead cleavage and elution of labelled probes. Alternatively, genetic encoding of the latest fluorescent proteins with high quantum yields can be performed. In **chapter 3** and **chapter 5** we have used this probe coupled to mNeonGreen in combination with DNA-PAINT to study the relation between actin and myosin mediated anchoring or cortactin respectively.

In contrast to PALM and STORM, transient binding probes such lifeAct and DNA-PAINT doe not require induction of blinking, which can only be effectively achieved by a limited set of suitable fluorophores [4, 5]. As a consequence, the transient binding of protein or DNA fragments for SMLM results in bleaching-free imaging with any dye. However, during acquisition, a large pool of lifeAct or imager strand coupled to a fluorophore remains in solution. One undesired effect of the soluble probe is that background intensities increase, resulting in a decreased signal to noise ratio. Future efforts could focus on fluorogenic or Förster resonance energy transfer (FRET) based probes that only fluoresce while the fluorophore is located at the structure of interest[6, 7]. Furthermore, in contrast to antibodies that can be generated towards selective targets by animal immunization, it will be challenging and labor intensive to identify selective protein fragments that transiently bind any target of interest. While at least one interactor for almost any protein is known, binding should be preserved after sample preparation and molecular engineering will be required to tune the affinity into the right range. High throughput screens with labelled compounds, drugs or small peptides could be employed to identify new probes to specific targets. Alternatively, a more generic approach could be developed. For example small peptide sequences that transiently bind Immunoglobulin subclasses species or small genetic tags could be engineered [8]. Specificity will then be obtained by the already available antibodies or (endogenous) genetic encoding. Subsequently, SMLM can be performed using a standard subset of small probes in solution that transiently recognize the specific combination of antibodies and genetic tags in the same sample.

Motor-PAINT: simultaneously probing microtubule orientations and architecture

While imaging techniques such as electron microscopy, dSTORM and PAINT-like techniques have provided high-resolution images of the microtubule cytoskeleton, they cannot directly visualize the polarity of microtubules. However, to understand complex processes such as cytoskeleton organization and directional transport, this information is of crucial importance. In **Chapter 6** we have developed a kinesin-based approach, termed motor-PAINT, to probe the nanoscale microtubule cytoskeleton and directly infer microtubule orientation along the whole lattice. This technique is performed through purified recombinant GFP-tagged kinesin that transiently walks towards the plus-end of extracted and fixed microtubule cytoskeletons. Detection and reconstruction of each track, color-coded for orientation, resulted in a super-resolved roadmap of microtubules in different cell types.

Several improvements should be considered in future studies. The quality of the final reconstruction and directional information of microtubules is directly dependent on the affinity and activity of the purified motor protein. Together with bright fluorophores, this determines the amount of tracks that are of high enough quality to be used in the final reconstructions. While GFP-labelled kinesin resulted in a highly efficient assay, different labelling strategies with brighter fluorophores should can explored. Initial attempts to genetically label kinesin with the SNAP-tag, followed by on-bead labelling with organic Alexa dyes resulted in brighter motors. However, upon addition of these motors to the sample, motor activity dropped while the diffusive background increased. One possible explanation of this reduced activity could be linked to impaired kinesin dimerization as a result of the negative charge of the organic dye or the attached SNAP-tag [9]. Future efforts can focus on alternative fluorophores, genetic tags (i.e. Halo-tag) or labelling via incorporated unnatural amino acids [10, 11]. Alternatively, (tandems of) improved fluorescent proteins like mNeonGreen could increase quantum yield without compromising motor activity [12].

Besides optimized fluorophore selection, more information could be obtained by improved extraction methods and correlative strategies that combine motor-PAINT with the detection of microtubule modifications or the labeling of additional structures. To resolve the connection between microtubule orientations and modifications we already combined motor-PAINT with subsequent post-fixation, antibody labelling for microtubule modifications and dSTORM. However, these experiments were labor-intensive and cytoskeleton rearrangements occurred often by the chemical post-fixation procedure and forces generated by manual washing steps. Automated protocols using microfluidic devices and more direct probes for microtubule identity, which do not require additional fixation steps, could optimize these procedures.

Similar to motor-PAINT, previous studies have shown that purified myosins are able to walk along a triton-extracted cytoskeleton [13-15]. While these studies could determine overall actin orientation in dense actin networks, the number of observed events was insufficient to reconstruct the dense actin networks and its orientation. Future efforts should increase myosin activity along extracted cytoskeletons. Probing the actin architecture in

specialized cellular compartments will be valuable to further understand polarized transport, as discussed in the next section.

Technical advances for high-resolution imaging

In addition to the development of new techniques to probe different features of the cytoskeleton, there have also been some major technical advances that increase the imaging depth, z-resolution and provide alternative methods to study the architecture of the cytoskeleton.

To reduce background fluorescence from out-of-focus fluorophores, SMLM is often performed by total internal reflection fluorescence (TIRF) microscopy, limiting the imaging depth to 200-300 nanometers. Recently, alternative illumination strategies are developed to overcome these limitation. Spinning disk confocal microscopy combined with bright DNA-PAINT probes and high laser powers has been shown to result in high quality reconstructions of the cellular cytoskeleton at imaging depths of ~10 μm [16]. This approach is relatively easy to implement by equipping a standard spinning disk microscope with high-power lasers. A more complex approach that can image even deeper within the sample is lattice light sheet microscopy (LLSM)[17]. LLSM uses thin Bessel beams to create a thin light sheet perpendicular to the imaging plane. The thickness of these beams is between 500-1000 nm and as a result, only fluorophores that are in focus will be excited. However, increased imaging depths also result in PSF aberrations. These aberrations can be corrected by point spread function (PSF) engineering through deformable mirrors in the emission pathway[18]. Simultaneously, PSF engineering can be employed to accurately localize single-molecules in the z-dimension [19, 20]. These illumination strategies provide exciting opportunities to further optimize motor-PAINT to understand cellular microtubule arrays deeper within cells and tissues.

Recently, an entirely different microscopy method, Expansion Microscopy, was introduced that achieves high-resolution imaging by physical expansion of the sample. After expansion, molecules that were previously spaced below the diffraction limit are now spaced far enough to be imaged by diffraction-limited microscopy. Confocal microscopy, STED and LLSM have all been used to image the expanded samples at very high resolution[21, 22]. Expansion microscopy is now widely used and can image deep into tissues with single-microtubule resolution. However, labelling, signal amplification and epitope preservation remain challenging.

UNDERSTANDING THE NEURONAL CYTOSKELETON AND ITS TRAFFIC RULES

Actin-dependent control of polarized transport at the axon initial segment

The axon initial segment (AIS) in neurons is a specialized structure in the proximal axon that is believed to function as a sieve for diffusion and directional transport[23, 24]. Previous studies proposed that the overall orientation of actin in the initial segment is organized with

its plus-end facing the soma. As a result myosinV could reverse somatodendritic cargo at the AIS whereas myosinVI could move cargo further into the axon[25, 26]. In **Chapter 3** we used an inducible assay to explore the role of myosinV-based retention at the AIS. Inducible recruitment of Kif5 to peroxisomes resulted in axonal targeting. However, subsequent recruitment of MyosinV immediately halted the peroxisomes at distinct patches in the initial segment, but did not reverse transport. Furthermore, recruitment of MyosinV to axonal Rab3 vesicles displayed identical anchoring at the AIS and did not drive retrograde transport. Our results therefore suggested that the AIS can act as a selective filter for myosin-attached cargoes, but does not facilitate actin-based retrograde transport. To further explore actin organization in the AIS, it would be valuable to develop motor-PAINT with myosins to directly probe the polarity of the actin patches at the AIS. Furthermore, the later fate of these mislocalized, myosin-anchored somatodendritic cargoes should be considered, as stalling alone will result in clogging of the axon. Therefore, after anchoring, additional mechanisms are necessary to account for long range reversals back into the somatodendritic compartment.

In **Chapter 4** we assessed the role of the AIS as a selective filter in the halting and reversals of cargoes attached to full length Kif17. Kif17 has mainly been described to function in transport within dendritic branches and transport of the K^+ channel Kv4.2 [27, 28]. However, chemically-induced recruitment of a constitutive active truncation of the motor-domain to peroxisomes results in axonal targeting [29]. In our study investigated the mechanisms that sort Kif17 to the dendrites. Surprisingly, recruitment of full length Kif17 that contained its C-terminal tail domain resulted in axonal entry, followed by halting of cargoes at the AIS. Subsequently, these retained cargoes began to reverse back towards the soma and entered into the dendrites in a dynein-dependent matter. Pharmacological depolymerization of actin showed that anchoring of these vesicles in the AIS was actin dependent. Furthermore, the patches on which cargoes anchored were similar to those described for myosin-anchored cargoes in the previous chapter. Future work could explore whether anchoring of Kif17-driven cargoes is also myosin dependent. Interestingly, axonal exclusion of the Kv4.2 channel is MyosinVa dependent [30]. An interactome study of the Kif17 tail domain could elucidate the key molecular players and could possibly identify a direct or indirect interaction between Kif17 and actin in the initial segment.

The findings described above are consistent with the function of the AIS as a filter for selective sorting. Microtubule and actin-based transport in the AIS act as an important regulatory mechanism to target or retain axonal and somatodendritic cargoes, respectively. Somatodendritic cargoes are anchored by actin-dependent mechanisms and reversed through dynein-mediated transport, whereas axonal cargoes can pass. To achieve this selectivity, an interplay of multiple kinesins, dyneins and myosins, activated at specific subcompartments is required. Because cargoes carry multiple motors of different subclasses simultaneously, spatiotemporal regulation of motor activity should be tightly controlled. The spatial distribution of specific activators can directly act as a molecular switch for the activity of

motor proteins and contribute to the regulation of trafficking direction. This is supported by previous work that has shown that dynein activators, CDK5 and NDEL, localize specifically at the AIS [31, 32]. Depletion of NDEL or dynein activity significantly reduces the number of reversals of somatodendritic cargoes that entered the AIS, whereas axonal cargoes are not affected [31, 32]. Similar spatiotemporal control mechanisms could apply for myosin-mediated retention in the AIS. Somatodendritic cargoes can be sorted by recruitment of myosins, which are activated in the AIS. Myosin specific-regulators should be tested for AIS localization to understand the regulatory mechanisms of compartment-specific anchoring. Interestingly, tropomyosin isoforms directly regulate the activity of specific myosins and their binding to actin. Furthermore, the spatiotemporal distribution of tropomyosins has been shown to be important in neurite outgrowth, cellular development, morphogenesis and cytoskeleton organization [33-35]. Therefore, it would be interesting to explore the function of tropomyosins at the AIS. In addition, more work is needed to determine the exact complement of motors and adaptors on different dendritic and axonal cargoes.

Interplay between actin and microtubules in dendritic spines

In **Chapter 5** we aimed to assess the relation between the actin cytoskeleton and microtubule entries in dendritic spines. Previously, it has been shown that activation of synapses results in actin-dependent microtubule entries into the spine [36]. To better understand the dynamic interplay we set out to visualize actin remodeling and identify its regulators. We identified cortactin as a regulator of actin remodeling in active spines. Translocation of cortactin to the spine base correlated with increased actin dynamics and microtubule entries upon stimulation. It has been shown that actin structures protrude from spine necks [37]. Using lifeAct-mNeonGreen combined with DNA-PAINT SMLM, we could visualize these distinct actin structures with high resolution at the spine base. Interestingly, whereas actin dense regions were confined to the spine base and often colocalized with cortactin, long actin cables protruded from the spine neck into the dendritic shaft. Based on our live-cell imaging, combined with advanced super-resolution microscopy, we proposed that activity-dependent actin dynamics results in the formation of actin cables at the spine base that can guide microtubules to enter spines.

Our study provides more in-depth insights into the actin architecture at the spine base and the interplay between actin and microtubule dynamics upon neuronal activity. However, the proposed model should be strengthened using two-color high-resolution live-cell imaging to show the frequency of microtubule polymerization events along these actin cables. State of the art SIM and STED microscopy should provide sufficient resolution to show these interactions. Furthermore, the contribution of increased microtubule entries on synaptic organization upon activation should be investigated. In contrast to transport along the existing actin cytoskeleton in spines [38], dynamic microtubule entries are required to control spine plasticity and size [39-41]. It has been proposed that the EB3 decorated tip

of dynamic microtubules targets p140Cap to the spines to control actin dynamics and spine plasticity [41]. Furthermore, it has been shown that kinesins can transport recycling endosomes or synaptotagmin-4 into the spine along these microtubules to provide essential molecules [42, 43]. Increased microtubule entries could therefore be required to fine tune the composition, size and plasticity of the synapse upon activation. Our results now suggest such an activity-dependent link between actin structures and the recruitment of dynamic microtubules to regulate synaptic plasticity.

The previous two sections demonstrated that the organization of actin directly underlies its function. Throughout the neuron a variety of actin structures with specific functions have been identified. In the last two decades, high resolution imaging has identified new actin structures and contributed to understanding their function. For example the actin rings that control neurite caliber and actin trails that emerge from actin hotspots and have been proposed to drive slow [44] axonal transport [44-47]. Interestingly, little is known about actin in the presynapse and its regulatory mechanisms. While several functions of presynaptic actin have been assigned, the reported results are often inconsistent [48]. High resolution mapping of actin architecture, dynamics and the regulators involved will be of importance to understand its functions at the presynapse.

Microtubule orientations dictate selective transport

The orientation of microtubules directly control the directions of kinesins and dyneins. In addition, other microtubule properties, such as modifications and associated proteins, are believed to module the affinity of different motors. In **chapter 6** we have developed motor-PAINT to explore the interplay between microtubules orientations and other microtubule properties in dendrites. While previous reports already established that microtubules in dendrites have a mixed polarity [49, 50], their exact spatial organization and the interplay between orientation and modifications had remained unknown. Using motor-PAINT, we found that even though the overall microtubule polarity in dendrites is mixed, microtubules with the same orientations in dendrites are often clustered in polarized bundles. On the size scale of cellular cargoes and motor proteins, these bundles can function as uniform highways for directional transport in the dendrites. Indeed, in neurons, vesicles that contain multiple motors often travel long distances in one direction. The limited reversals and trajectories longer than the typical run length of a single kinesin are consistent with transport along microtubule highways.

However, our data showed that bundles of microtubules with a preferred polarity exist in either direction and therefore do not explain why some kinesins only target the axon and others accumulate at dendritic tips. Pharmacological treatment and correlative super-resolution combined with motor-PAINT revealed that stable microtubules are predominantly orientated with their minus-end out. This has led to a new model for selective sorting into the axon by kinesins based on microtubule preference. Kinesins that prefer stable microtubules,

drive retrograde transport in the dendrites along the minus-end out microtubules whereas the uniform plus-end out orientation of microtubules results in axonal targeting. In contrast, kinesins that are non-selective or prefer dynamic microtubules will provide bidirectional transport in the dendrites or accumulate at the tips, respectively. Indeed Kif5, which prefers stable microtubules, does not enter dendrites and selectively targets the axon [29, 51, 52]. However, future efforts should provide direct live-cell evidence for the retrograde movement of Kif5 in dendrite. However, assessing Kif5 activity in the dendrites will be challenging. One possible method would be to express full-length (auto-)inhibited Kif5 linked to an inducible module which diffuses throughout the neuron. Subsequent inducible coupling to dendritic cargo relieves auto-inhibition and result in dendritic Kif5 activity. Retrograde motor activity of Kif5 will then result in an overall flow of the cargo out of the dendrite into the axon. In addition to Kif5 selectivity our model also provides an explanation for Kif1 accumulation in dendritic tips[51]. Whereas a previous study already suggested that Kif1 prefers dynamic microtubules[53], our quantification of a rigor-Kif1a showed a ~2-fold enrichment on tyrosinated microtubules. Therefore, the predominantly plus-end out tyrosinated microtubules in the dendrites will bias Kif1 transport into dendritic tips. Similar to Kif1, Kif21 accumulates in dendritic tips [51]. It would be interesting to determine the preference of these and other motors to understand if their neuronal localization is directly guided by the orientation of the microtubules to which they preferentially bind.

While not emphasized in **Chapter 6**, our results show that acetylated and minus-end out microtubules are often located at the center of the dendrite. In contrast, tyrosinated plus-end out microtubules are localized more peripherally. Consistently, preliminary 3D STED sectioning revealed that acetylated microtubules are often centrally located and surrounded by tyrosinated microtubules (**Fig 1**). Correlative live-cell imaging followed by 3D motor-PAINT can shed light on the cellular trafficking routes of different cellular cargoes attached to kinesin subsets. It can be expected that Kif5- or Kif1-propelled cargoes predominantly move in opposite directions along the microtubule network in the center or periphery of the dendrites respectively. Furthermore, previous work showed that dynein is preferentially loaded onto dynamic tyrosinated microtubules[54]. It will be interesting to see whether anterograde dynein-driven transport in dendrites initiates on the peripheral tyrosinated microtubules. To understand the complete distribution of microtubule orientations within the dendrite, PSF engineering and LLSM combined with optimized fluorescent dyes is necessary to perform 3D motor-PAINT.

In our motor-PAINT assay, microtubules were stabilized with taxol to ensure Kinesin-1 would sample each microtubule with similar probability. It would be valuable to develop protocols for motor-PAINT in which different motors maintain their preference for microtubule subsets. Microtubule extraction in the absence of the stabilizing drug taxol might result in the preservation of the endogenous pool of stable microtubules versus more dynamic microtubules. Subsequent motor-PAINT with Kif5 and Kif1, would then provide

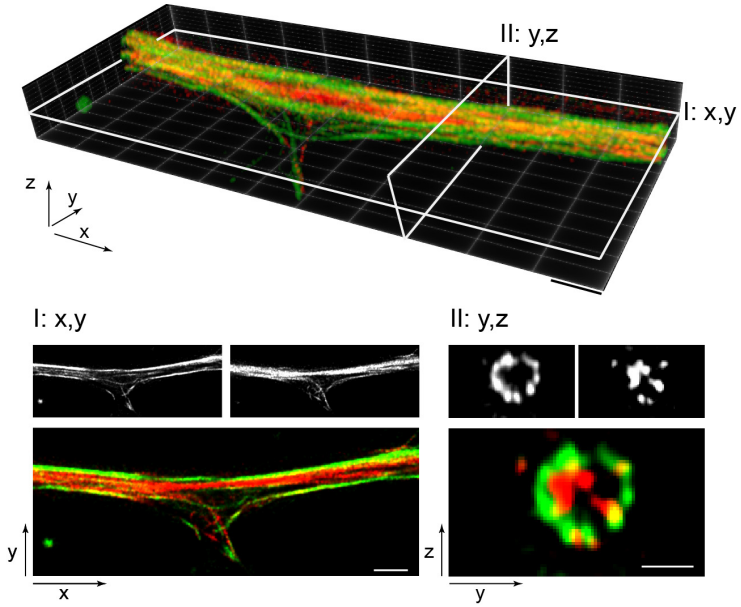

Figure 1: 3D dendritic microtubule organization
Top panel shows a 3D rendering (ClearVolume, ImageJ plugin) of acetylated (red) and tyrosinated (green) microtubules in a dendrite of a hippocampal neuron acquired by 3D gSTED microscopy. The indicated cross-sections through x,y (I) and y,z (II) are shown below. Individual and merged channels are displayed. Acetylated microtubules mostly localize in bundles in the center of the dendrite, whereas tyrosinated microtubules are distributed in the periphery.
Scale bar: top and I; 2 µm II; 1 µm

more in depth insights in the trafficking rules of individual motors along the different microtubule subsets. However, it should be noted that we currently do not understand how motors recognize different microtubule subsets. Perhaps selectivity depends on MAPs that slowly accumulate on stable microtubules and therefore requires the differential dynamics of different microtubule subsets. This will be lost on extracted cytoskeletons, precluding reconstitution of selectivity.

It should be noted that polarized sorting does not exclusively depend on the mechanisms described above. To control selective localization in either the axon or dendrites, additional mechanisms have been described. For example, after non-selective sorting throughout the neuron, local control of endocytosis can deplete proteins from specific compartments, resulting in compartment specific retention of molecules[55]. In addition, sorting is controlled before the AIS where dendritic cargo transport is excluded by the pre-axonal exclusion zone (PAEZ). This PAEZ consists of a subset of highly modified microtubules that are recognized by axon selective motors like Kif5 [56]. It was proposed that motor proteins on somatodendritic cargoes have reduced affinity for these microtubules

and are therefore excluded from the PAEZ. Finally, MAPs can regulate the activity and bias of different motor proteins in specific neuronal compartments [57, 58] and MAP-dependent mechanisms for selective sorting have been proposed [58, 59]. A recent study in hippocampal neurons revealed that septin9 localizes to dendritic microtubules and directly stimulates or inhibits transport by Kif1 and Kif5 respectively. As a result kif5 does not actively target the dendrite whereas Kif1 does. However, activation of Kif1 along all microtubules by septin9 in the dendrites does not directly explain the anterograde bias observed by the authors [59]. One explanation could be that Septin9 preferentially decorates plus-end out tyrosinated microtubules to drive the anterograde bias of Kif1 while further reducing Kif5 affinity for this subset. Exclusion of Septin9 from the acetylated minus-end out microtubules would also be consistent with our proposed role for Kif5 as retrograde dendritic motor. Studying the microtubule preference of septin9 and further characterization of Kif5 as retrograde motor will provide further insights in the synergistic effects of microtubule subset organization and MAPs on polarized sorting. Furthermore, since knockdown of Septin9 results in miss-sorting of Kif5, it would be interesting to study its role in controlling microtubule organization, orientation and stability.

Building the neuronal microtubule cytoskeleton

Our work has shown that microtubules are segregated by polarity and that minus-end out microtubules are more stable. One important question that remains is how such a specialized cytoskeleton is built. Additionally, the advantages of transport along the mixed microtubule array in dendrites of higher organisms needs to be elucidated. It would be interesting to assess if there is a correlation between microtubule organization and dendritic complexity in species throughout the evolutionary tree. In lower organisms, microtubule sliding and cortical interactions are involved in neurite outgrowth and the regulation and preservation of the minus-end out microtubule array in the dendrite[60-64]. In Drosophila, Kinesin-2 guides polymerizing plus-ends along dendritic microtubules to maintain the uniform polarity. Recently, in *C.elegans,* it has been reported that local nucleation of microtubules at the tip of the cilia contributes to uniform microtubule polarity[64]. Thus, local nucleation, microtubule sliding and cortical interactions can control microtubule orientation and integrity in uniform minus-end out microtubule arrays of these lower organisms. However, how these mechanisms are involved in the mixed dendritic neuronal microtubule arrays is unknown. Furthermore, selective stabilization of the minus-end out microtubules poses an organizational challenge. While compartmentalized stabilization of uniformly oriented microtubules has been described[65], selective stabilization of dendritic minus-end out microtubules would require specificity based on microtubule orientation within the same compartment. Based on the described mechanisms in lower organisms a potential model for neuronal cytoskeleton organization in mammals could be formulated. Upon polarization, anchored Kinesin-1/Kif5 preferentially slides stable, modified microtubules with their minus-

end outwards into the dendrites. Additionally, local nucleation or dynein mediated sliding could result in tyrosinated plus-end out oriented microtubules to generate a mixed array with stable minus-end out microtubules and dynamic plus-end out microtubules. Subsequently, the microtubules with opposing orientations and identity could be bundled by selective MAPs.

Mapping microtubule orientations, their identity and the distribution of motor proteins and MAPs throughout neuronal development will provide further insights in the maturation of neuronal microtubule arrays during polarization. State of the art genetic screens can now be used to identify the general proteins that regulate cytoskeleton diversity and dynamics[66]. Subsequently, neuron-specific knockout screens combined with live-cell imaging should then reveal the key molecular players for cytoskeleton specialization and selective trafficking. The recent development of endogenous tagging and knockout in neurons via CRISPR-Cas9[67, 68] will reduce the effects of overexpression or partial knock-out for a more reliable readout.

UNDERSTANDING KIF5 PREFERENCE

As described above, motor proteins can prefer different subsets of microtubules. The most striking and well-described example is Kinesin-1/Kif5, which binds exclusively to a subset of stable and highly modified microtubules. However the exact protein sequences that make Kif5 selective have remained elusive. Previous studies in dissociated hippocampal neurons have shown that the introduction of loop12 of Kif1 into the Kif5 motor domain reduces axonal selectivity[51]. In contrast, grafting loop12 of Kif5 onto Kif1 did not alter Kif1 localization into dendritic tips. Furthermore, an in depth *in vitro* study, proposed that the electrostatic interaction of the neck-coil with tubulin affects kinesin processivity[69]. However, the latter study did not assess the effect of the neck-coil on Kif5 selectivity within cells.

We set out to investigate whether Kif5b selectivity is solely dependent on its motor domain or whether its C-terminal coils are important for selective binding to microtubule subsets. To directly assess binding of Kif5 to microtubule subsets, we used a rigor Kif5 as previously reported[53, 56, 70] (**Fig 2a**). We argued that detection of the rigor construct provides a direct readout of Kif5 preference independent of processivity. Rigor Kif5 was truncated after its first coiled-coil (aa1-560), its neck-coil (aa1-370) or its neck-linker (aa1-336) (**Fig 2b**). Subsequently these constructs were expressed in CRISPR-Cas9 mediated Kif5 KO HeLa cells to prevent dimerization with endogenous Kif5 (**Fig 2c**). To avoid saturation along the lattice due to overexpression we amplified the signal of the recombinant protein by antibody staining. In addition, acetylated and tyrosinated tubulin was stained to identify stable and dynamic microtubules respectively.

Consistent with previous reports and **chapter 6,** rigor Kif5 that contains its first coiled-coil ($5b^{1-560}$) exclusively binds to highly modified microtubules marked by acetylation (**Fig 2c, top row**). Similarly, truncation of Kif5 after the neck-coil ($5b^{1-370}$) still resulted in

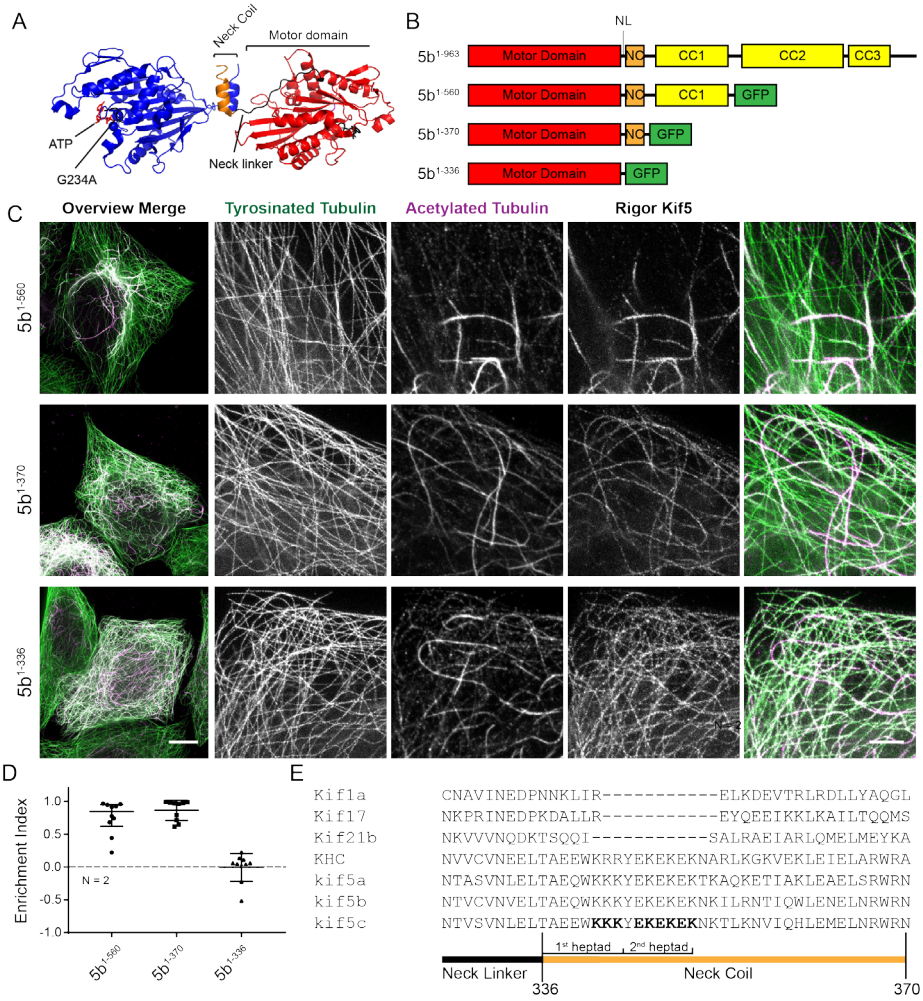

Figure 2: The Kif5 motor domain alone is not sufficient for selectivity

A) *Structure of dimeric KHC (pdb: 2Y5W). Monomer 1 (blue), the ATP binding pocket, rigor mutation (G234A) and the motor domain (red), neck-linker (black) and neck-coil (orange) are indicated.*

B) *Schematic representation of the full-length Kif5 and three truncations coupled to GFP that were used to assess Kif5 selectivity.*

C) *Expression and staining of the rigor truncations shown in (B) in Hela Kif5b KO cells, co-stained for the tyrosinated and acetylated microtubules. A merged overview (left panel) and zooms are shown.*

D) *Quantification of the enrichment index of each of the constructs shown in (C). Values approaching 1 or -1 indicate a preference for acetylated or tyrosinated microtubules respectively, whereas 0 indicates that the motor has no preference.*

E) *Multiple sequence alignment of the neck-linker and neck-coil of the Kinesin-1 superfamily compared to other kinesins. The charged residues specific for the Kinesin-1 family are indicated in bold in the Kif5c sequence.*

Scale bar overview: 10 µm; zoom: 2 µm

selective binding (**Fig 2c, middle row**). Preliminary quantitative comparison of Kif5 intensity on microtubule subsets, using the enrichment index as described in **chapter 6**, did not show any difference between these constructs (**Fig 2d**). Surprisingly, further truncation of Kif5, keeping only the motor domain and the neck-linker ($5b^{1-336}$), completely abolished selective binding for microtubule subsets (**Fig 2c, bottom row, Fig 2d**). These results strongly suggest that the Kif5 motor domain alone is not sufficient to recognize stable microtubule subsets marked by acetylation.

To better understand the role of the neck-coil in the selective recognition of stable microtubules, we aligned the transition between the Kif5 neck-linker and neck-coil for both other Kinesin-1s and other kinesin families. These included Kif1 and Kif21 that accumulate at dendritic tips and Kif17, which targets the axon when expressed as a constitutive active truncation [29, 51]. Strikingly, sequence homology of the first two heptad repeats (aa337-350) was only observed in other members of the Kinesin-1 superfamily but not in other superfamilies (**Fig 2e**). Interestingly, this domain is rich in Lysine and Glutamic acid residues and has a net positive charge. Furthermore, the previous report also identified that this charge is important for controlling kinesin processivity [10].

Next we wanted to investigate the role of the first two heptad repeats of Kif5 in selective microtubule recognition. To test whether dimerization alone is sufficient for Kif5 selectivity we used the GCN4 motif to artificially dimerize Kif5 truncated after the neck-linker ($5b^{1-336}$-GCN4). Even though artificial dimerization increased Kif5's preference for acetylated microtubules, it did not result in exclusive binding of Kif5 to microtubules marked by acetylation (**Fig 3 second row**). Preliminary quantification revealed an enrichment index of 0.44±0.08 whereas 0.86±0.07 was observed for the construct that contains the endogenous neck-coil (**Fig 3b**). These results suggest that dimerization alone contributes to, but is not sufficient for Kif5 selectivity. Next we generated artificially dimerized constructs in the presence of either the first ($5b^{1-342}$-GCN4, **Fig 3 third row**) or first two heptad repeats ($5b^{1-353}$-GCN4, **Fig 3a fourth row**). Interestingly, addition of the first heptad repeat resulted in increased selectivity and addition of both repeats completely rescued exclusive binding to acetylated microtubules (**Fig 3b)**. Removal of the GCN4 domain after the second heptad repeat resulted in aspecific binding ($5b^{1-353}$,**Fig 3b,)**. Finally, mutation of all charged residues to Alanine again reduced selectivity to levels comparable to Kif$5b^{1-336}$-GCN4(**Fig 3a, fifth row, 3b)**. These results suggest that both dimerization and the specific amino acid sequence of the first two heptad repeats are required for Kif5 selectivity.

Whereas previous studies could make Kif5 non-selective by replacing loop12 in the motor domain with that of Kif1, our results demonstrate that the motor domain alone is not sufficient for selective binding but requires dimerization by the C-terminal neck-coil. Previous work has shown that the positive charge present in loop12 of Kif1 results in increased microtubule affinity of this motor compared to Kif5 [59, 71]. It could be speculated that this reduced affinity of the Kif5 motor domain is compensated by an additional microtubule

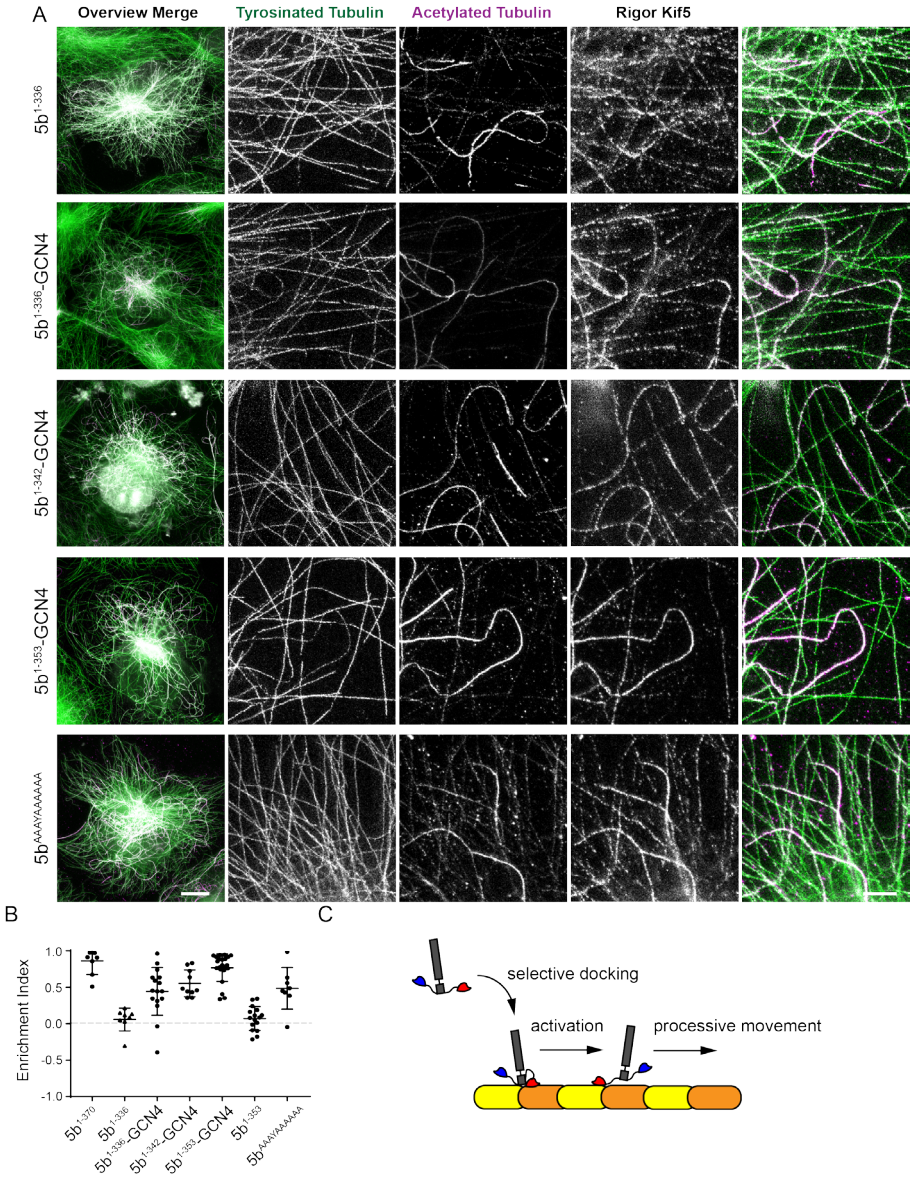

Figure 3: The Kif5 neck-coil contributes to microtubule preference

A) *Expression and staining of the rigor constructs that were either monomeric or artificially dimerized in the presence or absence of 1 or 2 heptad repeats of the Kinesin-1 neck-coil in Cos7 cells, co-stained for the tyrosinated and acetylated microtubules. A merged overview (left panel) and zooms are shown.*

B) *quantification of the enrichment index of each of the constructs shown in (A). Values approaching 1 or -1 indicate a preference for acetylated or tyrosinated microtubules respectively, whereas 0 indicates that the motor has no preference.*

C) *Model for selective microtubule recognition by Kinesin-1 involving the neck-coil and subsequent activation on the microtubule resulting in processive movement.*

Scale bar overview: 10 µm; zoom: 2 µm

binding domain in the neck-coil. This is supported by previous studies that showed an interaction of the Kif5 neck-coil with the C-terminus of tubulin which affects the affinity of the motor for the microtubule [69, 72, 73].

Our preliminary results suggest that in addition to increased microtubule affinity, the first two heptad repeats of the neck-coil and dimerization are also essential for Kif5 selectivity. Therefore, based on previous results and our new results, a two-step model for selective binding and activity of Kif5 can be proposed. In this model, selective Kif5 docking is mediated by the neck-coil. Subsequently, docked Kif5 is activated because the motor domains are close to the microtubules (**Fig 3c**). These results provide new insights into the domains involved in microtubule selectivity in cells. Further engineering and structural studies are necessary to fully understand the molecular interactions between motor proteins and tubulin. CryoEM studies of dimeric Kif5 in the presence and absence of the first heptad repeat will provide valuable insights into the docking mechanisms onto differentially polymerized microtubules. This might also reveal what features of the microtubule are recognized by the Kif5b neck coil. Additional studies should also aim to induce selectivity on a non-selective motor. Previous attempts to increase the selectivity of Kif1 by replacing its loop12 with that of Kif5 failed. However, our results suggest that the generation of a Kif1 motor domain with the loop12 and the neck-linker and neck-coil of Kif5 could potentially be selective.

CONCLUDING REMARKS

Studying how proteins and organelles are distributed throughout the cell is important to understand cellular organization and functioning in healthy and diseased tissues. Distribution of these cargoes is especially important in highly compartmentalized cells such as neurons. One of the major mechanisms to regulate this distribution is by active transport along the cytoskeleton. Throughout this thesis we have used advanced live-cell and super-resolution imaging to understand the cellular traffic rules. We have focused on improving, developing and combining SMLM probes to map the architecture of the microtubule and actin cytoskeleton. This brought us closer to a better understanding of the relation between cytoskeleton organization and directional transport. Moreover, by developing motor-PAINT, we discovered new organizational features of the neuronal cytoskeleton that can explain selective transport along directional microtubule highways by selective motor proteins.

These novel insights into cytoskeletal organization also pose a wide range of exciting new questions. For example, do actin orientations in the axon control directional transport? How does the distribution of microtubule orientation and composition contribute to directional transport in other polarized cell types, e.g. gut epithelial cells? Furthermore it will be of importance to understand how such specialized cytoskeletons are build. Technical advances will continue to push the resolution in all three dimensions to resolve cytoskeletal arrays in complex tissues. Direct comparison of the cytoskeletal architecture in healthy and

diseased tissues will increase our understanding in cellular defects. Additionally, endogenous protein tagging, high-throughput screens and single-cell specific techniques will provide valuable insights into the key players involved in cytoskeletal maturation during neuronal development. It will be exciting to see how multidisciplinary research teams will continue to push until the neuronal traffic rules are completely elucidated.

REFERENCES

1. Chen, J., et al., *Projection domains of MAP2 and tau determine spacings between microtubules in dendrites and axons.* Nature, 1992. **360**(6405): p. 674-7.
2. Huang, B., M. Bates, and X. Zhuang, *Super-resolution fluorescence microscopy.* Annu Rev Biochem, 2009. **78**: p. 993-1016.
3. Kiuchi, T., et al., *Multitarget super-resolution microscopy with high-density labeling by exchangeable probes.* Nat Methods, 2015. **12**(8): p. 743-6.
4. Jungmann, R., et al., *Multiplexed 3D cellular super-resolution imaging with DNA-PAINT and Exchange-PAINT.* Nat Methods, 2014. **11**(3): p. 313-8.
5. Chozinski, T.J., L.A. Gagnon, and J.C. Vaughan, *Twinkle, twinkle little star: photoswitchable fluorophores for super-resolution imaging.* FEBS Lett, 2014. **588**(19): p. 3603-12.
6. Auer, A., et al., *Fast, Background-Free DNA-PAINT Imaging Using FRET-Based Probes.* Nano Lett, 2017. **17**(10): p. 6428-6434.
7. Lukinavicius, G., et al., *Fluorogenic Probes for Multicolor Imaging in Living Cells.* J Am Chem Soc, 2016. **138**(30): p. 9365-8.
8. Choe, W., T.A. Durgannavar, and S.J. Chung, *Fc-Binding Ligands of Immunoglobulin G: An Overview of High Affinity Proteins and Peptides.* Materials (Basel), 2016. **9**(12).
9. Zanetti-Domingues, L.C., et al., *Hydrophobic fluorescent probes introduce artifacts into single molecule tracking experiments due to non-specific binding.* PLoS One, 2013. **8**(9): p. e74200.
10. Thorn, K., *Genetically encoded fluorescent tags.* Mol Biol Cell, 2017. **28**(7): p. 848-857.
11. Kim, C.H., J.Y. Axup, and P.G. Schultz, *Protein conjugation with genetically encoded unnatural amino acids.* Curr Opin Chem Biol, 2013. **17**(3): p. 412-9.
12. Shaner, N.C., et al., *A bright monomeric green fluorescent protein derived from Branchiostoma lanceolatum.* Nat Methods, 2013. **10**(5): p. 407-9.
13. Tee, Y.H., et al., *Cellular chirality arising from the self-organization of the actin cytoskeleton.* Nat Cell Biol, 2015. **17**(4): p. 445-57.
14. Sivaramakrishnan, S. and J.A. Spudich, *Coupled myosin VI motors facilitate unidirectional movement on an F-actin network.* J Cell Biol, 2009. **187**(1): p. 53-60.
15. Brawley, C.M. and R.S. Rock, *Unconventional myosin traffic in cells reveals a selective actin cytoskeleton.* Proc Natl Acad Sci U S A, 2009. **106**(24): p. 9685-90.
16. Schueder, F., et al., *Multiplexed 3D super-resolution imaging of whole cells using spinning disk confocal microscopy and DNA-PAINT.* Nat Commun, 2017. **8**(1): p. 2090.
17. Chen, B.C., et al., *Lattice light-sheet microscopy: imaging molecules to embryos at high spatiotemporal resolution.* Science, 2014. **346**(6208): p. 1257998.
18. Liu, T.L., et al., *Observing the cell in its native state: Imaging subcellular dynamics in multicellular organisms.* Science, 2018. **360**(6386).
19. Huang, B., et al., *Three-dimensional super-resolution imaging by stochastic optical reconstruction microscopy.* Science, 2008. **319**(5864): p. 810-3.
20. Gustavsson, A.K., et al., *Tilted Light Sheet Microscopy with 3D Point Spread Functions for Single-Molecule Super-Resolution Imaging in Mammalian Cells.* Proc SPIE Int Soc Opt Eng, 2018. **10500**.
21. Gao, R., et al., *Cortical column and whole-brain imaging with molecular contrast and nanoscale resolution.* Science, 2019. **363**(6424).

22. Gao, M., et al., *Expansion Stimulated Emission Depletion Microscopy (ExSTED).* ACS Nano, 2018. **12**(5): p. 4178-4185.
23. Leterrier, C. and B. Dargent, *No Pasaran! Role of the axon initial segment in the regulation of protein transport and the maintenance of axonal identity.* Semin Cell Dev Biol, 2014. **27**: p. 44-51.
24. Winckler, B., P. Forscher, and I. Mellman, *A diffusion barrier maintains distribution of membrane proteins in polarized neurons.* Nature, 1999. **397**(6721): p. 698-701.
25. Watanabe, K., et al., *Networks of Polarized Actin Filaments in the Axon Initial Segment Provide a Mechanism for Sorting Axonal and Dendritic Proteins.* Cell Reports, 2012. **2**(6): p. 1546-1553.
26. Balasanyan, V., et al., *Structure and Function of an Actin-Based Filter in the Proximal Axon.* Cell Rep, 2017. **21**(10): p. 2696-2705.
27. Setou, M., et al., *Kinesin superfamily motor protein KIF17 and mLin-10 in NMDA receptor-containing vesicle transport.* Science, 2000. **288**(5472): p. 1796-802.
28. Chu, P.J., J.F. Rivera, and D.B. Arnold, *A role for Kif17 in transport of Kv4.2.* J Biol Chem, 2006. **281**(1): p. 365-73.
29. Kapitein, L.C., et al., *Mixed microtubules steer dynein-driven cargo transport into dendrites.* Curr Biol, 2010. **20**(4): p. 290-9.
30. Lewis, T.L., Jr., et al., *Myosin-dependent targeting of transmembrane proteins to neuronal dendrites.* Nat Neurosci, 2009. **12**(5): p. 568-76.
31. Klinman, E., M. Tokito, and E.L.F. Holzbaur, *CDK5-dependent activation of dynein in the axon initial segment regulates polarized cargo transport in neurons.* Traffic, 2017. **18**(12): p. 808-824.
32. Kuijpers, M., et al., *Dynein Regulator NDEL1 Controls Polarized Cargo Transport at the Axon Initial Segment.* Neuron, 2016. **89**(3): p. 461-71.
33. Gunning, P.W., et al., *Tropomyosin - master regulator of actin filament function in the cytoskeleton.* J Cell Sci, 2015. **128**(16): p. 2965-74.
34. Gunning, P.W. and E.C. Hardeman, *Tropomyosin-directed tuning of myosin motor function: Insights from mutagenesis.* Cytoskeleton (Hoboken), 2018. **75**(4): p. 147-149.
35. Curthoys, N.M., et al., *Tropomyosins induce neuritogenesis and determine neurite branching patterns in B35 neuroblastoma cells.* Mol Cell Neurosci, 2014. **58**: p. 11-21.
36. Merriam, E.B., et al., *Synaptic regulation of microtubule dynamics in dendritic spines by calcium, F-actin, and drebrin.* J Neurosci, 2013. **33**(42): p. 16471-82.
37. Urban, N.T., et al., *STED nanoscopy of actin dynamics in synapses deep inside living brain slices.* Biophys J, 2011. **101**(5): p. 1277-84.
38. Dent, E.W., *Of microtubules and memory: implications for microtubule dynamics in dendrites and spines.* Mol Biol Cell, 2017. **28**(1): p. 1-8.
39. Hu, X., et al., *BDNF-induced increase of PSD-95 in dendritic spines requires dynamic microtubule invasions.* J Neurosci, 2011. **31**(43): p. 15597-603.
40. Merriam, E.B., et al., *Dynamic microtubules promote synaptic NMDA receptor-dependent spine enlargement.* PLoS One, 2011. **6**(11): p. e27688.
41. Jaworski, J., et al., *Dynamic microtubules regulate dendritic spine morphology and synaptic plasticity.* Neuron, 2009. **61**(1): p. 85-100.
42. Esteves da Silva, M., et al., *Positioning of AMPA Receptor-Containing Endosomes Regulates Synapse Architecture.* Cell Rep, 2015. **13**(5): p. 933-43.
43. McVicker, D.P., et al., *Transport of a kinesin-cargo pair along microtubules into dendritic spines undergoing synaptic plasticity.* Nat Commun, 2016. **7**: p. 12741.
44. Costa, A.R., et al., *The Regulation of Axon Diameter: From Axonal Circumferential Contractility to Activity-Dependent Axon Swelling.* Front Mol Neurosci, 2018. **11**: p. 319.
45. Ganguly, A., et al., *A dynamic formin-dependent deep F-actin network in axons.* J Cell Biol, 2015. **210**(3): p. 401-17.
46. Leterrier, C., P. Dubey, and S. Roy, *The nano-architecture of the axonal cytoskeleton.* Nat Rev Neurosci, 2017. **18**(12): p. 713-726.
47. Xu, K., G. Zhong, and X. Zhuang, *Actin, spectrin, and associated proteins form a periodic cytoskeletal*

structure in axons. Science, 2013. **339**(6118): p. 452-6.
48. Rust, M.B. and T. Maritzen, *Relevance of presynaptic actin dynamics for synapse function and mouse behavior.* Exp Cell Res, 2015. **335**(2): p. 165-71.
49. Yau, K.W., et al., *Dendrites In Vitro and In Vivo Contain Microtubules of Opposite Polarity and Axon Formation Correlates with Uniform Plus-End-Out Microtubule Orientation.* J Neurosci, 2016. **36**(4): p. 1071-85.
50. Baas, P.W., M.M. Black, and G.A. Banker, *Changes in microtubule polarity orientation during the development of hippocampal neurons in culture.* J Cell Biol, 1989. **109**(6 Pt 1): p. 3085-94.
51. Huang, C.F. and G. Banker, *The translocation selectivity of the kinesins that mediate neuronal organelle transport.* Traffic, 2012. **13**(4): p. 549-64.
52. Nakata, T. and N. Hirokawa, *Microtubules provide directional cues for polarized axonal transport through interaction with kinesin motor head.* J Cell Biol, 2003. **162**(6): p. 1045-55.
53. Guardia, C.M., et al., *BORC Functions Upstream of Kinesins 1 and 3 to Coordinate Regional Movement of Lysosomes along Different Microtubule Tracks.* Cell Rep, 2016. **17**(8): p. 1950-1961.
54. McKenney, R.J., et al., *Tyrosination of alpha-tubulin controls the initiation of processive dynein-dynactin motility.* EMBO J, 2016. **35**(11): p. 1175-85.
55. Bentley, M. and G. Banker, *The cellular mechanisms that maintain neuronal polarity.* Nat Rev Neurosci, 2016. **17**(10): p. 611-22.
56. Farias, G.G., et al., *Sorting of Dendritic and Axonal Vesicles at the Pre-axonal Exclusion Zone.* Cell Rep, 2015. **13**(6): p. 1221-1232.
57. Lipka, J., et al., *Microtubule-binding protein doublecortin-like kinase 1 (DCLK1) guides kinesin-3-mediated cargo transport to dendrites.* EMBO J, 2016. **35**(3): p. 302-18.
58. Gumy, L.F., et al., *MAP2 Defines a Pre-axonal Filtering Zone to Regulate KIF1- versus KIF5-Dependent Cargo Transport in Sensory Neurons.* Neuron, 2017. **94**(2): p. 347-362 e7.
59. Karasmanis, E.P., et al., *Polarity of Neuronal Membrane Traffic Requires Sorting of Kinesin Motor Cargo during Entry into Dendrites by a Microtubule-Associated Septin.* Dev Cell, 2018. **46**(4): p. 518-524.
60. del Castillo, U., et al., *Interplay between kinesin-1 and cortical dynein during axonal outgrowth and microtubule organization in Drosophila neurons.* Elife, 2015. **4**: p. e10140.
61. Qu, Y., et al., *Periodic actin structures in neuronal axons are required to maintain microtubules.* Mol Biol Cell, 2017. **28**(2): p. 296-308.
62. Winding, M., et al., *Role of kinesin-1-based microtubule sliding in Drosophila nervous system development.* Proc Natl Acad Sci U S A, 2016. **113**(34): p. E4985-94.
63. Yan, J., et al., *Kinesin-1 regulates dendrite microtubule polarity in Caenorhabditis elegans.* Elife, 2013. **2**: p. e00133.
64. Harterink, M., et al., *Local microtubule organization promotes cargo transport in C. elegans dendrites.* J Cell Sci, 2018. **131**(20).
65. van Beuningen, S.F.B., et al., *TRIM46 Controls Neuronal Polarity and Axon Specification by Driving the Formation of Parallel Microtubule Arrays.* Neuron, 2015. **88**(6): p. 1208-1226.
66. Nieuwenhuis, J., et al., *Vasohibins encode tubulin detyrosinating activity.* Science, 2017. **358**(6369): p. 1453-1456.
67. Suzuki, K. and J.C. Izpisua Belmonte, *In vivo genome editing via the HITI method as a tool for gene therapy.* J Hum Genet, 2018. **63**(2): p. 157-164.
68. Nishiyama, J., T. Mikuni, and R. Yasuda, *Virus-Mediated Genome Editing via Homology-Directed Repair in Mitotic and Postmitotic Cells in Mammalian Brain.* Neuron, 2017. **96**(4): p. 755-768 e5.
69. Thorn, K.S., J.A. Ubersax, and R.D. Vale, *Engineering the processive run length of the kinesin motor.* J Cell Biol, 2000. **151**(5): p. 1093-100.
70. Tas, R.P., et al., *Differentiation between Oppositely Oriented Microtubules Controls Polarized Neuronal Transport.* Neuron, 2017. **96**(6): p. 1264-1271 e5.
71. Soppina, V. and K.J. Verhey, *The family-specific K-loop influences the microtubule on-rate but not the superprocessivity of kinesin-3 motors.* Molecular Biology of the Cell, 2014. **25**(14): p. 2161-2170.

72. Wang, Z. and M.P. Sheetz, *The C-terminus of tubulin increases cytoplasmic dynein and kinesin processivity.* Biophys J, 2000. **78**(4): p. 1955-64.
73. Tucker, C. and L.S. Goldstein, *Probing the kinesin-microtubule interaction.* J Biol Chem, 1997. **272**(14): p. 9481-8.

Stony Beach, WH
photo: Anne Pipathsouk

&

Addendum

SUMMARY

The correct distribution of molecules to different compartments is important for the assembly of all cells in our body. Active transport of these molecular building blocks is especially important in large polarized cells, such as neurons, to develop and maintain their form and function. Neurons consist of two types of long protrusions, axons and dendrites, that differ in function and molecular composition. Upon excitation of a neuron, the axon releases a chemical signal into contact zones, called synapses, with the dendrites of the next neuron in the network that can propagate the signal through its own axon. The form of the axon and dendrites is determined by the cytoskeleton, a network of biopolymers and auxiliary proteins that provide mechanical stability and plasticity. Additionally, molecular motors use the cytoskeletal components as the highways of the cell for active transport. Motor proteins distribute cargoes into the axon and dendrites by walking along actin and microtubule filaments. These are structurally polarized biopolymers with a plus- and minus-end and different motor proteins exclusively walk either to the plus- or minus-end of a microtubule or actin filament.

The work presented in this thesis addresses how the exact organization of the neuronal cytoskeleton affects molecular transport. To map the architecture of the cytoskeleton as accurately as possible, we have used different advanced microscopy techniques, predominantly single-molecule localization microscopy (SMLM). One of the main challenges of SMLM is combining different strategies to visualize the cytoskeleton components at the same time. To better visualize actin filaments, we optimized the purification and labelling of a small protein fragment, called lifeAct (Chapter 2). This led to an easy to use actin labelling strategy that can achieve high resolutions and is compatible with other existing labelling methods such as dSTORM and DNA-PAINT. This resulted in more in depth insights into the organization of actin clusters and –cables at the initial segment of the axon and the spines of dendrites (Chapter 3 and 5). Additionally, we have studied transport in living cells to identify the function of these structures. Our results show that the clusters are important to retain small transport vesicles, called organelles, at the initial segment of the axon by myosin motor proteins that walk along actin (Chapter 3 and 4). The actin cables in the spines of dendrites and their dynamics are important to recruit microtubules upon activation of the synapses in those spines. These events contribute to the plasticity of the synapse (Chapter 5).

To better understand the traffic rules along the cellular microtubule highways in neurons, it is important to known the microtubule orientations with high precision. In order to achieve this, we have developed a new method that uses purified motors, walking along extracted cytoskeletons, to reconstruct a high resolution map of the neuronal microtubule network and their orientations (Chapter 6). We termed this method motor-PAINT. After protocol optimization, we focused on the dendritic microtubule organization in order to better understand how kinesins, motor proteins that walk towards the plus-end, selectively navigate in anterograde or retrograde direction along the mixed microtubules of the dendrites.

Our experiments showed that microtubules with the same orientation are bundled into unidirectional highways. Subsequent correlative and pharmacological measurements showed that microtubules that are oriented with their minus-end away from the cell body, are in general more stable. Because kinesins prefer different groups of microtubules, we could then propose a new model for selective transport. Kinesins (such as Kinesin-1/ Kif5) that strongly prefer more stable microtubules will mainly move in retrograde direction whereas kinesins (such as Kinesin-3/ Kif1) that prefer more dynamic microtubules will predominantly move in anterograde direction. This explains earlier experiments that show that Kinesin-1 does not target the dendrites while Kinesin-3 accumulates in dendritic tips.

The research in this thesis provides us with deeper understanding in the architecture of the neuronal cytoskeleton and the traffic rules in neurons. These fundamental insights are important to better understand how neurons are build and where it goes wrong in developmental disorders or during neurodegenerative diseases.

NEDERLANDSE SAMENVATTING

De juiste verdeling van moleculen naar verschillende compartimenten is belangrijk voor de opbouw van alle cellen in het lichaam. Actief transport van deze moleculaire bouwstenen naar verschillende compartimenten is vooral belangrijk in gepolariseerde cellen, zoals neuronen, om hun vorm en functie te ontwikkelen en te behouden. Neuronen hebben twee typen uitlopers, axonen en dendrieten, die beide een andere functie en moleculaire opbouw hebben. Na activatie van een neuron, laat het axon een chemisch signaal vrij in de contact zone, genaamd synaps, met de dendrieten van het volgende neuron. Deze kan als gevolg het signaal verder het netwerk in sturen met zijn eigen axon. De vorm van de axonen en dendrieten wordt bepaald door het celskelet, een netwerk van biopolymeren en andere eiwitten die de cel zijn vorm en stevigheid geeft. Daarnaast dient het celskelet als het wegenstelsel waarlangs het transport in de cel plaats vindt. Dit transport wordt verzorgt door motoreiwitten die moleculen naar het axon en de dendrieten vervoeren door over microtubuli en actine te lopen. Dit zijn structureel gepolariseerde biopolymeren met twee verschillende uiteindes, plus en min genaamd. Verschillende motoreiwitten lopen ofwel altijd naar het plus-einde of naar het min-einde van een microtubulus of actine filament.

In dit proefschrift hebben we bestudeerd hoe de exacte organisatie van het neuronale celskelet het transport in hersencellen beinvloedt. Om de architectuur van het celskelet zo nauwkeurig mogelijk in kaart te brengen hebben we verschillende geavanceerde microscopietechnieken gebruikt. Hierbij hebben we voornamelijk gebruik gemaakt van enkele-molecuul lokalisatiemicroscopie. Eén van de uitdagingen was het combineren van aankleuringstechnieken die de verschillende structuren tegelijkertijd in beeld brengen. Om de cellulaire actine structuren beter te visualiseren, hebben we in hoofdstuk 2 de zuivering en labelling van een klein eiwitfragment, lifeAct genaamd, geoptimaliseerd. Deze optimalisatie leidde tot een gemakkelijk in te zetten kleuring van actine met hoge resolutie die gecombineerd kon worden met bestaande technieken zoals dSTORM en DNA-PAINT. Dit leidde tot de opheldering van de organisatie van actineclusters en -kabels in respectievelijk het initieel segment van het axon en specifieke uitstulpingen (spines) van dendrieten (hoofdstuk 3 en 5). Daarnaast hebben we transport in levende cellen bestudeerd om de functie van deze structuren te achterhalen. Dit wees uit dat de clusters belangrijk zijn voor het tegenhouden van transportblaasjes die niet in het axon horen door myosine motoreiwitten (hoofdstuk 3 en 4). De actine kabels in de spines en de regulatie van hun dynamiek is belangrijk om microtubuli te recruiteren wanneer de in spines gelegen synapsen actiever worden. Dit draagt bij aan de plasticiteit van de synapse (hoofdstuk 5).

Om de cellulaire microtubule-snelwegen beter in kaart te brengen is het belangrijk om de orientatie van de microtubuli in neuronen met hoge resolutie te bepalen. Hiervoor hebben we in hoofdstuk 6 een nieuwe methode ontwikkeld die met behulp van gezuiverde motoreiwitten, lopend over een geëxtraheerd celskelet, een hoge resolutie weergave geeft

van de neuronale microtubuli en hun orientatie. Deze methode hebben we motor-PAINT genoemd. Na optimalizatie van de protocollen hebben we gefocust op de microtubule-organisatie in dendrieten van neuronen. Dit was om beter te begrijpen hoe specifieke kinesines, motoren die naar het plus-einde van microtubuli lopen, selectief anterograad of retrograad navigeren in de dendrieten die een array met gemengde microtubule-orientaties hebben. Onze experimenten toonden aan dat microtubuli met een gelijke orientatie clusteren om zo snelwegen voor directioneel transport te vormen. Farmacologische en correlatieve bepalingen lieten verder zien dat microtubuli die met hun min-eind van het cellichaam afwijzen meer stabiliteit vertonen. Omdat verschillende kinesines een voorkeur hebben voor een specifieke groep microtubuli konden wij een model opstellen voor selectief transport. Kinesines (zoals kinesine-1/ kif5) die een sterke voorkeur hebben voor stabielere microtubuli zullen voornamelijk retrograad transport vertonen, terwijl kinesines (zoals kinesine-3/ kif1) die meer dynamische microtubuli herkennen anterograad zullen bewegen. Dit verklaart eerdere resultaten die aantoonden dat kinesine-1 niet naar dendrieten transporteert, terwijl kinesine-3 juist accumuleert in dendritische uiteinden.

Door de studies in dit proefschrift hebben we dus een beter inzicht gekregen in de architectuur van het celskelet en de verkeersregels in hersencellen. Deze inzichten zijn belangrijk om beter te begrijpen hoe neuronen worden opgebouwd en welke processen verstoord zijn of raken bij ontwikkelingsstoornissen of tijdens verschillende neurodegeneratieve aandoendingen.

CURRICULUM VITAE

Roderick P. Tas was born on June 15th 1991 in Den Helder, after graduating from high-school (Zwin College Oostburg) he started his bachelor in Biology at Utrecht University in 2009. During his bachelor he focused on molecular cell biology and obtained his degree in 2012. He continued at Utrecht University to obtain his master degree in Molecular and Cellular Life Sciences. During his masters he performed his major research internship in the biophysics group of Prof.dr. Lukas Kapitein (Biophysics / Cell Biology, Utrecht University), studying selective transport in neurons using advanced live- and super-resolution microscopy. For his second internship he was further trained in molecular biology and biochemistry in the group of dr. Bert Janssen (Crystal and Structural Chemistry, Utrecht University), where he purified and studied the structure of a myelin-associated inhibitor. He concluded with his MSc thesis on 'the role of the centrosome in mitotic spindle formation', that was written under the supervision of Prof.dr. Geert Kops. After obtaining his MSc degree in 2014, he started as a PhD candidate in the lab of Prof. dr. Lukas Kapitein to study the relation between cytoskeleton organization and selective transport in neurons. The results of his research are presented in this thesis. During the last year of his PhD, he received training in at the Marine Biological Laboratory (Woods Hole, MA) in the Physiology: 'Modern Cell Biology using Microscopic, Biochemical and Computational Approaches' course. As of May 2019 he started as a postdoctoral researcher at the department of chemical engineering and chemistry in the lab of Prof.dr.ir. Ilja Voets at the Technical University of Eindhoven.

LIST OF PUBLICATIONS

TRIM46 organizes microtubule fasciculation in the axon initial segment.
Harterink, M., Vocking, K., Pan, X., Jerez, E.M.S., Slenders, L., Fréal, A., **Tas, R.P**., van de Wetering, W.J., Timmer, K., Motshagen, J., Beuningen, S.F., Kapitein, L.C., Geerts, W.J.C., Post, J.A., and Hoogenraad, C.C.
Journal of Neuroscience (2019). 3105-3118.

Guided by Light: Optical Control of Microtubule Gliding Assays.
Tas, R.P†., Chen, C.-Y†., Katrukha, E.A., Vleugel, M., Kok, M., Dogterom, M., Akhmanova, A., and Kapitein, L.C.
Nano letters (2018). *18*, 7524-7528.

Exploring cytoskeletal diversity in neurons.
Tas, R.P., and Kapitein, L.C.
Science (2018). *361*, 231-232.

APC2 controls dendrite development by promoting microtubule dynamics.
Kahn, O.I., Schätzle, P., van de Willige, D., **Tas, R.P**., Lindhout, F.W., Portegies, S., Kapitein, L.C., and Hoogenraad, C.C.
Nature communications (2018). *9*, 2773.

Activity-Dependent Actin Remodeling at the Base of Dendritic Spines Promotes Microtubule Entry.
Schätzle, P., da Silva, M.E., **Tas, R.P**., Katrukha, E.A., Hu, H.Y., Wierenga, C.J., Kapitein, L.C., and Hoogenraad, C.C.
Current Biology (2018). 28, 2081-2091

Purification and application of a small actin probe for single-molecule localization microscopy.
Tas, R.P., Bos, T.G., and Kapitein, L.C.
Single Molecule Analysis (Springer) (2018), pp. 155-171.

Differentiation between oppositely oriented microtubules controls polarized neuronal transport.
Tas, R.P., Chazeau, A., Cloin, B.M., Lambers, M.L., Hoogenraad, C.C., and Kapitein, L.C.
Neuron (2017). *96,* 1264-1271. e1265.

Nogo Receptor crystal structures with a native disulfide pattern suggest a novel mode of self-interaction.
Pronker, M.F., **Tas, R.P**., Vlieg, H.C., and Janssen, B.J.
Acta Crystallographica Section D (2017). *73*, 860-876.

Myosin-V induces cargo immobilization and clustering at the axon initial segment.
Janssen, A.F†., **Tas, R.P†**., van Bergeijk, P., Oost, R., Hoogenraad, C.C., and Kapitein, L.C.
Frontiers in Cellular Neuroscience (2017). *11*, 260.

Tissue-specific protein purification approach in Caenorhabditis elegans identifies novel interaction partners of DLG-1/Discs large.
Waaijers, S., Muñoz, J., Berends, C., Ramalho, J.J., Goerdayal, S.S., Low, T.Y., Zoumaro-Djayoon, A.D., Hoffmann, M., Koorman, T., **Tas, R.P**., Harterink, M., Seelk, S., Kerver, J., Hoogenraad, C.C., Bossinger, O., Tursun, B., van den Heuvel, S., Heck, A.J., and Boxem,
BMC biology (2016). *14*, 66.

MICAL3 flavoprotein monooxygenase forms a complex with centralspindlin and regulates cytokinesis.
Liu, Q., Liu, F., Yu, K.L., **Tas, R.**, Grigoriev, I., Remmelzwaal, S., Serra-Marques, A., Kapitein, L.C., Heck, A.J., and Akhmanova, A.
Journal of Biological Chemistry, (2016). M116. 748186.

Three-step model for polarized sorting of KIF17 into dendrites.
Franker, M.A†., da Silva, M.E†., **Tas, R.P†**., Tortosa, E., Cao, Y., Frias, C.P., Janssen, A.F., Wulf, P.S., Kapitein, L.C., and Hoogenraad, C.C.
Current Biology (2016). *26*, 1705-1712.

Microtubule minus-end binding protein CAMSAP2 controls axon specification and dendrite development.
Yau, K.W., van Beuningen, S.F., Cunha-Ferreira, I., Cloin, B.M., van Battum, E.Y., Will, L., Schätzle, P., **Tas, R.P**., van Krugten, J., and Katrukha, E.A., Jiang, K., Wulf, P.S., Mikhaylova, M., Harterink, M., Pasterkamp, R.J., Akhmanova, A., Kapitein, L.C., and Hoogenraad, C.C.
Neuron (2014). *82,* 1058-1073.

† Contributed equally

DANKWOORD

Dit is het dan, het einde van mijn proefschrift en ook het einde van mijn PhD. Ik heb zoveel lol gehad en dit is mede dankzij alle samenwerkingen, de leuke collega's en de fijne vrienden die ik om me heen had.

Lukas, vanaf het moment dat ik college van jou kreeg tijdens de 3e jaars cursus 'moleculaire celbiologie' en de pex-assays voor het eerst zag wist ik dat ik aan transport in neuronen wou werken. Niet geheel zonder twijfel van jouw kant kon ik uiteindelijk aan mijn bachelor stage beginnen. Het is inmiddels alweer acht jaar later waarvan ik bijna zes jaar met plezier in jouw lab heb gewerkt. Jouw enthousiasme en oneindige hoeveelheid ideeën blijven me verbazen en ik hoop dat ik daar iets van mee kan nemen. Je gaf me de vrijheid om lekker aan projecten te sleutelen en zelf dingen op te pakken. Je gaf me ook de kans mezelf te ontwikkelen (ook al zat het weer even tegen bovenop de vulkaan in Chili) en kwam me zelfs bezoeken in Woods Hole. Voor dit alles ben ik heel dankbaar en ik zal altijd met heel veel plezier terug kijken op deze jaren. Ik vond het mooi om je lab te zien groeien en hoe je uiteindelijk professor werd waardoor ik je gelukkig ook officieel mijn promotor mag noemen. Ik hoop dat we elkaar nog vaak gaan tegenkomen en bedankt voor alles!

Casper, als mede promotor heb je tijdens mijn PhD ook een belangrijke rol gehad. Ook al ben je nog zo druk, je hebt altijd tijd voor een praatje. Of dit nou over wetenschap is of gewoon even gezellig kletsen, je geeft altijd het gevoel dat iedereen echt deel van het lab is. Verder zal ik het bescheiden huisje en het geweldige eten tijdens de Cajal zomerschool ook niet snel vergeten. Ook al hoorde ik bij Lukas zijn lab, ik voelde me altijd ook een beetje deel van jouw lab omdat ik heb mogen meewerken aan veel geweldige projecten.

Beste Anna, wat ben ik je dankbaar voor elke keer dat je kritisch naar al mijn data hebt gekeken. Ik moet eerlijk zijn dat ik dit in het begin een beetje eng vond, maar uiteindelijk keek ik altijd uit naar jouw mening en verbeterpunten. Je bent altijd zo begaan met het departement en iedereen die daaronder valt en je was op vrijdagen vaak bij de borrel te vinden om de week even samen af te sluiten. Bedankt voor alles. Corette, door je vele vragen tijdens de vrijdag meetings kwam er toch altijd een beetje 'neuroscience' om de hoek kijken bij al die celbiologische projecten. Dit zorgde voor een beetje perspectief in de projecten maar verder kwam je er tijdens de lunch ook gewoon bij zitten om gezellig over van alles te kletsen. Harold, ik zeg altijd dat als ik nog een keer een PhD zou moeten doen, ik dat in jouw groep zou doen als het kon. Inmiddels heb je een hele leuke groep getalenteerde mensen verzameld die al die toffe projecten die je hebt bedacht gaan doen dus volgens mij komt dat wel goed. Ik denk dat er nog heel veel mooie verhalen uit jouw lab gaan komen. Paul, je kwam altijd even het kantoor binnen walsen met een interessante gedachten of wat wijsheden des levens. Of je kwam gewoon even kijken of er een stukje chocolade was. Jouw colleges en de mini-stage die ik in mijn tweede jaar van mijn bachelor in jouw lab heb gedaan, hebben mij toch zeker wel naar de celbiologie afdeling gelokt. Esther, je was altijd zo aardig, positief en lekker nuchter. Ik denk

dat je dit in je colleges ook mooi mee kan geven aan de studenten, maar ik hoop ook dat je net zo betrokken blijft bij het lab op de vijfde verdieping. Verder wil ik natuurlijk ook de andere PI's bedanken die de vijfde verdieping zo speciaal en verbonden maken. In de westvleugel waren Sander, Mike en Inge altijd bezig om de celbiologie dan ook daadwerkelijk te vertalen naar de ontwikkeling van een organisme. Dit zorgde voor hele mooie samenwerkingen en mooie multi-disciplinaire projecten die de vijfde verdieping verbond. Ginny, the newest PI of them all. I wish you all the best with your new lab and I hope that you will uncover many secrets of organelle localizations and their contacts in neurons. Fons, je was er altijd voor de studenten en hebt Lukas uiteindelijk weten te overtuigen dat hij me maar als bachelor student moest aannemen. Dus als je het zo bekijkt is het daar allemaal begonnen, waarvoor dank. De colleges waren altijd een feestje!

I would also like to thanks the other members of my comittee, Erwin Peterman, Geert Kops, Britta Eickholt, thank you so much for reading and evaluating my thesis.

Mijn paranimfen, Anne en Sybren. Anne, we zijn samen aan de PhD begonnen, zaten samen in een kantoor en zijn nu elkaars paranimfen. We hebben het hele traject dus samen meegemaakt, waarbij we af en toe elkaars klankbord konden zijn. Je was (bijna) altijd enorm vrolijk en nooit te beroerd om een feestje, labuitje of cocktailavond te organiseren. Je rolde in een project dat heel anders was dan de projecten in de rest van het lab en hebt dat helemaal eigen gemaakt. Je bent een top wetenschapper die ook een goed feestje niet overslaat. Ik denk dat het in Cambridge allemaal wel gaat lukken maar ik ga je toch wel een beetje missen. Sybren, als er iets te doen is in en rond het lab, weten we zeker dat jij er ook wel bij bent. We hebben veel lol gehad in het lab, aan de lunchtafel en buiten het lab. Je was toch wel echt mijn maatje binnen het lab. Heel veel succes met de laatste loodjes van je PhD!

Het plezier dat ik heb gehad tijdens mijn PhD is mede te danken aan de open sfeer die er in het Kapiteinlab heerste. We konden lekker met elkaar over wetenschap sparren maar ook het koude ochtendzwemmen, kerstdiners en andere activiteit waren een belangrijke factor. Hier ben ik de overige kapiteinlab leden veel dank aan verschuldigd. Eugene, the master of analysis. You make the lab run as smooth as it does. I've come to know you as the friendliest guy. You always seem to be relaxed and you are always excited to try something new. Thank you for all the input and help with my projects over the years. I am very happy that you started a new adventure with Desiree and I wish you all the best. Desiree, you had such a challenging task to push the setups further into the third dimension. I really appreciated your direct sense of humor, maybe about my 'babyface', and we had a lot of laughs and drinks. I am really happy that you've found your place in the Netherlands together with Eugene. Wilco, als er een probleem was met kloneren konden we altijd bij jouw terecht. Je deed van alles wat terwijl je ook nog studenten aan het begeleiden was en zelfs toen had je nog altijd tijd voor een grapje en lolletje op het lab. Het was heel tof om met je samen te werken en een biertje te drinken in de abdijbar bij de 'biophysics' meeting. Heel veel succes in de toekomst en met alle toffe verhalen die nog uit komen. Mithila, you're such a strong, little bit stubborn and focused

person that also knows how to have fun. I enjoyed our heavy discussions about the neuronal trafficking rules and I wish you all the best. Marijn, jij was de aangewezen persoon als het aankwam op het fixen van de microscoop en daar heb ik dankbaar gebruik van gemaakt. Uitgaan met krukken naar 't Gras van de buren en je mini-colleges over fourier transformaties zullen me nog lang bijblijven! Daphne en Klara, als nieuwste aanwinsten van het kapteinlab, aan jullie nu de zware taak om de sfeer en de mooie projecten op gang te houden. Ook de oud labgenoten: Bas, tijdens mijn master heb je me alles geleerd over superresolutie microscopie. Samen hebben we de eerste motor-PAINT experimenten gedaan waarbij we bijna dansend rond de microscoop stonden. Het was heel tof om met jou te werken en laten we blijven afspreken om af en toe eens een biertje te doen! Max, je ben een geweldige wetenschapper en als er iemand van een feestje houdt ben jij het wel, de chupitos traditie zal voortleven. Ik vond het erg leuk om je paranimf te zijn samen met Anael! Petra, jouw volhardendheid om de juiste constructen voor het optogenetica paper af te krijgen was inspirerend. Het werk van jou en Max heeft de basis gelegd voor het lab. Heel veel succes en plezier in de toekomst. Anaël, man you left an impression on me and everyone. Your dancing and dress-up skills were amazing and will not be forgotten. We could always have a laugh and you played an important part in finishing the motor-PAINT story. Thank you so much for the nice conversations and all your hard work. Last but definitely not least of the members of the kapiteinlab: Chiung-Yi, working on the light induced gliding assay project together was a true pleasure. During this project but also after work I've really gotten to know you as the nicest and funniest person. I hope to see you from time to time and good luck with the final stretch of your PhD! Marina, woman of a thousand projects and laughs. I wish you all the best with your own lab.

Verder wil ik all andere (voormalige) celbiology labgenoten bedanken voor alles binnen en buiten het lab. Sara and Vida, together with Dusan, Bram, Anne and Klara, we made up room N5.09. I'd like to consider our office messy and cosy because that big cleanup never came! It was always a lot of fun even though everybody seemed particularly busy. Keep up the busy work and I hope to see you soon. Phebe, elke dag weer ontferm jij je over het lab om te zorgen dat er geen chaos uitbreekt, waarvoor heel veel dank. Maar ik zal je vooral herinneren voor alle gezelligheid tijdens de lunch pauzes, labuitjes, borrels and andere activiteiten. Je deed altijd fanatiek mee en alles kon besproken worden. Feline, lekker optimistisch en altijd gewoon lekker gaan. Je zit vol met wilde ideeën maar ook heel veel gezelligheid. Je bent een topwetenschapper die er wel gaat komen maar ook zorgt voor heel veel gezelligheid en behulpzaamheid. Dennis, geen blad voor je mond en af en toe een denkbeeldige snor. Je bent toch onmisbaar aan de lunchtafel en bij alle andere activiteiten. Het is nooit stil en altijd gezellig als jij erbij bent. Dank je voor alle leuke gesprekken. Yujie, we've had a lot of fun discussing transport in neurons and finding methods to fix the cytoskeleton. Bart, je droge, soms grenzend aan flauwe grappen hebben me vaak erg laten lachten. We konden altijd op je rekenen bij de lunch om de sfeer er goed in te houden. Ook zorgde jij er samen met Phebe voor dat het lab niet in chaos verviel. Bedankt voor alles. Boris, unfortunately you only joined

while I was finishing up so it was a short time that we were colleagues but you already made a lasting impression. I really enjoyed bouldering with you and I hope that we'll see each other soon in the bouldering gym. Peter Jan, je gaat als een speer en hebt volgens mij wel honderd projecten. We konden altijd lekker over kinesines babbelen en je hebt me veel waardevolle input gegeven. Dankjewel en succes met de laatste loodjes van je PhD. Robbelien, ik ga je ietswat donkere humor aan de lunchtafel zeker missen. Nicky, je nam het initiatief voor de eerste 'wine and cheese' avond. Verder doe je altijd toffe proeven en ben ik blij dat we samen lekker over 'single molecules' konden praten. Ook heel erg bedankt voor het organiseren van leuke activiteiten zoals het gala! Lisa en Manon, jullie waren ook altijd gezellig aanwezig bij de wine en cheese avonden en bij alle gezellige uitjes. Amol, the king of the in vitro assays. Man your work ethic was incredible. Over the years I've come to know you as an amazing cheerful guy. Good luck with your adventures in the USA and I am sure that you will achieve great things. Anna, I really enjoyed our conversations the last year. You could be a little bit sarcastic/pessimistic at times but I will not forget my surprise when I got the kindest email to wish me good luck before my post-doc interview. Thank you for that! Jelmer, we hebben onze master een beetje hetzelfde ingevuld en volgens mij is dat een goed recept. Je gaat hartstikke lekker maar kan ook lekker meedoen met een biertje alleen is 'wine and cheese' misschien toch soms wel wat teveel. Ricardo, you might be the only person who was in the lab longer than I was. You feel like part of the furniture and I think you cannot be missed. Your Italian laid back attitude was nice and you never wanted to be in the spotlight while I think you should be sometimes because you're a great guy! Martin, man waar moet ik beginnen bij jou. Volgens mij verbind jij in je eentje de hele verdieping. Je doet EM, wormenwerk, hardcore celbiologie en verder ben je ook nog eens bij elk project betrokken. Je combineert je sociaal leven met je werk en laat het allemaal makkelijk lijken, je was bij vele feestjes waaronder ook de Cajal summer school in Bordeaux waar we in random huizen terecht kwamen en vele kurken het water in hebben kunnen schieten. Ik heb erg genoten van de samenwerking en alle discussies die we over de jaren hebben gehad. Dank je voor alles. Amelie, I think you can do everything. Do great science, enjoy good food, party and be a mother. I wish you all the best. Ilya, you run a tight ship around the microscopes, thank you for keeping all that amazing equipment running! Of course also all other (past) lab members of Cell Biology, Jessica, Liu, Eitan, Qingyang, Ivar, Lena, Xingxiu, Robin, Ankit, Ruben, York, Carlijn, Fangrui, Dipti, Phil, Mariella, Funso, Cynthia, Arthur, Hai Yin, Marvin, Jiang, Lotte, René, Katerina, Irati, Inês, Olga, Laura, Elena, Ruddi and Babet, thank you all for the great atmosphere and wonderful time. I would also like to thank all the members of the Developmental Biology team for the nice contributions and questions during the Monday meetings but also the fun during the lab outings.

I would also like to thank my supervisors during my master internships. Joanna, Hedwich en Bert, I've learned so much from you all and you prepared me very well for life as a PhD student. I remember driving you crazy sometimes by being stubborn and doing things

my own way but you always managed to steer me into the right direction. Thank you for this.

Verder heb ik om mijn beurt weer met hele leuke studenten mogen werken die veel hebben bijgedragen. Maaike en Daphne, jullie waren echt een team en jullie hebben veel waardevolle data gegenereerd die nog steeds niet allemaal verwerkt is. Dank jullie voor al het harde werk en heel veel succes met jullie PhD. Trusanne, halverwege moesten we het project even omgooien maar het was altijd erg gezellig. Uiteindelijk is het allemaal goed gekomen en hebben we zelfs nog een mooi boekhoofdstuk kunnen schrijven dat deel is van mijn thesis.

Naast het werk in het lab heb ik ook veel steun en soms nodige afleiding gehad van veel mensen buiten het lab. Pa en Ma, jullie hebben me alle mogelijkheden gegeven om te komen waar ik nu ben. Jullie hebben me altijd onvoorwaardelijk gesteund en een opvoeding gegeven op een mooie plek waar altijd alles besproken kon worden. Dank jullie voor alles en ik ben blij dat jullie vanuit de VS komen om bij mijn promotie te zijn! Pauline en Liselotte, of we nou pokemon speelden of ruzie maakten op de achterbank van de auto naar Frankrijk het was altijd leuk. Nu doen we heel veel samen en ik ben heel blij dat ik met jullie als zusjes kon opgroeien! Sam, jij bent ook niet meer uit ons gezin weg te denken. Al vele jaren zorg je voor extra gezelligheid tijdens alle familie aangelegenheden. Heel veel plezier samen met Lot in Haarlem (ahum sorry, Alkmaar). Oma Tas (Oma Speculaas), heel erg bedankt voor de leuke vakanties in Zeeland, het logeren en de speculaasjes op brood. Ook heel erg bedankt dat we vaak gewoon zomaar even bellen en dat je even vraagt hoe het gaat.

Ook wil ik de vrienden die ik heb gemaakt tijdens mijn studie bedanken voor alle goede tijden. Robin, mijn mentor papa. Samen met Julia hebben jullie de familie wat weten uit te breiden. Je hebt een tof huisje en bent ook door een PhD aan het buffelen. We hebben altijd wat om over te praten en laten we dat ook wat vaker gaan doen. De overgebleven mensen van 'Gecellig', de celbiologie studenten van de vijfde verdieping tijdens mijn eerste stage. Reini, Leon, Spiros, Frank en Jesminne, leuke dingen doen met jullie was één van de nieuwe hoogtepunten tijdens mijn master. Maisvelden ploegen en verbrande kip eten of lekker uitgaan. Jesminne heel erg bedankt voor al je steun, ik weet dat het zeker niet altijd makkelijk is geweest.

Davy, Tom, Vi, Jasper, Edwin, Daphne, An, Oscar, Fabian en natuurlijk ook Pauline. Al jarenlang met z'n allen op wintersport, uitjes, citytrips, mannenuitjes en lekker biertjes drinken in de Lane. Ik herinner me alleen maar leuke, zatte en mooie tijden en ben heel blij dat ik tijdens het turnen met jullie bevriend geraakt ben. Ook al is iedereen drukker en drukker, we maken nog steeds bijna maandelijks tijd voor elkaar om wat te gaan doen of gewoon even met elkaar te praten. Ik hoop dat dit in de toekomst nooit gaat veranderen. Inmiddels breidt de groep zich aardig uit en dat brengt alleen maar meer gezelligheid! Dennis, het kon niet toevalliger zijn dat we 100 meter van elkaar woonden toen we begonnen met studeren. We zaten 3 keer per dag samen koffie te drinken of frikandellen uit het tosti-ijzer te eten. Eerst besparen op eten dan pas op de belangrijke zaken! Over de jaren hebben we zoveel

gekke dingen gedaan maar nu we ouder worden moet ik toch wat tijd afstaan aan Manon en worden we wat tammer. Ik ben altijd welkom bij jullie voor een bbq of als het even tegen zit, heel erg bedankt daarvoor. Wesley, op weg naar survivalkamp in de 2e kwamen we erachter dat we het wel goed konden vinden. Je kwam wekelijks helemaal uit Aardenburg om bij Henk een zwaar ontbijt te nuttigen voor de lessen en tegenwoordig maak je ook nog wel eens een lekker ananasje klaar voor onderweg. We gaan wekelijks boulderen of eten en ik zal oprecht m'n best doen om vaker op tijd te komen. Martin, tijdens mijn tweede stage bood je aan om samen aan Python te beginnen. Dat is inmiddels al even geleden maar we gaan nog steeds wandelen en wat eten. Op nog vele mooie wandeltochten!

Julia, *me luv you long time*. Je was er om de laatste loodjes te verlichten en me lekker van mijn werk te houden, heel erg bedankt daarvoor! Ik heb heel veel zin in de toekomst.

Dat is m dan echt!

-Hora est.